CRANFIELD UNIVERSITY

Stephan Herbst

Investigation of a ceramic metal matrix composite functional surface
layer manufactured using gas tungsten arc welding.

School of Aerospace, Transport and Manufacturing
Research degree

PhD welding
Academic Year: 2013 - 2014

Supervisors: Dr. Supriyo Ganguly, Prof. Stewart Williams
September 2014

CRANFIELD UNIVERSITY

School of Aerospace, Transport and Manufacturing
PhD

Doctor of Philosophy in welding

Academic Year 2013 - 2014

Stephan Herbst

Investigation of a ceramic metal matrix composite functional surface
layer manufactured using gas tungsten arc welding.

Supervisors: Dr. Supriyo Ganguly, Prof. Stewart Williams
September 2014

ABSTRACT

Wear resistant surfaces with high toughness and impact resistant properties are to be created to improve the life cycle cost of brake discs for trains. A potential solution to this industrial problem is to use an arc cladding process. This work describes the application of gas tungsten arc welding (GTAW) for a structural ceramic Metal Matrix Composite (MMC) on steel. The structure of the two ceramics examined indicates the possibility of development of a wear resistant surface, which would extend the life of the brake disc. Silicon Carbide (SiC) and Tungsten Carbide (WC) ceramics were studied to embed them in a steel matrix by an advanced GTAW method. WC particles penetrated the liquid weld pool and also partially dissolved in the steel matrix, whereas, SiC because of the physical properties never penetrated deeper into the weld pool but segregated on the surface. Successful embedding and bonding of WC led to the decision to exercise an in-depth analysis of the bonding between the WC particles and the matrix. Chemical analysis of the matrix revealed more WC dissolution as compared to particle form within the clad. It was observed that WC reinforcement particles built a strong chemical bond with the steel matrix. This was shown by electron backscatter diffraction (EBSD) analysis. The hard clad layer composed of WC reinforced steel matrix gave an matching friction coefficient to high-strength steel in cold wear conditions through Pin-on-Disc wear and friction testing. A prototype railway brake disc was created with the established GTAW parameters to find out the difficulties of producing industrial scale components.

Keywords:

Silicon carbide (SiC) ceramic, Tungsten Carbide (WC) ceramic, steel based clad layer, Tungsten Inert Gas welding (TIG)

旻睿, 謝謝 我的 好 寶寶!

Minrui Zhang, ich danke Dir von allem Herzen, mein Baby!

ACKNOWLEDGEMENTS

To my girlfriend, Sissi Minrui Zhang: Dear Baby, we met in the most difficult time for a relationship. You are the most grateful present to me. Without your engagement and drive the thesis would have had more and more delays … . Nevertheless, we had some nice days in Britain and Germany. My friends, family and working colleagues (from both, Cranfield and the MTC) like you and your breath-taking smile. You even satisfied my grandfather with your elegance and intelligence. Let's take the future for more cheerful moments together and let them never end. **We will make it!**

To my friend and his wife Niels and Stefanie Püschner: Vielen Dank euch beiden für eure aufrichtige und seelische Unterstützung. Ihr wart und seid immer für mich da, ob in guten oder schlechten Zeiten.

To my brother and my sister: Danke euch, Christian Herbst und Vanessa Sissi Herbst, für eure einfühlsvolle Mithilfe und die langen nächtlichen skype-Telefonate. Ihr gebt mir immer einen Rat, wenn dieser gerade nötig ist. Wir unterstützen uns alle. Insbesondere immer dann, wenn wir uns brauchen.

To my grandfather: Vielen Dank, Herbert Max Herbst, für Deine aufrichtigen und weisen Ratschlägen. Du hast eine sehr große Familie durch eine sehr schwierige Zeit gebracht und kannst diese hoffentlich noch lange genießen. Wir werden Dir noch weitere schöne Zeiten geben!

Finally, I am grateful to all staff and students of Cranfield University who gave me full assistance, guidance, education and social support during my time at Cranfield.

TABLE OF CONTENTS

LIST OF FIGURES

xxi

LIST OF TABLES

LIST OF EQUATIONS

NOMENCLATURE

µ	'coefficient of friction' or 'friction coefficient' (-)
A	area (mm^2)
a	distance between tungsten electrode and work piece (mm)
at%	atomic per cent
bw	bead width (mm)
c	distance between the feeder nozzle and the substrate base plate (mm)
d	distance between the feeder nozzle and the tungsten electrode (mm)
F_N	Force generated by a normal load (N)
F_T	Friction force (N)
HB	hardness according to Brinell
HLD	hardness according to Leeb rebound
HRB	hardness according to Rockwell (measured by a ball)
HRC	hardness according to Rockwell (measured by a cone)
HV	hardness according to Vickers
I	electrical current (A)
id	distance of the centre of the plate to the inner clad (mm)
I_{max}	maximum electrical current (A)
IP	[powder] impingement point (mm)
l_x	length of the number x (mm)
M_t	Momentum ($kg \cdot m \cdot s^{-1}$, also equivalent $N \cdot s$)
P	power (W, also equivalently J/s)
p	pressure (MPa, whereby 1 MPa = 10 bar)
PCE	powder capture efficiency
PFR	powder feeding rate (g/min)
R_c	rate of cooling (K/s, also equivalent °C/s)
R_h	rate of heating (K/s, also equivalent °C/s)
TS	Travel Speed (m/min)
v	velocity (m/s)
vol%	volume per cent
v_{rot}	rotation velocity (rpm)

w	weight (kg, whereby 1 kg = 1000 g)
WFS	Wire Feed Speed (m/min)
wt%	weight per cent
ΔG	energy of Gibbs (J)
ΔH	change of standard enthalpy (J)
ΔS	change of standard entropy (J/K)

LIST OF ABBREVIATIONS

AC	alternating current
AMV	real time weld quality analyser
AR	aspect ratio
bcc	body-centred cubic [phase]
BSE	back-scattered electron [imaging]
CAD/CAM	computer-aided design and manufacturing
CJC	cold junction coefficient
DC	direct current
DL	dilution
DTV	disc thickness variation
EBSD	electron backscatter diffraction
EDX	Energy-dispersive X-ray spectroscopy (EDS, EDX, or XEDS)
fcc	face-centred cubic [phase]
FE	finite element
GMAW	Gas Metal Arc Welding (also MIG or MAG)
GTAW	Gas Tungsten Arc Welding (Tungsten Inert Gas welding [TIG])
HVOF	high-velocity oxygen fuel [thermal spraying]
M	metal
MAG	Metal Active Gas [welding process]
MIG	Metal Inert Gas [welding process]
MMC	Metal Matrix Composite
NDT	non-destructive testing
NLPM	gas flow in normal litre per minute
POD	Pin-on-Disc [wear test]
PTA	Plasma-transferred arc [welding process]
SEM	scanning electron microscope
TIG	Tungsten Inert Gas [welding process] (also GTAW)
UTS	Ultimate Tensile Strength
WELPC	Welding Engineering and Laser Processing Centre [of Cranfield University]
YS	Yield Strength

LIST OF CHEMICAL SYMBOLS

Al	Aluminium
Al_2O_3	Aluminium oxide [ceramic]
Ar	Argon
C	Carbon
Co	Cobalt
Cr	Chromium
Cu	Copper
Fe	Iron
He	Helium
HNO_3	nitric acid
N_2	Nitrogen (gas)
Ni	Nickel
O_2	Oxygen (gas)
Si	Silicon
SiC	Silicon carbide [ceramic]
SiO_2	Silicon oxide
W	Tungsten
WC, W_2C	Tungsten carbide (different structures)

1 Introduction

There is a requirement to improve the lifetime of railway brake discs without hugely increasing the cost. Current technology uses cast iron which is cost-effective but has a relatively low performance. Much higher performance can be achieved with other materials such as SiC infused – carbon fibre composite but the cost puts them out of reach for many applications. There is a need for high performance discs but with only marginally increased costs compared to the cast iron variant [1]. The key factors for a high performance brake disc are higher energy consumption per wear loss (MJ/cm^3), heat conduction of the wear surface away from the interface and weight reduction compared to cast iron discs. A solution is the replacement of the wear surface, which can be as thick as 18 mm, by a functionally graded material. The following benefits will result out of it:

- Using a ceramic reinforcement clad reduces the thickness of the wear surface. Therefore, it reduces the disc weight, which results in a weight reduction of the whole bogie.
- Brake discs need to be replaced every two years, which is a complex process. The reiteration can be reduced.
- To avoid cracking patterns the wear surface layer must be functionally graded. This improves the mechanical integrity.
- A commercial device, like a brake disc, is cost restrained and a low cost layer production process is needed.

A potential solution to this industrial problem is to use an arc cladding process. Cladding is an interdisciplinary science utilizing laser or arc technology, computer-aided design and manufacturing (CAD/CAM), robotics, sensors and control, and powder metallurgy. It is a technique in which the laser or arc is used as a source of heat to melt materials in the form of powder and/or wire, depositing it on a substrate to build a desired thin layer coating [1].

A great variety of materials can be deposited on a substrate using laser or arc cladding by powder injection. Functionally graded materials can be made by

the injection of two different powders or by using a wire and powder combination [1].

The latest production methods in surface cladding focus on laser welding or vapour deposition. The latest investigation concentrates on these production methods for new materials or different product geometries. However, Gas Tungsten Arc Welding (GTAW) can be a viable alternative to laser welding or vapour deposition with similar production time [2] and reduced cost. Surfaces of components subjected to high frictional forces and wear should be very hard and have high toughness to prevent cracking. This thesis focuses on developing ceramic based Metal Matrix Composite (MMC) layers on a steel base. The GTAW method generates a metallic bonding to the component by deposition of a metal based matrix material. The reinforcement phase is fed as powder in the process. In contrast to a laser based process, its matrix phase is widely supplied by melting a wire rather than powder. Moreover, the metallic bond of the matrix and the substrate is easy to achieve, when compared to vapour deposition coating. The change from powder to wire in the GTAW process enables the use of reduced Ni, Cr and Cu contents in the matrix as these materials are commercially accessible. This limits the toxic and carcinogenic dust developed in high wear and friction cases. The brake disc cladding layer complies with current environmental standards.

GTAW is used only for high precision metal cladding because of its low production rate. Inner wall cladding of pipelines is a good example as the access is limited. The advantage of GTAW, in comparison to Gas Metal Arc Welding (GMAW), is that the heat input is independent from the material (wire) addition. This is an important control factor when two different material addition units, e.g. a powder feeder and a wire feeder, are used. However, with the GTAW process the production speed is very similar to the laser cladding process for a work piece with the same dimensions and features [2]. This was also shown in the manufacturing performed within this study. In the described GTAW process, powder and wire were added in the same weld pool. GTAW can be performed in an autogenous mode and therefore, is capable of adding

only powder into the weld pool, whereas in the GMAW process wire feeding is necessary. In laser cladding processes, matrix and reinforcement powders are mostly premixed and applied by a powder nozzle. Therefore, the ratio of matrix and reinforcement depends on the pre-prepared mixture.

An indicator of the productivity is the dimension of a single cladding track in transverse cross section. For a specific welding parameter, a wide and flat cladding bead covers a surface area, whereas, a higher single bead track could be used for a thicker surface layer.
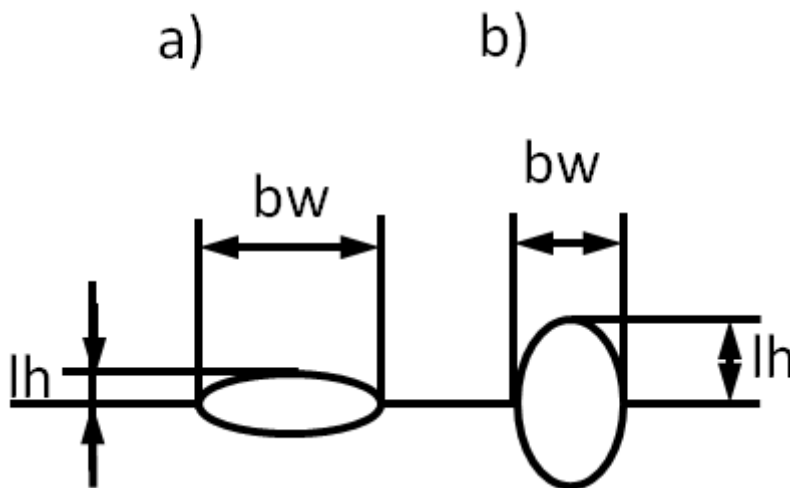
Figure 1-1: Schematic drawing of the different weld bead shapes; a) wide and flat bead; b) high and narrow bead; lh – layer height, bw – bead width

As seen in figure 1-1, a wide cladding bead is usually flat (Figure 1-1 a) and a high bead is usually narrow (Figure 1-1 b). In the experiments performed here, the suitable welding parameters were found to cover the surface efficiently. Experiments to alter the welding parameters were focussed on changing the shielding gas and the tungsten electrode angle. As expected, the microstructural characteristics and bead dimensions alter when changing the shielding gas and the tungsten electrode angle.

In the microscopic investigations of the wear resistant surface layer, three main phases were recognised: the matrix material phase; the ceramic phase; and a

new matrix composition with ceramic dissolved in it. In this thesis the ceramic proportion in the composite structure was analysed and the amount dissolved was interpreted.

In Pin-on-Disc wear and friction tests with moderate operating temperature (up to 290 °C) and wear speed (up to 24.48 km/h), it was shown that the friction coefficient does not change significantly with increase in ceramic reinforcement content. Even a comparison with railway disc high strength steel values has not shown any significant change. The developed surface layer is capable of maintaining a similar friction coefficient to the high strength steel. Prototype discs were prepared to evaluate extent of issues during cladding when scaling up into practical welding conditions. Microscopic cracks appeared on the surface during cladding and grinding of the prototype disc.

The main focus of this thesis is investigation of the underpinning process mechanism of GTAW for MMC cladding. This was achieved throughout the alternation of welding and set-up parameters to obtain a reliable and, cladding process wise, repeatable structure. A ceramic Metal Matrix Composite (MMC) surface layer creates a functional layer for friction resistant purposes. Additions of ceramic powder also resulted in a hardened layer as the ceramic dissociated and precipitates formed solid solutions within the matrix phase. The influencing GTA cladding parameters were established. SiC ceramic provides only the possibility of reinforcement with intermetallic phases. These show a lower hardness than the ceramics but a regular configuration.

2 Research aim and objectives

The research aim of this thesis is the investigation of conventional arc based welding methods to generate ceramic reinforced cladding layers with specific levels of reinforcement and steel as the matrix for the purpose of producing a functionally graded material. Furthermore, the layer is analytically characterised and friction tested.

2.1 Objectives

This research is to understand the layer microstructure and its effect by laying down overlapped layers with various ceramic materials and determining their interaction with GTA welding parameters. The objectives are listed below:

- Identification of suitable ceramic reinforcement after literature refinement,
- Investigation of optimum arc source and welding parameters,
- Determination of process parameters which affect the level of reinforcement obtained,
- Investigation of the microstructural characteristics of the MMC layer,
- Characterisation of the tribological properties of MMC clads,
- Investigation of the suitability of GTA cladding for a full size railway brake disc.

2.2 Structure of the thesis

The thesis is structured based on the chapters as given below. It is worth mentioning at this point that each chapter has its own description of experiments, results and summary.

The different chapters are as follows;

- Introduction: An overview of the benefits of GTA cladding and the outcomes of the present investigation are given.

- This chapter: Defines the objectives of this thesis and the way it is structured.

- Background: Focuses on state-of-the-art knowledge from scientific and industrial sources based on applications of GTAW for cladding purposes. It also describes the physical effect of ceramic particles in steel used as reinforcement phase. Additionally, the basic mechanism of metal loss by friction and wear is reviewed with the aim to understand the microstructural condition suitable for braking application.

- Chapter 4: Defines the process window, the boundary conditions of the GTAW process and of the ceramic powder flow during powder feeding.

- Experimental chapter 5: This is about the published work on SiC ceramic powder infused in a GTA cladding process and its results for microstructure and mechanical properties. SiC did not retain in the steel matrix.

- Chapter 6: Deals with the basic measurements of the above parameters when the shielding gas and electrode angle change. The mechanical effects on the microstructure are also disclosed here.

- Chapter 7: Examines the effect of GTAW process parameters on the interaction of WC with a steel matrix and also its influence on mechanical properties.

- Chapter 8: This chapter is about understanding the effect of different MMC compositions on friction coefficients.

- The industrial usage of the development is illustrated in chapter 9: This chapter discusses the effect of the continuous and prolonged use of GTAW to create the prototype for dynamometer testing.

- Chapter 10: Provides a broad summarisation of all the previous chapters and discusses the results obtained.

- Chapter 11: Concludes the findings and their impact on the current scientific developments.

This thesis structure provides an understandable overview of the work written.

3 Background: Cladding processes on steel

The principle of a cladding process is usually the covering of a relatively inexpensive substrate material with a more expensive alloy that will increase the resistance of the component to wear or corrosion [3]. In this particular case a ceramic reinforced Metal Matrix Composite (MMC) surface layer is to be clad on steel.

3.1 Gas Tungsten Arc Welding process

The Gas Tungsten Arc Welding (GTAW) process, also known as the Tungsten Inert Gas (TIG) process, is a widely used welding process. It has a welding torch with a non-consumable tungsten rod as an electrode which establishes a stable arc to the counterpart electrode, the base material. The GTAW system has a coaxial shielding gas cover which creates an inert atmosphere to protect the weld pool and the tungsten electrode. The arc liquefies with a high current (usually between 100 A and 350 A) and low voltage (approximately between 15 V and 25 V) generated heat the surface of the base material. The current is usually controlled by the power source. The voltage is controlled by the distance between the two electrodes (a) and the shielding gas. For a firm weld bead the torch moves relative to the base material with a set Travel Speed (TS). This system can work autogenously without additional material, as seen in figure 3-1.
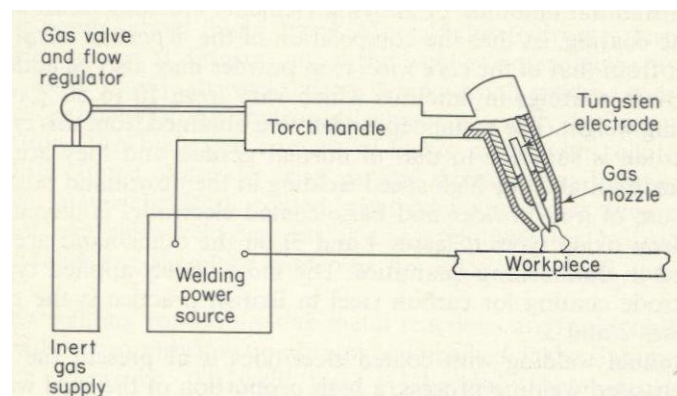
Figure 3-1: Schematic Gas Tungsten Arc Welding equipment [4]

7

Welding in various working positions, as described in BS EN ISO 6947:2011 [5] is possible but generates different issues with gravity. The working position PA according to BS EN ISO 6947:2011 was chosen for the cladding process. As seen in figure 3-2, this replicates a downhand welding in a flat position.
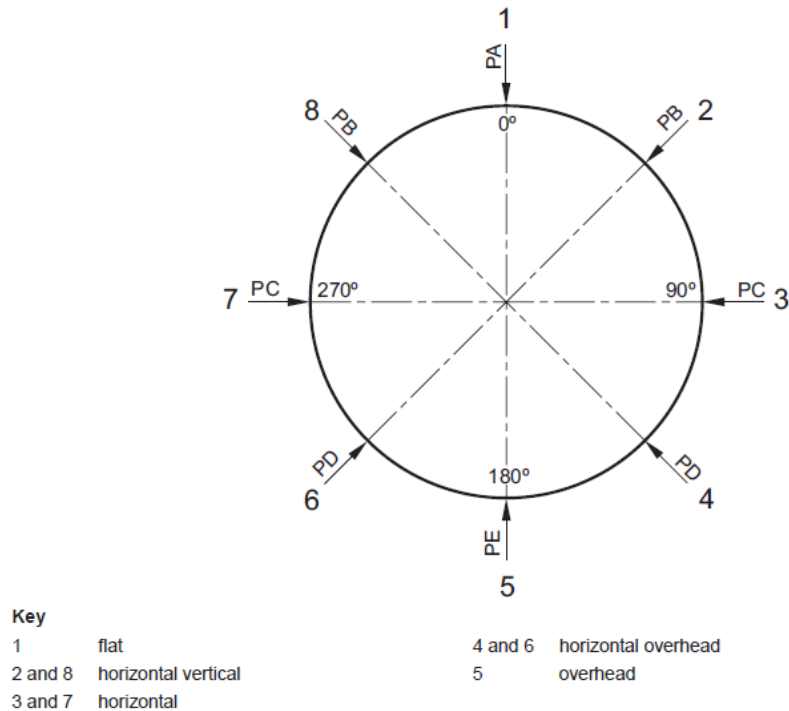
Figure 3-2: Main welding positions according to BS EN ISO 6947:2011 [5]

Although in the PA position, the torch is often held at an angle which is different from 90°, as shown in figure 3-1. Usually additional metal wire is fed into the arc to deposit weld metal. The wire must be dry and dirt-free as impurities could disturb the welding process and could result in defects of the weld bead [6]. The wire is usually fed from the front (leading) of the arc into the melting pool of the base material, but can also be fed at the back (trailing) [7]. Front feeding of wire is most common as it gets the most heat from the arc. The deposition rates can progressively be increased by using cold wire, hot wire and hot wire with oscillation systems, respectively [8]. Feeding of metal powders is also possible but rarely used [9]. The waveform of GTAW power sources can be in direct current (DC) or in alternating current (AC). A pulsed current is usually a modified direct current. In GTA cladding is usually DC used [7], [10]–

[12]. In the GTAW system inert gases such as argon (Ar), helium (He) or mixtures of Ar and He are mainly used. Active gases such as oxygen (O_2), hydrogen (H_2) and carbon dioxide (CO_2) can be mixed into Ar or He. The active gases are used in low proportions (under 1 %) and would destroy the tungsten electrode in higher concentrations [13].

3.2 Application of GTAW as a Cladding Process

A cladding process is usually used to put a layer of material on to a base or substrate material. According to the type of application the layer should have either different mechanical or chemical properties, or both. Welding processes are mainly used for strong metallic and chemical bonding [14]. There are three purposes for which cladding technics are usually used:

- To repair parts with worn down areas or broken edges [15], [16],
- To improve the corrosion resistance of a surface of a low corrosion resistant material [17], [18],
- To increase the wear and friction behaviour of a low resistance material [11], [19].

In this thesis, the aim is to look at surface cladding for any improved wear resistance and friction properties. An improved wear resistance, compared to the substrate, is usually achieved by significantly increasing the hardness [20], [21]. Therefore the substrate, also called bulk material, must provide the toughness needed. Surface layer generated by arc cladding methods show principally two different layer morphologies;

- Either a metal matrix composite (MMC) is generated where the ceramic reinforcement phase increases the wear performance [10], [22], [23], or
- the particles fed into the process react with the matrix, and form a uniform layer with new chemical and mechanical properties [21], [24], [25].

9

In the first case, the microstructures of the matrix and the reinforcement are clearly seen in the microsection. Therefore, the chemical and mechanical properties of the matrix and the reinforcement phase are different. The reinforcement, for example, from approximately 1800HV to 3000HV, can be as hard and brittle as a ceramic. The hardness of steel matrices increases to values between approximately 500HV and 670HV [26], [27]. The hardness of steel (150HV to 270HV [28]) wasn´t reached in the matrix of MMCs in the literature assessed. However, the matrix material and the reinforcement have usually different mechanical and chemical properties from the substrate.

The second method creates uniform surface layers with hardness of up to approximately 1390HV [20] which cannot be divided into separate phases.

3.3 Effect of particle size on Metal Matrix Composites

In MMCs, a wide range of particle sizes are used. The European recognised standard FEPA 42-1:2006 describes a particle size (in µm) as the shortest side of the particles used. This principle comes from mesh sieving methods used to divide the different fractions of ceramics. Instead of the actual particle size, sometimes the mesh numbers are shown, whereby increasing mesh numbers show decreasing particle sizes [29], [30]. Generally the ceramics are divided into nano- and microscale particle sizes.

Nanoscale ceramic particles (shortest side smaller than 1 µm) are not often used in wear resistance applications, although some Al-based MMCs were analysed for their mechanical strength [31], [32].

Ceramic particles in microscale (shortest side bigger than 1 µm) are widely used and are the most common reinforcements in surface cladding layers as well as metal matrix composites. The particle size, used as reinforcement varies from 1 µm to 1000 µm [29], [30]. Particle sizes between 3 µm and 500 µm are widely implemented for their thermal and mechanical properties [22], [33].

Regarding the nature of particles, the boundary between nano- and microscale is sometimes not very clear [34] and should only be seen as an indication. Powder particles are mainly delivered in a range of particle sizes. An example is particles with the shortest length of 1 µm. In this case is the size and range of delivery in nano- and microscale.

Ceramic particles are mainly produced in either a spherical shape [35] or a broken form without any specific shape [36]. The shape and orientation of ceramic particles has an important influence on the mechanical properties, such as yield strength, ultimate tensile strength (UTS) and Young´s modulus, of an MMC. Spherical particles in a metal matrix have the most predictable properties. However, non-uniform shaped particles have shown improvements in the yield strength and ultimate tensile strength compared to the pure matrix material [37].

Papers describing ceramic particles giving a notch effect (, with dropping yield strength and ultimate tensile strength,) instead of a reinforcement were not found for the assessed concentrations of between 5 % and 70 % volume fraction.

The type of bonding between the matrix and reinforcement phase has a significant influence on the mechanical and thermal properties of MMCs. There are physical and chemical bonds which influence the plastic response and physical properties, e.g. thermal conductivity of the composite structure [33], [34], [38].

In pure physical bonding, demonstrated on spherical steel particles in phenolic based matrix material, a cohesive law determines the relation between matrix and reinforcement [39] (see figure 3-3).
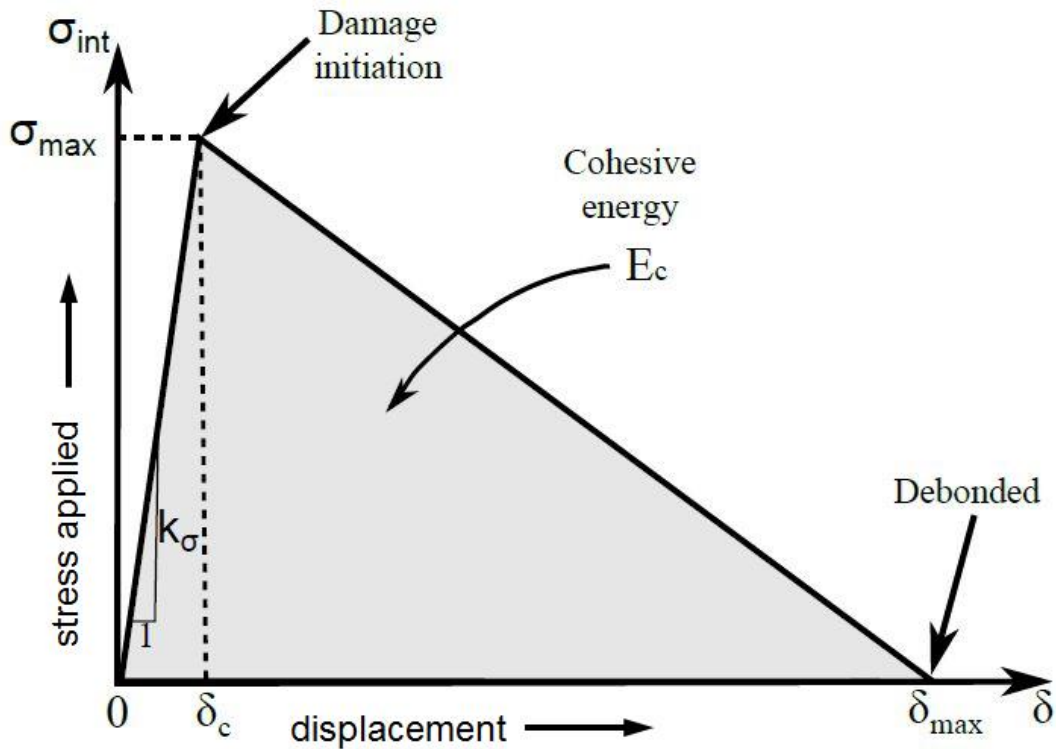
Figure 3-3: Cohesive law of bonding between reinforcement particles and matrix material with pure mechanical bonding [39]; k_σ cohesive stiffness, σ_{int} cohesive strength, σ_{max} maximum cohesive strength, E_c cohesive energy, δ displacement, δ_c displacement until σ_{max}, δ_{max} maximum displacement of the composite.

The theoretical strength-displacement curve, according to the cohesive law of a composite with mechanical particle bonding, is shown in figure 3-3. In an ideal mechanical bond and with initiated displacement (δ), the strength (σ) increases linearly between particle and matrix in the elastic region first until damage occurs (δ_c, σ_{max}). The cohesive stiffness (k_σ) can be calculated from the slope of the curve in the elastic region, as demonstrated in figure 3-3. Further application of stress results in more deformation and crack propagation until failure (δ_{max}). The cohesive energy (E_c) is the integral of the strength over the displacement until failure (δ_{max}) [39], [40].

Chemical bonding depends on ideal ambient conditions, such as chemical composition, size of the system, temperature and partial pressure, to start a

reaction [41]. In the case of a chemical bond, part of both the ceramic and matrix are used to create a new structure which forms the bonding between the matrix and the ceramic. In some cases the ceramic becomes fully dissolved in the microstructure and it is not possible to create an MMC. One example is the reaction between SiC and Fe [42]. In the case of the WC ceramic and steel, the Fe component is an important factor to build W_xFe_yC intermetallics. These can either form out of the molten phase of steel infused with the WC or, more commonly, in the solid state during cooling down. The large amount of Fe and the ability of C to diffuse in the solid state of steel gives the possibility of solid-state reactions to build up a bond between reinforcement particles and the matrix [41][43]. Figure 3-4 shows an isothermal section of the W-Fe-C system for the temperature of 1250°C.
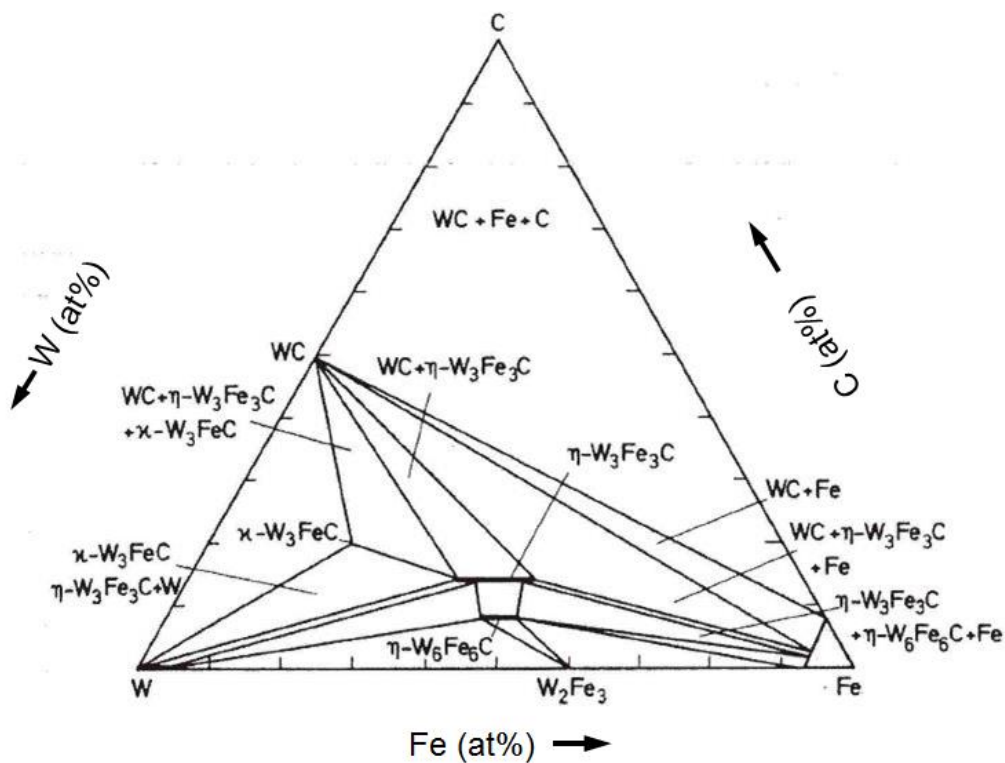
Figure 3-4: Isothermal section of W-Fe-C system at 1250°C [41].

At this temperature, iron with a C content lower than 3.3 wt% C is solid. Low alloyed carbon steel is commonly described as iron with a C content from >0 wt% C to 0.59 wt% C. As a result, all carbon steel grades infused with WC

ceramic would try to reach the W_xFe_yC phases in the diagram in figure 3-4 at 1250°C. However, the W-Fe-C diagram is only for the equilibrium cooling conditions. This means a chemical reaction between Fe and WC to form W_xFe_yC phases depends on the time the temperature is applied [41]. When the temperature decreases, the affinity of WC and Fe to build intermediate compounds diminishes. According to Liu *et al.* [43], the minimum temperature for the reaction between Fe and WC is 927°C, which is known as the "temperature of carbonizing". Their tests at 930°C show the diffusion of C out of WC into steel and a surface alloy formed of W_xFe_yC-phase. The Gibbs free energy change of reaction (ΔG) formula, as shown in equation (3-1) [44], determines the feasibility of thermodynamic formation of a phase.

$$\Delta G = \Delta H - T * \Delta S \qquad\qquad \textbf{(3-1)} [44]$$

Where ΔH is the standard enthalpy change of reaction in kJ $\cdot$ mol^{-1}, T is the absolute temperature in K and ΔS is the standard entropy change of reaction in J $\cdot$ K^{-1} $\cdot$ mol^{-1} [43].

Calculations of the free energies of the formation of Fe_3C and WC at 927°C are as follows:

$$C + 3Fe = Fe_3C, \qquad \Delta_f G_m^\Theta = -712.99\ kJ \cdot mol^{-1} \qquad\qquad \textbf{(3-2)}$$

and

$$C + W = WC, \qquad \Delta_f G_m^\Theta = -757.08\ kJ \cdot mol^{-1} \qquad\qquad \textbf{(3-3)} [43].$$
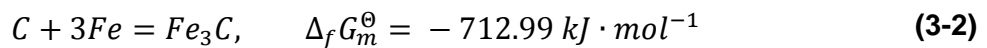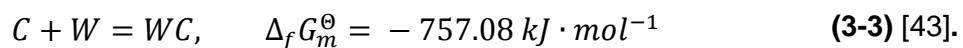
The smaller enthalpy change of WC ($\Delta_f G_m^\theta$) means that this compound is more stable than Fe_3C. Both reactions form compounds instead of carbon and metal because the values are negative. This was demonstrated by the microsections shown in the article [43].

A mixture of chemical and mechanical bonds is often seen in ceramic MMCs. Many mechanisms are in place in case of applied stress to these MMCs. The particles have two strengthening effects: direct and indirect. Loads which are transferred from the matrix to the particle and back into the matrix result in

direct strengthening. Matrix and particle would deform in the case of plastic strain.

However, indirect strengthening (dislocation strengthening) is the influence of reinforcement particles on the microstructure of the matrix. The presence of particles induces an inhomogeneous deformation pattern in MMCp, even if the composite is subject to uniform loading and high dislocation density in the composite matrix, thus leading to higher yield strength in the composite matrix [33].
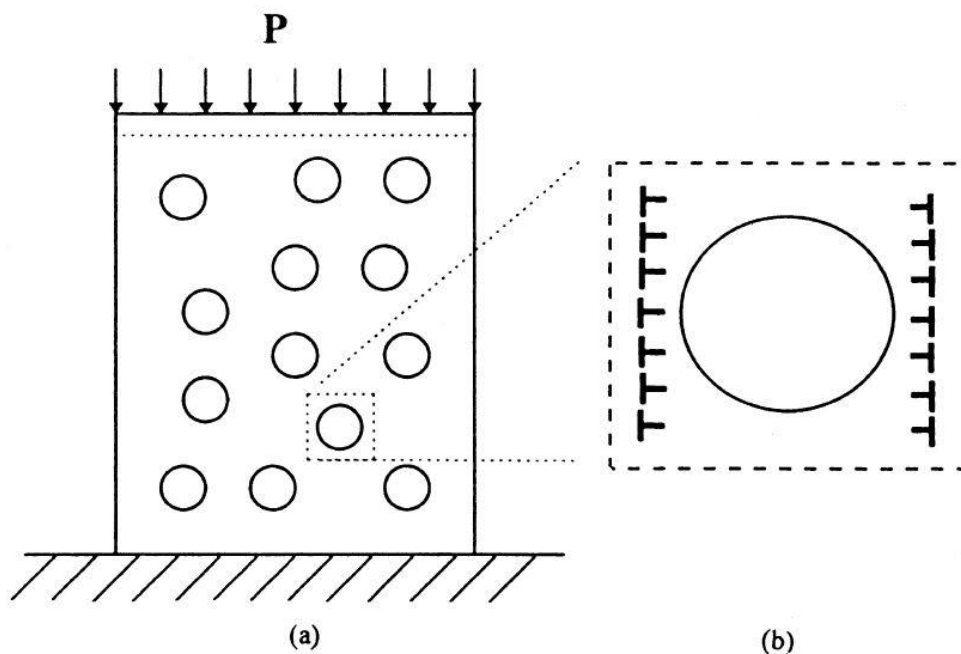
Figure 3-5: Configuration and elastic modulus mismatch dislocation model for MMCp under compressive loading; a) configuration, P: pressure; b) dislocation model [33]

It is generally known that metals and ceramics have significant differences in stiffness (Young's Modulus). Therefore the dislocation strengthening is the most common phenomenon in ceramic MMC´s. Dislocation strengthening is mainly caused by an elastic modulus mismatch and thermal expansion mismatch between the matrix and the reinforcement particles. The model for compressive load is shown in figure 3-5, whereby the dislocations illustrated in figure 3-5 b) generate shear stresses around the particle [33]. This dislocation

15

strengthening effect comes from dislocation population around the reinforcement. The dislocation population was discussed in detail for SiO_2 microfiber in aluminium matrix [45].
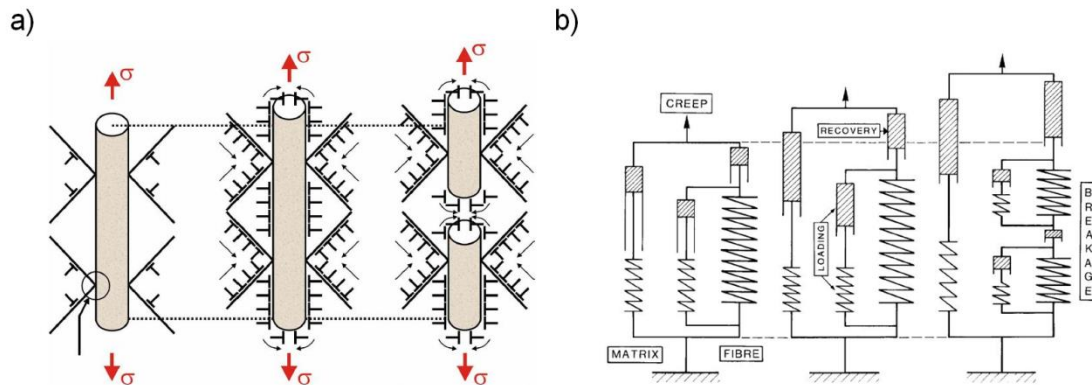
Figure 3-6: Dislocation strengthening into the matrix induced from a microfiber due to stress; a) population of dislocations around the fibre [46]**; b) A spring/dash pot analogue of the micromechanical model of a matrix with microfiber under stress** [45]

As shown in figure 3-6 a), the first stress generates dislocations in 45 ° angle to the reinforcement. Therefore the matrix material can be seen as a spring and a damper and the reinforcement phase as a spring and damper (from the direct strengthening) as well as a second spring and damper attached to the spring (indirect strengthening), as seen in figure 3-6 b). In the stage of deformation, more and more dislocation accumulate (Figure 3-6 a)). First they generate only in a 45 ° angle, later also perpendicular to the reinforcement phase. This can be seen as the extension of the springs and dampers of the mechanical system (Figure 3-6 b)). However, when the microfiber fails, the crack can be seen as dislocations (Figure 3-6 a)). In the mechanical system, the two halves of the microfiber are seen as two separate fibres connected with a dumper, simulating the crack. The matrix is seen as a fully expanded damper and spring (Figure 3-6 b)).

Tests were performed with increasing reinforcement volume fractions from 0 % to 30 % of non-uniform broken silicon carbide (SiC) particles in an aluminium (Al) matrix (at a constant particle size of 5 µm). This examination shows a

significant increase in the Young's Modulus, yield strength and ultimate tensile strength (UTS). As a result, the plastic strain decreases. Compared to the pure Al (0 % volume fraction), the ductility (sum of elastic and plastic strain until failure) of the composite for 30 % volume fraction is reduced by 50 % [37].

Tests in the same paper were executed with increasing particle size from 5 μm SiC to 23 μm SiC (at 20 % volume fraction) [37]. The results indicate a gradually diminishing Young's Modulus with larger particle sizes, shown in figure 3-7.
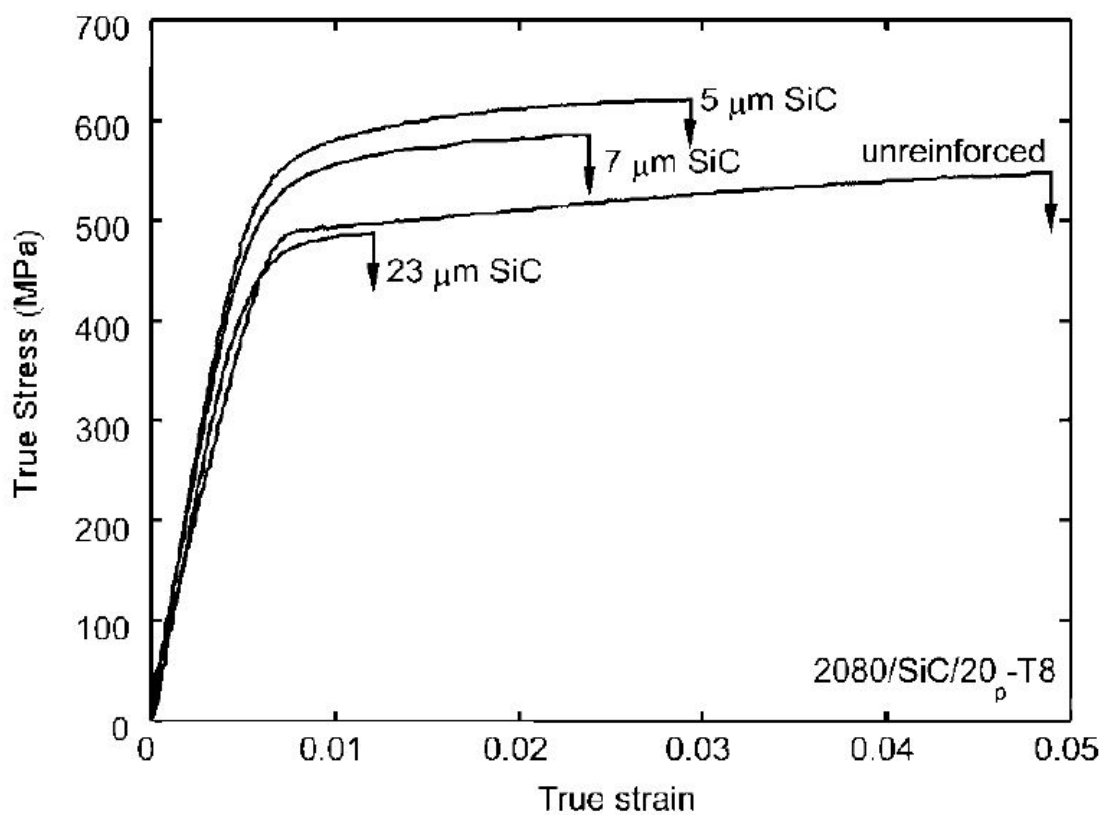
Figure 3-7: True stress-strain curves of Al SiC MMCs with 20 % SiC volume fraction (constant) and from unreinforced to 23 μm particle size (real tests) [37].

However, the yield strength, UTS and plastic strain reduce significantly with particle size. The plastic strain was under the unreinforced matrix material value. The particle size of 23 μm even reveals that all three values (yield strength, UTS and plastic strain) are lower than the matrix material. Further investigation shows that particles with 23 μm particle size were cracked prior to

17

the tensile testing. Cracked particles can act as voids rather than reinforcement [37].

Contradicting these results, Nan and Clarke [34] stated that increasing the particle size had no effect on the Young's Modulus. Their model was also based on Al and SiC. However, the volume fraction was fixed at 15 % and the particle size varied between 0.01 µm and 50 µm. There is no comparison given for pure matrix material. The results in figure 3-8 appear with an elasto-plastic deformation in the particle sizes between 0.01 µm and 0.5 µm.
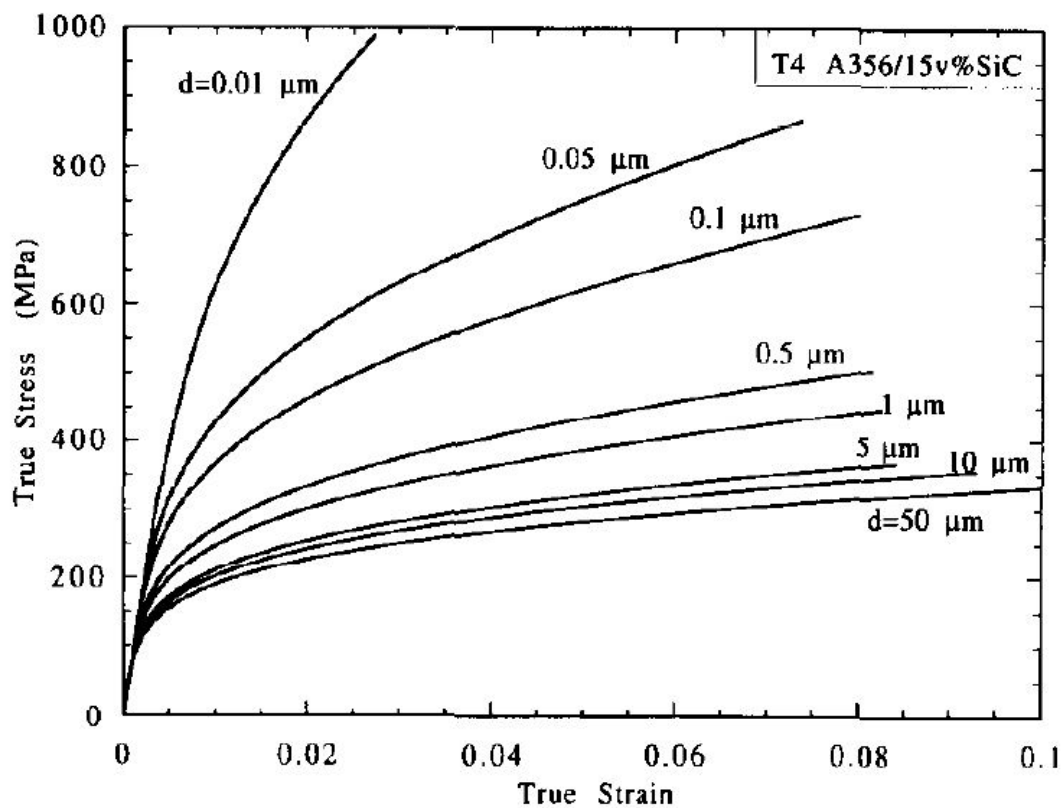
Figure 3-8: True stress-strain curves of Al SiC MMCs with constant volume fraction of 15 % SiC and different particle sizes in modelling prediction (volume fraction from 0.01 µm to 50 µm particle size) [34]

Additionally opposing the previous test, the plastic strain is a gradual increasing, while the UTS decrease with increasing particle size.

According to a paper by Molina *et al.* [47], the thermal conductivity of an Al SiC MMC reduces when the particle size reduces. On the other hand, the electrical

conductivity increases with smaller particle size. In the test, particle sizes varied between 8.9 µm and 167 µm and volume fraction varied between 53 % and 60 %.

The change in thermal conductivity and dislocation strengthening could explain why spherical WC particles in a Ni matrix show high compressive residual stresses at RT (in the paper 300 K) and lower temperature. It was found that when temperature is varied between 100 K and 900 K, the compressive residual stress reduced from approximately $\sigma = -1050$ MPa to $\sigma = -150$ MPa, respectively, with increasing temperature. At room temperature (300 K), stresses of approximately $\sigma = -810$ MPa were found [48].

3.4 Functionally graded materials

FGMs are created by varying the physical properties along one dimension of the structure, also known as the functional graded structure. These structures have already been modelled for brake discs and are explored to obtain either weight reduction or improved material performance using a similar weight.
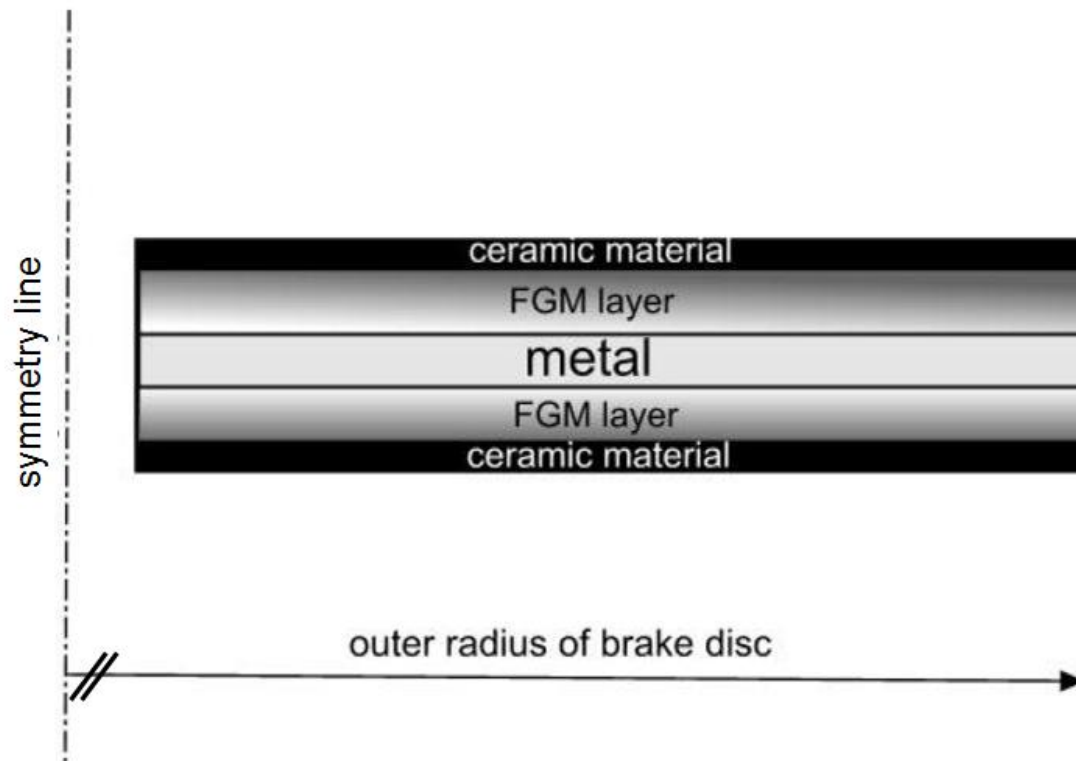
Figure 3-9: Scheme of the material structure of a brake disc made of an FGM [49]

The structure modelled by Hernik [49], as seen in figure 3-9 should improve the wear performance of a brake disc because of the ceramic layer and give an adequate heat absorption during braking because of the metal core. The FGM layer is there to reduce the gradient between thermal conductivity, thermal expansion and Young´s Modulus between the ceramic and the metal. The best combination given by the model is

- a ceramic layer (4 mm thick, both sides) of titanium diboride (TiB_2),
- a functionally graded layer made of an aluminium alloy and TiB_2 (8 mm thick, both sides, from 0 % to 100 % volume fraction ceramic), and
- a metal core of stainless steel (4 mm thick) [49].

The joining of an aluminium matrix and stainless steel is very difficult to perform in reality. In welding, for example, Fe forms very brittle and hard intermetallics with Al. While these are beneficial in the friction layer, they weaken a joint significantly [50]. The use of TiB_2, instead of SiC ceramic, reduces the issue of a weak joint a little because of the chemical resistance of TiB_2 to stainless steel.

Another point is to have an FGM layer with the same matrix material as the base material which was modelled for steel, cast iron and aluminium. In the model, it was considered to have pure ceramic on the top surface and a reducing gradient of ceramic towards the centre of the part. The outcome of papers on the subject is that the tribology of wear surfaces can be improved significantly by the FGM layer on the point of wear rate [51], [52]. The important parameters to investigate were friction coefficient and wear rate. In the model, it was found that the elastic modulus and the thermal expansion coefficient of the MMC are the important factors for the FGM layer [51]–[53]. The kind of ceramic used defines these factors but it was not fixed for this model. It was demonstrated that higher volume fractions of ceramic initiate local hot-spots. A model cannot predict whether the hot-spots are responsible for crack initiation or not. However, the model can demonstrate that hot-spots generate stress from a thermal expansion and contraction difference to the surrounding material. Crack initiation in the bond between the layer and the bulk material (peel-cracking) can be excluded, when the gradient is smooth between both and the bond is metallurgical [52].

3.5 Principles of Friction and Wear

The clad MMC surface layer should improve the frictional behaviour of a surface in contrast to the present substrate. Therefore, the principles of friction and wear needs to be understood. To describe these effects, the mechanisms of friction and wear are explained separately.

3.6 Mechanism of Friction

The friction properties of materials against each other are characterised by the tribology effects and mechanism. These effects are principally guided by the fundamental laws of friction (Amontons´ Laws of Friction), which are as follows:

    (1) the friction force is proportional to the normal load;

    (2) the friction force is independent of the apparent area of contact; and

    (3) the friction force is independent of the sliding velocity [54].

However, these three laws of friction vary in their reliability. Today these laws are more regarded as useful summaries of empirical observations. The first law may be expressed as

$$F_T = \mu F_N \qquad \textbf{(3-4)}$$

Rearranging gives:

$$\mu = \frac{F_T}{F_N} \qquad \textbf{(3-5)}$$

Whereby F_T is the friction force, F_N is the force generated by the normal load and μ is known as the friction coefficient or coefficient of friction [54]–[56]. The first law can be observed for friction on unlubricated sliding of solid materials. The second law is not as widely explored but is well attested for most materials. Both laws are excluded to explain the friction of polymers. The third law is more a result of common observation than well founded. The frictional force (F_T) needed is usually higher, to initiate sliding rather than to maintain the movement, hence the coefficient of static friction is greater than the coefficient

of dynamic friction. When a movement is established, the coefficient of friction shows an independency on the sliding speed. Nevertheless, some metals demonstrate a decreasing coefficient of dynamic friction for sliding speeds higher than tens or hundreds of metres per second [54]. During the 'running-in' or 'wearing-in' stage of a movement with friction, structural changes to the surfaces take place. These changes cause either an increasing or decreasing friction coefficient. This is known as an S-shaped curve, as seen in figure 3-10 [56].
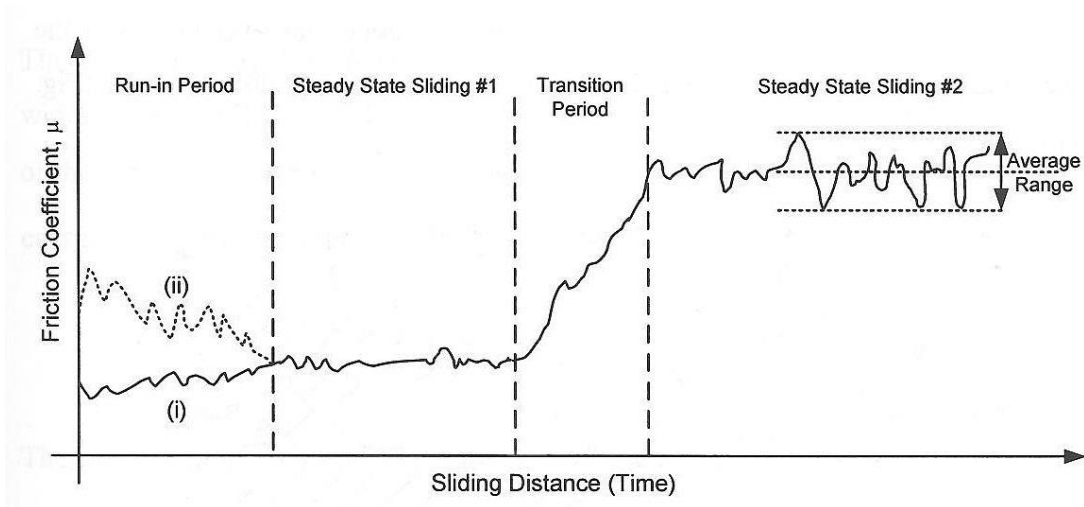
Figure 3-10: Schematic illustration of the coefficient of friction as a function of sliding distance with a typical S-shaped curve showing the running-in period [56], [57]; Possible start of the S-shape: (i) slightly increase of μ, (ii) decrease of μ.

Metal components usually have a temperature dependent friction coefficient which is dependent on whether temperature is increasing (heating) or decreasing (cooling), as seen in figure 3-11. This effect can result in a steady temperature if the heating rate into the material of the friction surface is the same as the cooling rate.
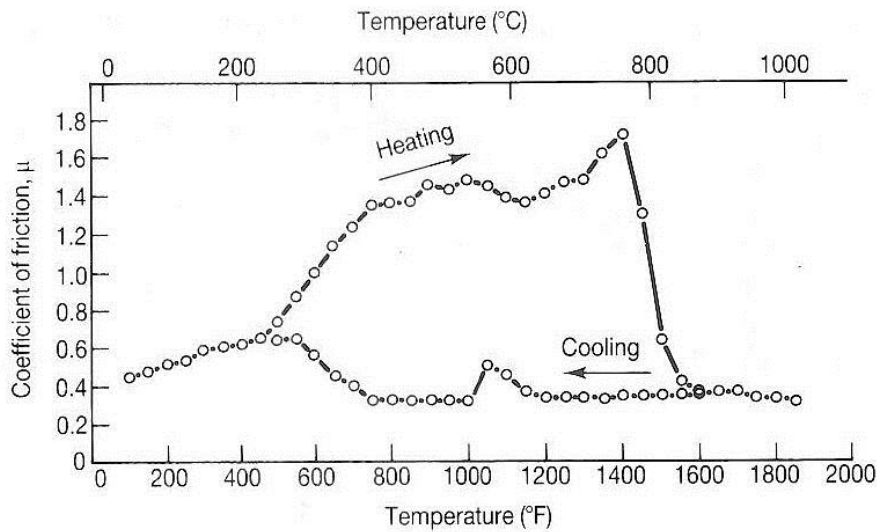
Figure 3-11: Dependence of the friction coefficient on temperature in the sample of austenitic stainless steel sliding against pure nickel in air. The two curves relate to data gathered while the specimens were being heated (upper curve) and subsequently cooled (lower curve) [54], [58].

The effect of the dramatic drop in friction coefficient in figure 3-11 between 750 °C and 800 °C occurs because of localised heat melting partially one of the friction surfaces. This causes a drop in the friction force to a low value determined by viscous forces in the liquid layer.

3.7 Mechanism of Wear

Wear is the removal of the material from the surface of a solid body as a result of mechanical action of the counterbody [59]. In case of brake discs, the solid body is the disc and the counterbody is the pad.

The mechanisms of wear are:

- abrasion

- fatigue

- erosion [59]

- adhesion

- corrosion

Wear on a micro-alloyed steel brake disc paired with an organic pad occurs in the following four stages respectively the temperature increase [60]:

1. At RT, hard parts of the pad plough into the brake disc surface at a two-body abrasive wear mechanism.

2. At low temperature, localised oxidation occurs. The oxides deform, sinter, fracture, adhere and being compacted into furrows under further compression of the brake pad. Additionally, free abrasive oxide grains occur between the disc and the pad, which results in greater plastic deformation of the disc surface.
Three-body abrasion and adhesion are the main wear mechanism at this stage.

3. At medium temperature, the oxidation intensifies and it's cracking and regenerating becomes a major behaviour of wear. On the other side, wear of the brake pad escalates. A surface film of wear products coming from the brake pad and brake disc grows up rapidly and extends soon. The surface film shows some fatigue flaking as an effect of cycle contact stress.
At this stage the oxide cracks due to fatigue wear, however, adhesion and abrasion continue to be the main mechanisms of wear.

4. At high temperature, the plastic deformation of the disc as well as the pad becomes more serious. The surface film becomes compacted by the pad pressure and scaling of it occurs by adhesive wear. Deoxidation of the surface generates reactive iron, which sinters easily together with grinding debris. Deep grooves get generated quickly in the disc surface.
The high temperature leads to aggressive wear in form of adhesion tear. The surface film as well as plastic material welds with the pad and tears off on either pad or disc side [60].

Unfortunately, this article does not describe the different temperatures for the stages [60]. However, it shows that the main mechanisms of wear on a brake disc are:

- adhesion
- abrasion

Therefore, these effects are followed up in more depth.

3.7.1 Effect of Adhesion

In most cases, the result of physical or chemical interaction of two surfaces in contact leads to bonding. This adhesive bond needs to shear if a relative sliding of the two surfaces is required to re-establish. Shearing occurs at the weakest region with increasing lateral force. The weakest region can be one of the contacting asperities of the sliding bodies, as seen in figure 3-12 [56].
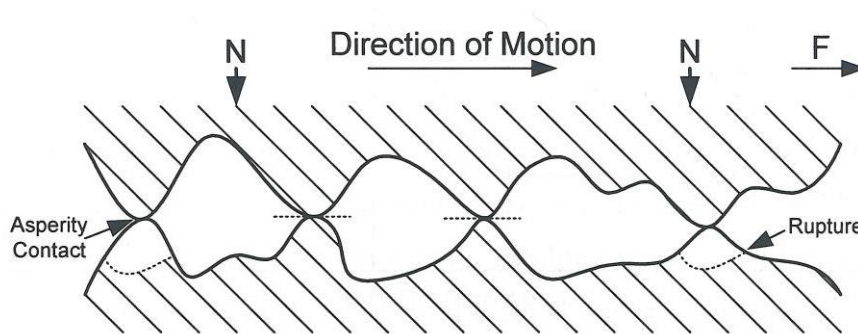
Figure 3-12: Adhesion in contacting surfaces; F: Torque force applied, N: normal load [56], [57]

3.7.2 Effect of Abrasion

The effect of abrasion, also deformation, has two causes:

(a)   An interaction which is the plastic deformation of interlocking asperities,

(b)   An interaction where the asperities of hard material plough through a softer surface figure 3-13.

To deform two contacting surfaces due to relative motion, a friction force (F_T) is required. The case (b) of ploughing can also be the result of particles trapped between the two surfaces (three body abrasion). An obvious case of ploughing is when two rough surfaces come into contact (two body abrasion), figure 3-13 [56].
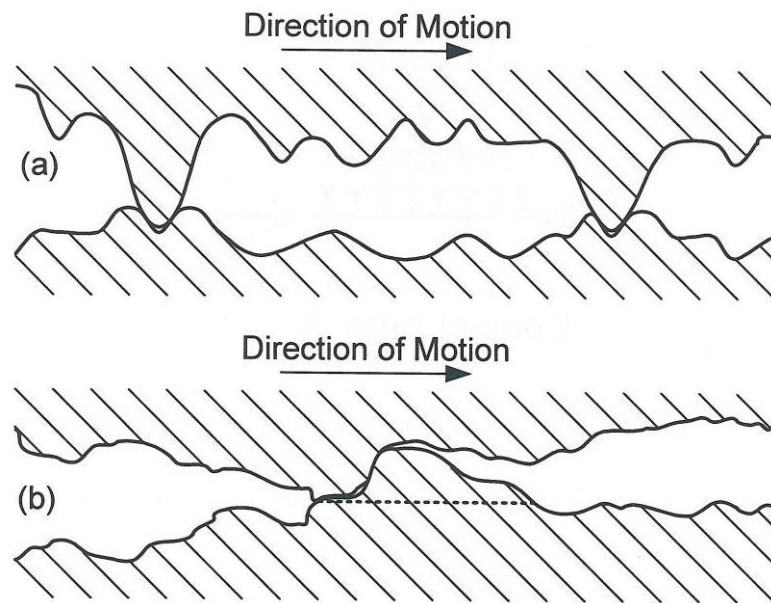
Figure 3-13: Deformation in contacting surfaces, (a) asperity interaction, (b) ploughing of a harder surface into a softer surface [56], [57]

3.8 Tribology behaviour of SiC metal matrix composites

For railway brake discs, the friction coefficient should vary between $\mu = 0.25$ and $\mu = 0.45$ [61]. Silicon carbide shows a very constant friction coefficient of $\mu = 0.40$ when worn against itself (Figure 3-14 area III). The friction conditions of a railway brake disc are very similar as the temperature rises quickly above 250°C (or 523 K) and the normal force F_N is relatively low. The low normal force results in a large wear surface of the pad. SiC is a promising candidate material to be used as reinforcement phase for railway brake disc material based on this data.
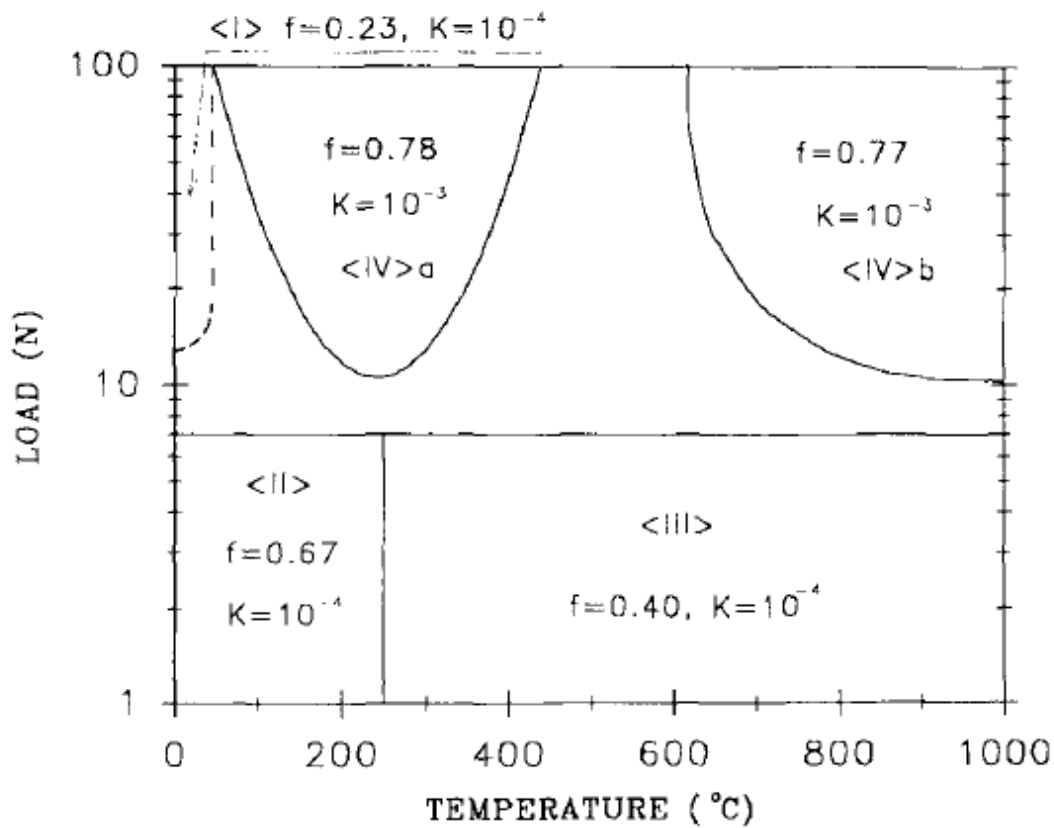
Figure 3-14: Wear transition diagram for sintered silicon carbide; SiC ball sliding against an SiC flat surface (linear sliding); four distinct regions plus one transition zone; f: friction coefficient, K: Wear coefficient [62]

Further investigation in the wear behaviour of SiC-MMCs reflects their use as brake disc material in the automobile industry. Unfortunately, there is only one literature paper dealing with the wear rate of SiC in a steel matrix which states that SiC was not maintained in the composite layer structure [24]. The majority of papers have SiC-MMCs in an Aluminium matrix [63]–[67]. The base material in all these papers was the same as the matrix material but with a slightly different alloy denomination. The friction behaviour of Al-SiC-MMCs shows a dropping friction coefficient with increasing sliding speed. This effect comes from the SiC particles as these particles break in the form of shear delamination with slower sliding speeds. But they wear into a polished condition before being released from the surface with faster sliding speeds. In a Pin-on-Disc (POD) test with a normal force of 15 N and a 5 mm diameter pin, the friction coefficient

falls from $\mu = 0.44$ for a sliding speed of $v = 1.62$ m/s down to $\mu = 0.31$ for a sliding speed of $v = 4.17$ m/s, as shown in figure 3-15 [68].
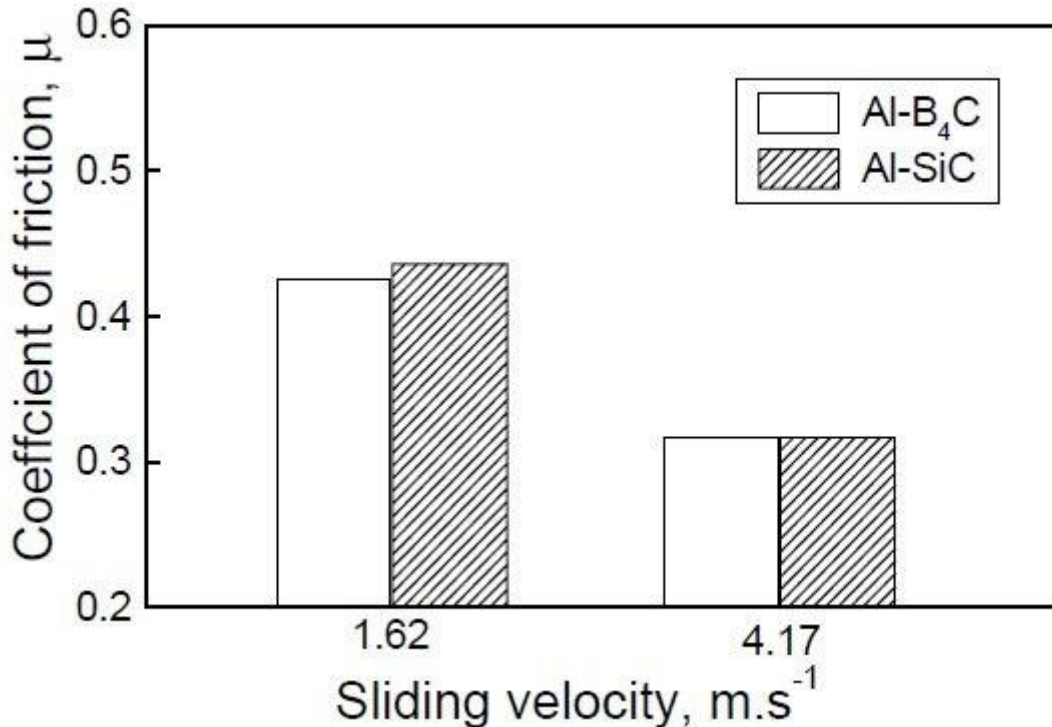
Figure 3-15: Coefficient of friction μ against sliding speed for Al-B$_4$C and Al-SiC MMCs measured with 15 N (area pressure of 0.75 MPa) on a POD tester [68]**.**

3.9 Tribology behaviour of WC metal matrix composites

The friction behaviour of Co-WC and Co-Cr-WC coatings was examined in different reinforcement to matrix volume rates and dry sliding conditions. It was found that the friction coefficient was constant over the matrix mixture Co to Cr with $\mu = 0.30$ [69]. What is important for the friction coefficient is the production process. Wood [69] used a plasma spraying process with the friction coefficient changing from $\mu = 0.29$ to $\mu = 0.42$. The challenge of using sprayed coatings as brake disc layers is to contain the peel cracking of the coating from the surface; this occurs as a result of weak physical bonding [70]. This can be avoided by plasma transferred arc and GTAW cladding processes as the layers have a metallurgical bonding (chemical and physical bonding) [10], [71]. However,

these types of clad layers were not found to be tested for brake discs. A friction coefficient for Fe-Co-WC MMC was found in a ball-on-disc test with a normal load obtained by a 50 g weight (ball material: pure SiC).
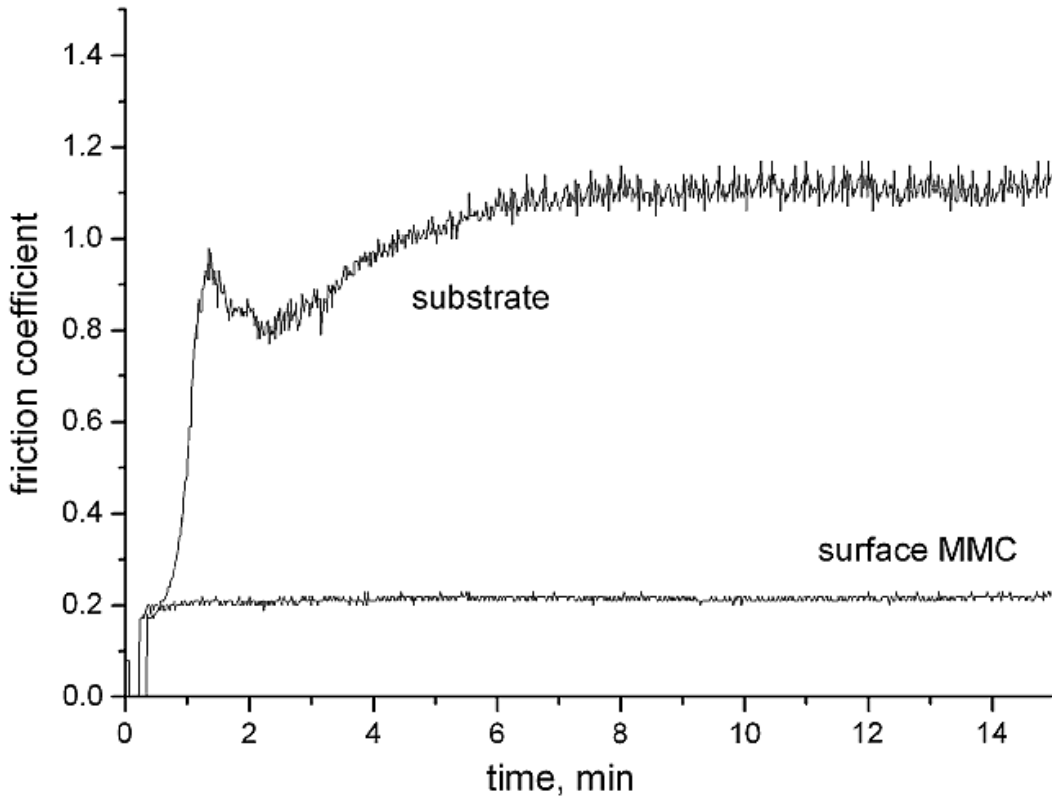
Figure 3-16: Friction coefficient against wear time of a ball-on-disc test; Fe-Co-WC MMC as the surface MMC; Q235 steel as a substrate. Test parameters: 6 mm disc radius SiC ball with F_N = 0.49 N load; 2 mm ball radius; 300 rpm [72]

The value of μ = 0.2 is very low (Figure 3-16) which mean too little braking for brake discs. Nevertheless, the improvement from a pure low alloyed steel surface with a friction coefficient of approximately μ = 1.1, as seen in figure 3-16, is very high for brake disc applications and gives a good perspective to use WC. The composition in this test was 37.59 wt% WC ceramic in a mixture of Q235 steel and Cobalt [72].

3.10 Research gap

There is not very much knowledge available regarding GTA cladding of MMCs in steel. This is for both SiC and WC. In addition there is very little about the behaviour of WC when it is added to mild and high strength steel as the matrix. This is the focus for this research project.

Some of the found literature is listed in the following table 3-1 to underpin the knowledge gap regarding GTA cladding of MMCs in steel.

Table 3-1: Previously done work describing the GTAW process with MMCs

Author	Source title	Ref	Difference to this thesis
Edmilson Otoni Correa	Weldability of Iron Based Powder Metal Alloys Using Pulsed GTAW Process	[9]	The author discusses the use of Fe powder in GTAW for fusion processes. He also changes soon into Ni alloyed Fe based powders.
A. P. Patel	The Study of the Deposition of Hardfacing Alloys using the GTAW Process	[73]	Mr Patel gives details about Carbides building up in cladding products. However, the ceramic did not overcome the heat input of the cladding process.
Y.C. Lin, S.W. Wang	Wear behavior of ceramic powder cladding on an S50C steel surface	[11]	The two authors used a tubular 316 stainless steel wire filled with SiC and an autogenous GTAW process to fill up a groove in mild steel.

Author	Source title	Ref	Difference to this thesis
Y.C. Lin, S.W. Wang (continuing)			Their result shows a uniform microstructure giving high hardness. The Ni content is still above the in this work defined limit of 3 wt%.
Soner Buytoz, Mustafa Ulutan	In situ synthesis of SiC reinforced MMC surface on AISI 304 stainless steel by TIG surface alloying	[74]	The authors used an autogenous GTAW process with SiC infused shielding gas. The substate was an AISI 304 stainless steel, which Ni and Cr content is higher than 3 wt%. The outcome is a hardfacing structure without SiC particles left. Moreover, the corrosion properties of the stainless steel and SiC mixture are now to be investigated.
Qingbao Wang, Xiaoyan Li	Effects of Nb, V, and W on Microstructure and Abrasion Resistance of Fe-Cr-C Hardfacing Alloys	[75]	The two authors investigated GTA cladding with core-filled wires. They used multiple carbides, some of them where retained in the microstructure. The Cr content was higher

Author	Source title	Ref	Difference to this thesis
			than the in this work defined limit of 3 wt%.

The behaviour of WC when it is added to mild or high strength steel was previously described by the authors in table 3-2 as follows:

Table 3-2: Previously done work describing the behaviour of WC when added to mild or high strength steel.

Author	Source title	Ref	Difference to this thesis
Qingmao Zhang, Jinjiang He, Wenjin Liu, Minlin Zhong	Microstructures and properties of Ceramic particles-reinforced metal matrix composite layers produced by laser cladding	[21]	The authors used a CO_2 laser to produce a cladding layer and the WC was not retained in the microstructure. The layer produced was a homogenous hardfacing layer.
Robert J.K. Wood	Tribology of thermal sprayed WC–Co coatings	[69]	Mr Wood used high-velocity oxygen fuel (HVOF) thermal spraying to make a very dense WC coating with Co and Cr as matrix. Thereby, the Carbides were retained. However, HVOF spraying could lead to peel-cracking and the matrix does not contain Fe.

Author	Source title	Ref	Difference to this thesis
J.M. Amado, M.J. Tobar, J.C. Alvarez, J. Lamas, A. Yáñez	Laser cladding of tungsten carbides (Spherotene) hardfacing alloys for the mining and mineral industry	[35]	The authors used WC from the same production company as in this thesis. Their cladding process was made with a Nd-YAG laser on mild steel. However, their power was premixed with a matrix which is high in Ni. The WC particles retained sphere and had similar dissociation pattern as in this thesis with low Fe content.

4 Experimental set-up and pre-study of Cladding

This chapter is an examination to understand the physical limits of the welding process for cladding. An operating window for the surface layer production is established in this chapter. The experimental set-up of the Gas Tungsten Arc Welding process is explained in section 4.1 of this chapter and the materials used in the thesis are described in section 4.2 of this chapter.

Additionally, a short summary of a Gas Metal Arc Welding process for cladding is given in Appendix D. The characteristics of the tribological test machines are described later in chapter 8 and Appendix K.

4.1 Gas Tungsten Arc Welding set up for cladding

The idea for the brake disc cladding was a FGM made of a ceramic reinforcement in a steel matrix, whereby more matrix material in the first layer should bring a strong metallurgical bonding on the base material. Besides, an increasing ceramic content should bring a higher wear resistance towards the braking surface. The FGM wear layer of the brake disc should be built up clad layer by clad layer.   The principle behind the FGM is schematically demonstrated in figure 4-1.
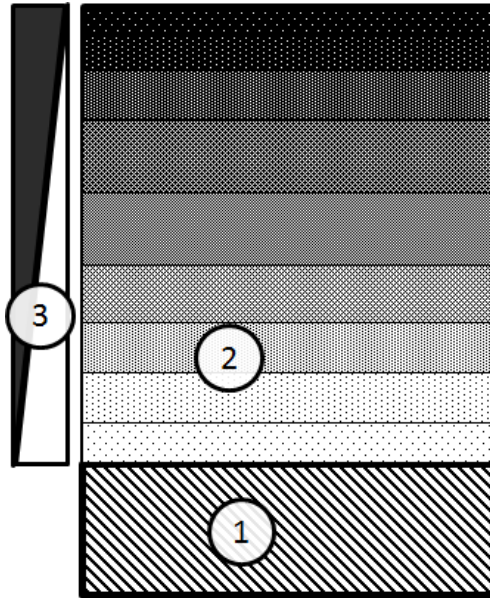
Figure 4-1: Schematic: Functionally graded material (FGM); 1: base plate, 2: graded layer, white: matrix, black: ceramic reinforcement, 3: interdependency of matrix and reinforcement

An assumption of a minimum single layer height of 1.0 mm was made to give the necessary material composition gradient.

The Gas Tungsten Arc Welding (GTAW) process was completed using a migatronic TIG/plasma welder Commander 320 AC/DC, as seen in figure 4-2 a). The operation mode was TIG DC. Thus the electrical current (I) and voltage (V) waveform was not manipulated. The table below summarises the described power source set-up:

Table 4-1: Welding power source set-up

Welding power source	Welding process	Operation mode	Waveform
Migatronic TIG/plasma welder Commander 320 AC/DC	GTAW	TIG DC	Continuous

For a good welding time buffer, a decision was made to reduce the maximum current (I_{max}) of the machine by 10 % from I = 320 A to I = 288 A in the tests.

According to the manual [76], this gives the tests a 100 % duty cycle and means the welding machine does not need to rest for cooling at any time. As a lower limit, half of the current with I = 144 A was set. The table below summarises the described parameters:

Table 4-2: Basic welding power source parameters

I_{max} welding machine	allowed welding current buffer	I_{max} in tests	reached duty cycle	resting time for cooling	I_{min} in tests
A	%	A	%	min	A
320	10	288	100	0	144

A water cooled WeldTec Automated Machine TIG Torch was assembled vertically to maintain a perpendicular set-up to the work piece for all experiments. The motion of the torch and the work piece was provided by a Trio Motion 5-axis-rig with three linear axes, one rotating axis and one manual rotating axis. The four automated axes were able to be programmed by a controller and were able to work simultaneously. In figure 4-2 b), the Trio Motion 5-axis rig is shown. Travel speeds of TS = 0.1 m/min to TS = 4.0 m/min were maintained from all automated axes, whereby, the linear speed must be converted into a rotational speed of a specific position on the rotation axis. An additional fume extractor, as shown in figure 4-2 b) 7, was used for improved fume extraction and safety measures, like increased air changes.
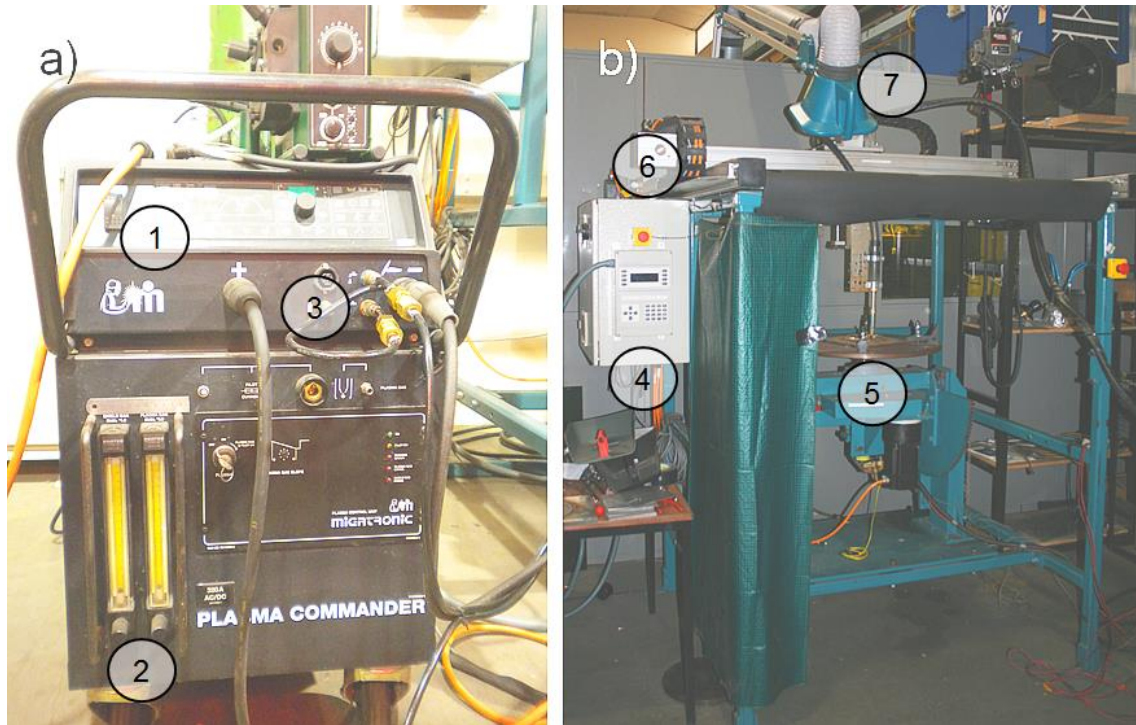
Figure 4-2: GTAW welding machine and 5-axis rig; a) migatronic TIG/plasma welder Commander 320 AC/DC, 1: control panel power source, 2: shielding gas flow meter, 3: power and cooling water connections; b) 5-axis rig, 4: Trio Motion control panel, 5: turntable with two rotating axes (one manual, one automated), 6: two horizontal axis (x,y) and one vertical axes (z), 7: fume extractor

The Trio Motion controller was calibrated with the increments of the stepper motor to transform these in distances on the axis, as seen in Appendix E.

Wire feeding was carried out by the migatronic KT-4 wire feeder for cold wire feeding. The possible wire feeding speeds (WFS) ranged between WFS = 0.39 m/min and WFS = 4.00 m/min [77]. These speeds were calibrated for a specific set-up and wire. The wire feeder is shown in figure 4-3 a). It had a run-in function for shielding gas and arc establishing; therefore the shielding gas was released, the arc established and the wire was fed, respectively. The time between these operations was able to be adjusted. For the run-out moment, the reverse operations were used. Additionally, a wire retraction took care of the possibility of wire becoming stuck in the solidifying weld pool. The wire was released into the weld pool over the wire feeder nozzle shown in figure 4-3 b). The wire feeder nozzle was a bent brass pipe with a copper contact tip for

guidance. This configuration was found to be ideal to provide a heat-sink away from the nozzle.
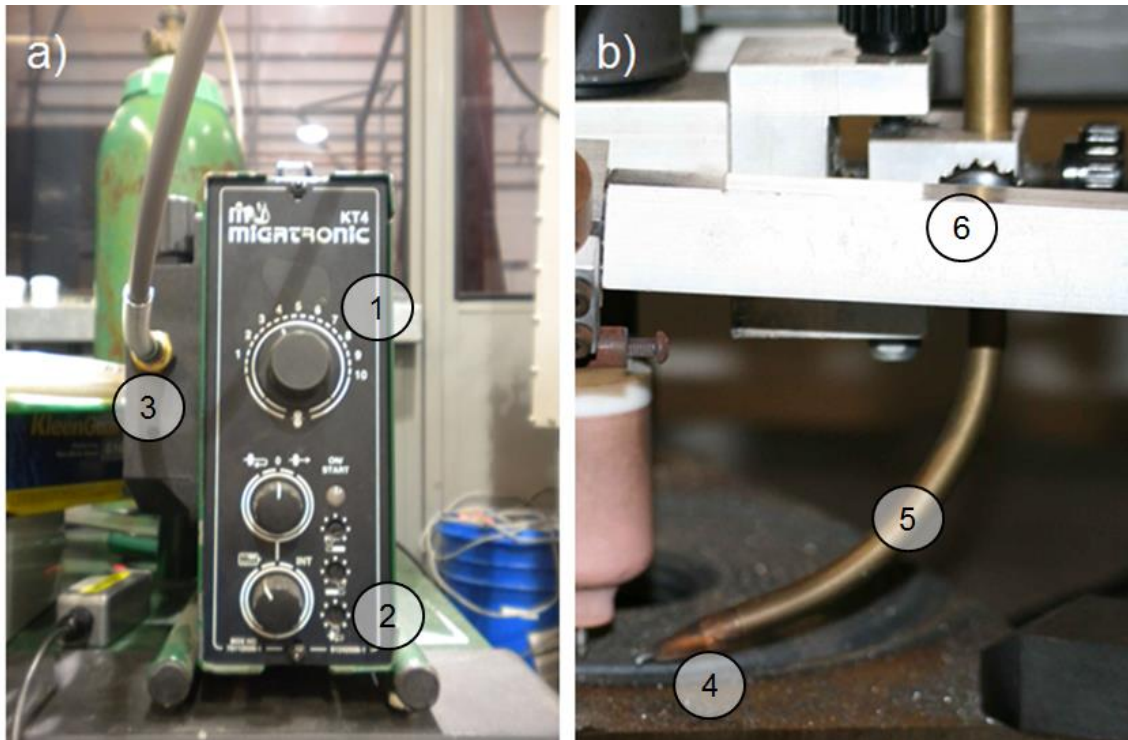
Figure 4-3: a) migatronic KT-4 wire feeder, 1: Wire feed speed regulator, 2: run-in and run-out function panel, 3: wire guidance hose; b) wire feeder nozzle mounted on the welding system, 4: Copper contact tip, 5: brass pipe, 6: three axes fine adjustment

The configuration of the guide hose (conduit), brass pipe radii and condition of the contact tip influences the friction on the wire after the wire feeder unit. Friction limits the maximum wire feed speed of the wire feeder. As it has a major impact on the maximum wire feed speed, the wire material has to be mentioned as well. Steel is more rigid than aluminium and titanium. The wire feeder unit must be calibrated for different wire compositions.

Ceramic powder in the clad was supplied by the powder feeder Sulzer Metco TWIN-10-C [78], [79] with the APS Powder Insert [80]. The different units of the powder feeder are shown in figure 4-4.
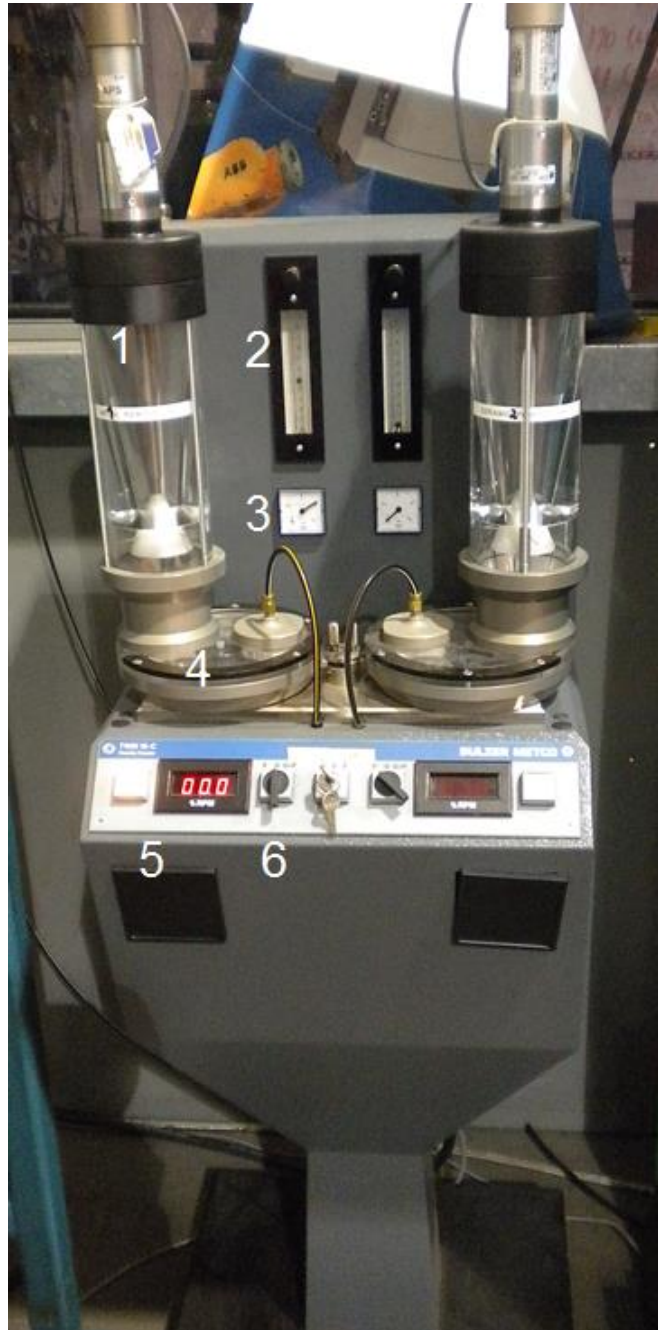
Figure 4-4: Sulzer Metco TWIN-10-C Powder Feeder; 1 APS Powder insert, powder hopper [80]**; 2 transport gas flow meter; 3 transport gas pressure manometer; 4 APS Powder insert, powder feeding disc** [80]**; 5 feeding disc speed display; 6 On/Off or gas only controller** [78], [79]

The Sulzer Metco TWIN-10-C Powder Feeder can be used either with argon (Ar) or with nitrogen (N_2) as powder transport gas [78]. A special calibration enables it to use helium (He) as a powder transport gas, too. This twin system provides the possibility of feeding two different powders at the same time. However, only one powder transport gas can be used. The working pressure of the transport gas is 3 bars. A pressure valve and a calibrated pressure gauge on the powder feeder can be used for re-adjustment (figure 4-4, 3). The flow rate can be set up with a built-in flow meter (figure 4-4, 2), which is calibrated on a flow curve close to N_2 and Ar. The molecular weights of these two gases is with 28.0 g/mol and 39.9 g/mol, respectively, close to each other [78]. The flow rate displayed on the flow meter is the flow in normal litre per minute (NLPM) which can be converted into the Ar flow in litre per minute using the chart below [78]. Charts for N_2 and He (molecular weight of 4.0 g/mol) are also available.
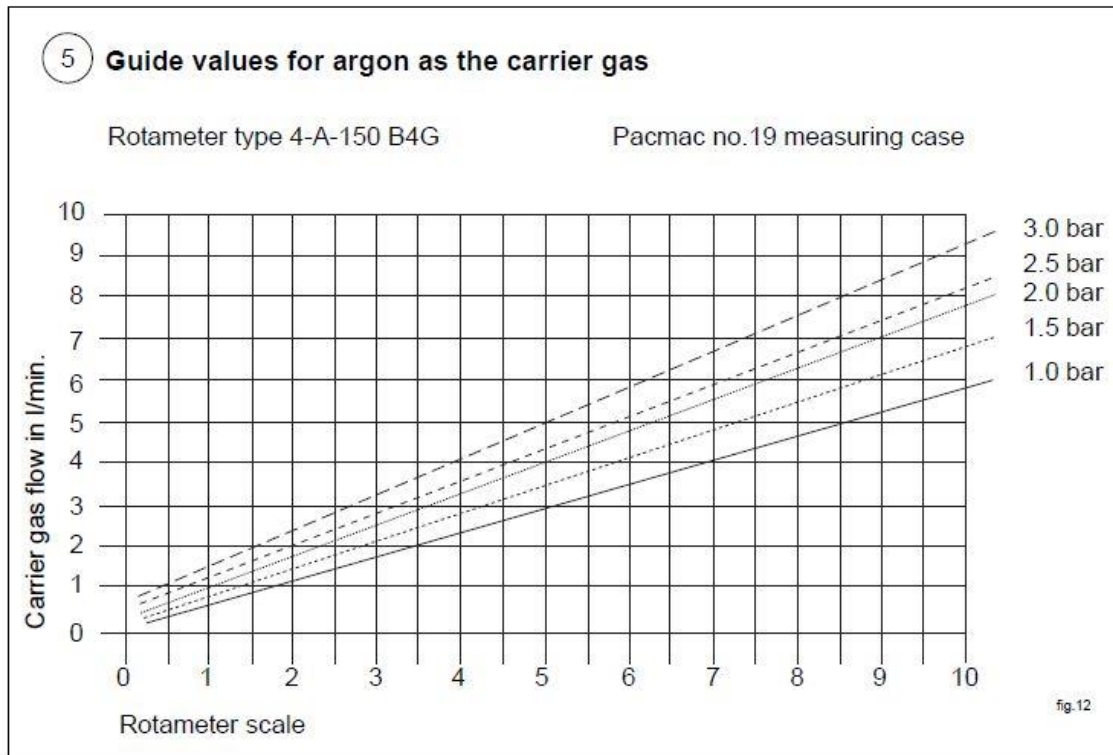
Figure 4-5: Ar flow rate of the powder feeder (y-axis) converted from the NLPM (x-axis) [78]**.**

The powder hopper on the powder feeder has a stirrer inside to give as much as possible a homogeneous powder mix during the entire feeding operation.

However, differences in the density, shape and size of powders make it difficult to guarantee a consistent mixture [80]. The powder feed speed can be adjusted very accurately with the speed of a powder feeding disc (figure 4-4, 4). The rotating speed of the disc, with a scale from 2.5 % to 100 %, is equivalent to the powder feed rate in grams per minute. However, the actual powder feeding rate must be calibrated for each powder and disc type. The calibration chart for the powders used is given in section 4.3.3.

The majority of tests were made with a pressure reducing container which was connected to the powder feeder through a nylon hose to the upper inlet. This container was developed to release the Ar transport gas pressure shortly after the highest point of the powder feeding system. As seen in figure 4-6 a), a slightly positive pressure at the powder feeding nozzle was able to be obtained with a valve at the top of the container.
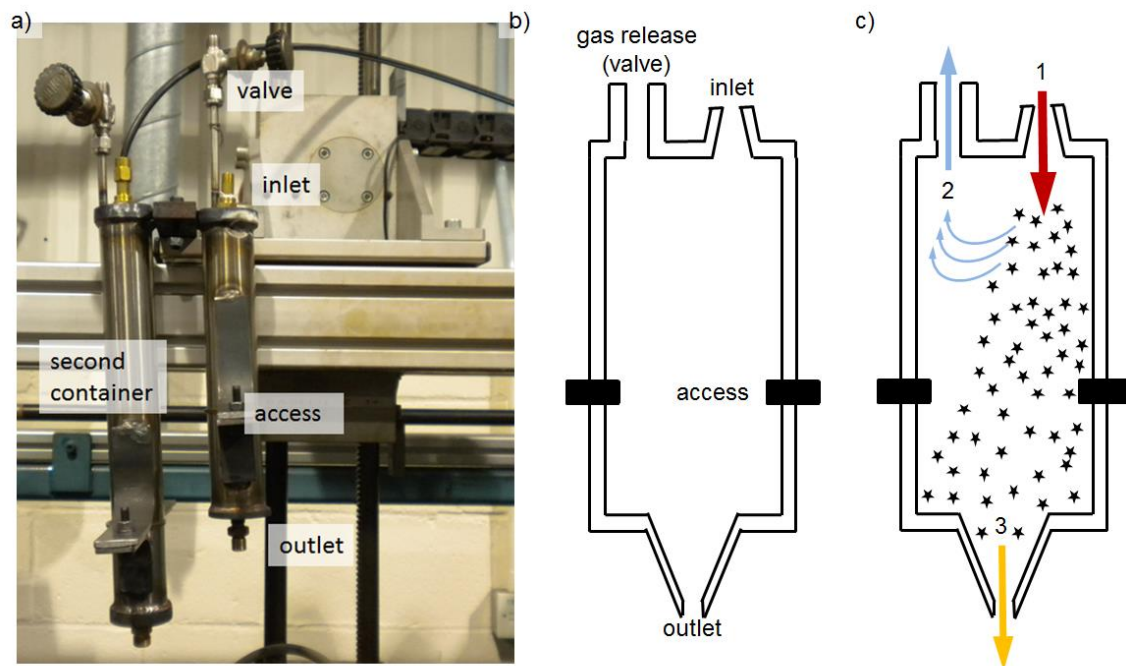
Figure 4-6: Pressure reducing container; a) image; b) schematic, inlet: powder with transport gas intake, access: opener for maintenance with seal ring, outlet: powder exit, gas release: pipe to valve, valve: pressure release regulator, second container: reducing container for different powders; c) principal, 1: powder transported by pressure of transport gas, 2: separation of powder by gravity and transport gas release, 3: powder falls by gravity to the powder feeder nozzle

The powder fell from the container through the outlet and another hose to the powder feeding nozzle mainly by gravity. To withstand the heat, the powder feeder nozzle was either a wholly copper (Cu) pipe (Figure 4-7 a)) or half aluminium oxide ceramic (Al_2O_3) pipe and half Cu pipe (Figure 4-7 b)).
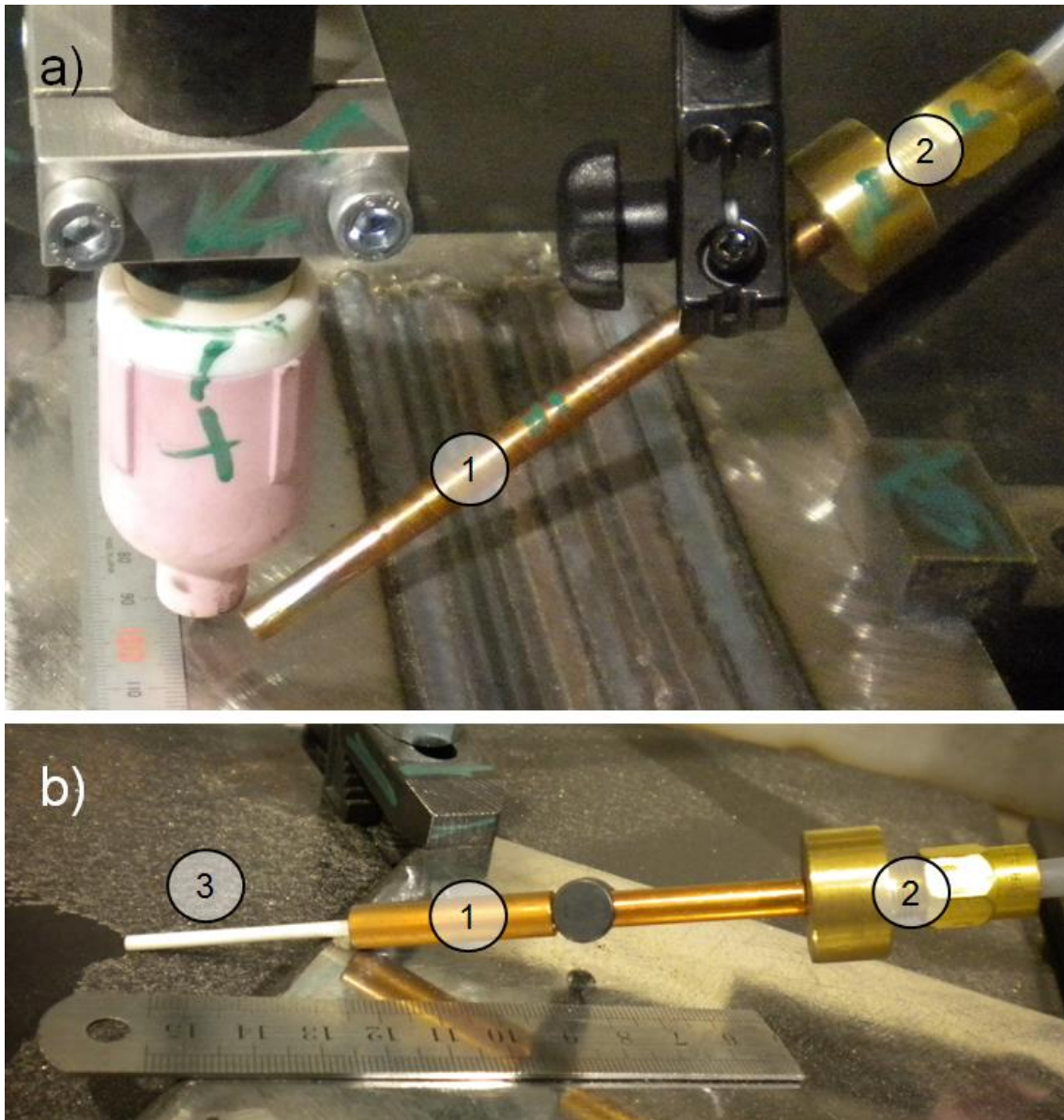
Figure 4-7: Powder feeder nozzle; a) Cu nozzle mounted next to the torch; b) ceramic nozzle connected at the end of the Cu nozzle; 1 Cu pipe, 2 brass connection to hose, 3 aluminium oxide ceramic pipe.

Copper has high electrical and thermal conductivity. It conducts heat from the weld bead and in some cases arc jumping was observed between the tungsten

electrode and the nozzle. Over longer welding times Cu pipes were beneficial as the heated Cu pipe had a pre-heating effect of the ceramic powder. Aluminium oxide ceramic as a pipe builds a heat barrier and is non-conductive. Therefore, the weld bead maintained its temperature. However, the ceramic pipe reduces the pre-heating effect of the powder.

The kind of powder feeding nozzle used is stated in each of the experimental chapter.

4.2 Properties of the materials used

Important factors in this thesis are the materials used as their properties and application conditions are relevant to the outcome of each examination. First, the base material and the matrix material as a wire are described in section 4.2.1. In section 4.2.2, the properties of the ceramics used are discussed.

4.2.1 Matrix and base materials

The matrix and base materials are mild steels and higher strength steels. The matrix material was standard welding wire on reels. The chemical composition is shown in table 4-3 and table 4-4, whereas, the mechanical composition is shown in table 4-5.

Table 4-3: Chemical composition of the base and wire materials

	Grade	Carbon	Silicon	Manganese	Phosphorus	Sulphur	Aluminium	Chromium	Nickel
	-	wt%	wt%	wt%	wt%	wt%	wt%	wt%	wt%
Base	S275JR	0.14	0.18	0.82	0.021	0.016	0.028	0.13	0.42
	S355J2+N	0.12	0.23	1.46	0.014	0.009	0.025	0.03	0.02
	15CDV6	0.15 - 0.20	max 0.60	0.40 - 0.80	max 0.040	max 0.040	x	0.80 - 1.20	max 0.50
	G-22 NiMoCr 5 6	0.18 - 0.24	max 0.60	0.80 - 1.20	max 0.015	max 0.015	max 0.050	0.60 - 1.10	0.80 - 1.30
Wire	G3Si1	0.07	0.82	1.45	0.01	0.01	0.005	0.025	0.03
	G4Si1	0.06	0.94	1.64	0.013	0.016	x	0.02	0.02
	15CDV6	0.13	0.15	0.93	max 0.009	max 0.015	x	1.4	x
	G89 6 M Mn4Ni2CrMo	0.1	0.8	1.8	x	x	x	0.35	2.0

Table 4-4: Continuation of table 4-3

(cont.)	Grade	Molybdenum	Vanadium	Tungsten	Niobium	Copper	Titanium	Nitrogen	Zirconium	Carbon equivalent
	-	wt%	wt%	wt%	wt%	wt%	wt%	wt%	wt%	-
Base	S275JR	0.02	0.03	x	0.02	0.09	0.03	0.004	x	0.347
	S355J2+N	0.01	0.005	x	0.023	0.03	0.005	0.004	x	0.376
	15CDV6	0.85 - 1.15	0.15 - 0.30	x	x	x	x	x	x	0.897
	G-22 NiMoCr 5 6	0.50 - 0.80	-	x	x	-	-	max 0.010	x	1.007
Wire	G3Si1	0.01	0.005	x	x	0.021	0.003 [1]	x	0.0 [1]	0.323
	G4Si1	0.005	x	x	x	0.02	0.004	x	0.002	0.341
	15CDV6	0.9	0.24	1.7734	x	x	x	x	x	0.793
	G89 6 M Mn4Ni2CrMo	0.5	x	x	x	x	x	x	x	0.703

x – Content not mentioned in data certificate (see appendices L.1 and L.2)

[1] – Ti value stands for Ti + Zr total measurement

Table 4-5: Mechanical properties of the base and wire materials

	Grade	Yield Strength	Ultimate Tensile Strength	Elongation at fracture	Test temperature	Impact Work	Hardness
			Tensile test		Impact test (average out of three)		
	-	MPa	MPa	%	°C	J	HB
Base	S275JR	300	470	30	20	85	x
	S355J2+N	415 [2]	586	26	-20	152	x
	15CDV6	min 900	min 1030	min 10	20	min 20	331 - 388 HB 10/3000
	G-22 NiMoCr 5 6	min 900	1050 - 1200	min 10	20	min 27	330 - 375 HBW 10/3000
Wire	G3Si1	466 [3]	577	30 [5]	-40	92	x
	G4Si1	500 [3]	566	26 [5]	-40	86	x
	15CDV6	x	x	x	x	x	x
	G89 6 M Mn4Ni2CrMo	min 890 [4]	940 - 1180	min 15 [5]	-60	min 47	x

x – Properties not mentioned in data certificate (see appendices L.1 and L.2)

[2] – R_{eh}, upper yield

[3] – R_{el}, lower yield

[4] – $R_{0.2}$, proof strength

[5] – A5, short proportion specimen

Table 4-5 above shows that the mild steels S275JR [81], [82], S375J2+N [81], [82], G3Si1 [83] and G4Si1 [83] are very similar in composition. Welding wire usually has lower carbon content and higher silicon content than the base material in order to reduce the possibility of imperfections. However, the higher strength steels 15CDV6 [84], G-22 NiMoCr 5 6 (according to SEW 520:1996-09), and G89 6 M Mn4Ni2CrMo [85], show a similar composition, too. Differences between mild steel and higher strength steel are slightly increased in Cr, Mo and in 15CDV6 the W. These differences and the heat treatment improve the higher strength steels significantly in their mechanical properties, which are shown in table 4-5. High strength steels shown in the tables above are mainly air hardener and develop a high ultimate tensile strength (UTS) straight after welding. The properties in table 4-5 for the base material are as delivered and for the wire are as welded. The toughness reduces significantly with higher strength steels, compared to mild steels, as high strength steels result in a hardened microstructure. A hardened microstructure, with proportions of martensite or bainite, tends to crack during cooling. This cracking is called cold cracking, and no cracking is understood as high weldability; weldability is usually established over the carbon equivalent. In the literature, different carbon equivalents are found, the most common being from the International Institute of Welding [86] and is calculated from the chemical analysis as follows:

$$CE\ [-] = C\ [wt\%] + \frac{Mn\ [wt\%]}{6} + \frac{Cr\ [wt\%] + Mo\ [wt\%] + V\ [wt\%]}{5} \qquad \textbf{(4-1)}$$
$$+ \frac{Cu\ [wt\%] + Ni\ [wt\%]}{15}$$

Whereby: CE   - carbon equivalent

C   - Carbon

Mn   - Manganese

Cr   - Chromium

Mo   - Molybdenum

V   - Vanadium

Cu   - Copper

Ni   - Nickel

Steels with carbon equivalent up to 0.40 are recognised as having good weldability. As seen in table 4-4, the weldability of mild steels is excellent. The higher strength steels could cause difficulties in the experiments as their carbon equivalents are between 0.70 and 1.01.

The parent material (base) is generally ground to remove oxides and acetone cleaned prior to the welding tests.

4.2.2 Ceramic powders SiC and WC used in the GTA cladding process

For the cladding process, the two ceramic powders SiC and WC were used. These ceramics are known to give increased wear resistance [66], [72], [87]–[89] which could be adopted for brake disc applications [90]. The most important chemical, mechanical and physical properties of the ceramics are shown in table 4-6.

Table 4-6: Physical and chemical properties of SiC and WC ceramic [91]–[93]

Property	Tungsten Carbide	Silicon Carbide
Phases	- W_2C (subcarbide) - WC (also called α-WC) - β-WC$_{1-x}$ (unstable, forming only above 1530°C)	- α-SiC - β-SiC

Property	Tungsten Carbide	Silicon Carbide
Crystal Structure and Lattice Parameters (nm)	- W_2C: hexagonal, a 0.30008, c 0.47357 - WC: hexagonal, a 0.2907, c 0.2837	- α-SiC: hexagonal-6H, a 3.073, c 15.08 - β-SiC: cubic, a 4.358
Composition	Narrow range of homogeneity, α-$WC_{0.98}$-$WC_{1.00}$	SiC (very narrow range)
Molecular Weight (g/mol)	- W_2C: 379.71 - WC: 195.86	40.097
Colour	grey	colourless to yellow if pure, brown if doped with boron, nitrogen or aluminium
X-ray Density (g/cm^3)	- W_2C: 17.2 - WC: 15.8	- α-SiC(6H): 3.211 - β-SiC: 3.214
Melting Point	- W_2C: 2730°C - WC: 2870°C WC decomposes by melting incongruently. WC has a large stability domain but reacts with W_2C or W. W_2C starts to decompose at 1300°C into W and hexagonal WC	2545°C at 1 atm. SiC decomposes to Si, Si_2C, Si_2, and SiC_3
Specific Heat C_p (J/mol·K)	39.8	- α-SiC: 27.69 - β-SiC: 28.63
Heat of Formation -ΔaH_f at 298 K (KJ/g-atom metal)	37.7	
Heat of Formation -ΔH at 298.15 K (KJ/mol·K)		- α-SiC: 25.73 ± 0.63 - β-SiC: 28.03 ± 2
Thermal Conductivity (W/m·K)	63	- α-SiC: 41.0 - β-SiC: 25.5

Property	Tungsten Carbide	Silicon Carbide
Thermal Expansion (x 10^{-6}/K)	- a: 5.2 - c: 7.3 depending on Lattice Parameter	- α-SiC: 5.12 - β-SiC: 3.8
Electrical Resistivity ($\mu\Omega\cdot$cm)	17 - 22	- α-SiC: 0.0015 to 10^3 - β-SiC: 10^{-2} to 10^6
Vickers Hardness (HV)	2243	2498 - 2875 (varies with crystal face)
Young's Modulus of Elasticity (GPa)	620 - 720	475 at 293 K 441 at 1773 K
Shear Modulus (GPa)	262	192
Bulk Modulus (GPa)		96.6
Poisson's Ratio	0.18	0.142
Transverse Rupture Strength (MPa)	550	
Flexural Strength (MPa)		350 - 600

For the cladding process, some of these properties are important to obtain an indication of the behaviour of the ceramics during the process. For example, a too low melting point could lead to melting the ceramic in the liquid weld pool. However, the melting point is less important under one of the following conditions: either the cooling rate is fast enough to overcome the effect of melting, or the ceramic gets into a chemical reaction with the matrix and/or the base material. The melting point is dependent on the phases of the ceramic. The high difference in the density of steel (steel: 7.85 g/cm^3 [94]) and the ceramic could lead to floating for SiC and sinking for WC. Too low or too high electrical resistivity of the ceramic could affect the arc during the cladding process. The electrical resistivity of the ceramic should be similar to steel (steel: 10^{18} $\mu\Omega\cdot$cm [94]). As the matrix and base materials are steel, the SiC ceramic has a chemical reactivity with Fe as a solid state reaction down to approximately 850°C [95]–[98] during cooling.

The solid state reactions during cooling of the ceramical compounds can be seen in the phase diagram of SiC and WC in figure 4-8.
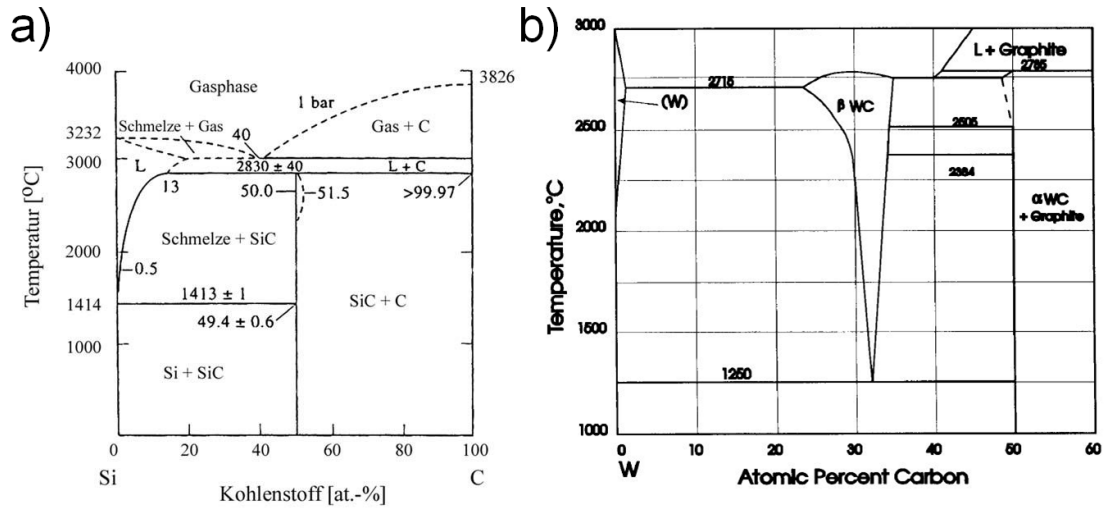
Figure 4-8: Phase diagrams; a) SiC phase diagram, Schmelze is liquid phase, Kohlenstoff is carbon content in at% [99]**, b) WC phase diagram (part: 0 at% W to 60 at% W), L is liquid phase** [92]

The preferred chemical composition of both ceramics is 50 at% M and 50 at% C whereby M stands for W or Si. These phases are eutectic phases, a sign of high hardness. Tungsten Carbide has a metastable phase at 66 at% W and 33 at% C which is called W_2C and has high hardness as well. The wear resistance of the ceramic would depend on the hardness [62], [100], [101]. SiC and WC show hardness values with approximately 2200 HV to 2900 HV as shown in table 4-6, which are significantly harder than that of steel. For comparison, the hardness of mild steel is approximately 180 HV and that of high strength steel is approximately 350 HV.

4.3 Calibration of the GTA cladding process

The GTA cladding process must be calibrated before use and the window of operation needs to be understood. This was done using the following steps:

- Calibration of the wire feeder

52

- Calibration of the motion axis
- Calibration of the powder feeder.

A minimum tolerance of the welding and cladding process can give reproducible values.

4.3.1 Wire feeder calibration

The migatronic KT-4 wire feeder has a feeding speed adjustment of 0 % - 100 % wire feeding rate, whereby the feeding rate depends on the wire used. Steel can require a higher wire feeding rate for the same wire feed speed (WFS) than i.e. aluminium because of its density and yield strength. Therefore, steel keeps its stiffness for longer and avoids wire collapsing (bird nests). The force needed to feed a wire depends on the set-up of the experiment as well as on the wire stiffness and surface roughness. The consequences of the wire set-up, stiffness and roughness can be significant. Nonetheless, some minor differences can occur from the inliner of the feeding hose, for example grease on the wire or the pressure of the feeding rollers. The calibration was executed for all possible feeding rates to find the minimum and maximum wire feeding speeds. A linear correlation between wire feed rate and wire feed speed illustrates an accurate working wire feeder.
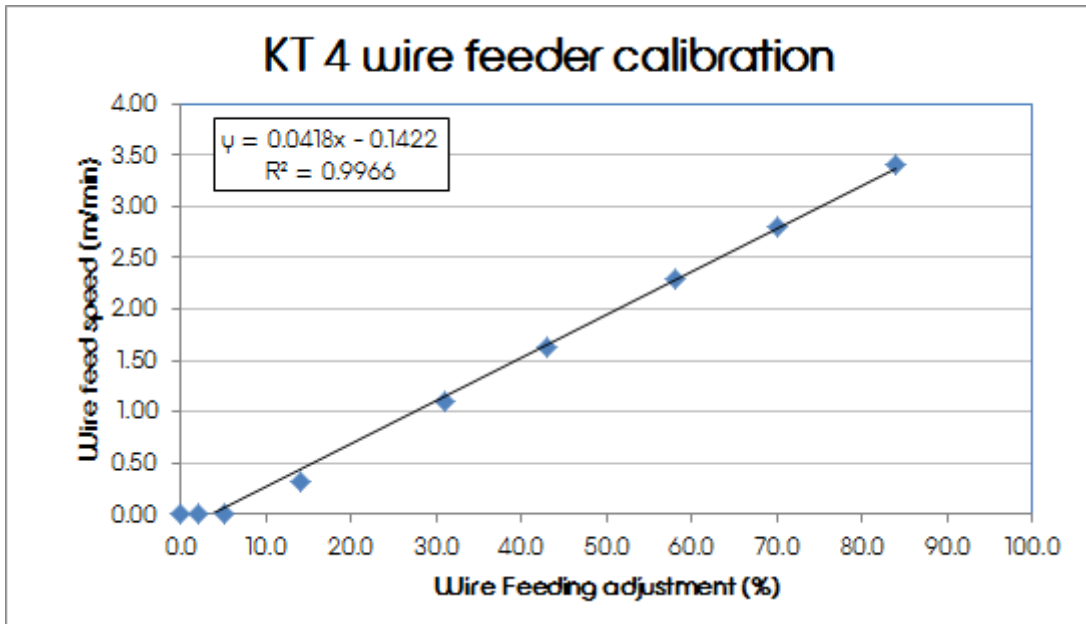
Figure 4-9: Wire feeding adjustment to wire feeding speed calibration chart for the KT-4 wire feeder with G4Si1 wire

As seen in figure 4-9, the wire feeding rate to wire feeding speed is a linear function between WFS = 0.3 m/min and WFS = 3.4 m/min. Outside this range the wire feeding becomes unstable if not impossible but it gives a very good operation area for the experiments planned.

4.3.2 Control of the motion axis

The distances on the 5-axis rig shown in figure 4-2 b) were driven and controlled by a Trio Motion controller. The Motion Coordinator MC216 and software of the system on the 5-axis rig was "Motion Perfect" from Trio Motion. Further explanation about the calibration of the motion system can be found in Appendix E.

4.3.3 Powder feeder calibration

The powder feeder described in figure 4-4 has to be calibrated for each powder and for each feeding disc configuration. The SiC powder used was the F90 SiC

with 150 μm – 180 μm particle size (see appendix L.3). However, the WC powder was Spherotene with 40 μm – 160 μm particle size (see appendix L.3). These powders were calibrated for different Ar transport gas pressures and flow rates over one minute feeding times. A useful operating window for powder feeding is achieved when the powder feeding rate and the feeder disc rotation correlate linearly. Results shown in figure 4-10 were achieved with SiC and the feeding disc (NL 16 / 1.2) for higher feeding rates [80].
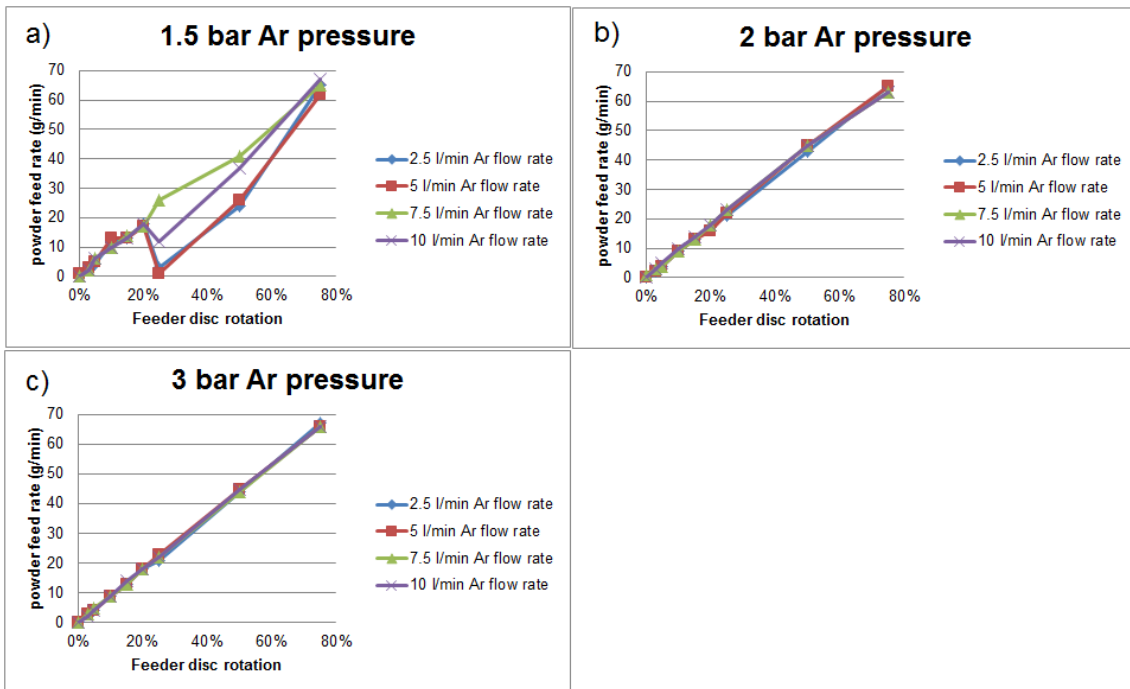
Figure 4-10: F90 SiC powder feeding calibration plotted against the feeder disc rotation (see 4.1 powder feeder range) for an NL 16 / 1.2 [80] type feeding disc with an Ar transport gas flow rate from NLPM = 2.5 l/min to NLPM = 10 l/min; a) 1.5 bar Ar transport gas pressure; b) 2 bar Ar pressure; c) 3 bar Ar transport gas pressure

As seen in figure 4-10 a), the SiC powder feeding with the 1.5 bar Ar transport gas pressure is unsteady. Therefore, an adjustment for a specific powder feeding rate would be difficult. Figure 4-10 b) and c) illustrate that the powder feeding rate (in g/min) becomes linear to the feeder disc rotation speed (see 4.1 powder feeder range) with increasing Ar transport gas pressure. Linear powder feeding rates in a stable area can only be used for the powder feeding. SiC

powder feeding is possible for all tested Ar transport gas flow rates from NLPM = 2.5 l/min to NLPM = 10 l/min.
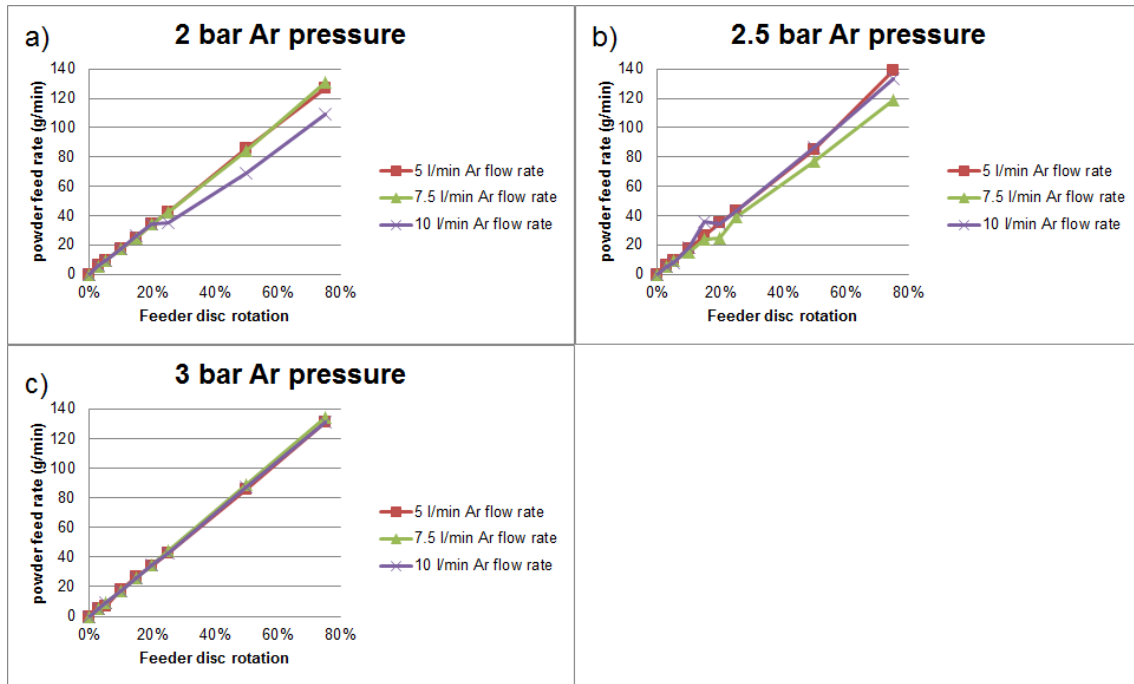
Figure 4-11: WC Spherotene powder feeding calibration plotted against the feeder disc rotation (see 4.1 powder feeder range) for an S 5 / 1 [80] type feeding disc with an Ar transport gas flow rate from NLPM = 5 l/min to NLPM = 10 l/min; a) 2 bar Ar transport gas pressure; b) 2.5 bar Ar pressure; c) 3 bar Ar transport gas pressure

For the WC powder Spherotene 40 µm - 160 µm, the rotation disc S 5 / 1 for lower feeding rates was employed. The WC Spherotene calibrations with Ar transport gas pressures under 2 bars were not possible as it was only clogging up the pipe. A calibration was only possible from 2 bars to 3 bars. Ar transport gas flow rates under 5 l/min exhibited a heap of WC powder on the rotation disc. WC could not be carried without an Ar flow rate of minimum 5 l/min. High WC density (ρ = 16.4 g/cm^3), therefore weight, makes it difficult to transport the Spherotene powder with gas. The illustration of figure 4-11 a) and b) reveals even for 2 bars and 2.5 bars unsteady powder feeding. Even increasing the Ar flow rate to the maximum of 10 l/min indicates a non-linear powder feeding area at approximately 20 % powder feeder disc rotation. Ar flow rates from 5 l/min

and over 3 bars yielded linear variable between feeder disc rotation and powder feed.

As seen in figure 4-11 c), the WC powder feeding rate (in g/min) with 3 bars transport gas pressure is stable for disc rotation speeds between 2.5 % and 75 % and Ar transport gas flow rates from NLPM = 5.0 l/min to NLPM = 10 l/min. Only WC Spherotene was calibrated on the S 5 / 1 type feeding discs for lower feeding rates. As WC has a high density, clogging might easily be possible and a calibration over 1 min feeding time could be too little. Therefore it was compared with a calibration of 10 min feeding time. Figure 4-12 b) shows a 10 times longer calibration time of 10 min which still gives a stable WC powder feeding rate with Ar transport gas of 3 bars pressure and NLPM = 5.0 l/min flow rate.
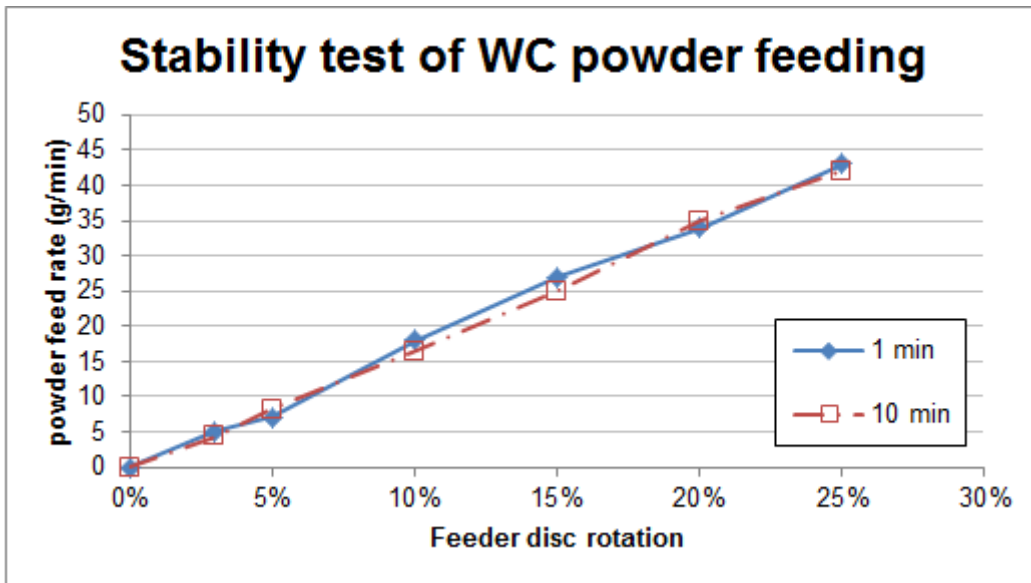
Figure 4-12: WC Spherotene feeding rate, feeder disc rotation for the S 5 / 1 type feeding disc, 3 bars Ar transport gas pressure, NLPM = 5 l/min Ar flow rate; 1 min and 10 min powder feeding for each calibration point

4.4 Investigation of GTAW process limits

The GTA welding process window in terms of combination of I, TS and WFS with the equipment described in 4.1 has its physical limits. Welding seams in a bead-on-plate shape were examined. To investigate the boundaries of a welding process, without any ceramic reinforcement, some pre-trials were performed. The purpose was to find a process window suitable for the intended application. S275JR base plate (12 mm thick) was clamped on the four edges and G4Si1 wire with $\varnothing$ 1 mm was used. The details of the materials can be found in 4.2.1 and Appendix L. A smooth round weld bead is expected within the process window. Variation in current (I), travel speed (TS) and wire feed speed (WFS) were undertaken to establish the process window. Phenomena on the boundaries of the process window are explained here.

All other parameters were defined as minor influences and kept constant; the parameters are listed in table 4-7:

Table 4-7: Constant parameters for GTAW process limits investigation

Parameter	torch angle	a	b	electrode angle	wire feeding direction	wire feeding angle
Unit	-	mm	mm	°	-	°
Setting	perpendicular to work piece	3.5	0	57	lead feeding	15

Parameter	c	d	Shielding gas	Shielding gas flow rate
Unit	mm	mm	-	l/min
Setting	3	13	Ar	7

Whereby:

a   distance between tungsten electrode and work piece – arc length

b   electrode stick out

c   distance between the feeder nozzle and the substrate base plate

d   distance between the feeder nozzle and the tungsten electrode
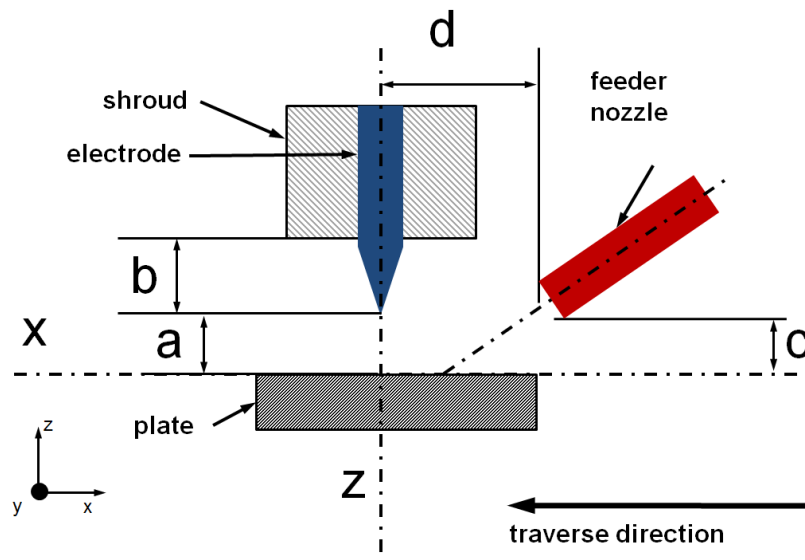
Figure 4-13: Schematic set-up of the torch with wire feeder, *a* distance between tungsten electrode and work piece, *b* electrode stand-off to the shroud, *c* distance between the feeder nozzle and the substrate base plate, *d* distance between the feeder nozzle and the tungsten electrode; front view

Deeper explanation of the parameters and the torch set up can be found in a schematic illustration in figure 6-1.
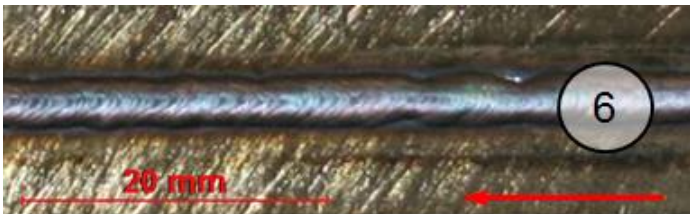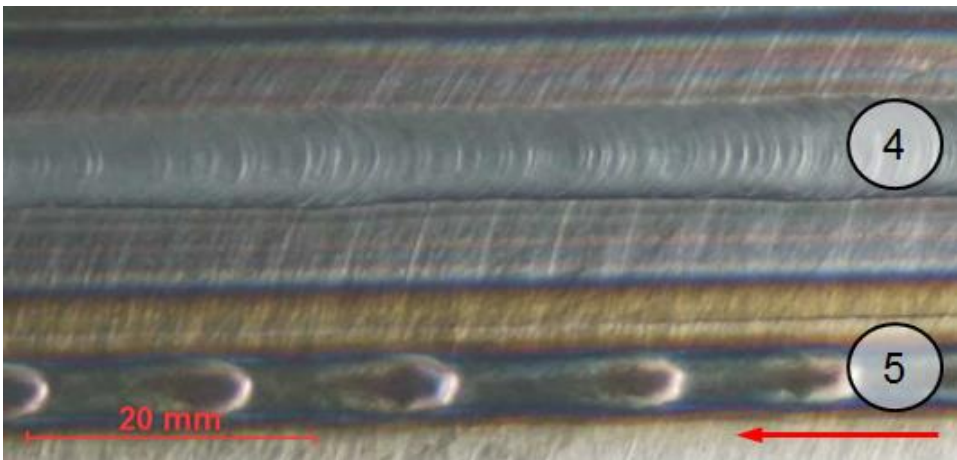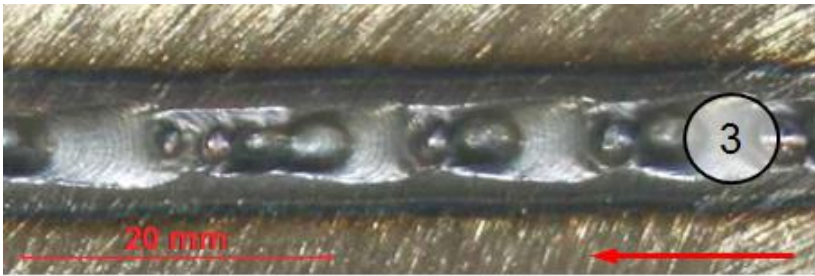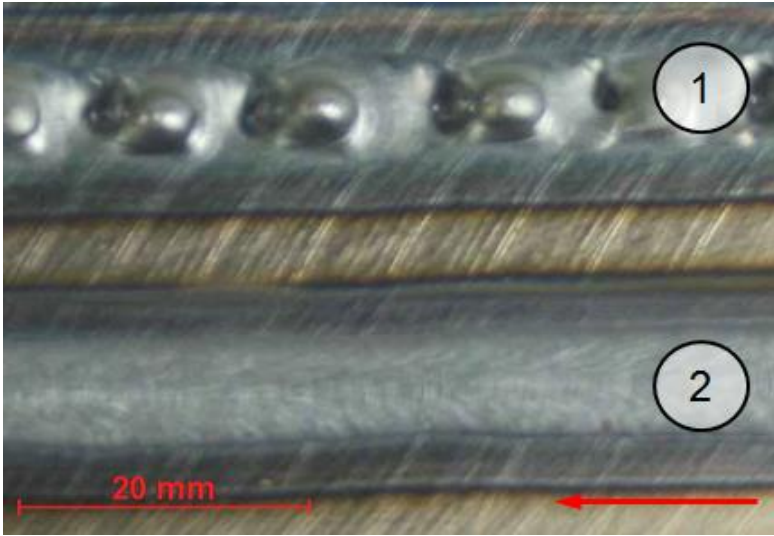
Figure 4-14: Bead-on-plate welding seams; 1: lumpy deposit, upper current; 2: smooth seam, upper current; 3: humping; 4: smooth seam, lower current; 5: lumpy deposit, lower current; 6: narrow seam

The results in figure 4-14 demonstrate a broad process window. The correlating parameters to the welding seam are as below:

Table 4-8: GTAW process parameter of figure 4-14

Figure 4-14 Seam No.	I	TS	WFS	Bead surface
	A	m/min	m/min	-
1	216	0.3	1.5	lumpy deposit
2	216	0.3	1.0	smooth
3	216	0.5	1.0	humping
4	144	0.1	0.3	smooth
5	144	0.5	0.3	lumpy deposit
6	144	0.5	1.0	narrow bead

Welding with too high WFS at high currents causes lumpy deposits. Figure 4-14 seam 1 illustrates the lumps; however, a reduced WFS at the same current results in a smooth bead (Figure 4-14 seam 2 and table 4-8 seam 2). If the travel speed is too high, the welding process results in a humping effect. The grooves of the effect can be seen in figure 4-14 3 although the lumps are not clear in this view. Figure 4-14 seam 4 is evidence of a smooth bead at a lower current. Nonetheless, high TS cause a melting of the wire to a droplet and deposited it in lumps on the base plate. This lumpy deposit at low current is demonstrated in figure 4-14 seam 5. Increased wire feed speed compensates for the lumpy deposit and indicates a very narrow seam, as observed in figure 4-14 seam 6.

The parameters developed will be used in the remaining experimental work.

4.5 Conclusions

Functional graded structures need small increments of cladding layer heights; therefore the GMAW (see Appendix D) and GTAW processes were tested. The GTAW process can achieve the lowest layer heights as the current and voltage are controlled independently from the wire feed speed. In fact, autogenous

welding even makes zero layer height possible. The following conclusions can be drawn from the experimental set up of the GTAW process:

- The 5-axis rig, the Migatronic TIG/Plasma power source and the Migatronic KT4 wire feeder were chosen as suitable.
- The Sulzer Metco TWIN-10-C powder feeder is found to be appropriate for uniformly ceramic powder feeding.
- Investigation of the GTAW limits demonstrates a broad range of the process window which provides a practical variety of parameters.

Statement:

- The materials used in this work were considered as suitable for brake disc applications.
- All GTAW process appliances were calibrated.

5 Feasibility study on manufacturing of functional graded structures using SiC ceramic powder in a steel-based matrix

This chapter presents a paper [102] examining the feasibility of the application of a Gas Tungsten Arc Welding (GTAW) process to obtain a metal-composite functional coating for advanced tribological application. Silicon carbide (SiC) particles (see table 4-6) in the form of powder were added to a weld pool in autogenous mode as well as with an additional filler wire. Powder feeding was carried out from different angles and with varying separation distances from the welding torch. The metallurgical characterisation of the clad structure was carried out using optical as well as Scanning Electron Microscopy (SEM). Energy Dispersive X-Ray Spectroscopy (EDS) was performed for a semi-quantitative analysis of the composition of the deposited weld metal. It was observed that due to lower particle density, it was difficult for SiC to penetrate the weld pool. The added SiC found to be dissociated into Si and carbon and the large amount of dissolved carbon in the weld pool resulted in formation of graphite phases.

S. Herbst did the cladding development, planning of the experiments and analysis of the welds as well as presenting the topic at the Euromat 2011 conference [103] in the symposia B13 Novel steels and steel matrix composites.

S. Ganguly and S. Williams brought in their expertise in welding and metallography and provided the supervision.

Herbst, S., Williams, S., & Ganguly, S. (2012). A Feasibility Study on Manufacturing of Functionally Graded Structures Using SiC Ceramic Powder in a Steel-Based Matrix by Gas Tungsten Arc Welding (GTAW). steel research int., 83(6), 546–553. doi:10.1002/srin.201100271

5.1 Introduction

The aim of the presented work is to achieve a functionally graded layer of metal matrix composite on a steel substrate, with significant improvement in frictional wear performance. The presented study focused on achieving a metal matrix composite layer using SiC as the reinforcement phase in a low carbon steel matrix. A different low carbon grade structural steel plate was used as a substrate material. The F90 grade of SiC ceramic powder (size fraction range 150 μm – 180 μm) was studied as the reinforcement phase for low carbon steel. A gas tungsten arc welding (GTAW) process was used to create the metal matrix composite layer structure. In addition, the issues associated with the process were described. To achieve a metal matrix and ceramic reinforced coating layer, two different methods were used.

An autogenous GTAW process was used where the ceramic powder was fed into the molten substrate metal. An S275JR grade of steel (see table 4-3) was used as the substrate plate.

In a separate trial, a G4Si1 (see table 4-3) mild steel filler wire was fed into the TIG welding process as the matrix material along with the SiC ceramic powder.

Silicon is not a natural carbide former and therefore, the main objective of this work is to study the stability of SiC particles in the melt pool. Also iron has a catalytic effect on SiC, which reduces the dissociation temperature of SiC from 1415°C to approximately 850°C [95]. In steel, Si creates bulk silicides which promote the graphite formation [104]. Carbon has a low solid solubility in ferrite and it promotes pearlitic structures up to 0.8 wt% C [105]. Dissociation of SiC would result in excessive carbon content in the weld pool and would exceed the eutectoid composition of 0.8 wt% C. When the Si content is low, carbon content above 0.8 wt% C would result in the formation of iron carbides (Fe_3C) in the microstructure. At levels above 2.0 wt% C, the eutectic ledeburite phase forms out of the liquid phase - known from the metastable iron carbon diagram [28], [105]. If the C content is well above 0.8 wt% and the Si content is high, the carbon forms graphite. Depending upon the cooling rate and presence of graphitising elements, the graphite can be either in a flake or sphere form [106],

[107]. This is known from the stable iron carbon diagram [28]. To avoid the dissociation of SiC ceramic particles and retain them in powder form, the heat input into the weld pool should be sufficiently low or in other words the energy available for SiC dissociation should be restricted. The separation distance between the point of powder feeding and the GTAW arc, which is controlled by the position of the powder feeder and the powder feeding angle is, therefore, vital in determining the thermal energy of the weld pool available to the SiC particles and thereby critical in controlling the composition and microstructure of the deposited layer. The work presented here shows the microstructural conditions as observed from the different positions and feeding angles of the powder feeder in the horizontal and vertical planes.

5.2 Experimental Procedures

For the TIG cladding, the Migatronic TIG/Plasma commander 320 A AC/DC power source (see chapter 4.1), with a WeldTec TIG welding torch WT-28A-B was used. Wire feeding was enabled through a Migatronic KT-4 wire feeder (see chapter 4.1) for cold wire feeding. The SiC ceramic powder was fed by the Sulzer Metco TWIN-10-C R2 Powder Feeder (see chapter 4.1) which was calibrated for a volume flow of 4 g/min to 66 g/min SiC. Pure argon (see figure_apx I-15) was used as transportation gas under 2 to 3 bar pressure and a flow rate of 2.5 l/min. The torch, wire feeder nozzle and powder feeder nozzle were mounted on a motion system to generate the cladding track. The torch was in a vertical position and at 90° to the base material, which was mounted horizontally underneath (welding position PA according to BS EN ISO 6947:2011). Table 5-2 shows the important process parameters used for the autogenous TIG clads of SiC ceramic powder. The mixing of the SiC particles in the weld pool and subsequent microstructural features were investigated for a given separation distance between the arc and position of powder addition (d and c) and the angle of the powder feeder with the direction of traverse in vertical (β) and horizontal planes (α) (Figure 5-1 and table 5-1)
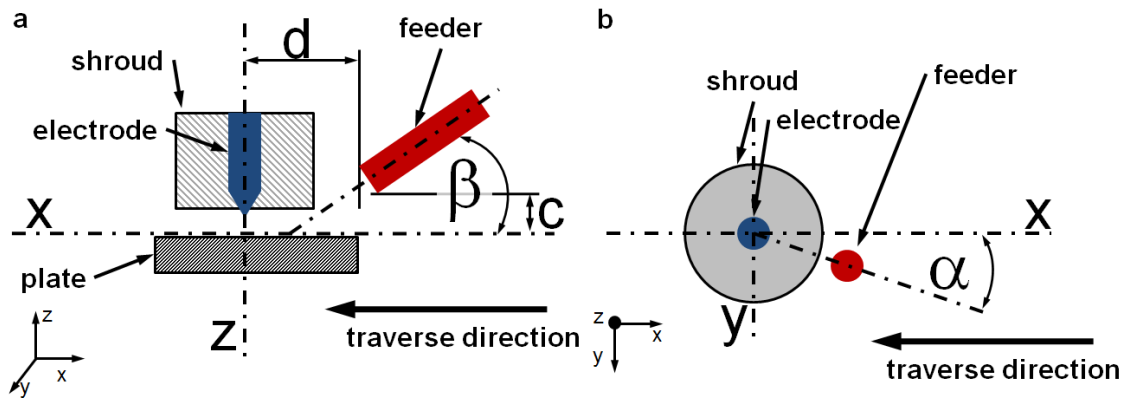
Figure 5-1: 1a schematic β angle in x and z direction (traverse direction, front view); 1b schematic α angle in x and y direction (orthogonal to traverse direction, top view), torch travel direction is from α = 180° to α = 0°; and d separation distance between the feeder and the electrode, c distance between the plate and the feeder.

The parameters of the experimental set-up of figure 5-1 are shown in the table below. It should also be mentioned that the powder feeder is always straight-aligned with the travel direction. The angle α is therefore either α = 0° or α = 180°.

Table 5-1: Set up parameter of the TIG cladding experiments refer to figure 5-1; α angle in x and y direction, β angle in x and z direction, d separation distance, IP impingement point, PF powder feeder, WF wire feeder, Exp. Experiment

Exp.	Name	α	β	d in mm	IP in mm
Exp. 1	SiC clad 30°	PF 0°	30°	16	11
Exp. 2	SiC clad 90°	PF 0°	90°	11	11
Exp. 3	SiC clad 30° with wire	WF 180°	8°	28	0
		PF 0°	30°	16	11
Exp. 4	SiC clad 30° with wire front feed	WF 180°	8°	28	0
		PF 168°	30°	32	11

The constant TIG cladding parameters of the power source, torch, materials and powder feeder used for the SiC clads are listed in table 5-2.

Table 5-2: Cladding parameters of the TIG clads of SiC; Matrix material and wire feed speed are only used where written in this chapter.

Cladding parameters	Set value
Current I in A	216
Tungsten electrode diameter in mm	3.2
Angle tungsten electrode	30°
Arc length in mm	3.5
Feeder to work piece distance (c) refers to figure 5-1 in mm	3.0
Travel speed in m/min	0.35
Ar shielding gas in l/min	10
Ar transport gas in l/min	2.5
SiC ceramic	F 90 SiC, 150 µm – 180 µm particle size
SiC feeding rate in g/min	22
Base material	S275JR
Matrix material	G4Si1 mild steel welding wire
Wire feed speed in m/min	1.5

5.3 Results and Discussion of the SiC cladding procedure

Bead profiles for the reference autogenous welds without powder feeder were shown in figure 5-2 $\underline{a}$ and with powder feeder transport gas (Ar) ($\beta = 30°$, $\alpha = 0°$

angle set up) were shown in figure 5-2 <u>b</u>. These welds show that the humping effect, due to excessive travel speed in the autogenous TIG weld (Figure 5-2 <u>a</u>), is eliminated by the Ar transport gas only (Figure 5-2 <u>b</u>). The humping effect still occurs between the arc and the point of the transport gas impact. This effect gets evened out because of significant turbulences in the liquid weld pool. These turbulences appear from a combination of the pressure of the argon transport gas and the changed surface tension due to the flow of trailing argon instead of steady air.
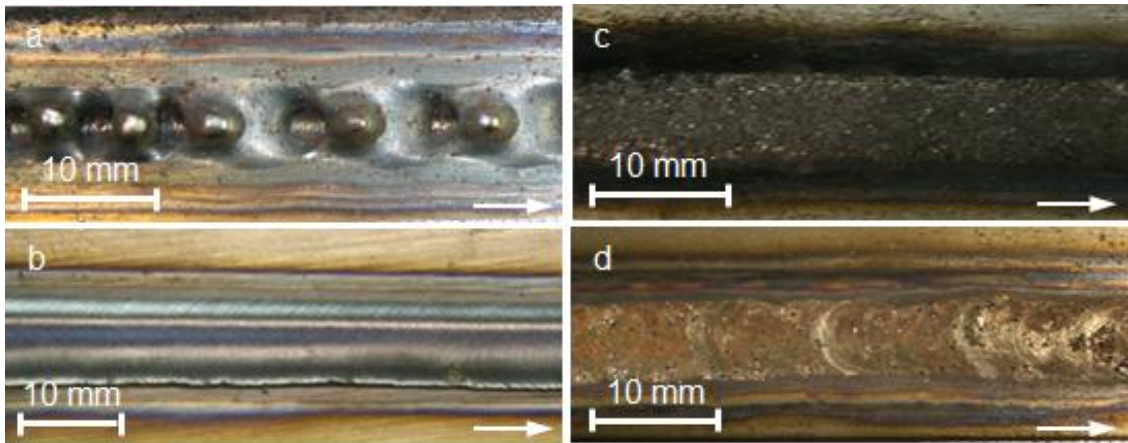
Figure 5-2: <u>a</u> autogenous TIG welding track; <u>b</u> TIG welding track with Ar transport gas from the powder feeder; <u>c</u> TIG cladding track with SiC powder feeding Exp. 1; <u>d</u> TIG cladding track with SiC powder feeding Exp. 2

In the TIG cladding tracks with SiC powder, the humping effect is still prevented by the Ar transport gas (Figure 5-2 <u>c</u>, <u>d</u>). The Exp. 1 shows a very rough surface with a dense SiC particle distribution on the surface (Figure 5-2 <u>c</u> and figure 5-3 <u>a</u>). The smooth powder feeding angle of $\beta = 30°$ gives an optimum bonding on the weld pool surface. However, Exp. 2 was chosen because of the density difference of steel and SiC ceramics. SiC powder has a Loose Pack Density (LPD) between 1.41 g/cm^3 and 1.51 g/cm^3 and a single SiC particle has a density of 3.21 g/cm^3, identified from the material delivery note [108], [109]. The steel S275JR has a density of 7.85 g/cm^3 [94]. As the density of SiC is approximately five times lower than the density of steel it was necessary for the SiC powder to be fed deeper into the weld pool, otherwise it would have coagulated near the surface without any penetration. The surface lustre of the

TIG clad in Exp. 2 (Figure 5-2 <u>d</u> and figure 5-4 <u>b</u>) indicates a significantly increased SiC particle incorporation, as more powder got into the clad instead of floating. In comparison, the clad in Exp. 1 had a rough dark surface of SiC particles, as seen in figure 5-2 <u>c</u> and figure 5-4 <u>a</u>.
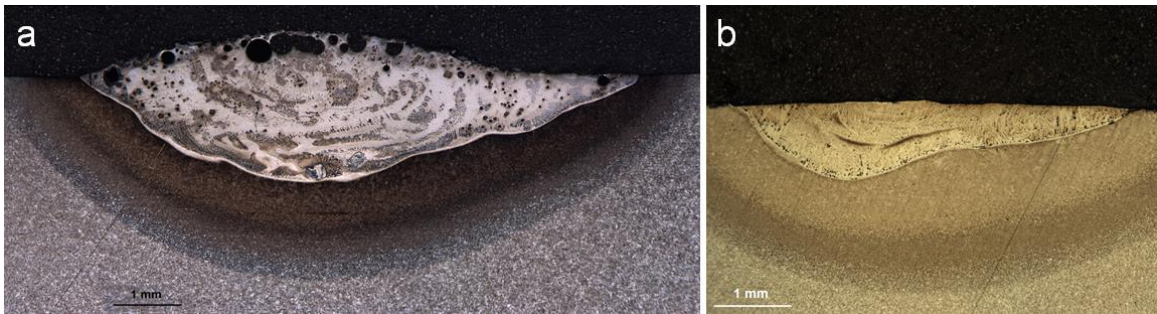
Figure 5-3: Microsection of the SiC clad; <u>a</u> microsection of the SiC clad from Exp. 1; <u>b</u> microsection of the SiC clad of Exp. 2

In the overview of both samples, it is seen that the $\beta = 90°$, $\alpha = 0°$ angle powder feeding (Exp. 2) gives a uniform cladding bead (Figure 5-3 <u>b</u>), whereas the $\beta = 30°$, $\alpha = 0°$ angle powder feeding (Exp. 1) shows a mixture of different phases figure 5-3 <u>a</u>. The cross section sample preparation is given in Appendix G and the light microscope tolerances are in section G.2.
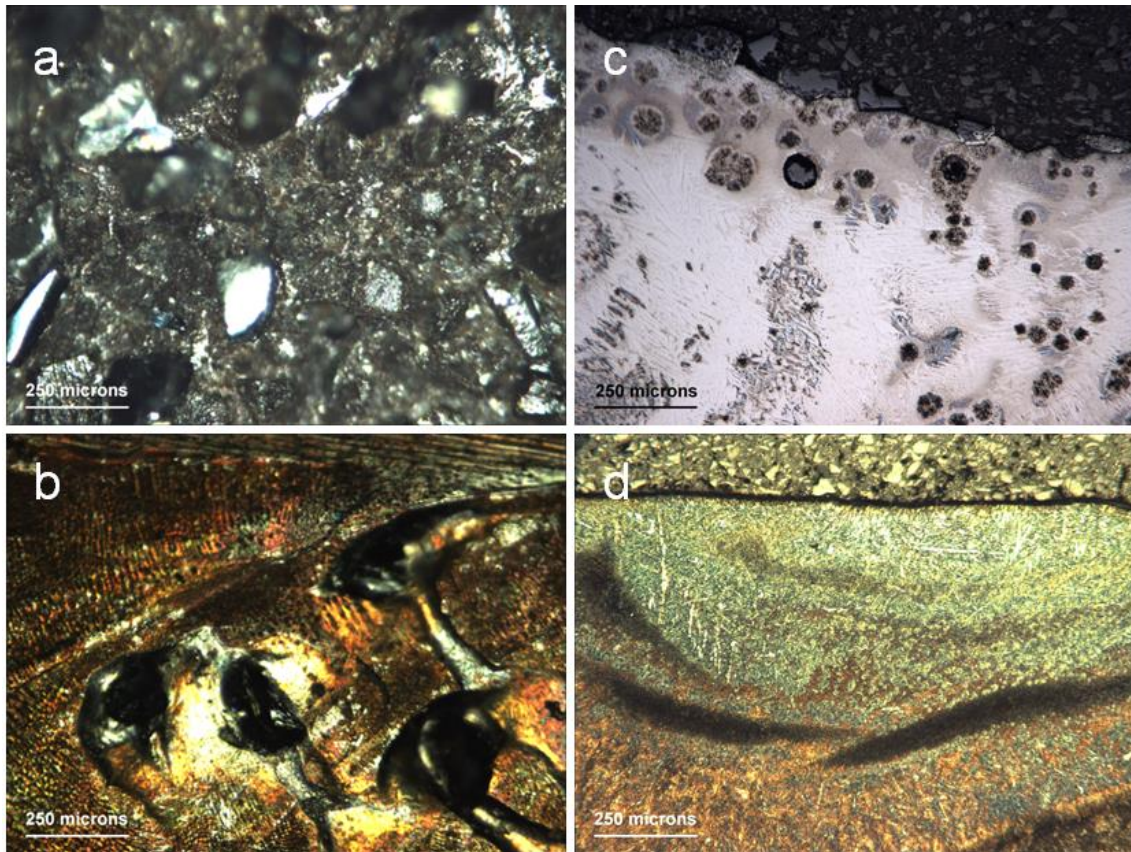
Figure 5-4: Surfaces and microsection of the SiC clad; <u>a</u> surface of the SiC clad of Exp. 1; <u>b</u> surface of the SiC clad of Exp. 2; <u>c</u> microsection of the SiC clad of Exp. 1; <u>d</u> microsection of the SiC clad of the Exp. 2

Nevertheless, the SiC cladding tracks appear to be different in the microsection when compared to the surface. As seen in figure 5-3 <u>a</u>, <u>b</u> and in figure 5-4 <u>c</u>, <u>d</u>, the SiC particles are only on the surface of the cladding track. There is a distinct absence of SiC particles seen in the microsection of the Exp. 2 (Figure 5-4 <u>d</u>). Further detailed investigation to understand the dissociation of SiC powder of the sample of Exp. 1 (Figure 5-2 <u>c</u>, figure 5-3 <u>a</u> and figure 5-4 <u>a</u>, <u>c</u>) was undertaken using the Scanning Electron Microscope (SEM) and analysed with Electron Dispersive X-Ray Spectroscopy (EDS, EDX). The analysis is based on the Si content as a quantitative analysis of carbon is not advisable using the EDS spectroscopy. The EDS analysis shows that the SiC is dissociated into Silicon (Si) and Carbon (C). This is seen due to the Si content being very high compared to the Si content in the steel (0.18 wt% Si). It is in all depths of the weld metal between 6.19 wt% Si and 9.41 wt% Si. This is shown

in figure 5-5 <u>b</u> A 3 and <u>c</u> A 4 with the EDS values of table 5-3 Areas 3 and 4. However, the SiC particles on the surface as seen in figure 5-5 <u>a</u> are chemically bonded to the surface of the clad. This is due to the fact of a graduated transition zone (Figure 5-5 <u>b</u> A 2) analysed in table 5-3 Area 2 from the particle to the matrix material. This transition zone shows Manganese (Mn) of 0.51 wt% Mn and a Si content of 6.19 wt% Si because of the diffusion of steel into the SiC and Si out of the SiC. The EDS analysis of figure 5-5 <u>c</u> A 5, given in table 5-3 Area 5, shows an indication that these particles in the clad are graphite, as in cast iron. In comparison with the literature available on cast iron and figure 5-5 <u>b</u>, it is reasonable to suggest that these particles are graphite [105].

Table 5-3: Chemical analysis of the raw materials and the EDS analysis. All results in weight per cent (wt%).

Material	C	Si	Mn	Cr	Ni	Others	O	Fe
S275JR base	0.14	0.18	0.82	0.13	0.42	0.24		bal.
SiC ceramic	29.95	70.05						
G4Si1 matrix	0.06	0.94	1.64	0.02	0.02	0.06		bal.
EDS analysis								
Area 1	35.70	63.51						0.79
Area 2	47.68	6.19	0.51					45.6
Area 3	10.43	9.41	0.98					79.2
Area 4	6.52	8.91	0.84					83.7
Area 5	88.75	0.40					8.38	2.47
Area 6	4.23	0.00	1.00					94.77
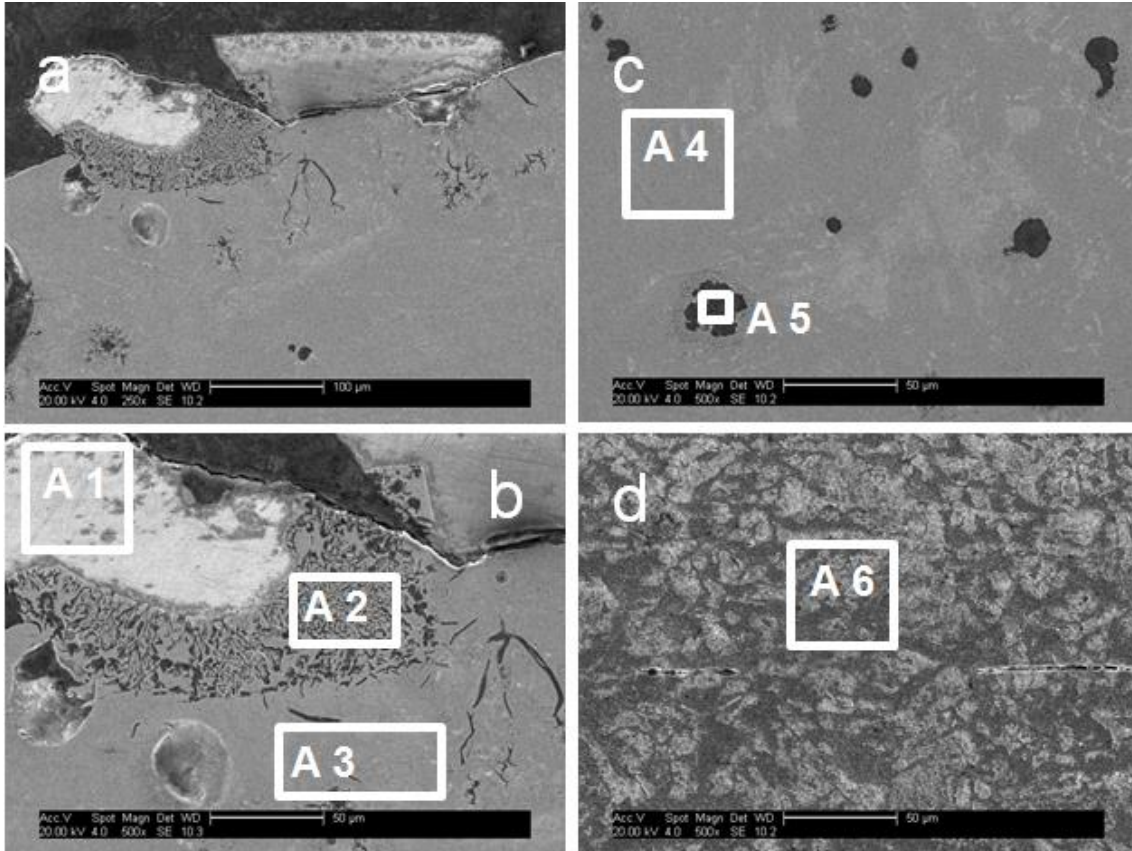
Figure 5-5: SEM images of the SiC clad of Exp. 1 and the S275JR base material; <u>a</u> overview surface; <u>b</u> magnification of <u>a</u> with EDS analysis: A 1 is Area 1, A 2 is Area 2, A 3 is Area 3 in table 5-3 ; <u>c</u> middle of the SiC clad with EDS analysis A 4 is Area 4, A 5 is Area 5 in table 5-3 ; <u>d</u> S275JR base material with EDS analysis A 6 is Area 6 in table 5-3

The trend of Si throughout the microsection, starting from the base to the weld material surface, can be shown in a graph. The graph reflecting the wt% Si of table 5-3 is given in figure 5-6.
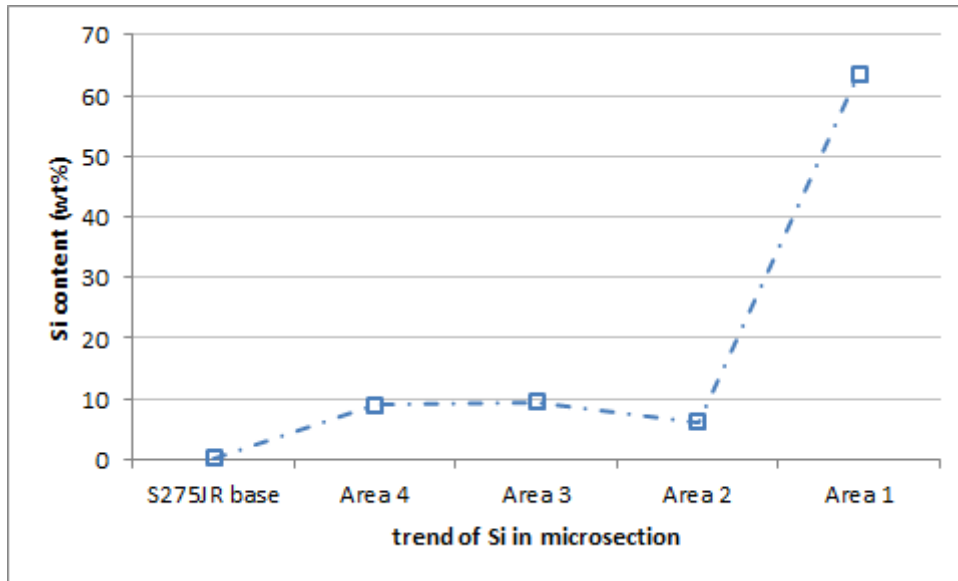
Figure 5-6: trend of Si in the microsection from figure 5-5 and table 5-3.

Figure 5-6 shows an increase of Si from the base to the weld bead by 8.73 wt% Si (from S275JR base to Area 4). This significant increase keeps stable to the top of the weld material (from Area 4 to Area 3). Within the dissociating area of the SiC particles (Area 2) is a slight decrease of Si by 3.22 wt% Si measured (from weld bead of Area 3 to Area 2). The original SiC particle reveals an increase of 54.1 wt% Si compared to the weld material (Area 3 to Area 1).

When an additional matrix material was fed in form of wire, two experimental set-up positions were used. The first was powder feeding trailing the arc with a $\beta = 30°$, $\alpha = 0°$ feeding angle (Exp. 3) and the second was powder deposition in front of the arc with a $\beta = 30°$, $\alpha = 168°$ feeding angle (Exp. 4) (Table 5-1). In both set-up positions the wire was fed prior to the arc with a $\beta = 8°$, $\alpha = 180°$ feeding angle (Table 5-1).

The additional matrix material should have two effects:
Firstly, the weld bead should have the same energy input but more volume to melt as without the wire, particles of the SiC ceramic feeding trailing the arc would feed into a liquid melt pool with lower temperature (Exp. 3).
Secondly, when the powder deposition in front of the arc was used, the SiC particles should form a layer on the base material which would be covered by

74

the molten wire and be bonded to the base material to overcome the floating effect (Exp. 4). However, the full energy of the arc would be on the particles. The results in figure 5-7 a and b show that the SiC particles still dissociate.
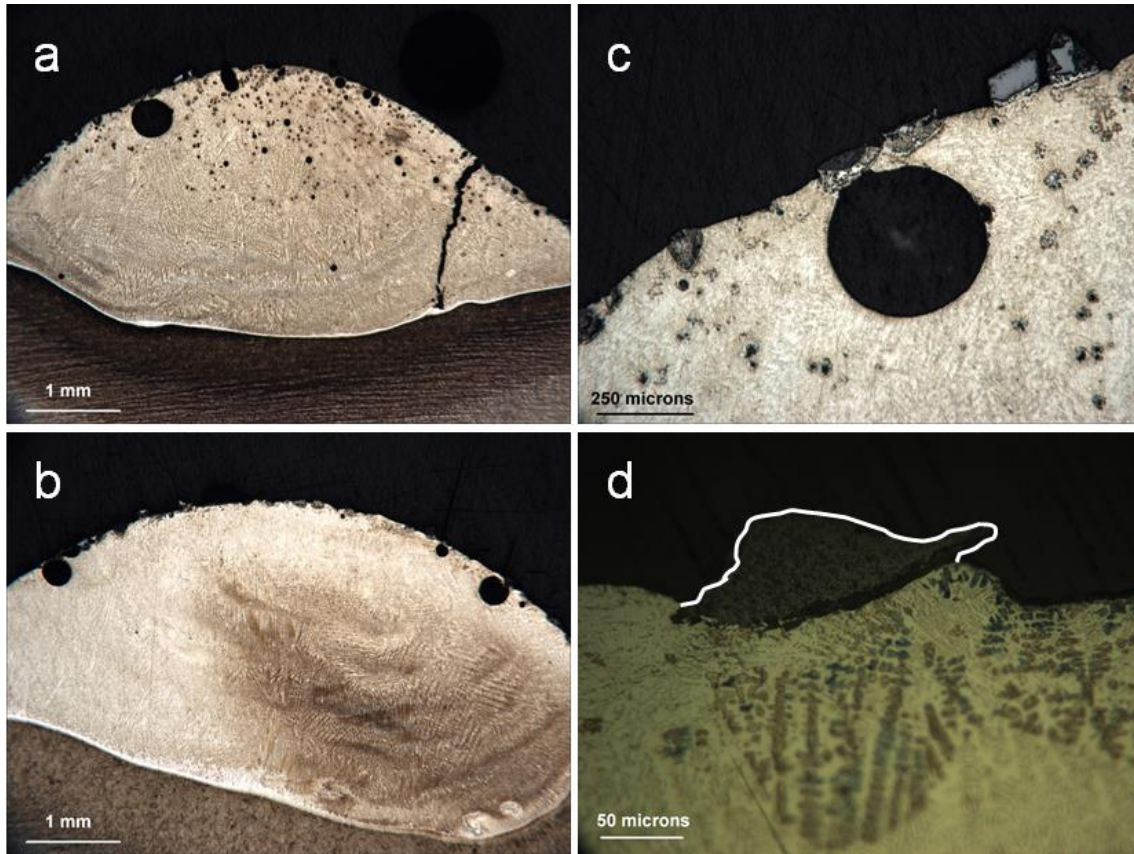
Figure 5-7: microsection of SiC clads with matrix material; a feeding of SiC particles trailing the arc (Exp. 3), overview; b SiC particles deposition in front of the arc (Exp. 4), overview; c Exp. 3, surface magnification; d Exp. 4, SiC particle on the surface in magnification

As can be seen in figure 5-7 b, a slight misalignment of the powder feeder out of the travel direction of the GTAW torch (out of $\alpha = 0°$ or $\alpha = 180°$) caused an uneven penetration of the weld bead (Exp. 4). SiC powder deposition prior to the arc cannot be aligned to a $\alpha = 180°$ angle as the wire feeder is in this position. Without misalignment, the penetration difference has not appeared in powder feeding trailing the arc (Exp. 3) (Figure 5-7 a). Unfortunately, a crack initiated by the high hardness was on one side of the track in Exp. 3 trailing the arc. Figure 5-7 a and b shows the dissociation of the penetrated SiC. Figure 5-7 c also shows how the SiC particles on the clad bead surface are bonded.

The SiC particles form graphite close to the surface. However, the SiC particles form only a brittle cast iron structure together with the matrix deeper into the clad. In the SiC powder deposition and wire feeding prior to the arc, the SiC particles dissociate on the surface, as shown in figure 5-7 d, and no graphite was identified.

5.3.1 Microhardness test according to Vickers

The following microhardness test according to Vickers shows a significant increase of hardness in all clads with SiC. The hardness Vickers test with 0.5 kg mass or 4.903 N nominal load (Figure 5-8) shows an average hardness of the S275JR base material with 171HV0.5 (the in test indentation distance is 0 mm to 5 mm for all test tracks). The hardness in the Heat Affected Zone (HAZ) illustrates a similar progression for all test tracks either with wire or without. The hardness of the HAZ is in the test indentation distance from 0 mm to -1.5 mm. For the SiC clad Exp. 1, the increase of 182HV0.5 in the HAZ is from 173HV0.5 to 355HV0.5 - the highest of the specimen. The specimen of the SiC clad Exp. 2 has the lowest hardness improvement in the HAZ, with 58HV0.5 - from 176HV0.5 to 234HV0.5. The Vickers hardness of the HAZ in SiC particles feeding trailing the arc (Exp. 3) with wire feeding, indicates a growth of 120HV0.5 from 199HV0.5 to 319HV0.5. The SiC particles feeding in Exp. 4 (deposition prior to the arc) confirms this development in the HAZ with 115HV0.5 - from 196HV0.5 to 311HV0.5.
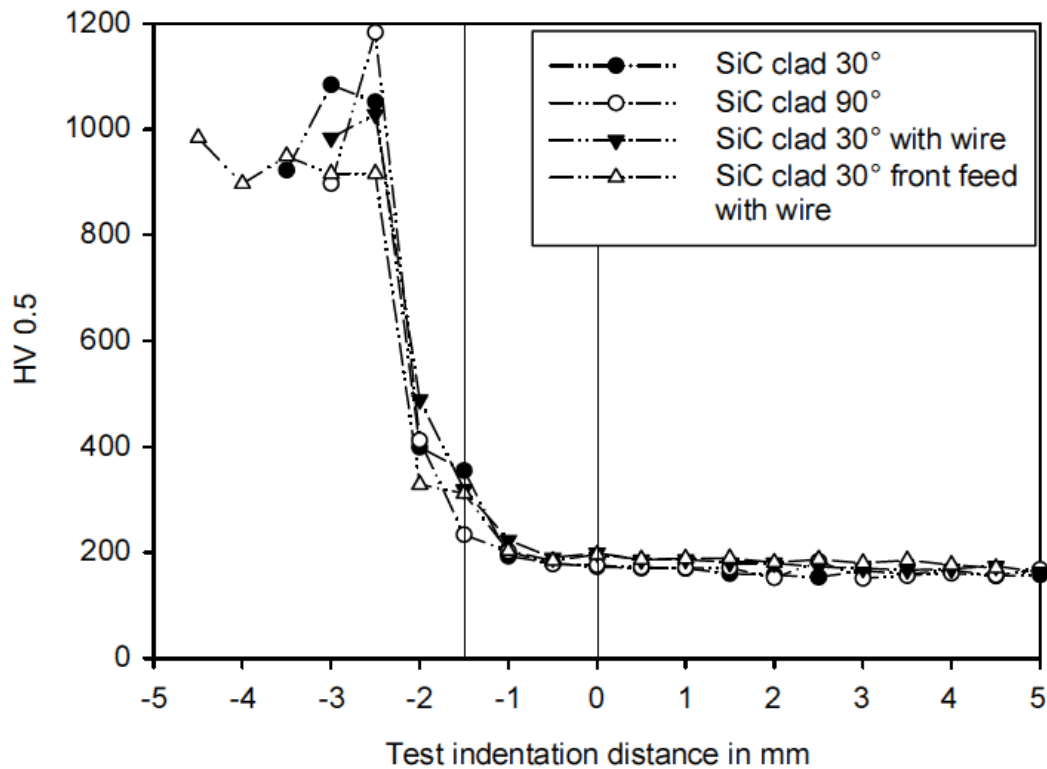
Figure 5-8: Microhardness test according to Vickers of the SiC clads, at 0 mm indentation distance is the last test point in the base plate, at -1.5 mm indentation distance is the last point in the Heat Affected Zone (HAZ); SiC clad 30°: Exp. 1; SiC clad 90°: Exp. 2; SiC clad 30° with wire: Exp. 3; SiC clad 30° front feed with wire: Exp. 4

While in the two HAZ of the SiC clads without wire the increase of hardness is significantly different with 182HV0.5 and 58HV0.5, the hardness growth in the two HAZ of the SiC clad with wire has a minor difference with 120HV0.5 and 115HV0.5.

As seen in figure 5-8, all SiC clads have a very steep rise in hardness from the HAZ (at -1.5 mm indentation distance) to a peak point in the clad (at -2.5 mm to -3.0 mm) which could come from the excessive carbon inclusion. The result then goes along with the previous findings that graphite is in the upper area of the SiC clads (Figure 5-5 and figure 5-7). The hardness Vickers value of Exp. 1 rises from the HAZ with 355HV0.5 to 1084HV0.5 (Figure 5-8 from -1.5 mm to -

3.0 mm indentation distance). After that the hardness drops towards the SiC clad surface from 1084HV0.5 to 922HV0.5 at -3.5 mm indentation distance. The peak value in Exp. 2 is the hardest with 1183HV0.5. This peak appears at a 1 mm distance from the HAZ which has a hardness of 234HV0.5. The hardness drops after the peak down to 897HV0.5 (at -3.0 mm indentation distance). For Exp. 3, the peak is at -2.5 mm indentation distance and achieves a hardness of 1028HV0.5. The reduction following the peak to 984HV0.5 (at -3.0 mm indentation distance) is not as great as the SiC clads without matrix material. As seen in figure 5-8, the SiC particles' deposition in Exp. 4 has the lowest hardness with a peak of 984HV0.5 directly at the surface (at -4.5 mm indentation distance). Nevertheless, the hardness improves shortly following the HAZ from 311HV0.5 to 916HV0.5 and stays on a stable level to the surface. Summarising all HV0.5 hardness values are dropping down towards the surface which could be because of decarbonisation. This phenomenon was not observed for Exp. 4.

5.4 Conclusions and Future Work

Due to two major problems, SiC clads with ceramic particles in a uniform distribution are difficult to achieve:

- Firstly, SiC has an immense density difference from steel. This causes floating of the SiC particles on the surface of the molten weld pool.
- Secondly, SiC has an extreme chemical reactivity with iron. The catalytic effect of iron on the dissociation of SiC allows the SiC particles to evenly react in a solute-state reaction in lower temperatures. This effect cannot be easily prevented by changing the cooling rate.

All cladding tracks show a very hard cast iron structure on steel with less cracking. Importantly in this case is the hardness of clads of up to 1183HV0.5, which could give a significant abrasive resistance. The SiC clad in Exp. 2 indicates a deeper indentation of SiC particles in the weld pool. This development will help in future examinations. Thus if SiC ceramic has an abnormal reaction to iron, then either the ceramic or the matrix material needs

to be changed to form a layer with a ceramic distribution in a tough matrix material.

6 Effect of welding parameters on bead shape, dilution and retrieval of WC ceramic powder

Ceramic metal matrix composites (MMC´s), by the GTAW process can only be achieved if the ceramic retains its particle form after the cladding process or reprecipitates as ceramic in the cladding process.

The objectives for this chapter are the following:

- Firstly single bead welding tests with a tungsten carbide (WC) powder addition were surveyed to examine the behaviour of the bead. Shielding gas and electrode grinding angle were chosen as the most influencing GTAW process parameters on the single bead and WC particles.
- Later on, a range of WC powder feeding rates was examined to understand the interaction of WC with molten steel.

Chapter 6 describes the WC influence on single beads in a bead-on-plate set-up using the following steps:

1. Process configurations
2. Shielding gas and electrode angle influence on
   - Process parameters
   - Single bead dimensions
   - WC powder addition and retrieval
   - Matrix hardness in interdependency of WC absorption
   - Cracking of the layer.
3. Study of WC powder addition
   - Effect of WC on single bead dimension
   - Matrix hardness in interdependency of WC absorption
   - Cracking of the layer.
4. Summary and conclusion

6.1 Process configuration for WC single bead trials

GTA welding was performed with the machines and materials of chapter 4.1 in which the base and wire material were chosen as G-22 NiMoCr 5 6 and G89 6 M Mn4Ni2CrMo, respectively. Single bead trials were accomplished in the set-up sketched in figure 6-1. The tip of the electrode is the point of measurement for the distance to the work piece (a), regardless of the grinding angle (γ).
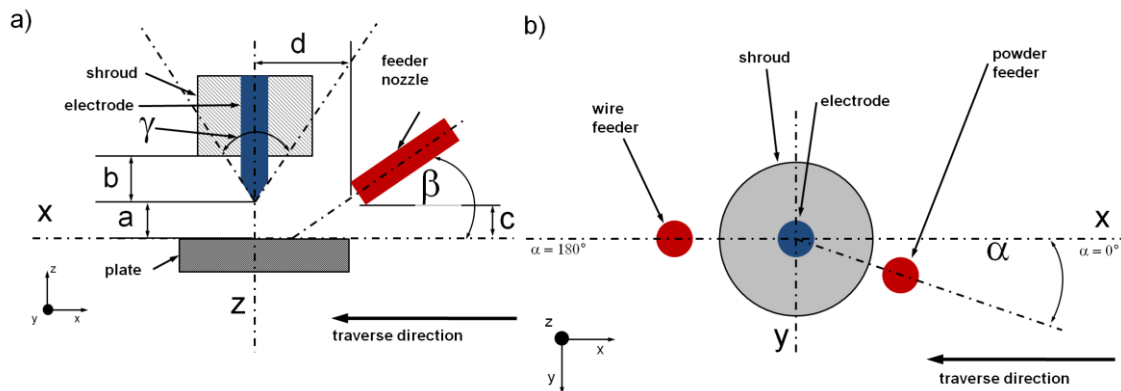
Figure 6-1: Schematic set-up of the torch, wire feeder and powder feeder for GTA cladding, *a* distance between tungsten electrode and work piece, *b* electrode stand-off to the shroud, *c* distance between the feeder nozzle and the substrate base plate, *d* distance between the feeder nozzle and the tungsten electrode, α horizontal angle of the feeders to the torch (0° = trailing, 180° = leading), β vertical angle of the feeders to the base plate, γ electrode grinding angle; a) front view; b) top view

Wire feeding was done using a leading (α = 180°) wire feeder nozzle. Therefore, the wire must pass through the whole arc and a fully melted wire can be ensured within the process window established in chapter 4.4. For an MMC with ceramic as reinforcement phase, the liquid metal of the weld bead should not be too long above a certain temperature. For WC ceramic this temperature is at about 1300 °C (see table 4-6). Consequently, the WC ceramic was fed at the back of the arc with a trailing powder feeder nozzle. In chapter 6 the ceramic powder feeder nozzle, as seen in figure 4-7 b), was only used. Chapter 5 has shown that a straight powder feeder (α = 0° or α = 180°) leads quickly to

ceramic particles burning and attaching to the electrode. This is an outcome of reflected particles from the work piece surface.

Table 6-1: Constant parameters for GTA cladding of ceramic MMC single bead trials; IP: WC powder impingement point, calculated

Current	travel speed	wire feed speed	a	b	wire feeder nozzle			
					c	d	α	β
A	m/min	m/min	mm	mm	mm	mm	°	°
200	0.3	1.5	3.4	8	1.5	14.1	180	19

powder feeder			powder feeder nozzle				
Ar pressure	Ar flow rate	Ar flow rate	c	d	α	β	IP
bar	NLPM	l/min	mm	mm	°	°	mm
3	5	5	5.8	3.9	103	37	8.2

The constant parameters in table 6-1 were chosen from the experimental range established in chapter 4. Figure 5-2 <u>a</u> and <u>b</u> demonstrates the significant effect of the Ar transport gas pressure as the humping effect is just flattened by the powder nozzle without powder feeding. Therefore, in further tests a pressure reducing container shown in figure 4-6 was used. GTA cladding demonstrated a homogeneous single bead welding seam with the fixed process parameters displayed table 6-1. Variable parameters were:

- Shielding Gas type, 7 l/min flow rate   (Ar, Ar/He 50/50, He)
- Electrode angle (γ)   (34°, 57°, 98°)

- WC powder feeding rate   (0 g/min – 100 g/min).

The set-up for the GTAW process configuration is illustrated in figure 6-2.
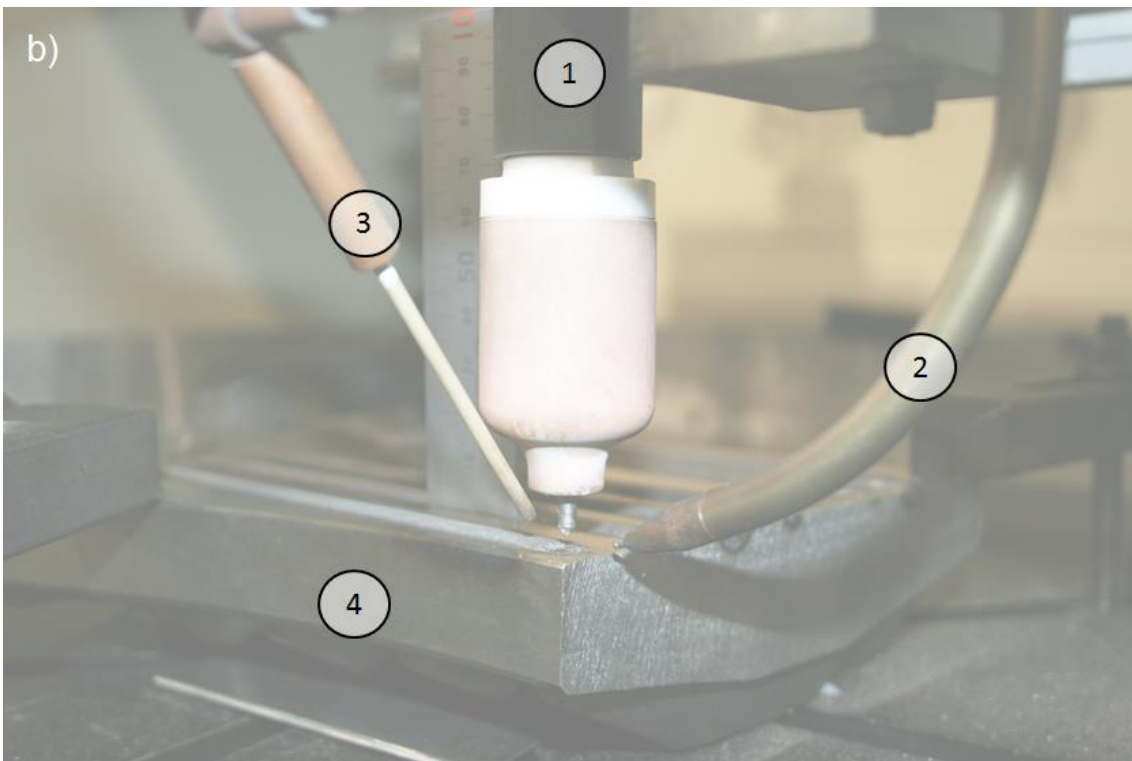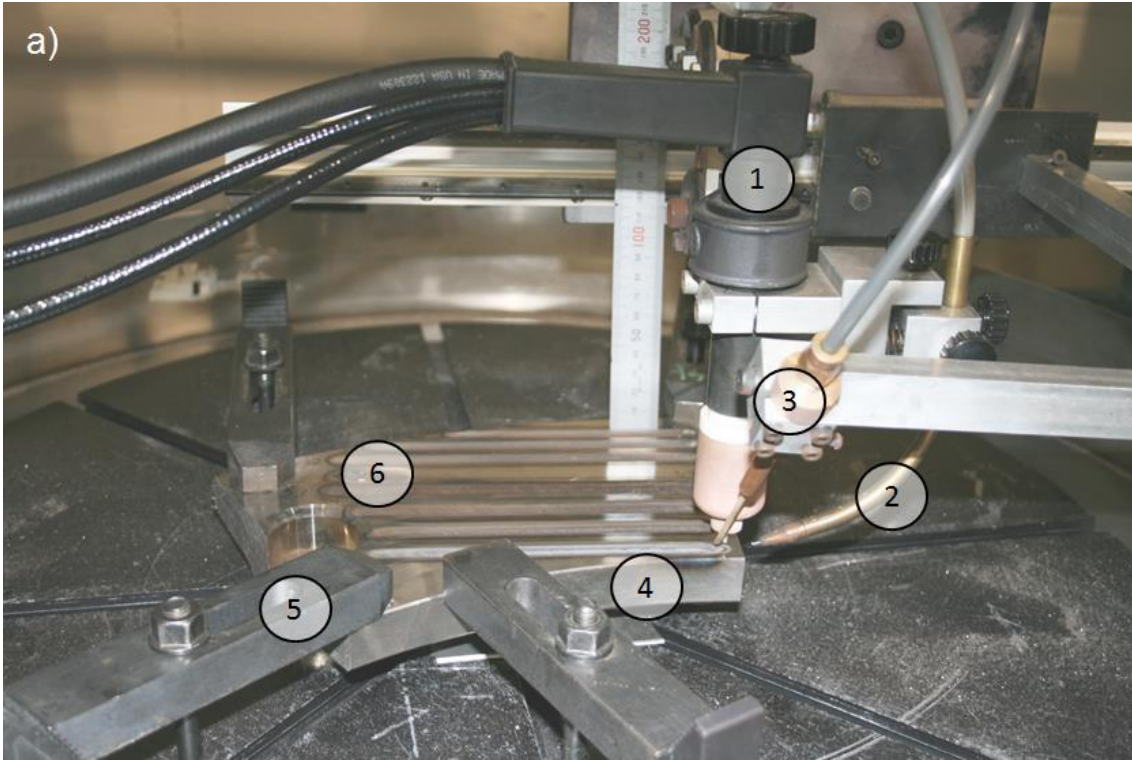
Figure 6-2: Configuration of the GTA cladding with WC powder in single bead trials; 1: torch, 2: wire feeder nozzle, 3: powder feeder nozzle, 4: work piece, 5: clamping system, 6: cladding deposits

The electrode angle, shielding gas and WC powder feed rate were chosen to understand the conditions which will yield optimum bead dimensions and powder intake. Whereby, the bead should have low penetration and the ceramic particles uniformly distributed.

The error bars in this chapter are calculated with the formula shown in Appendix F.

6.2 Shielding gas and electrode angle influence on WC single bead trials

Shielding gases for GTA welding are usually pure argon (Ar) or argon/helium mixtures as explained in chapter 3.1. Argon is the inert gas for universal usage and is preferred due to its low costs. Helium (He) generates a "hotter" arc compared to Ar [110][18] which provides much greater penetration. The effect originates from a higher voltage (V) with constant current (I) and work piece to electrode distance (a). Following equation

$$P = I \times V \qquad \text{(6-1)}$$

Where Power (P) increases linearly with the voltage if the current is kept constant. Thus more heat is generated (called a "hotter" arc) in the welding arc.

The grinding angle of the tungsten electrode (Figure 6-1 γ) can be used to control the level of penetration (and dilution). Figure 6-3 indicates that a smaller electrode angle results in a wider weld pool.
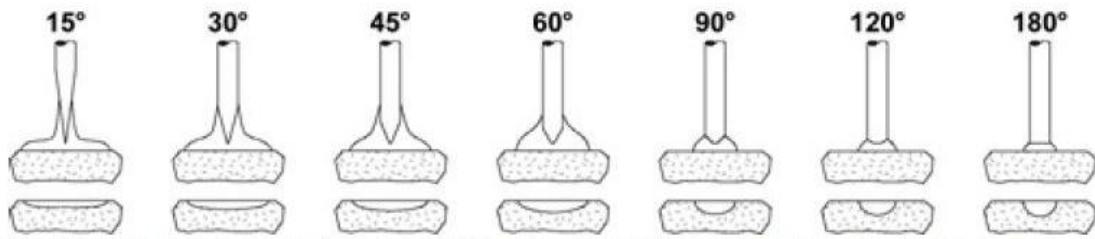
Figure 6-3: Schematic display of the interaction between the arc and the electrode grinding angle (γ) with the resulting weld pool shape [111]

Thus the penetration is not so deep and the weld bead width is large. A larger electrode angle generates a narrow arc instead, with a deep penetration and low weld bead width. Consequently, the electrode angle is responsible for the power density of the arc in GTAW.

In cladding a low penetration is required. In previous studies the effect of WC powder was not accounted for. In the following study the effect of the shielding gas and the electrode angle was determined.

WC powder feeding was kept constant for the trials at 15 g/min. Thus this study includes the effect of WC powder in the weld bead dimensions. The Ar transport gas of the powder feeder was released with the valve on the pressure reducing container fully open (see chapter 4.1), and a constant gravity driven powder flow was therefore guaranteed.

For a final control, the electrode angle (γ) was measured under the microscope. Hereby, it is showing that the grinding angles used were $\gamma = 33.56°$, $\gamma = 56.94°$ and $\gamma = 97.51°$, as seen in figure 6-4. The tolerance of the light microscope is described in Appendix G section G.2. The electrode grinding angles have been rounded to $\gamma = 34°$, $\gamma = 57°$ and $\gamma = 98°$ to bring the measurements in the measurable tolerance.

Figure 6-4: GTAW 3.2 mm ⌀ tungsten electrode tips after grinding with the angle γ = 33.56°, γ = 56.94° and γ = 97.51° measured under the microscope

The following shielding gases were chosen:

- 100 % Ar   BOC Pureshield Argon (see figure_apx I-15)
- 50/50 Ar/He (50 % He, Ar bal.)   BOC   Alushield   Universal   (see figure_apx I-16)
- 100 % He   BOC   Helium,   compressed   (see figure_apx I-17)

These electrode angles and shielding gases should show if both effects are contrarious or elevating in WC ceramic MMC cladding. The shielding gas flow rates for 100 % Ar, 50/50 Ar/He and 100 % He were adjusted to 7 l/min, 11 l/min and 22 l/min, respectively, to keep the mass flow rate stable.

6.2.1 Influence on the process parameters

Cladding trials with the GTAW configuration of section 6.1 and the parameters from section 6.2 showed different visual welding behaviour. The shielding gas changes gave the biggest visual effects. Argon left the arc appearing blue and helium orange. The more helium was used, the more fume appeared. This was still indicated on the surface of the weld beads after acetone cleaning of the dust, as seen in figure 6-5.
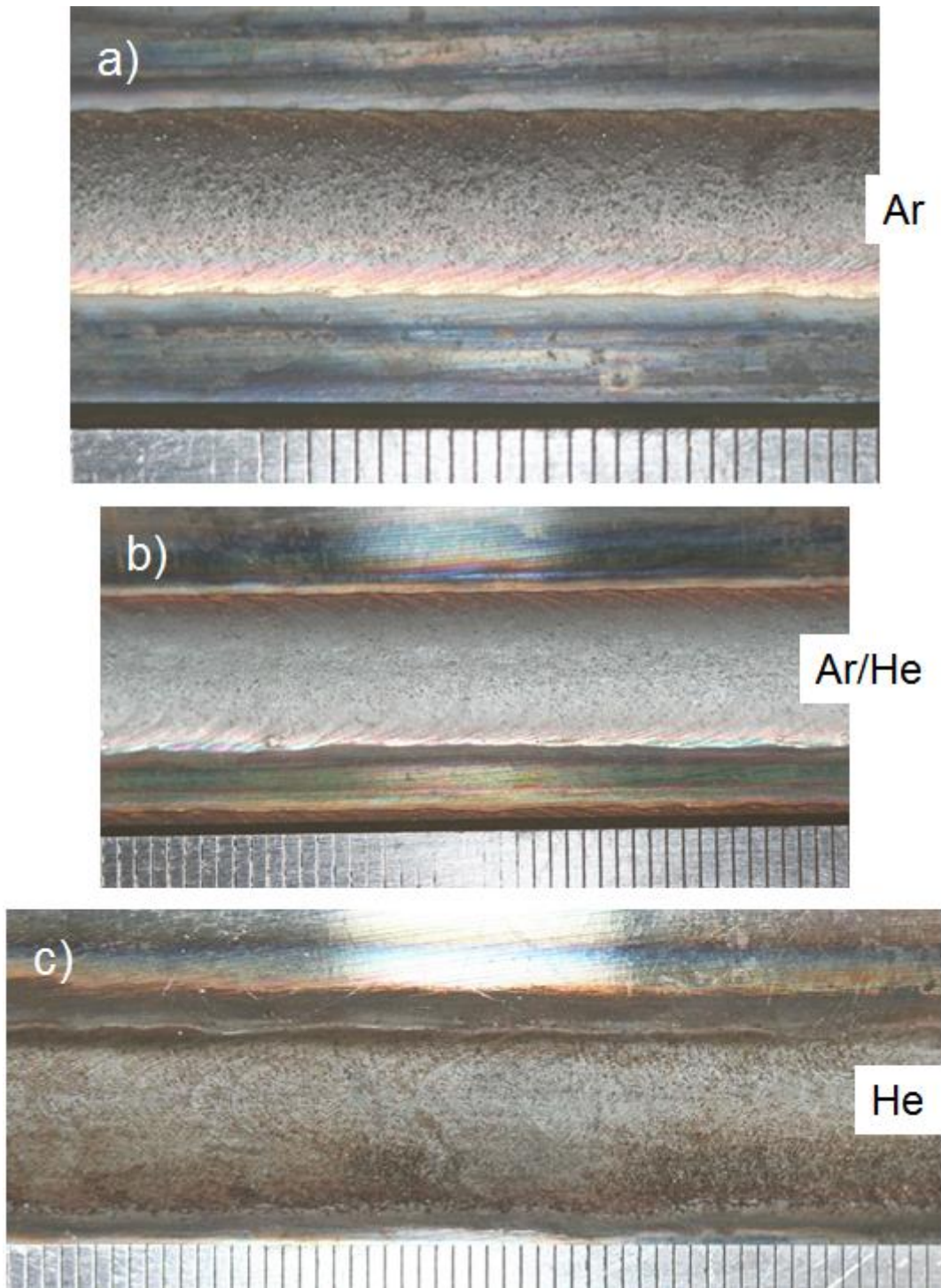
Figure 6-5: Surface of single bead welding seams in bead-on-plate mode with 15 g/min WC powder feeding rate and a constant electrode angle of γ = 34°, ruler scale: 1 mm distances, microsections in figure 6-6; shielding gases: a): 100 % Ar; b) 50/50 Ar/He; c) 100 % He

Figure 6-5 a), with pure Ar shielding, seems to have many more particles than b) (50/50 ArHe mixture) and c) (pure He) on the surface. Figure 6-5 b) (50/50 ArHe mixture) appears darker on the top with only some WC particles. The bead with He shielding in figure 6-5 c) showed a very dark surface. The fumes during welding with He built slags which hindered further oxidisation after the shielding gas atmosphere of the torch. He dilutes quickly with air due to its atomic weight. Additionally, He makes the weld bead hotter, which results in a longer liquid weld bead. The longer weld bead is not covered by shielding gas; therefore, more oxidation is developing a slag, which is black. Figure 6-6 shows the transverse cross sections of the cladding beads in figure 6-5.
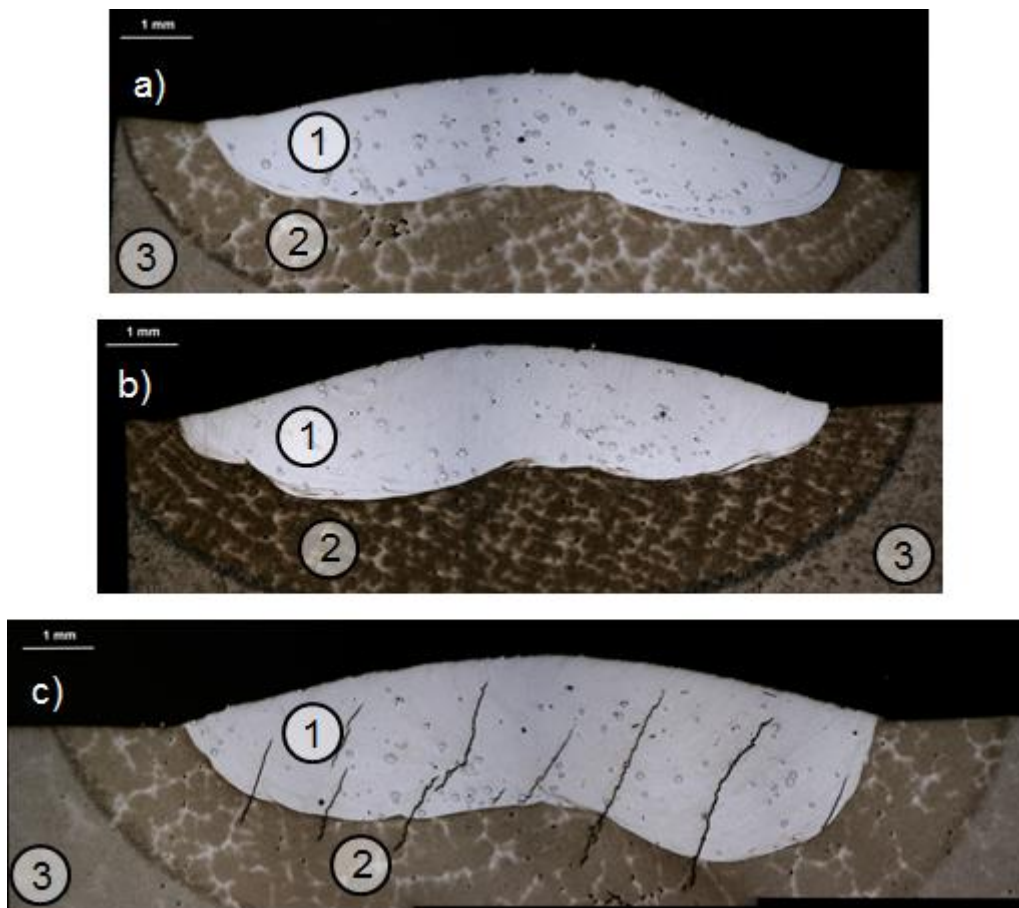
Figure 6-6: Microsections of single bead welding seams in bead-on-plate mode with 15 g/min WC powder feeding rate and constant electrode angle, 1: weld bead, 2: Heat Affected Zone (HAZ), 3: base material, surface in figure 6-5; shielding gases: a): 100 % Ar; b) 50/50 Ar/He; c) 100 % He

Compared to steel welds, MMC bead-on-plate welds showed a wavy penetration. The layer was generally wider and more even than the GMA weld in Appendix D. WC pick-up was achieved with all three gas types. Pure He tended to crack under the surface, as reflected in figure 6-6 c). The sample preparation for cross sections is explained in Appendix G. Whereby, the light microscope tolerance is in section G.2.

To understand the influence of the shielding gas on the weld bead shape and the cracking, the process parameter arc current (I), arc voltage (V) and wire feed speed (WFS) were monitored during the GTA cladding. As DC welding was used, the welding power (P) was calculated according to equation (6-1). To plot all observed single bead trials the instantaneous average of the recording was taken and each electrode angle is shown against the shielding gas type. In figure 6-7, the readings are summarised to give an overview of the process parameters of cladding with WC powder.
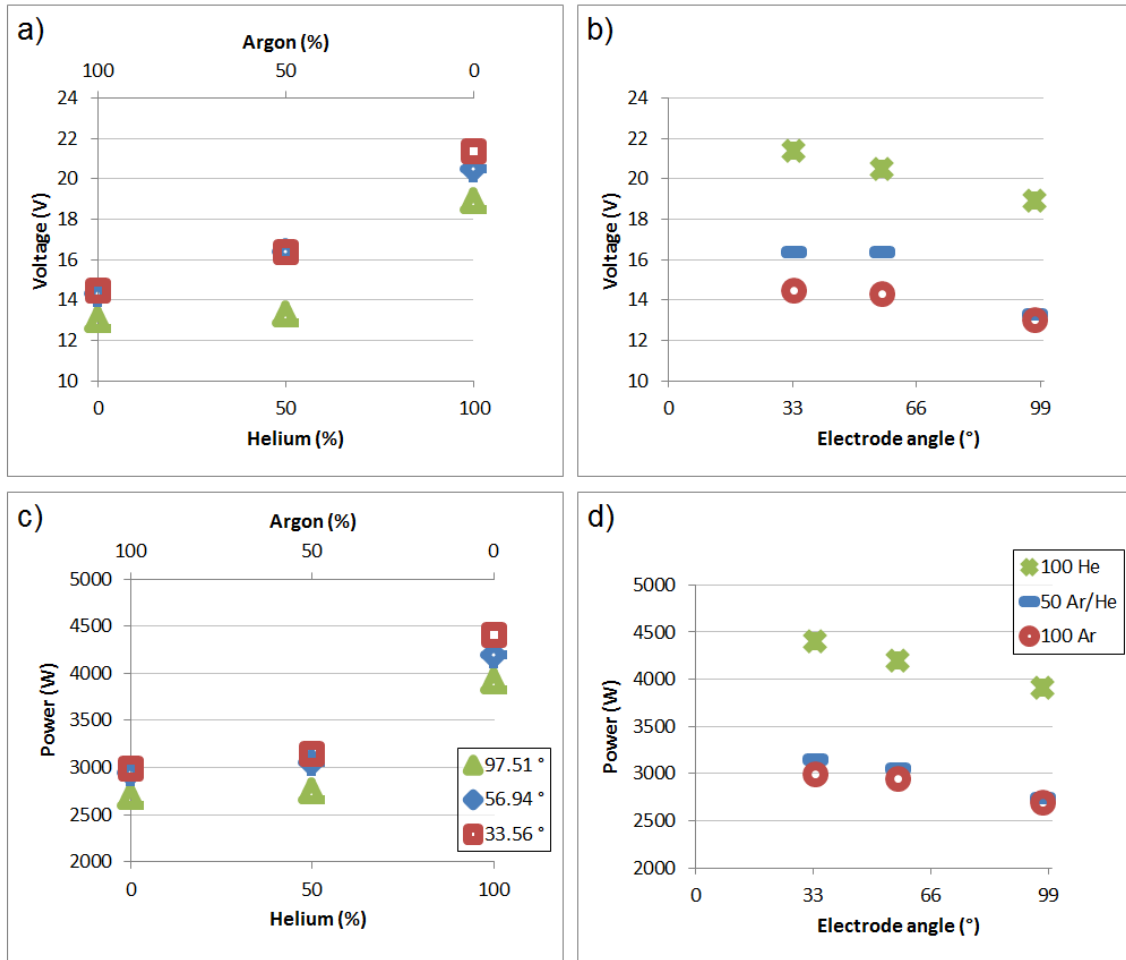
Figure 6-7: Process parameter readings for the single bead cladding trials for increasing He in Ar shielding gas and increasing electrode angle (γ); a) voltage (V) to shielding gas; b) voltage (V) to electrode angle c) Power (W) to shielding gas; d) Power (W) to electrode angle

It can be understood from the reading of the current and WFS, that the input of I = 200 A and WFS = 1.5 m/min was not obtained during the real process. The set values and the measured values are very close with lower WFS of approximately 0.2 m/min and increased current of approximately 4 A. As the change is constant over the whole experiment, the results are still comparable. Changing of the electrode angles (γ = 34°, γ = 57° and γ = 98°) exhibits decreasing voltage resulting in decreasing power (see figure 6-7 b and d). Conversely, the shielding gas significantly influences the voltage. The welding machine and the wire feeder maintain the current and the WFS independently of the shielding gas and keep both stable. Thus figure 6-7 a) confirms rises in

the voltage with decreasing Ar content. This result from the higher ionising potential of He compared to Ar. Pure helium showed escalations in the range from 43.3 % to 47.6 % (to pure Ar) in voltage.

This increase in the voltage gives a power increase due to the use of He and/or the use of a lower electrode angle. Figure 6-7 a) confirms a "hotter" arc is generated with He in WC ceramic MMC trials with a GTAW process. Power increased by about 29.7 % to 31.2 % with pure He in comparison to pure Ar. On the other hand, 50 % He in Ar had only a low impact, with approximately 4.1 % power rise compared to pure Ar.

The lower the electrode angle the higher is the power. The increase of power is between 10.2 % - 12.8 %. However, the electrode angle has a smaller influence than the shielding gas.

In figure 6-6, it can be seen that this effect of power increase has a huge impact on the cracking of the single beads. Figure 6-6 c) has many cracks due to the changes in the welding power, so the WC powder inclusion must be analysed to understand the mechanisms of the cracking.

6.2.2 Influence on the single bead dimensions

Previously it was shown that the shielding gas has a major influence on the arc power. The electrode angle on the other hand does not influence the power significantly. However, the power density is controlled by the electrode angle.

To measure the influence of the electrode angle on the weld pool, crossections were made in the transverse direction of the single cladding beads. The schematic drawing in figure 6-8 illustrates the geometric features that were measured. The width of the heat affected zone (HAZ) was measured as an indicator of the heat input to the base material. In comparison to the HAZ width, the bead width indicates the heat conduction into the base material and therefore loss of welding energy into the base material.
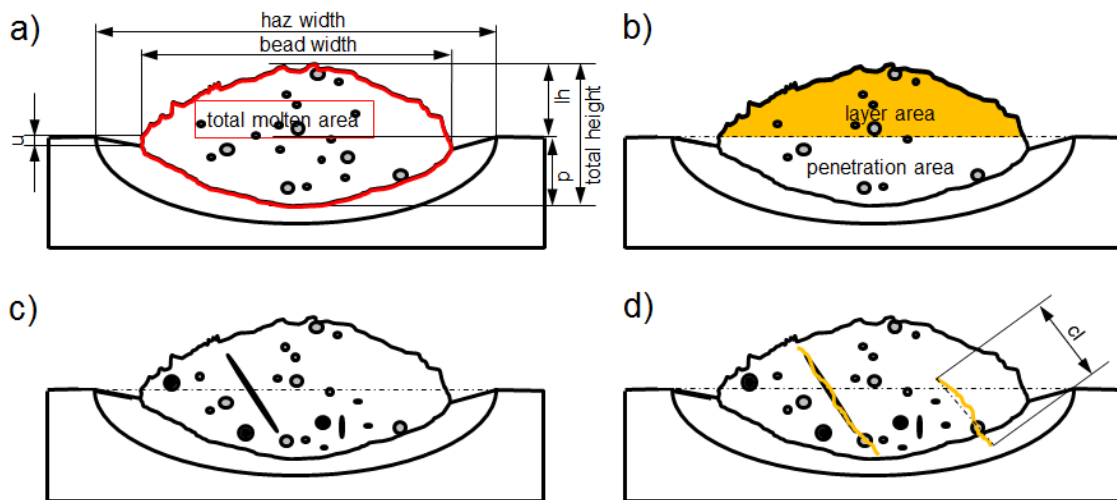
Figure 6-8: Schematic of transverse cross section and dimensioning; a) total molten area; b) layer area (dark yellow) and penetration area; c) porosity and cavities; d) cracks (yellow)

Whereby:

⬤	particle	u – undercut	
◉	particle with pore	lh – layer height	
▪❙	pore, cavity	p – penetration	
〰	crack	cl – crack length	

The layer height, total height and penetration measurements are established for future cladding layer height optimisation. The depth of penetration is necessary for the evaluation of the aspect ratio, with the following formula:

$$aspect\ ratio\ = \frac{penetration}{bead\ width} \tag{6-2}$$

Any undercut could disturb cladding trials due to overlapping of the existing clad. Bead-on-plate weld beads are usually characterised by their aspect ratio and dilution. Where, the dilution is a ratio between the penetration area and the total molten area. To establish the total molten area, either direct measurement or adding up of the penetration and layer areas was used, as follows:

$$total\ molten\ area = penetration\ area + layer\ area \qquad \textbf{(6-3)}$$

Whereby the dilution is determined as follows:

$$dilution = \frac{penetration\ area}{total\ molten\ area} \qquad \textbf{(6-4)}$$

If cracking appeared, the crack length of the longest crack was measured as a straight line between the farthest ends.

The cross section sample preparation is described in Appendix G. Additionally, the light microscope tolerances are given in section G.2 and the single weld bead analysis method is detailed in section G.3.

Figure 6-9 presents the results of the bead-on-plate single bead dimensions for different shielding gas and the electrode angles $\gamma = 34°$, $\gamma = 57°$ and $\gamma = 98°$.
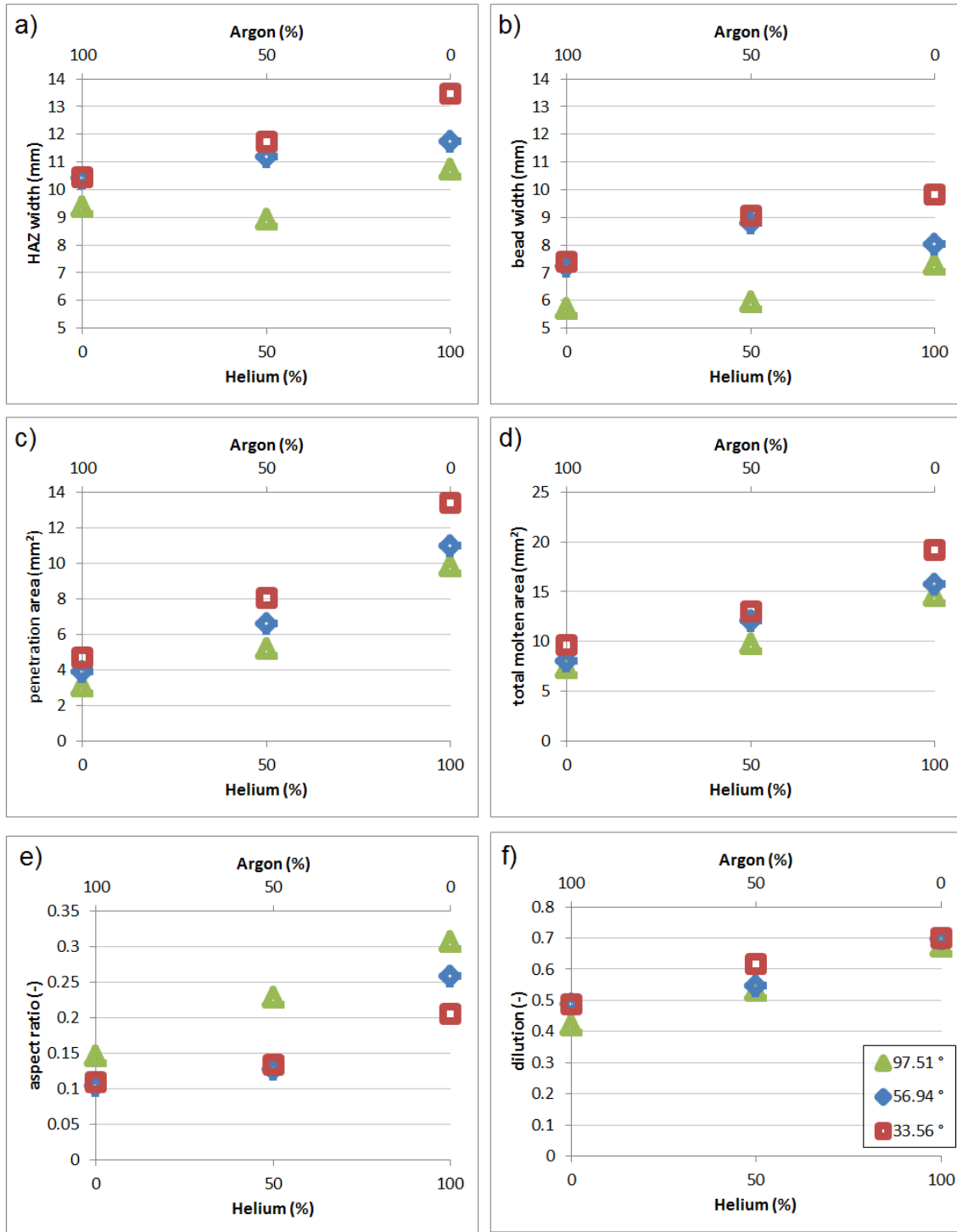
Figure 6-9: Single bead dimensions measured on the microsection for trials with γ = 34°, γ = 57° and γ = 98° electrode angle and increasing He in Ar shielding gas; a) HAZ width; b) bead width; c) penetration area; d) total molten area; e) aspect ratio; f) dilution

From figure 6-9 it can be seen that with increasing He percentage all factors (HAZ width, bead width, penetration area, total melted area, aspect ratio and dilution) of the single bead are increased. This is commensurate with power increase as observed in figure 6-7 c).

It can also be seen that the smaller electrode angle gives greater values for these factors except for the aspect ratio. The aspect ratio does not increase because the penetration does not increase as much as the width. These results are also expected due to the increase in arc power with increasing electrode angle (see figure 6-7 d)). It is clear that the smaller electrode angle gives higher HAZ width, bead width and especially penetration area – this adds to the increase measured due to the He percentage.

It is to mention that low porosity was found with the largest total area of 0.151 mm^2 measured. The undercut was minimal with 146 µm measured as the maximum value.

6.2.3 Effects in the WC powder addition and retrieval

All single bead seams were made in PA position (see figure 3-2). The WC powder was fed at 15 g/min in the bead-on-plate trials. For simpler calculation purposes, the WC feed rate was converted into a WC deposition rate per unit length, as follows:

$$WCpa = \frac{PFR}{TS \times 1000}$$

(6-5)

Where:

WCpa – WC powder addition (deposition per unit length) in g/mm

PFR – Powder feeding rate in g/min

TS – Travel speed in m/min

Unlike wire feeding, powder feeding results in a loss of material in MMC in-situ processes. Therefore from the feed rate (WCpa = 0.05 g/mm), the amount of

WC reinforcement cannot be calculated directly. A loss of powder must be included. The following parameters were introduced:

lop - loss of WC powder (in g/mm)

ppu - WC powder pick-up (in g/mm)

Following the observation of WC powder feeding, the above parameter results in this formula:

$$WCpa = lop + ppu \qquad \qquad \textbf{(6-6)}$$

At this point, WC powder pick-up by the weld metal can be straight forward. For most MMC studies, equation (6-5) is used to examine ceramic reinforcement [112]–[114]. It was measured from the microsection as the particles are clearly visible. However, as explained in section 4.2.2 in chapter 4 W_2C decomposes at about 1300°C (Table 4-6) into W and WC. W_2C, also known as β-WC, dissociates as illustrated in figure 4-8 b), at 33 at% C from 1280 °C upwards. The low carbon mild steel has a melting temperature of about 1500 °C. It is, therefore, unknown how much W_2C and WC is in a particle and the relevance of dissociation. Therefore further analysis is necessary. To establish the powder pick-up, an assumption was made that W reprecipitated in the weld pool to WC and is in the matrix. As a result the following formula can be added:

$$ppu = WCpt + WCrm \qquad \qquad \textbf{(6-7)}$$

Where:

WCpt – WC particles (in g/mm) reinforcement

WCrm – WC reprecipitated in matrix (in g/mm)

Measurement of the particle area in the microsection was used to calculate WC reinforcement. A simple formula gives the reinforcement:

$$WC\ reinforcement = \frac{particle\ area}{total\ melted\ area} \times 100\ [\%] \qquad \textbf{(6-8)}$$

During the measurement, pores in the particles were found and measured as well. These areas were subtracted from the WC particle areas.

The focus, therefore, was on the total WC powder pick-up (ppu). In this chapter, a reverse path technique was used to establish this number. Analysis of dissolved WC in the matrix was performed by Energy-Dispersive X-ray Spectroscopy (EDX, EDS) using the Scanning Electron Microscope (SEM). The equipment is detailed in Appendix H. For the establishment of WC in the matrix, the full matrix could not be analysed as there are simply too many particles in the way. Therefore a point to point analysis of 18 points was chosen. Average values were taken for calculation. The carbon content is difficult to measure as carbon can come easily onto the sample surface by contamination. Thus the W content was measured and the WC content calculated as follows:

$$amount\ of\ WC\ formed\ from\ 1mol\ W \qquad\qquad \textbf{(6-9)}$$
$$= \frac{atomic\ weight\ of\ W\ + atomic\ weight\ of\ C}{atomic\ weight\ of\ W}$$

followed by

$$amount\ of\ WC\ formed\ from\ W \qquad\qquad \textbf{(6-10)}$$
$$= amount\ of\ WC\ formed\ from\ 1mol\ W$$
$$\times\ W\ from\ analysis$$

whereby

$$matrix\ area\ =\ total\ melted\ area\ -\ porosity\ in\ matrix \qquad \textbf{(6-11)}$$
$$-\ particle\ area$$

merged to

$$WC\ in\ matrix\ [\%] = \frac{Matrix\ area\ *Amount\ of\ WC\ formed\ from\ W}{100} \qquad \textbf{(6-12)}$$

The results give a valuable overview of the role of matrix material in WC ceramic MMCs with mild steel or a high strength steel matrix. Figure 6-10 shows the results measured for the different electrode angles and shielding gases. In figure 6-10 a), it can be seen that the particle retrieval is not dependent on the shielding gas. The reduction of particle retrieval with a large electrode angle ($\gamma = 98°$) can be considered as within the experimental errors and not significant.
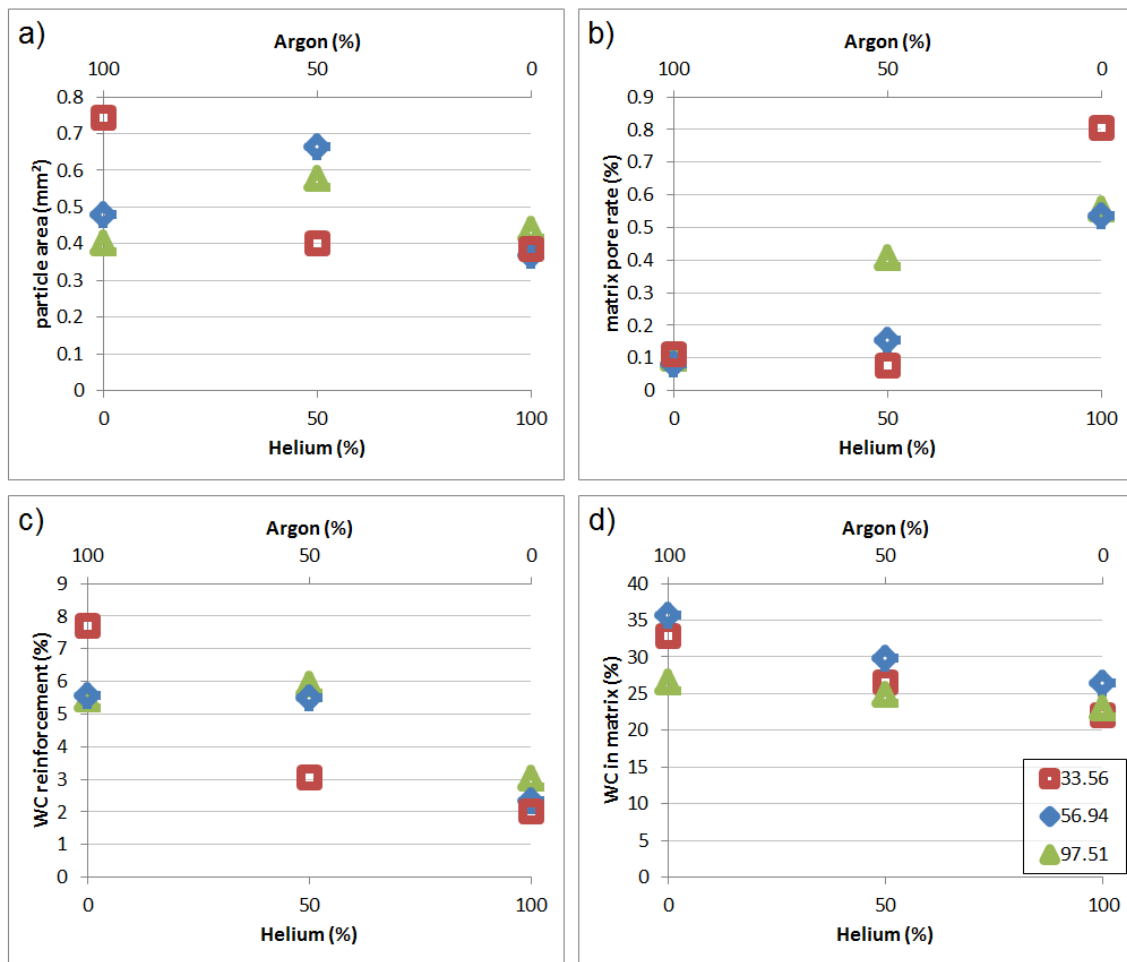
Figure 6-10: WC powder pick-up; a) particle area in microsection; b) pore rate in matrix; c) WC reinforcement as a percentage of the particle area to the matrix area; d) WC dissolved in the matrix (WCrm) measured with EDX analysis

Pores in the WC particles cannot be considered as reinforcement. For a wear resistant layer, pores could eventually be a weakness. It was confirmed by the supplier that the pores in the WC are formed by the WC production process [2].

Porosity resulting from entrapped gases in the matrix was measured and the result is plotted in figure 6-10 b). It can be seen that the porosity increases with increasing He content in the shielding gas. However, the scale of the porosity is very small and a variation between 0.08 % (γ = 34° and 50/50 Ar/He) and 0.80 % (γ = 34° and 100 % He) pore rate in the matrix area is not much.

Generally, the total pore rate had a maximum of 0.81 % area fraction (γ = 34° and 100 % He). In the literature, one example with bead-on-plate welds was found with porosity values as high as 5.5 vol% and 3.0 vol% for Ar and He shielding gas, respectively [115].

The number of WC particles retained is low. A maximum of 10.9 % WC reinforcement (in the matrix area), with Ar as shielding gas and electrode angle at γ = 57°, is shown in figure 6-10 c). Helium reduces the WC reinforcement further. Conversely, the tests with different electrode angles come closer and, therefore, the effect of the electrode angle becomes smaller with He.

The most significant result is shown in figure 6-10 d). A very high portion of the matrix contains reprecipitated WC. A maximum of 35.6 % WC was found (Ar, γ = 57°). Ar shielding gas demonstrates the highest amount of WC for all three electrode angles. Mixing He into the shielding gas reduces the dissociation, but the values even with pure He are still high. Minor changes can be seen between the electrode angles, as the γ = 98° angle gives a lower dissociation with Ar shielding gas.

To compare the WC content retained both as particles and in the matrix, the measurement was calculated into a uniform unit.

For the retained WC particles (in g/mm), the following equation was used:

$$WCpt = (particle\ area - porosity\ in\ particles\ ) \times \text{density of WC} \qquad \textbf{(6-13)}$$

For the reprecipitated WC particles in the matrix (in g/mm), the following equation was used:

$$WCrm = WC\ in\ matrix \times \text{density of WC} \qquad \textbf{(6-14)}$$

The result is shown in figure 6-11.
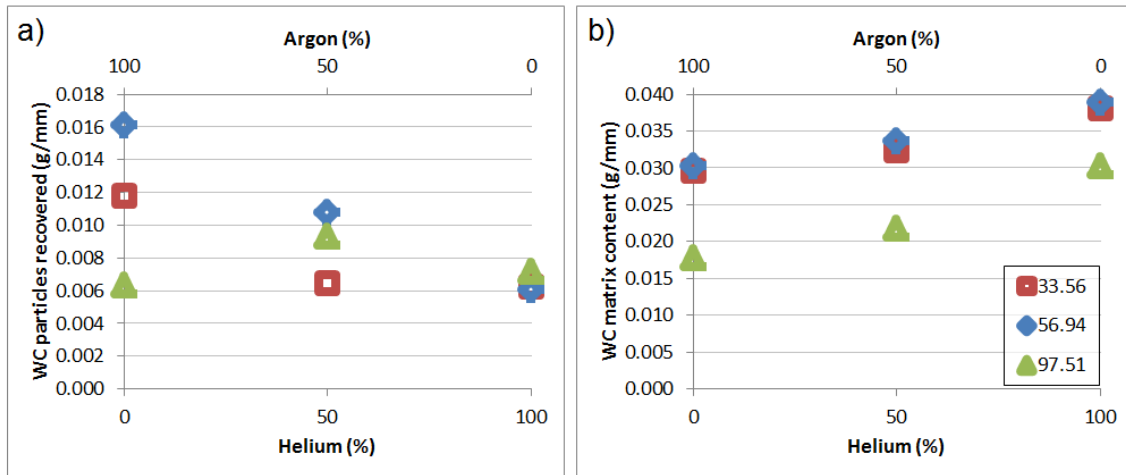
Figure 6-11: WC powder addition; a) WC particles retained; b) WC content in matrix

In figure 6-11 a) and b), it can be seen that the concentration of WC per unit length is so different between both the WC particles and the WC content in the matrix that they need to be illustrated on different scales. It was shown that the dissociation effect of W_2C has a big influence on the matrix of the MMC. In fact the WC particles were less than the dissolved WC in the matrix. Figure 6-11 a) confirms that, when Ar is used the WC retrieval depends on the electrode angle which is not the case when He is used.

A different picture is drawn by looking at the dissolved WC in figure 6-11 b). Here it is clear that the He has a significant effect to promote dissociation. All electrode angles demonstrate a rise in WC in the matrix. This is due to a higher arc power when He is used (see figure 6-7 c)). The electrode angle of $\gamma = 98°$ expresses the lowest dissociation values. This is the case even though the power density is higher than with low electrode angels, as illustrated in figure 6-3. It is a result of the lower arc power (see figure 6-7 d)).

From figure 6-11 it can be seen that the WC particle retrieval goes down and the WC in the matrix goes up with increasing He shielding gas. This is because

of the increased power and weld bead symmetry. This means that the metal is liquid for longer, which dissolves more WC particles.

The WC is most likely in different structures from WC or W_2C. These structures were built up as the steel matrix was cooling down from the liquid during the dissociation and reprecipitation of W_2C or WC and W. Physical and chemical reactions with Fe cannot be excluded. Further analysis is given in a cladding area with overlaps in chapter 7.3.

The process efficiency of WC powder pick-up can now be measured by the sum of the WC content in the matrix and the retained WC particles. For this the powder addition with 0.05 g/mm (PFR = 15 g/min) was set at 100 %. The outcome is displayed in figure 6-12.
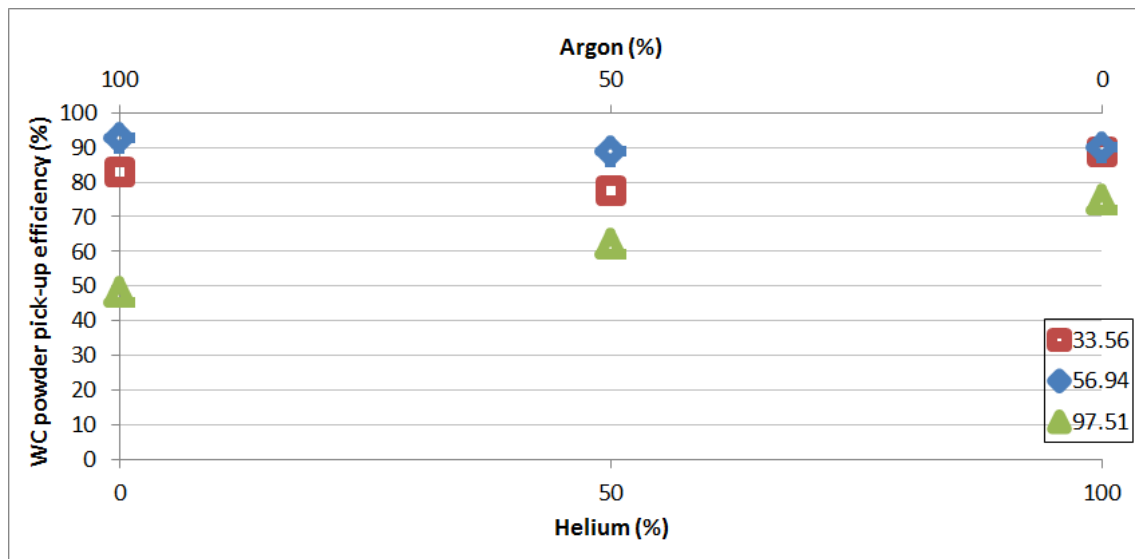
Figure 6-12: WC powder pick-up efficiency, 0.05 g/mm was the powder addition and is set at 100 %

In terms of total absorbed WC, the performance of the GTA cladding process is at its best with 100 % Ar and an electrode angle of $\gamma = 57°$. However, every trial with $\gamma = 57°$ and $\gamma = 34°$ has an efficiency of above 70 %. Trials with $\gamma = 98°$ indicate a better efficiency with He than with Ar. In summation, He is a shielding gas of greater tolerance. However, it allows less WC particle capturing.

6.2.4 Influence of the solution of WC on the matrix hardness

Microstructures with different chemical composition and phase mixtures alter the mechanical properties. The previous section showed a significant increase of dissolved WC in the matrix of a weld bead with WC powder feeding amount. Hardness measurement was carried out to determine the performance of this mixture to the mild steel wire and the high strength steel base plate. Microhardness testing, according to Vickers, was decided to be the best method (instead of the also available testing methods like macro HV, macro HB or Leeb rebound). Here the indenter can be used on the matrix while avoiding the embedded particles. Further details about the machine used are in Appendix I and the tolerance measurement is in section I.1. Results are presented in the figure below.
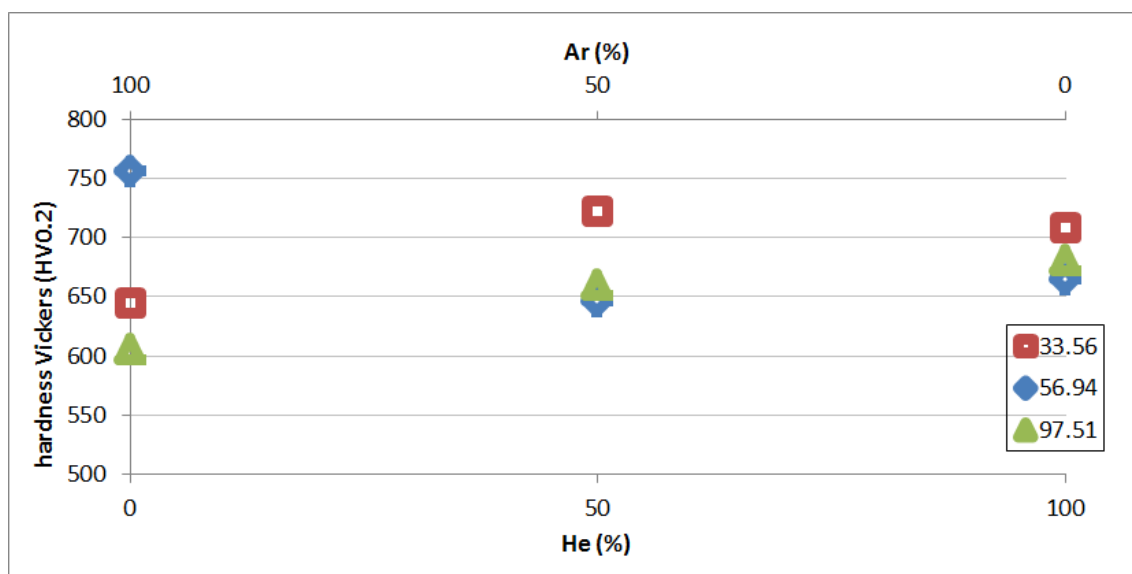
Figure 6-13: Hardness Vickers of the matrix material of single bead trials on the dependency of the shielding gas and electrode angle

In figure 6-13, it can be seen that the average hardness of the matrix of single bead trials with WC powder is between 606HV0.2 and 756HV0.2.

The steel had only approximately 346HV – 393HV (converted after ASTM E 140 – 02 [116] from 330 - 375 HBW 10/3000, value of G-22 NiMoCr 5 6 steel in

table 4-5). The dissolved WC increased the matrix hardness by about 260HV – 363HV. This improvement comes from the perspective of the WC content rather than the different process parameters. A unique specimen analysis would give a clearer understanding of the necessary amount of WC needed to increase the hardness considerably.
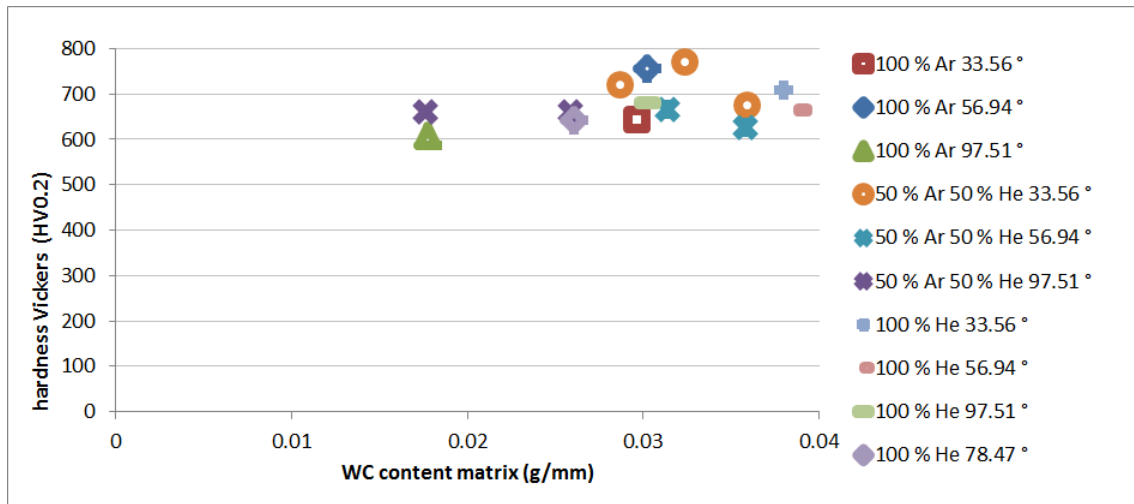
Figure 6-14: Average hardness Vickers of the matrix material of single bead trials on the dependency of the WC content; unique specimen analysis

All samples in figure 6-14 are ordered by the amount of WC found in the matrix (from 0.0176 g/min at 659HV0.2 to 0.389 g/min at 664HV0.2). The hardness of the matrix remained between 606HV0.2 and 771HV0.2 in the full range of WC retrieval. For comparison: The WC powder addition was at a deposition rate of 0.05 g/mm (PFR = 15 g/min). As a result no correlation between WC content in the matrix and hardness was found. This can be from either local varieties or a matrix saturated with WC. A hardness line test of the crossection will identify local varieties. Therefore, all specimens were plotted in figure 6-15. It can be seen that the hardness of the clad reduces toward the weld base. A significant reduction is shown in the HAZ. The base has a further decrease in hardness towards the core.
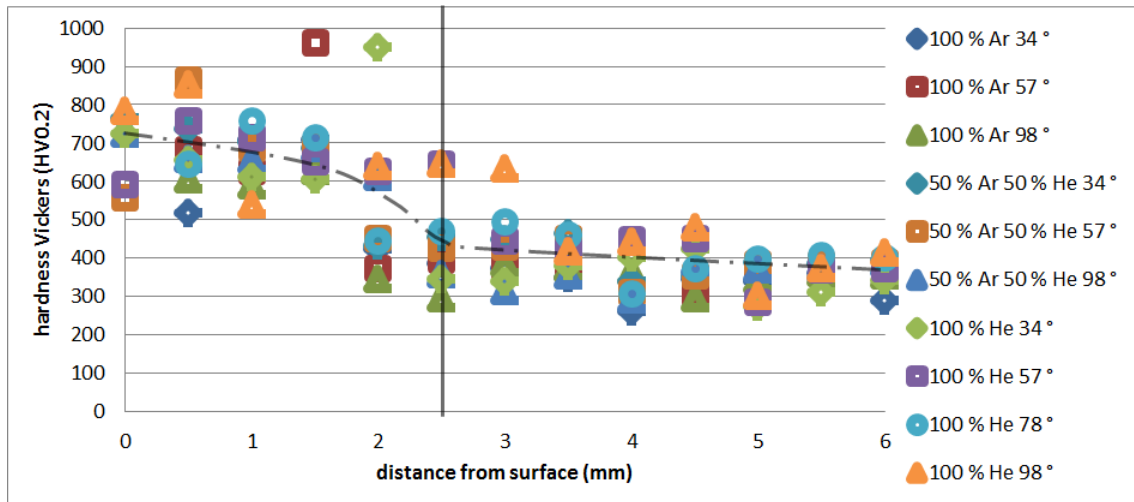
Figure 6-15: Hardness Vickers line test of the crossection of the matrix material; 0 mm distance is the first indentation under the surface of the clad; at 2.5 mm starts the HAZ

As shown in figure 6-15 in the area between 0 mm and 1.5 mm distance, local varieties of the hardness occur. The hardness of all trials shows a difference of 334HV0.2 at 0.5 mm distance and the average does not show all these peaks. This shows that local varieties have an influence on the hardness and a deeper analysis of the dependency of hardness and WC in matrix is recommended in future applications.

6.2.5 Appearance of cracking

Cracks, depending upon their orientation, can cause serious weakening of WC ceramic MMC clad layers used in wear or abrasion resistance surfaces. Cracks from the GTA process could become larger with post-processing or in service. Fatigue cracks usually generate in service into the bulk material if the HAZ is affected. The contrast between the hard surface and the tougher bulk material could stop cracking when no previous damage to the HAZ happened [117]. Cracks were counted in the single bead microsections and the longest crack length was measured. If one single crack in any sample of a process configuration appeared to be in the HAZ, the process configuration was marked with a "*". A control sample without powder feeding was used to look at the

cracking behaviour of a standard GTA weld bead. The control sample was made under the following conditions: Ar shielding gas, $\gamma = 57°$ electrode angle, no WC powder feed, Ar transport gas switched off and all other parameters kept as mentioned in section 6.1.

The measurement revealed the results illustrated in figure 6-16.
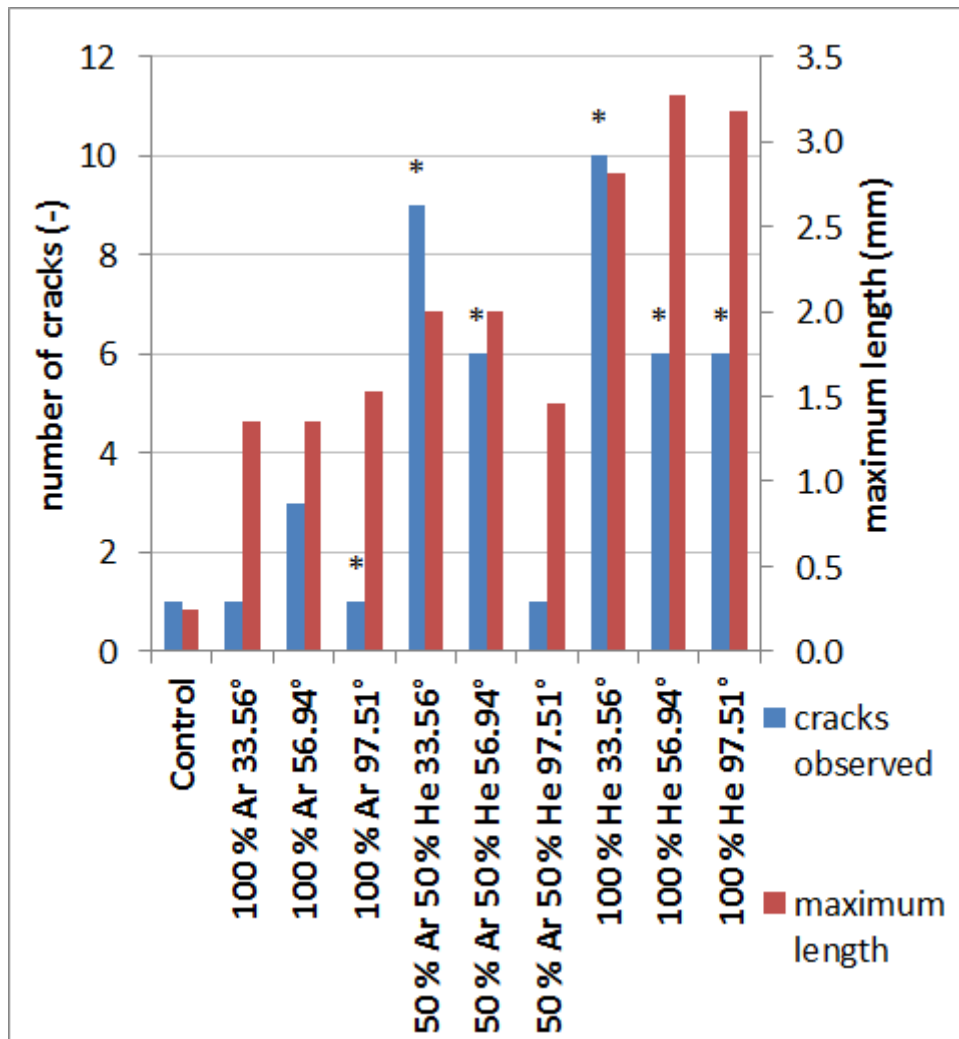
Figure 6-16: Observed cracking in single bead trials separated in all process parameters chosen; control is without WC powder; "*" is for minimum one crack proceeded into the HAZ

The base material with a carbon equivalent substantially more than 0.3 (G-22 NiMoCr 5 6 steel has 1.007), cracks are likely to appear. Only one short crack was found in the control sample. The additional carbon from the WC dissociation and the formation of hard structures in the matrix made cracking

more likely when WC powder was fed. The low carbon high strength steel wire G89 6 M Mn4Ni2CrMo tends to compensate as much as it can, however, the carbon coming from the WC particles is significantly higher than that of the matrix. Significantly, all samples made with He have cracks which went into the HAZ. For the future usage of non-destructive testing, it is to say that almost all cracks in the samples made with 100 % He were under the surface, whereas the samples with Ar and Ar/He shielding gas had cracks reaching the surface. Dye-penetrant testing would be difficult to use on trails made with 100 % He. Differences in the electrode angle do not show any influence on the cracking.

The length of the cracks increased with He content commensurate with increasing power input (see figure 6-7 c)). This is probably caused by the increasing aspect ratio increasing the stress level during cooling [118]. In addition the cracks are located in the HAZ rather than the surface. This is also likely caused by the changing shape of the weld bead, especially the deeper penetration.

6.3 WC powder addition as an influence on WC single bead trials

The consequences of a modification in the WC powder addition are discussed here.

Based on previous experience (see section 6.2), a decision was made to keep the shielding gas as argon and the electrode angle at $\gamma = 57°$. This will ensure a low cracking and gives a probability of higher WC particle retrieval.

To establish the impact of WC on the GTAW single beads, smaller steps of addition increase were chosen in the low to medium region and large steps towards higher WC powder feeding. Feed rates as listed in table 6-2 were selected.

Table 6-2: Comparison between key WC powder feed rates and WC deposition rates

WC feed rate	deposition rate
g/min	g/mm
0	0
5	0.01667
10	0.03333
15	0.05000
20	0.06667
25	0.08333
40	0.13333
60	0.20000
80	0.26667
100	0.33333

The GTAW process was set up under the configurations described in section 6.1 and were kept constant despite the increase in material addition.

6.3.1 Influence of increasing WC powder addition and its retrieval on the single bead dimensions

As shown in figure 6-17, increasing the WC powder addition exhibited a very stable process up to 20 g/min. Only the microstructures revealed some uncertainties in higher feeding rates. This was not able to be seen on the process stability (such as fume or arc wandering). The effect on the particle area in the single beads is illustrated in figure 6-17 a). To normalise the measurements, the WC reinforcement was calculated after equation (6-8) and displayed in figure 6-17 b).
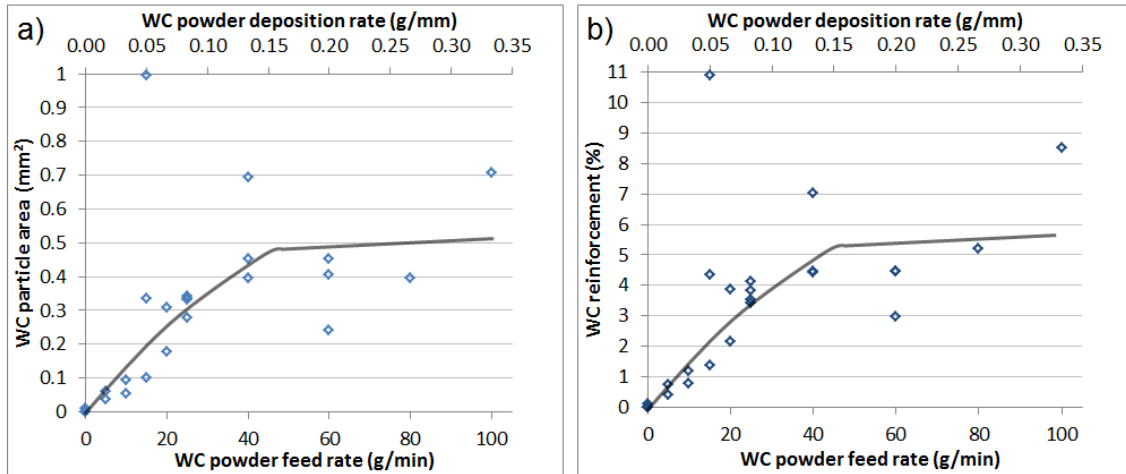
Figure 6-17: Results of increasing WC powder addition; a) WC particle area (mm^2) in dependency of the powder addition; b) WC reinforcement (%) to the powder addition; scaled in the WC PFR (g/min) and WC powder deposition rate (g/mm)

From figure 6-17, it can be understood that the total matrix area (see equation (6-8)) has very little effect on the WC reinforcement which is the reason for the identical trends of figure 6-17 a) and figure 6-17 b). WC particle retrieval increases initially linearly but then saturates at about 40 g/min. There are some outliers which were ignored.

Increased WC powder feeding rate cools the weld pool and makes it shorter. The powder feeder position was kept constant so the temperature of the liquid weld pool, where powder was being fed, was lower. The result is, although more powder is fed in, the amount entering the weld pool does not increase.

Single bead dimensions are usually more dependent on the WC embedding than WC addition. A covering of loose powder could have an effect. However, the WC influence on single bead dimensions can be better understood by a comparison with WC reinforcement. Figure 6-18 shows the major findings.
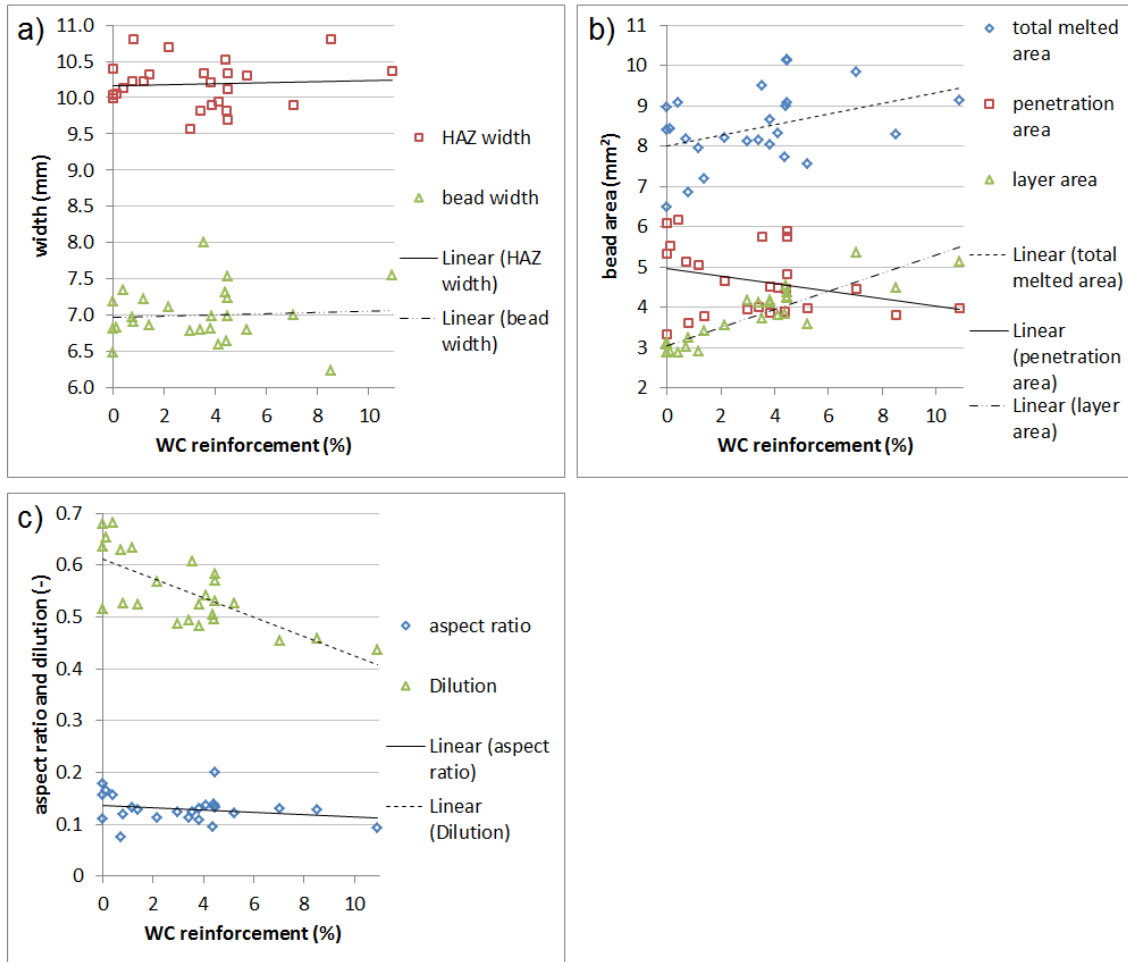
Figure 6-18: Single bead dimensions in dependency on the WC reinforcement (%); a) the HAZ and bead width (mm); b) penetration area, layer area and total area (mm^2); c) aspect ratio and dilution (-)

The HAZ and weld bead width in figure 6-18 a) are independent of WC reinforcement. However, the difference between the bead width and the HAZ width gives an impression of the influence of the GTAW process on the non-molten base material. Larger differences indicate lower cooling rates of the base material as microstructure changed after welding. The measured values had an average difference of 3.16 mm. With the areas changing in figure 6-18 b) and the bead width relatively stable (Figure 6-18 a)), it consequently discloses major effects in the layer height and/or penetration. Increasing WC reinforcements result in increasing layer areas. In contrast, the penetration area becomes smaller. The fact that the total molten area expands when the penetration area decreases shows WC reinforcement (Figure 6-18 b)) is

particularly located in the clad layer. This proves clearly an enlarging bead with lower penetration area, if more particles are retained. The dilution dramatically falls with increasing WC reinforcement. Figure 6-18 c) makes it clear that the changes in figure 6-18 b) in penetration area and total molten area significantly influence the dilution with equation (6-4). The aspect ratio in figure 6-18 c) confirms the comparison of the bead width (Figure 6-18 a)) and the areas in figure 6-18 b). Minimal declines can be seen in the aspect ratio with increasing WC reinforcement, thus the penetration depth reduces slightly (see equation (6-2)).

What is important to mention is that all bead-on-plate welds shows extremely good profile with a maximum undercut of 197 μm and a maximum total porosity of 0.050 mm^2. Thus a very good starting point for overlaps with a dense weld bead is achieved.

If the WC powder addition (WCpa) is broken down into the WC retrieval of added powder (ppu) and WC powder loss (lop), the WC retrieval (ppu) can be further broken down to WC particles (WCpt) and dissolved WC content in the matrix (WCrm). The result is illustrated in figure 6-19. Nevertheless, the WC loss does not need to be plotted as it is the difference between the WC powder addition and WC retained.
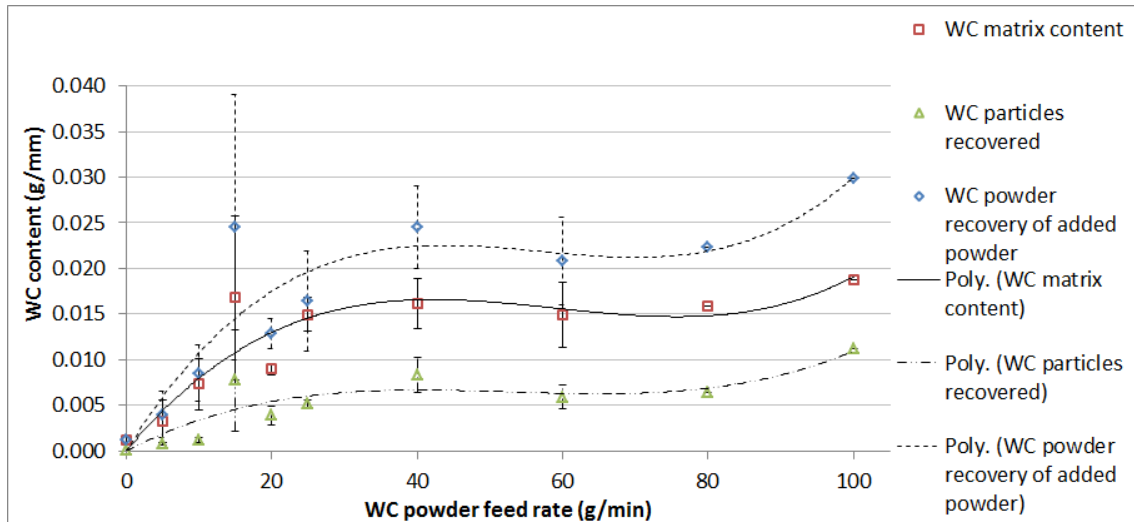
Figure 6-19: WC content on the dependency of the WC addition. WC powder retrieval (g/mm) is shown in total and split into WC in matrix (g/mm) and WC particles (g/mm). WC addition scaled in WC powder feeding rate (g/min)

More and more WC powder feeding does not automatically result in a higher WC retrieval in the weld bead. As seen in figure 6-19, increase in WC powder retrieval reaches a plateau after PFR = 25 g/min powder feed rate (blue points) and approximately ppu = 0.02 g/mm WC retrieval. From PFR = 25 g/min to the end of testing with PFR = 100 g/min, the WC powder retrieval was stable between about 0.02 g/mm to about 0.03 g/mm. The WC particle retrieval, which makes the composite, and the WC content in the matrix followed the same trend. The WC content in the matrix is constantly higher than the WC particle retrieval.

The WC retrieval of added powder (ppu) and its trend can be explained by introducing a powder capture efficiency (PCE). The following equation shows the relationship:

$$PCE = \frac{ppu}{PFR} \qquad \textbf{(6-15)}$$

Whereby:

PCE – powder capture efficiency

ppu – WC retrieval of added powder

PFR – powder feed rate

The PCE depends on the weld pool length because the powder feeding point is fixed. Figure 6-20 shows schematic how the weld bead size changes with powder feed rates changes.
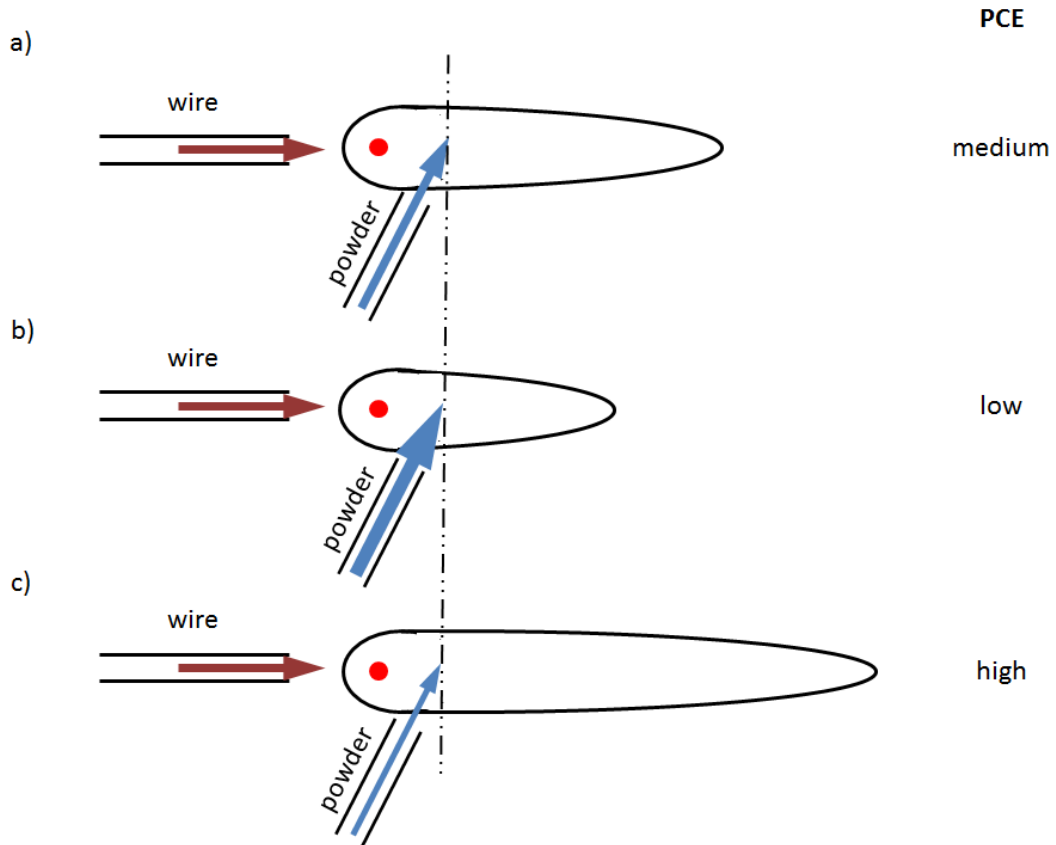
Figure 6-20: Changes in weld pool length and PCE; a) medium powder feed rate makes medium weld pool length and PCE; b) high powder feed rate cools the weld pool and the weld pool length shortens and PCE is low; c) low powder feed rate increases the weld pool length and the PCE

More PFR with constant heat input is shortening the weld pool length because of the cooling effect of the WC powder. This effect stabilises at about PFR = 40 g/min as shown in figure 6-19. No more WC powder gets into the single bead with further increase of WC powder feeding.

6.3.2 Matrix hardness on the dependency of WC absorption

A hardness test on the matrix of the WC ceramic MMCs in bead-on-plate welds was performed to investigate the change of one mechanical property. The normal load was 200 g, which gives the possibility of two to three indentations from the surface to the HAZ on the microsection. The distance between the indent centres was 0.5 mm.

Hardness test results of the single bead welds are displayed in figure 6-21.
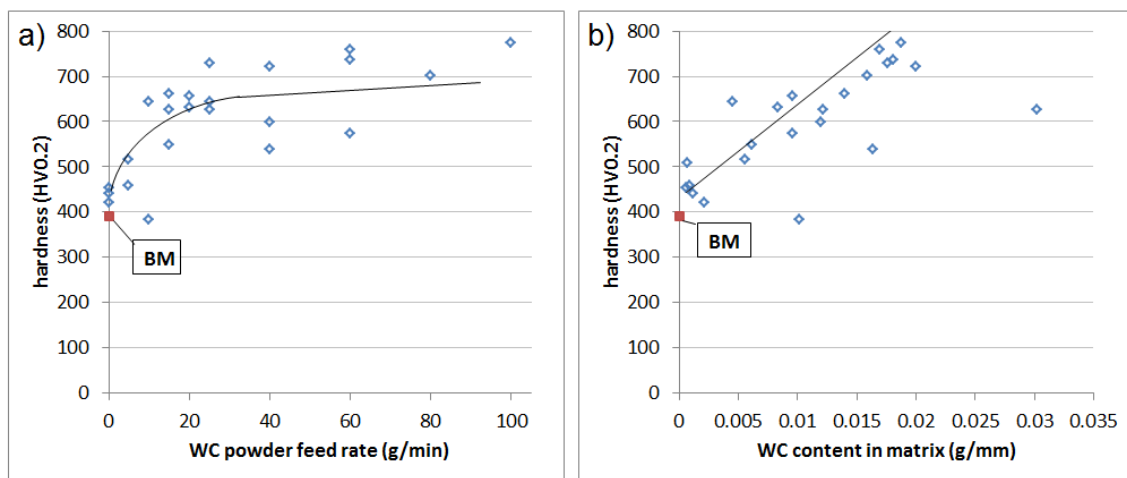
Figure 6-21: Hardness in HV0.2 of the matrix; a) on the dependency of the WC addition; b) on the dependency of the dissolved WC content in the matrix; BM: base material hardness

For the comparison:

- Base material: measured average of 392HV0.2; value in standard for G-22 NiMoCr 5 6 steel: 346HV – 393HV (see section 6.2.4)
- Wire material: approximately 293HV – 368HV for G89 6 M Mn4Ni2CrMo steel (value converted according to the standard DIN 50150:2000-10 from the Tensile strength of R_m = 940 MPa – 1180 MPa, see table 4-5.)
- Reinforcement ceramic: 2498HV - 2875HV for WC powder (see table 4-6)

The matrix hardness of the weld bead without WC powder has increased from that of the base material and the wire material. The increase in hardness to the base is likely to have come from a hardening process during welding. Figure

115

6-21 a) shows that the hardness increases as more WC powder is added up to about 25 g/min. A closer look on the hardness in figure 6-21 b) shows an improvement with enhanced WC content in the matrix. As the amount of dissolved WC increases the hardness also increases up to about 700HV0.2 compared to the average of 392 HV0.2 for the base material. Only a small increase in hardness was observed as the limit of dissolved WC was reached. This is because under the constant heat input conditions used the powder capture dropped at high powder feed rates due to the likely cooling of the weld bead.

6.3.3 Appearance of cracking

A few cracks were observed. The amount of cracks per single bead clad and the short maximum length confirmed the assumption made in section 6.2.5 that Ar shielding gas helps to reduce cracking. Nevertheless, any crack is bad for the wear resistance, as described in section 6.2.5. The number of cracks was counted and the longest crack length was measured. The results are presented in figure 6-22 below.
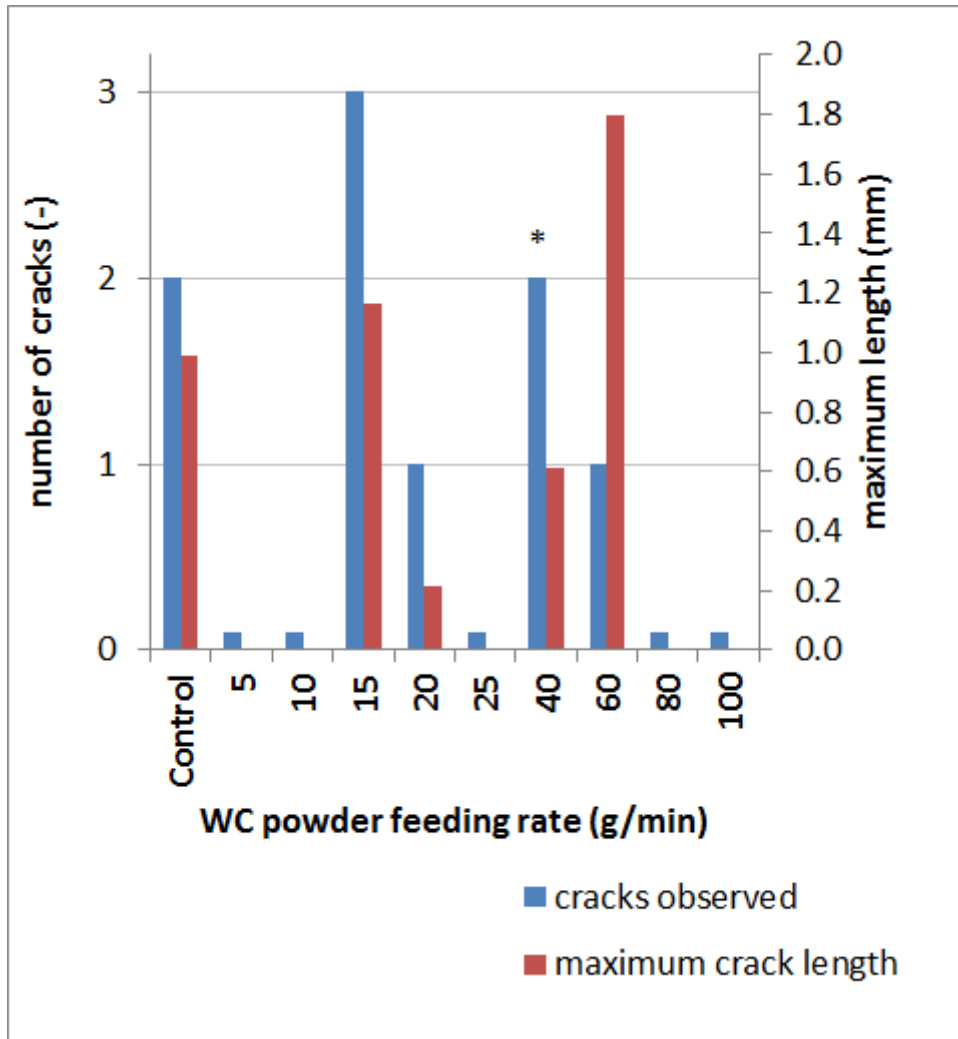
Figure 6-22: Observed cracking in single bead trials separated by WC powder feeding rate; control is without WC powder; "*" is for minimum one crack proceeded into the HAZ; Number of cracks at "0.1": No cracks found in sample.

A crack was observed going into the HAZ only in the samples clad with 40 g/min.

Here, the control samples had twice as many cracks which were up to five times longer than those mentioned in section 6.2.5. The fact is that the base material has a high hardness (see sections 6.2.4 and 6.3.2) and high carbon equivalent (see chapter 4.2.1) and, therefore is prone to cracking during welding. Cracking was shown in both sections for the control samples (PFR = 0 g/min). When measuring cracks using crossections there will be a statistical variation due to random distribution of cracks. This may explain why cracks are observed in this

control sample. Further analysis of cracking is in chapter 7 section 7.4.2 on overlap welds.

Good results are shown with the use of WC powder. Despite the high number of samples only seven cracks were found (Two weld beads for each powder feeding rate). The longest crack for samples with WC powder feeding is just 1.8 mm long (PFR = 60 g/min).

6.4 Summary

In this chapter, the effect of shielding gas, electrode angle and WC powder deposition rate were studied regarding WC particle retrieval, WC content in the matrix, WC powder pick-up, hardness of the matrix and cracking.

It was observed that helium clearly increases the welding voltage for the same process configurations compared to argon. Therefore the welding power increases significantly by about 1300 W which is an increase of about 30 % compared to Ar.

The single bead dimensions correlate with the change of power. As the electrode angle decreases the power increases by about 10 %. These are corresponding to the changes in the weld bead profile.

A maximum WC reinforcement with Ar as the shielding gas is shown in figure 6-10 c). Helium reduces the WC reinforcement. A very high proportion of the matrix is actually reprecipitated WC. Highs of 35.6 % WC were found (Ar, γ = 57°). Ar shielding gas demonstrates the highest amount of WC for all three electrode angles. Mixing He into the shielding gas minimises the dissociation of WC.

It was shown that the dissociation effect of W_2C has a big influence on the matrix of the MMC. In fact, the amount of WC particles was less than the dissolved WC in the matrix. In many ceramic MMC's (e.g. Al-Si$_p$ [36]), a volume fraction of ceramic can easily be measured over the area fraction in the

microsection. WC MMCs in steel, however, have a significant dissociation of WC which must be included.

Matrix hardness improved significantly with a very low amount of dissolved WC and was stable in the range between 606HV0.2 and 771HV0.2. Therefore a dependency of the shielding gas and the electrode angle could not be seen.

Samples made with He or 50/50 Ar/He have more and longer cracks. It was found that many samples had cracks going into the HAZ. This is particularly bad for the use of the product later on.

In summary, a major role in cracking can be concluded from the use or mixing of He. This increase in number of cracks and their increased length is probably the result of the intensification of the welding power. More power generates a longer weld bead, thus the huge volume of the bulk material creates a quicker cooling rate. Dust made from the fume gives a lower cooling on the surface area. Higher stress in the samples made with He than with Ar is generated by the change in weld bead shape. Produced stresses release shortly after the cladding trial and build cracks which explain why the cracks are all close to the HAZ and not at the surface.

Intensifying WC reinforcement causes a decreased penetration area and a larger total molten area. This fact is particularly good for cladding. An enlarged bead with lower penetration area is achieved, if more particles are retained. The dilution dramatically falls with increasing WC reinforcement. Changes in the penetration area and total molten area influence the dilution significantly. Minimal declines can be seen in the aspect ratio with increasing WC reinforcement.

An increase in WC powder retrieval is almost linear until PFR = 25 g/min up to approximately ppu = 0.02 g/mm WC retrieval. From PFR = 25 g/min to the end of testing with PFR = 100 g/min, the WC powder retrieval was fluctuating in a range of about 0.02 g/mm to 0.03 g/mm. The WC particle retrieval, which makes the composite, and the WC content in the matrix are following the same

trend. The weld bead is saturated with WC at about PFR = 25 g/min. The WC content in the matrix is constantly higher than the WC particle retrieval.

The hardness growth in the matrix is relatively constant from 458HV0.2 (PFR = 5 g/min) to 539HV0.2 and stabilises in the area of 539HV0.2 (PFR = 25 g/min) to 775HV0.2 (PFR = 100 g/min).

As seen in figure 6-22, even with increasing powder feed rate, the use of pureshield Argon shielding gas gives a low number of cracking and the crack length is relatively short.

6.5 Conclusions

The following conclusions can be drawn from the objectives set:

- The amount of WC reinforcement as particles increases with increasing powder feed rate until saturation of the weld bead at about 25 g/min. This is shown due to reduced WC powder particle pick up efficiency.
- It was observed that a significant dissolution of some of the particles happens during cladding. These are then reprecipitated in the matrix. This significantly increases the hardness of the matrix.
- Cracking was more extensive with He, probably due to higher heat input leading to high cooling rates and also the change in weld bead shape. This effect also probably explains why the cracks are located in the HAZ and lower part of the bead for the clad layers made with He.

Argon shielding gas was selected for further cladding trials as this provides the lowest occurrence of cracking in the single bead trials. Experiments on overlap clads are described and analysed in chapter 7 following.

7 Effect of GTA process on the MMC layer structure

Only single bead cladding trials were scrutinised in the last chapter. Multi bead layers are examined in this chapter. These cladding layers in overlap are required to cover full wear surfaces of a brake disc.

- This chapter is to study and understand the effect of the GTAW process on the WC ceramic and matrix of the layer.
- The dimensions of the layers are compared for different feeding rates.
- The microstructure shows the effects of distributed and reprecipitated WC in the matrix.

7.1 GTAW process set-up for MMC layer cladding

The principal set-up of the GTAW process is identical to that shown in chapter 6.1, to maintain the same process conditions. Therefore, the base material is G-22 NiMoCr 5 6 steel and the wire material is G89 6 M Mn4Ni2CrMo steel. The welding parameters, powder feeding parameters and nozzle angles can be seen in table 6-1 of chapter 6.1. The error bars are calculated with the formula shown in Appendix F. As shown in figure 7-1 the base materials for the MMC cladding layers are sections of railway brake discs.
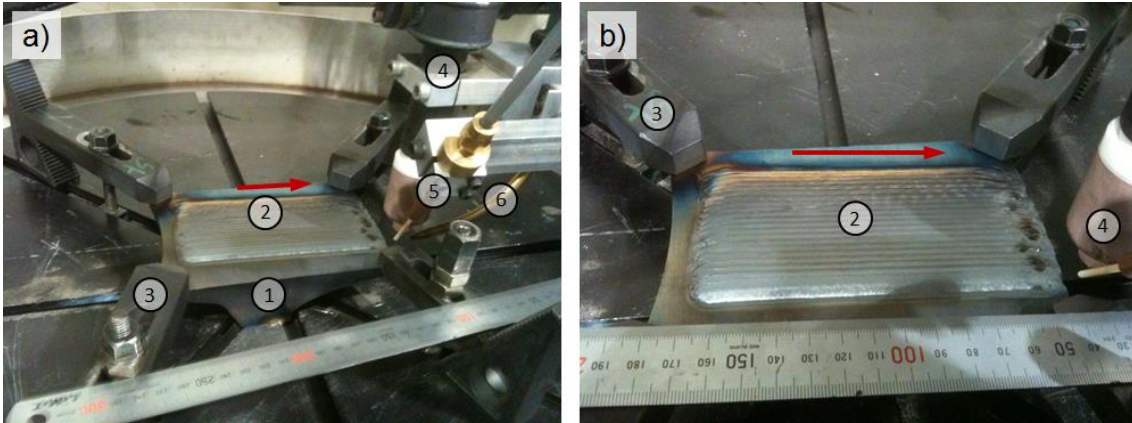
Figure 7-1: Principal of GTA overlap cladding; a) Clamping system and torch; b) Layer clad on a plate; 1: base material (section of a railway brake disc); 2: cladding layer (approximately 100 mm x 130 mm coverage); 3: clamping system; 4: TIG welding torch; 5: powder feeder nozzle; 6: wire feeder nozzle; red arrow: welding direction

This gives a cladding area of approximately 130 mm x 100 mm. The GTA welding torch drives along the longer distance of the section, as in the single bead trials in chapter 6. The clamping system ensured a levelled and secured work piece.
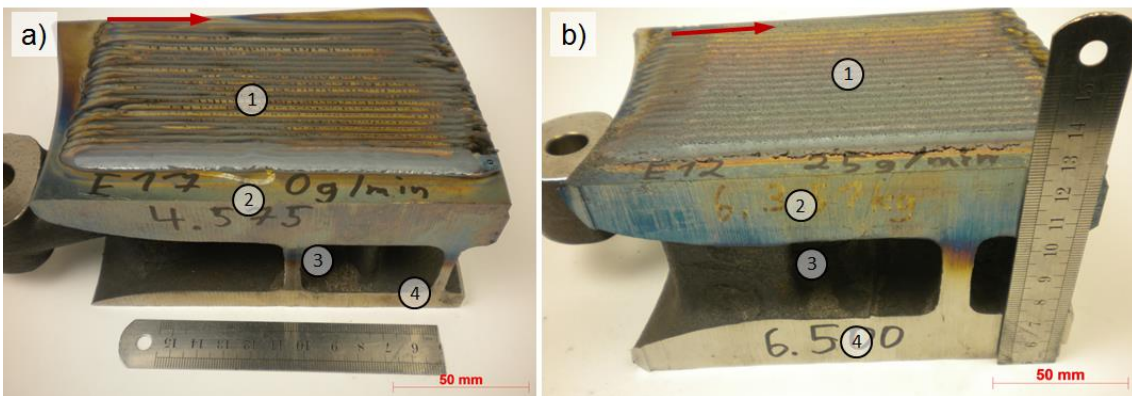
Figure 7-2: Clad layer on railway brake disc section (axel mounted); a) GTA cladding with PFR = 0g/min or 0 g/mm; GTA WC cladding with PFR = 25 g/min or 0.0833 g/mm deposition rate; 1: Cladding layer; 2: brake disc wear surface; 3: brake disc cooling vanes; 4: lower brake disc wear side; red arrow: welding direction

Figure 7-2 gives an overview of the clad brake disc sections. The cooling vanes of the brake disc are seen here. The type of cooling vane depends on whether the brake disc is wheel-mounted or axle-mounted. Type and shape of the cooling vanes can be important for different heat sinks in the braking service [119]–[121]. This might have an effect on the welding trials as well. The sections were chosen in a big enough size to ensure sufficient material could be deposited.

7.2 Influence of the GTAW process parameters

The main focus of the cladding process was on the powder deposition and the response on its change. The overlap was set at 50 % of the single bead width. Nevertheless, with increasing powder feeding rate (PFR) the bead width will increase. To maintain the overlap at a constant level, the bead width of the first bead was measured at three different positions and half of the average value was used as an off-set. The off-sets are shown in figure 7-3.
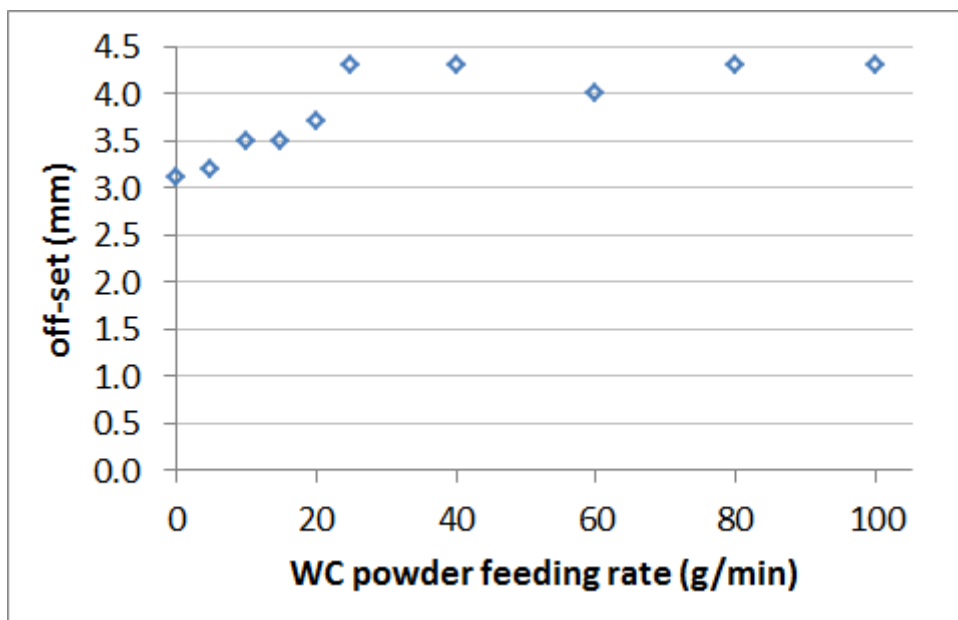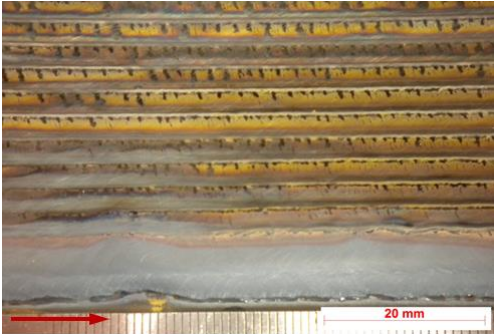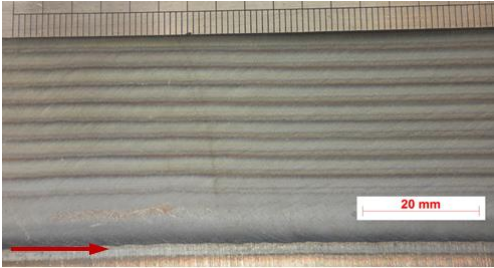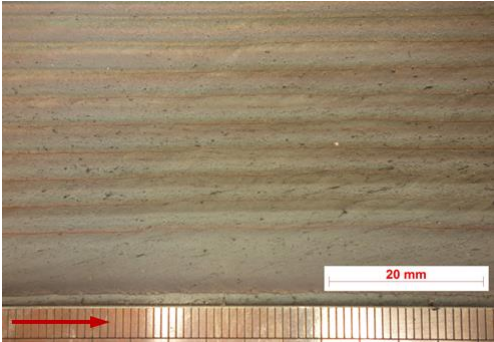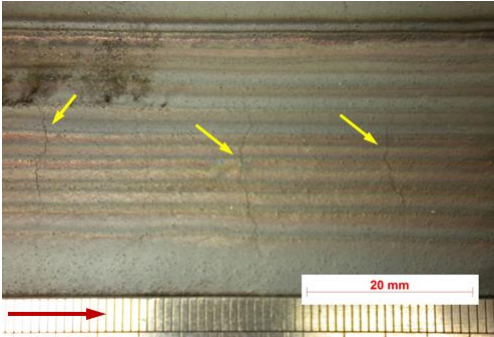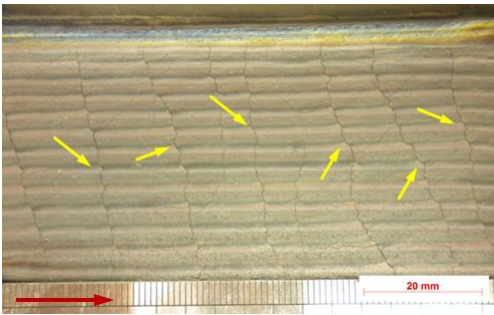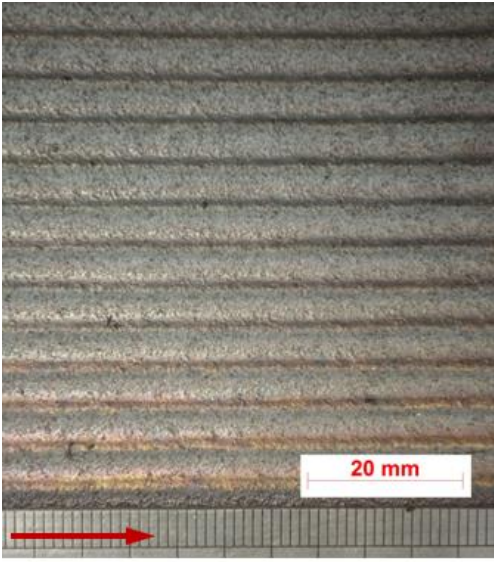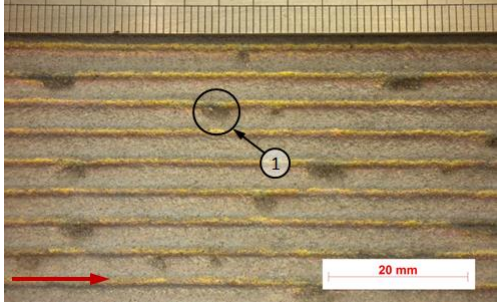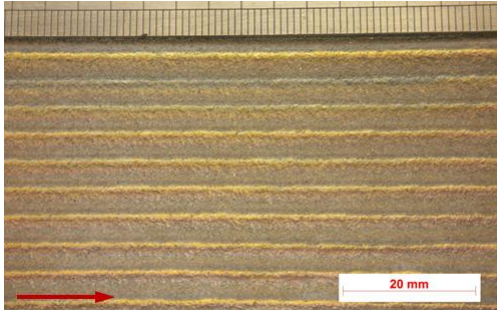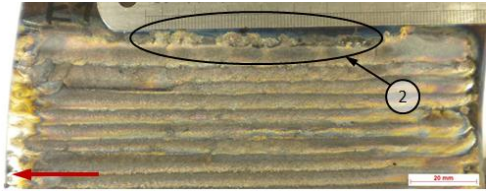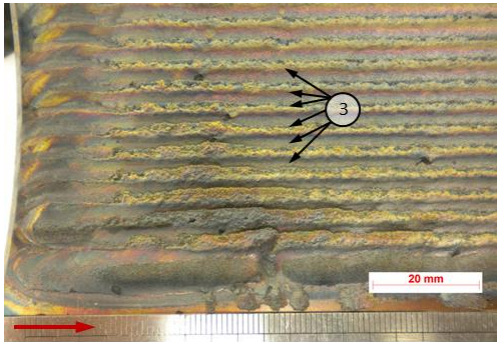
Figure 7-3: Off-set of overlap distances to maintain 50 % overlap

The off-set values show that there is no effect on bead width with powder feeding rates above 25 g/min. The clad surface is shown in table 7-1 and more detailed in Figure_apx J-1 to Figure_apx J-10 of Appendix J.

Table 7-1: Surface of the clad trials with increasing WC powder feed rate; detailed figures are in Appendix J

Powder feed rate	Comment	Surface
g/min	-	-
0	flat and smooth surface; colours from scales	
5	slightly rougher surface than with 0 PFR	
10	rough but flat surface	

Powder feed rate	Comment	Surface
g/min	-	-
15	check cracking (yellow arrows); flat surface	
20	intensive check cracking at the beginning of the layer; surface is rough and increases in waviness	
25	rough surface with high waviness	

Powder feed rate	Comment	Surface
g/min	-	-
40	high waviness of surface; patches of unbonded segregation of WC powder (as seen in 1)	
60	rough surface with high waviness; WC particle agglomerates come out of the layer side	
80	WC particle agglomerates come out of the layer side (as seen in 2)	
100	very wavy surface with saw teeth structure (as seen in 3)	

The increasing powder feed rate caused:

- Increased waviness of the beads
- Increased agglomeration of WC powder next to the cladding bead

- Increased surface cracking
- Initial increase in width up to 25 g/min and then increase in layer height due to the agglomeration of powder on the top.

It can be seen that the surface of cladding trials with PFR = 0 g/min (wire only) are flat and smooth (Table 7-1 image 0 PFR and Figure_apx J-1). Some colours appear from the building up of scales. As soon as the first WC powder was fed, the scales disappear and a slightly rougher surface develops (Table 7-1 image 5 PFR and Figure_apx J-2). The waviness is still low. A further increase in WC powder feeding with PFR = 10 g/min illustrates a still rough but flat surface (Table 7-1 image 10 PFR and Figure_apx J-3).

Surface layers made with PFR = 15 g/min indicate first check cracking, as seen in Figure_apx J-4 b), whereas the surface of the clad is still flat (Table 7-1 image 15 PFR). Further increase in WC powder feeding to 20 g/min (Table 7-1 image 20 PFR and Figure_apx J-5) shows a lot of cracking at the beginning (Figure_apx J-5 b)), which is reduced towards the finish (Figure_apx J-5 c)) of the cladding layer. These cracks are obviously caused by high lateral stresses during the building up of the layer. These stresses build up in a 90° angle to the overlap tracks. The surface is still rough but has also increased in waviness.

Surface cladding with PFR = 25 g/min indicates some colouration at the beginning (Figure_apx J-6 a)). No cracks are visible. A rough surface with a high waviness is generated.   The high waviness continues with further increasing of WC powder feeding rate to PFR = 40 g/min. Cracks were not visible on the surface in Figure_apx J-7 a). The development of patches with unbonded segregation of WC powder was a phenomenon only seen when the PFR is increased to 40 g/min (Table 7-1 image 40 PFR and Figure_apx J-7 b)). A plate clad with an additional increase in WC powder feeding to PFR = 60 g/min is shown in Table 7-1 (image 60 PFR) and in Figure_apx J-8. The rough surface and high waviness of the clad shows no cracking.   WC particle agglomerates starts to come out of the cladding layer on side without supporting cladding trial. This effect was more visible with the PFR = 80 g/min (Table 7-1 image 80 PFR and Figure_apx J-9).

Welding above the agglomerates magnified the waviness and roughness of the surface. Nonetheless, no visible cracks appear. This effect is shown in the extreme when PFR = 100 g/min was used (Table 7-1 image 100 PFR and Figure_apx J-10). A WC powder feeding rate of 100 g/min resulted in a WC powder bond in the configuration of saw teeth on the surface (Figure_apx J-10 b) 7 and figure 7-7 e)). Further analysis of all cladding trials in the microstructure will show the embedding of WC; the results are given in section 7.3. The cracking on the microsection will be described in section 7.4.2 as well.

7.3 Microstructure analysis of the WC particle incorporation

Microsections were prepared to provide evidence of the embedding of WC particles and the kind of bonding of WC to the matrix material. Furthermore, the particle distribution and dissolved WC were measured. For this, the clad layer thickness was divided into a peak cladding layer and a useful cladding layer (see figure 7-5 and figure 7-6). The so-called total cladding layer is the layer with peaks and valleys. However, a uniform braking condition requires a relatively flat surface of consistent frictional response. Thus the cladding layer without peaks and valleys can be seen as useful and is measured separately.

7.3.1 Sample cutting directions and microsection analysis definition

The sampling for microsections of the cladding trials is essential for a reliable statistical analysis. Two plates were welded for each WC powder feeding rate. Samples taken in transverse cross section are cutting through the overlapping layers and, therefore, are preferred. Cross section samples longitudinal to the cladding beads were made to obtain a 3-dimensional variation of the WC distribution. The sampling areas are shown schematically in figure 7-4.
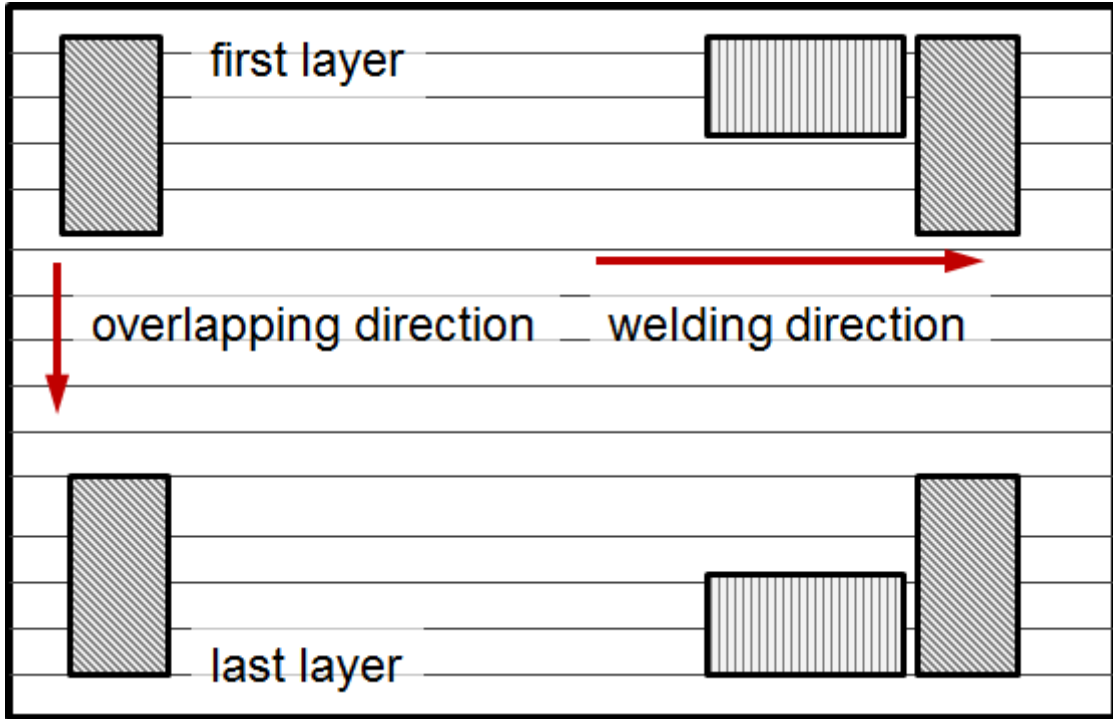
Figure 7-4: Schematic cladding trial in overlap, four microsections were made in transverse cross section (diagonal pattern); two microsections were made longitudinal at the finish of the trials (vertical pattern)

The microsection is schematically illustrated in figure 7-5 and figure 7-6.
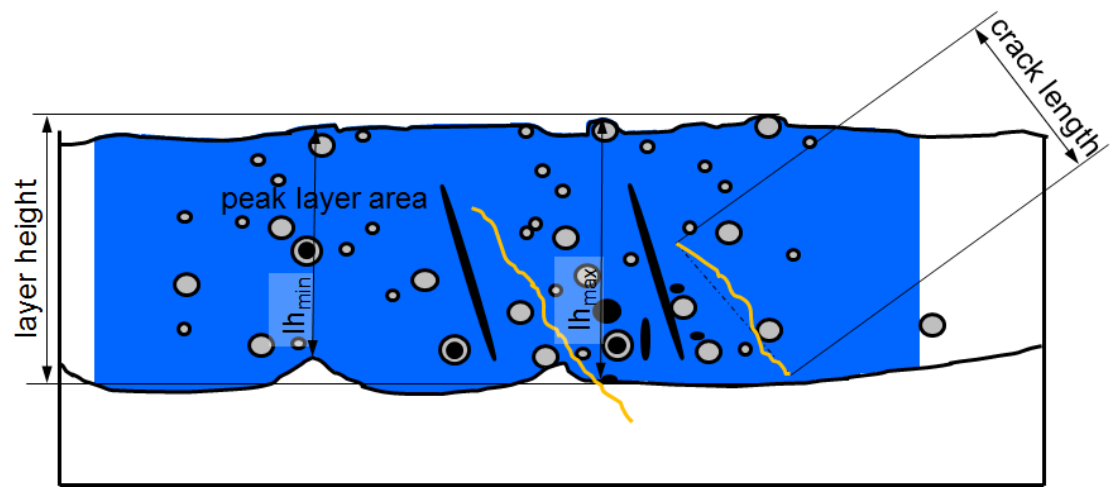
Figure 7-5: Schematic representation of cross sections for micrographs. A minimum of 3 and maximum of 5 layers were taken in the study; blue: peak layer area; legend given below figure 7-6

As seen figure 7-5, the peak layer area is measured out of the full cladding layer height with peaks and valleys and in a length which stretches between three and five overlaps. The layer height is measured at the minimum layer height (see figure 7-5 lh_{min}), maximum layer height (see figure 7-5 lh_{max}) and useful layer height (see figure 7-6 lh_{use}).
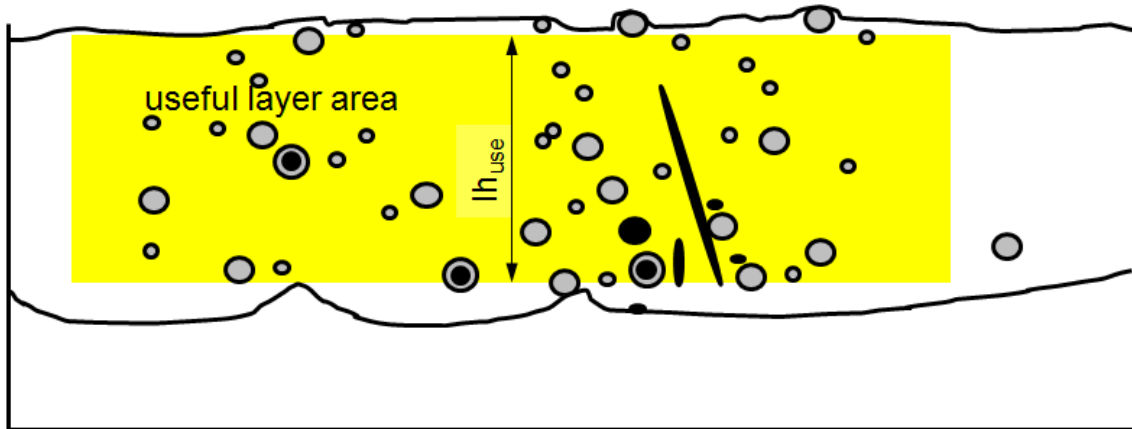
Figure 7-6: Schematic representation of cross sections for micrographs. A minimum of 3 and maximum of 5 layers were taken in the study; yellow: useful layer area; legend below

Legend:

⬤	particle		
◉	particle with pore	lh – layer height	
▬ ▌	pore, cavity		
〜	crack	cl – crack length	

The minimum layer height is the height between the highest heat affected zone and the lowest point of the surface (see figure 7-5 lh_{min}), whereas, the maximum layer height is the height between the deepest penetration point and the highest peak (see figure 7-5 lh_{max}). The useful layer height is the vertical distance of a rectangle that can be drawn within the clad layer boundaries (see figure 7-6 lh_{use}). It is worth mentioning that the useful layer area is defined by the

130

maximum surface, which can be drawn rectangular into the peak layer area (see figure 7-6). The upper line of the rectangle is the tangent of two lowest points of the surface.

The following additional measurements were taken:

- Cracks were counted,
- the longest crack was measured,
- all particles were measured by their area,
- the pores in the particles were measured by their area   and
- porosity and cavities in the matrix area were measured separately by their area.

These measurements were necessary to make the microsection analysis as accurate as possible. Therefore, a standardised microsection preparation as described in Appendix G was used. The tolerances of the light microscope are in section G.2 and more details about the multi-layer analysis are given in section G.4.

7.3.2 WC particle incorporation and its microstructure

The bonding of WC with the matrix will be an important factor in the wear resistance of railway brake discs with a WC MMC cladding layer. Therefore, it is vital to understand the bonding principle.
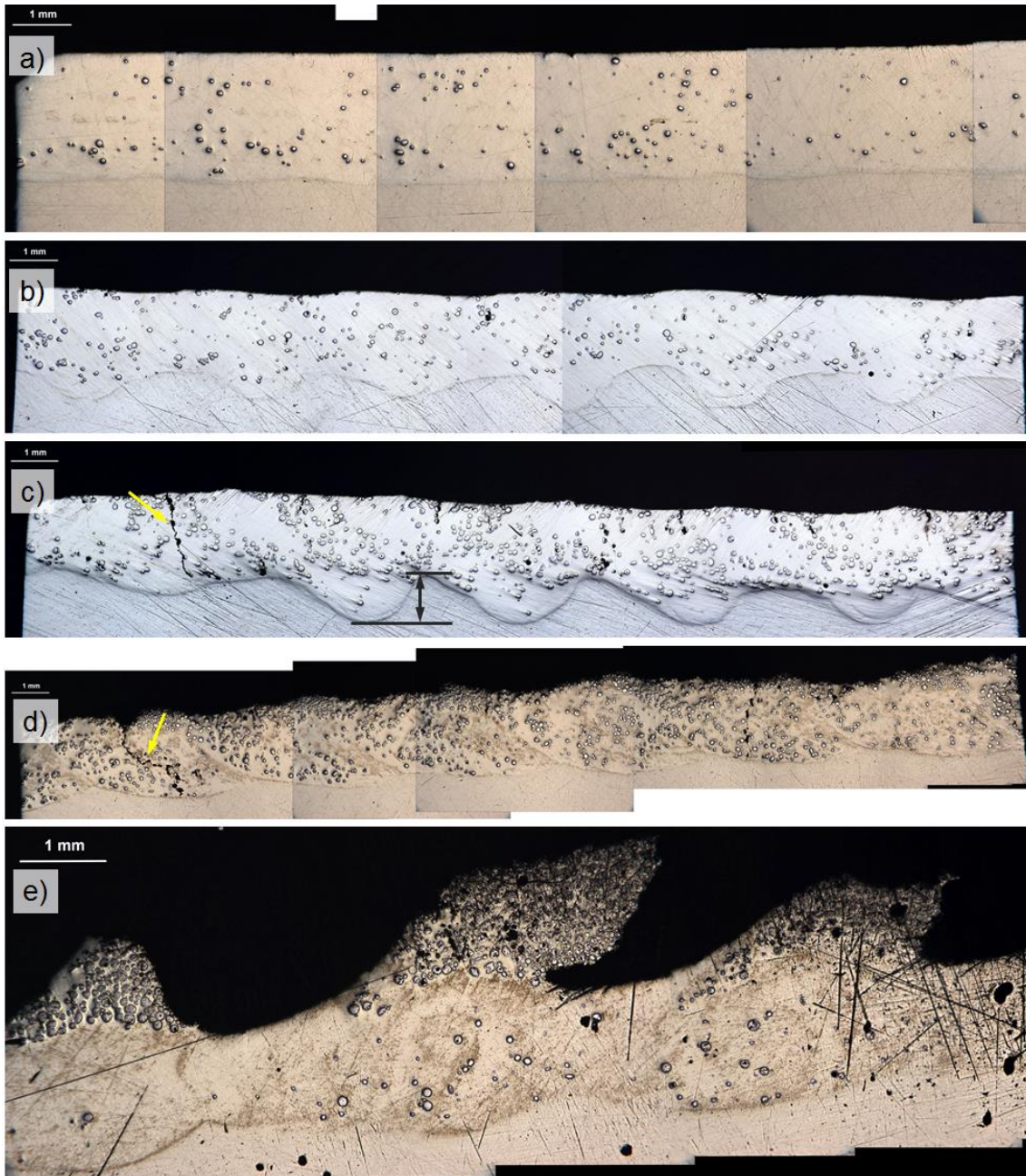
Figure 7-7: Light microscope images of the WC cladding layer microsections; a) Sample with PFR = 5 g/min; b) Sample with PFR = 10 g/min; c) Sample with PFR = 20 g/min; d) Sample with PFR = 80 g/min; e) Sample with PFR = 100 g/min; yellow arrows: selected cracks; black arrow: example for penetration difference

For this, samples with different powder feeding rates have been used to examine the bonding structure between the matrix and the particles. Additionally, the dissolved WC and new-build phases reprecipitated were examined. As shown in figure 7-7, the WC particles are visible under the

microscope in macroscopic inspection. The fusion zone between the HAZ and layer matrix can also easily be seen. The samples were examined after polishing and without any etching. Only water and isopropanol was used for cleaning after polishing. The fusion zone, matrix and particles are visible because of the very different hardness's in the bulk material, matrix material and WC particles. Materials with lower hardness are polished away more easily than harder material. The layers with low WC powder feeding rates in figure 7-7 a) and b) with PFR = 5 g/min and PFR = 10 g/min, respectively, show a smooth surface. The cladding layer with PFR = 5 g/min also indicates a low penetration variation of up to 246 µm. The penetration variation (illustrated with the black arrow in figure 7-7 c)) becomes significantly higher with PFR = 10 g/min and PFR = 20 g/min of up to 1043 µm. The surface is still smooth as seen in figure 7-7 c) and Figure_apx J-5. Only with figure 7-7 d), does it appear that the WC particles are actually making the rough surface, as seen in Figure_apx J-9. The cracks mentioned in sections 7.2 and 7.4.2 are seen in figure 7-7 c) and d) (yellow arrows pointing at cracks). The very wavy surface of the WC cladding layer with PFR = 100 g/min from Figure_apx J-10 b) marked with the number 7 is clearly seen in figure 7-7 e). Particles are segregated in a semi-fused condition resulting in periodic projection resembling a saw tooth profile. That is why the WC reinforcement is less in the useful area of cladding, as shown in figure 7-12 a).

High resolution images using SEM microscopy show the particles embedded within the matrix. Figure 7-8 a) shows the top of a cladding layer in the SEM microscope. The white round shapes are the WC particles surrounded by the matrix material. Some white long needles of the matrix can also be seen in this image in the matrix. These are dissolved WC dissociated out of the particles and built Fe-W-C phases. The boundary between the matrix and the HAZ is shown in figure 7-8 b). Parts of the substrate material melted and diluted the clad matrix. The dilution level was calculated from the area of the single bead tracks shown in chapter 6 section 6.3.1.
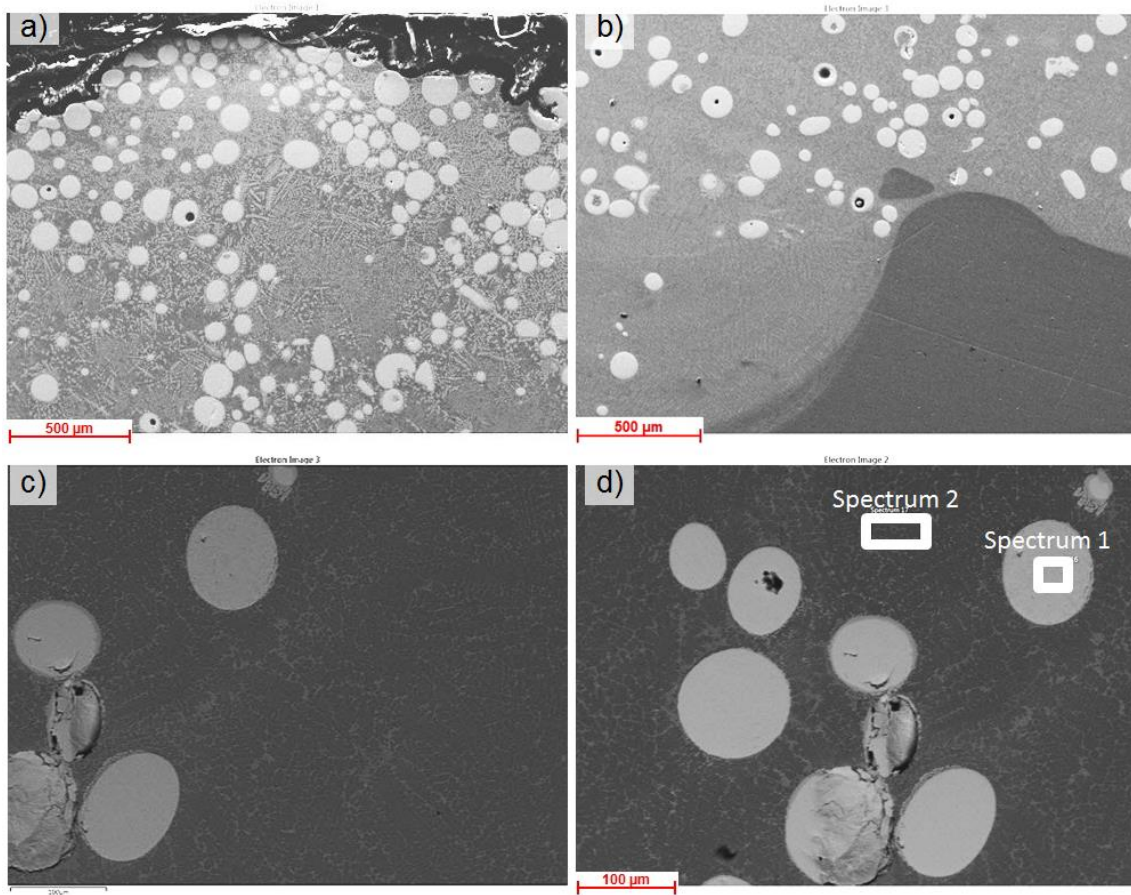
Figure 7-8: SEM images of selected WC cladding layers in the microsection; a) low magnification image of the layer close to the surface; b) low magnification image of the layer close to the HAZ; c) Image displaying some WC particles within the matrix; d) Image of some WC particles embedded in the matrix with the EDX spectrum 1 on a particle and 2 on the matrix

Further, higher magnification (Figure 7-8 c)) exhibits how the WC particles were captured within the matrix material. Some WC particles were damaged during the grinding; while others show smooth and flat profiles after polishing. The matrix reveals irregular formation of Fe-W-C phases. To get an understanding of the matrix and the particles, a chemical analysis with the EDX system was done, as shown in figure 7-8 d). The area analysed on the particle is shown as spectrum 1; the area analysed on the matrix is shown as spectrum 2. Subsequently the analysis results are presented in table 7-2. WC particles show high purity in the chemical analysis. Carbon was not analysed in the EDX. Despite the heat input of the welding process the EDX analysis confirms

99.35 wt% of W. The WC particles were not analysed in the EDX because of the possibility of particles getting sucked into the vacuum pump of the SEM microscope. Compared to the material certificate delivered with the WC particles the Fe content (with 0.41 wt% Fe) is nearly twice as much as the certified maximum. Figure L-13 in the Appendix shows the certificate with a maximum of only 0.23 wt% Fe. Ni is not applicable according to the certificate but was analysed with 0.24 wt% Ni. In contrast to the certificate, Ti and Ta should have shown up with a maximum of 0.05 wt%. However, Ti and Ta were not measured in Spectrum 1 of figure 7-8 d) as shown in table 7-2. All of this could be the result of diffusion during the GTA cladding procedure or a result of the cutting, grinding and polishing process of the microsection.

Table 7-2: EDX spectra of the area in the microsection of figure 7-9 d); Spectrum 1: WC particle; Spectrum 2: matrix area

Spectrum 1	Line Type	Apparent Concentration	k Ratio	Wt%	Wt% Sigma	Atomic %	Standard Label
Cr	K series	0	0	0	0	0	Cr
Mn	K series	0	0	0	0	0	Mn
Fe	K series	0.23	0.00229	0.41	0.25	1.33	Fe
Ni	K series	0.15	0.00145	0.24	0.32	0.75	Ni
W	M series	47.92	0.47918	99.35	0.41	97.92	W

Spectrum 2	Line Type	Apparent Concentration	k Ratio	Wt%	Wt% Sigma	Atomic %	Standard Label
Cr	K series	0.39	0.00387	0.52	0.13	0.64	Cr
Mn	K series	0.61	0.0061	0.94	0.19	1.11	Mn
Fe	K series	51.76	0.5176	77.5	0.57	89.58	Fe
Ni	K series	1.05	0.01048	1.71	0.27	1.88	Ni
W	M series	7.68	0.07685	19.32	0.51	6.78	W

Spectrum 2 represents the matrix with an iron content of 77.5 wt% and 19.32 wt% W. Some accompanying elements of Cr, Mn and Ni come from the wire and base material. Nonetheless, the high W content provides evidence of the dissociation effect of WC. It is necessary to remember that the particles are formed of WC and W_2C, and that W_2C is reactive with iron. A selective analysis with higher magnification of the W content will illustrate the W distribution in the cladding layer. Figure 7-9 exposes the area captured with higher magnification. The chemical analysis areas are pointed out by rectangular shapes or crosses in figure 7-9.
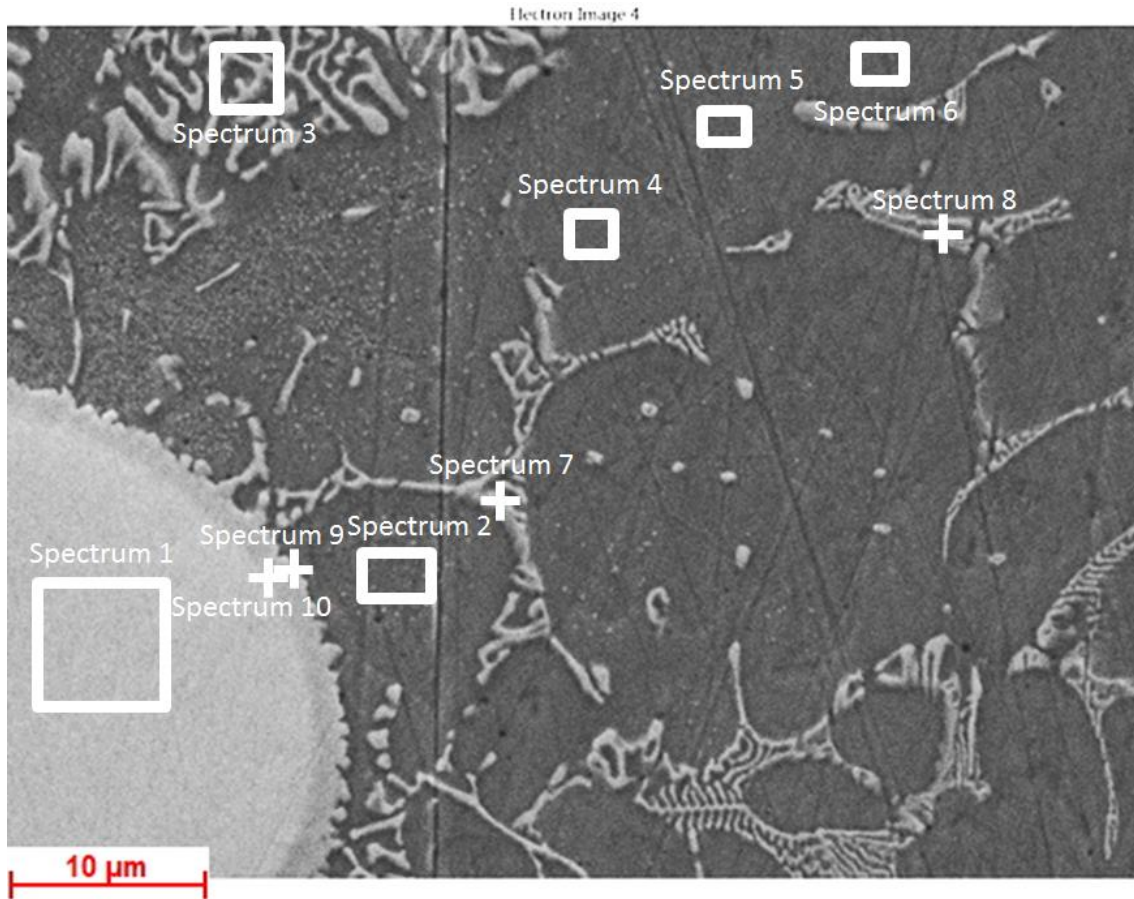
Figure 7-9: High magnification SEM images of matrix material surrounding a WC particle with EDX analysis

Tungsten values illustrate a significant dissociation of WC during the cladding process as the weight per cent of W is constantly above 10 wt% W in the matrix. The numbers of W variations are shown in table 7-3.

Table 7-3: W content of the EDX analysis made of figure 7-9; Distance measured between the middle of the spectra to spectrum No. 1

Spectrum No.	-	1	2	3	4	5	6
Distance	µm	0	16	30	33	41	49
W	wt%	98.99	17.07	34.48	15.61	14.9	14.08

Spectrum No.	-	7	8	9	10
Distance	µm	22	48	11	9
W	wt%	17.34	14.35	17.59	48.51

All W contents measured in the EDX analysis of figure 7-9 in table 7-3 are above 14 wt% W. Therefore, it is certain that WC gets in to solution in the matrix. The W content of the brake disc base material and the wire matrix material is not mentioned in the material certificate (see table 4-4 of section 4.2.1 in chapter 4). The spectra ordered in the distance to the WC particle are shown in figure 7-10.
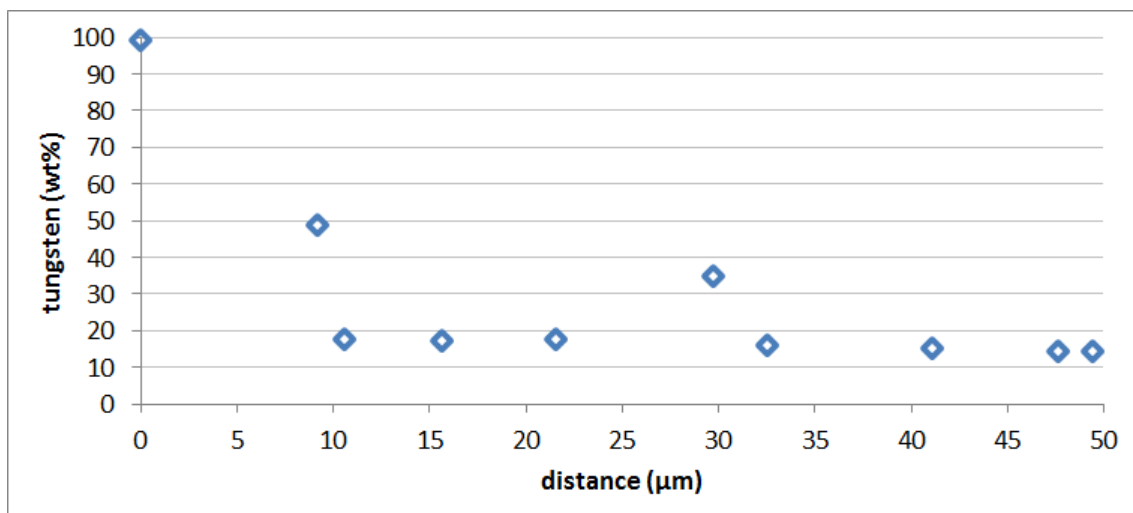
Figure 7-10: W content in wt% of spectra 1 to 10 of figure 7-9 and table 7-3 ordered in the distance to the WC particle (middle of spectrum 1)

The W content reduces at the boundary of the particle dramatically from 48.51 wt% W to 17.59 wt% W. Regardless of the white and the dark phases, the W content in the matrix stays between 14.08 wt% W and 17.59 wt% W with one outlayer. A detailed microstructure analysis will bring a picture of the Fe-W-C phases and structures in section 7.3.3 below. It becomes interesting to see in what phases this WC appears from the perspective of the wear resistance. Phase analysis was taken up by EBSD analysis.

7.3.3 Detailed microstructure characteristics of the WC MMC matrix

At this point, the focus is on the microstructure of the matrix of the WC cladding layer in overlap. It was shown that WC particles partially dissolve in the Fe matrix during GTA cladding. However, it is still not clear which structure the W and C builds up in the matrix during solidification and cooling down. Thus an Electron backscatter diffraction (EBSD) scan is done at selected points. The EBSD detector calibration is explained in Appendix H section H.1. A preparation of a microsection sample was done by ion-beam sputtering. Before any EBSD scan could happen, the Densities of Electronic States at the Fermi Level of each phase to be investigated had to be found. This background data had been originated for the phases Fe bcc (body-centred cubic iron, ferrite) [122], Fe fcc (face-centred cubic iron, austenite) [122], Fe_3W_3C [123], Fe_6W_6C [123], WC [123] and W_2C [41], [124]. The crystal structure and the lattice spacing distance can be obtained from the literature. The crystal structure and lattice spacing distance are used afterwards to obtain a calibration diffraction pattern. The calibration diffraction pattern enables the EBSD detector to identify the phases which were measured by quantity and location. A coloured picture gives an overview of the majority of elementary cells in each location. The colour code chosen for the EBSD pictures are the following according to table 7-4:

- red phase: Fe bcc;
- fuchsia phase: Fe fcc;
- green phase: Fe_6W_6C;

- blue phase: WC;
- yellow phase: Fe_3W_3C;
- turquoise blue: W_2C (not in colour code).

Table 7-4: Colour code for EBSD scan

phase	colour code
Fe bcc	Phase-RED
Fe fcc	Phase-Fuchsia
Fe_6W_6C	Phase-GREEN
WC	Phase-BLUE
Fe_3W_3C	Phase-YELLOW
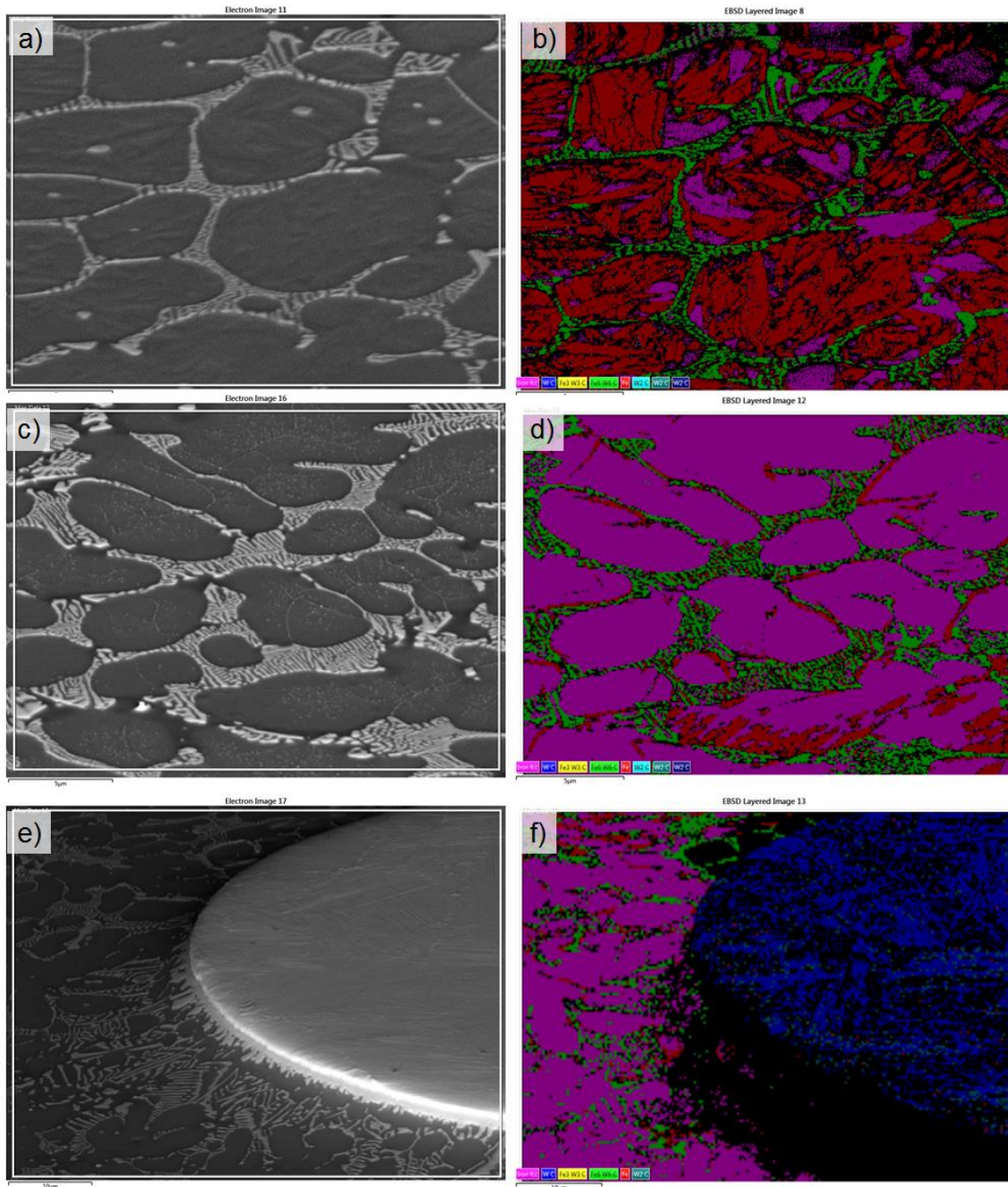
Figure 7-11: SEM images and the EBSD scan from selected samples of the cladding layer for PFR = 5 g/min and PFR = 15 g/min; a) BSE scan of the matrix of a sample with PFR = 5 g/min; b) EBSD scan of a); c) BSE scan of the matrix of a sample with PFR = 15 g/min; d) EBSD scan of c); e) BSE scan of the boundary between matrix and particle of a sample with PFR = 15 g/min; f) EBSD scan of e); black colour in EBSD: no data received

A backscattered electrons (BSE) image of the area for the EBSD scan was taken before the scan to identify the exact area for scanning. Both the BSE

142

image and the EBSD scan are shown in figure 7-11. The grain size in the matrix material is approximately 67 µm^2. In figure 7-11 a) and b), the images of a clad made with PFR = 5 g/min are exhibited. The EBSD scan in figure 7-11 b) shows grains of ferrite (Fe bcc) and austenite (Fe fcc) surrounded by Fe_6W_6C. Interestingly, increasing WC powder feeding causes more austenite phases in the grains. A comparison of Figure 7-11 b) and Figure 7-11 d) shows the increased austenite fraction. This is probably caused by the high amount of soluble C in the iron based matrix. Austenite can incorporate more C than ferrite in the structure. This might give an additional strengthening effect to the matrix by forming martensite during deformation. Despite this fact, a wider and more linked grid of Fe_6W_6C forms throughout the cladding layer.

The strengthening effect is known in TRIP or TWIP steels and needs to be confirmed in future work. In TRIP steels the retained austenite progressively transforms to martensite with increasing strain, thereby increasing the work hardening rate at higher strain levels. TWIP steels are fully austenitic at room temperatures. A large amount of deformation is driven by the formation of deformation twins. The twinning causes a high value of the instantaneous hardening rate as the microstructure becomes finer and finer. The resultant twin boundaries act like grain boundaries and strengthen the steel [125].

A BSE scanning image of the boundary between the matrix and WC particle indicates a step from the ion beam sputtering from the matrix to the particle (Figure 7-11 e)). This step could cause reflections of the electron beam and no responding X-rays in some areas of the EBSD scan in figure 7-11 f). However, the black area without data in figure 7-11 f) could also come from non-stoichiometric phases close to the WC particle. A distinct response of the WC particle and the matrix is illustrated. The WC particle is shown to be of WC phase and a very little bit of W_2C phases; it is surrounded by a matrix of mainly austenite and Fe_6W_6C phases.

7.4 Effect of WC powder feeding rate on the bead dimension and WC inclusion

Effect of WC powder feeding rate on the bead dimensions and WC inclusion are analysed in this chapter. These are the following:

- WC powder inclusion and its embedding in the matrix
- Appearance of cracking in the layer (cross sectional)

7.4.1 WC powder inclusion and its effects in the layer

First the equation (6-5) from section 6.2.3 of chapter 6 was used to convert the PFR into a WC powder deposition rate (WCpa). Each bead length of the cladding layer and number of welds was measured to calculate a theoretical total bead length. The observation made for single beads in equation (6-6) from section 6.2.3 was also observed for the overlapping layer. As a result, the equations (6-7), (6-8), (6-9), (6-10), (6-11), (6-12), (6-13) and (6-14) of section 6.2.3 were used to establish the following parameters from the microsection of the cladding layer:

WCpa – WC powder addition (deposition per unit length) [g/mm]

lop – loss of WC powder [g/mm]

ppu – WC powder pick-up [g/mm]

WCpt – WC particles reinforcement [g/mm]

WCrm – WC reprecipitated in matrix [g/mm]

WC reinforcement – classical ceramic reinforcement [%]

The WC content in the cladding was established from the microsections and the optical and chemical analysis. The following equations give an insight into the calculation of WC powder pick up. First the welding time for each sample was determined by:

$$theoretical\ total\ welding\ time = \frac{theoretical\ total\ bead\ length}{travel\ speed} \qquad \textbf{(7-1)}$$

In the next step the total wire length was found by:

$$total\ wire\ length\ = theoretical\ total\ welding\ time\ \times\ wire\ feed\ speed \qquad \textbf{(7-2)}$$

followed by the wire consumption:

$$total\ wire\ consumption \qquad\qquad\qquad\qquad\qquad\qquad \textbf{(7-3)}$$
$$= wire\ area\ \times\ total\ wire\ length\ \times\ \text{density of steel}$$

The density of steel was taken as 7.65 g/cm^3, which is equivalent to 0.00765 g/mm^3 [94].

The results were observed from the bead dimensions and WC particle incorporation. This explained some fundamentals in the WC embedding process.
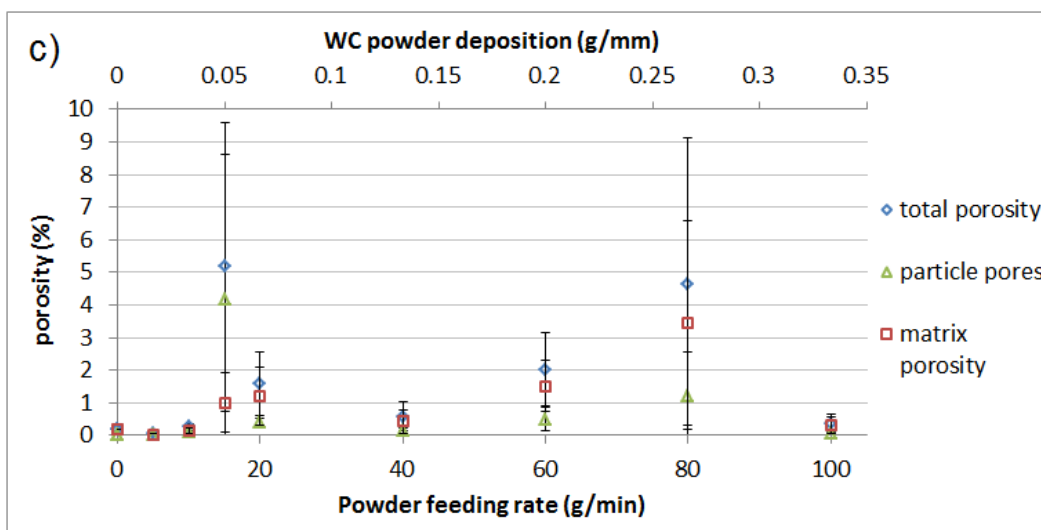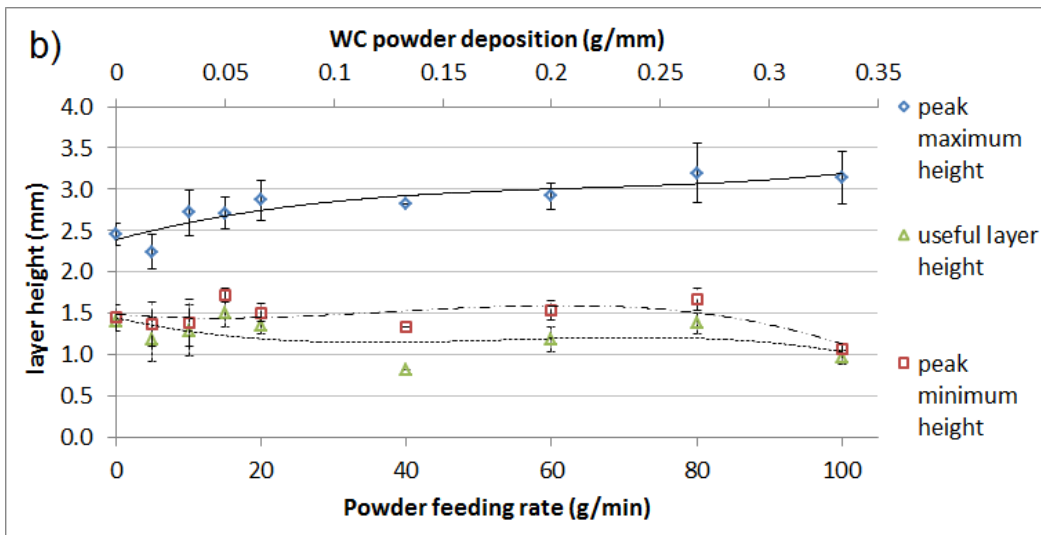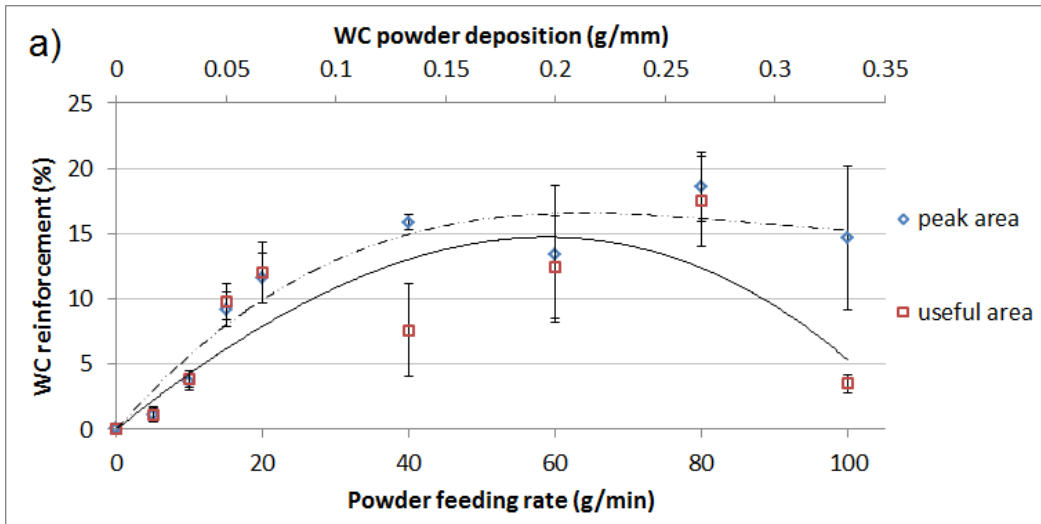
Figure 7-12: WC cladding layer dimensions and WC incorporation; a) WC reinforcement particles; b) layer height; c) porosity and cavities in useful area

Figure 7-12 a) illustrates the WC reinforcement in the area with the peak and the useful area, the WC reinforcement increase until PFR = 80 g/min in the useful area and until PFR = 40 g/min in the peak area. Moreover, the particle inclusion in the peak area stays constant from PFR = 40 g/min to PFR = 100 g/min in the range between 13.4 % and 18.6 %. The particle inclusion in the useful area drops with PFR = 100 g/min significantly down to 3.5 % WC reinforcement which was explained in section 7.3.2. A covering of loose powder could have an effect (cooling or heat treatment).

The layer height of the useful and the peak minimum height stay relatively constant (Figure 7-12 b)). The values for the useful layer height are naturally the lowest with values, ranging from 0.83 mm to 1.5 mm. Heights of the minimum peak follow closely in the range between 1.07 mm and 1.72 mm. Even when no powder is added, the useful and minimum peak heights are relatively unaffected. A different trend is shown for the peak layer height (Figure 7-12 b)) as it increases with intensifying WC powder feeding from 2.25 mm (PFR = 5 g/min) to 3.15 mm (PFR = 100 g/min). The sample without WC powder addition stays at 2.46 mm layer height. The maximum peak values compared to the minimum peak layer height shows the material, which needs to be removed for a flattening in post-processing. For a useful application, the difference excess height needs to be machined off. It also demonstrates that additional WC powder of too high powder feeding rates stays on top of the weld bead, when it can just be bonded (generates the waviness in section 7.2). Higher weld pool energy could be necessary to overcome this phenomenon as the WC powder cools the weld pool too quickly. A kind of cooled down skin of WC powder and matrix prevents further WC powder from penetrating the weld pool. The excess WC powder does not get incorporated.

As seen in figure 7-12 c), the porosity in the useful area had the highest value of 5.2 %. Even in the total area with peaks, the highest value measured was 3.7 %. The matrix porosity only increases when the particle pores are increasing as well. The particle pores are in the WC particles and usually a manufacturer's

issue. This means the GTA cladding process does not contribute in increasing porosity and the porosity depends on the WC quality delivered.

The EDX analysis on the cladding layer microsection was in the layer height orientation. The WC measurement is a result of the W content in the matrix. It was not possible to divide the WC measurement in the SEM into useful and peak areas.

The averages of the WC measurements are illustrated in figure 7-13.
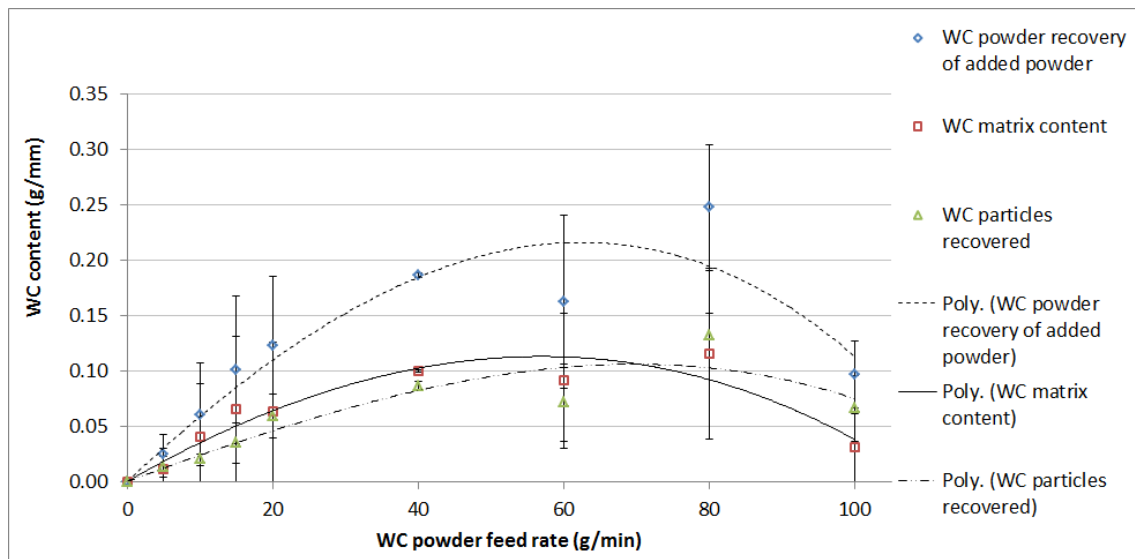
Figure 7-13: WC content measured in the microsections over optical and chemical analysis

As seen in figure 7-13, the WC content initially rises with increasing WC powder feed rate and the weld bead gets saturated when reaching 40 g/min powder feed rate. No further increase is seen. At 100 g/min the WC content in the weld bead decreases because of the agglomerates on the top of the weld bead building up a skin layer hindering further WC particles enter the weld pool. This trend is shown equally for the WC matrix as well as for the WC particle retrieval. Therefore, the total amount of added particles to the weld bead follows the trend. The total amount of added WC particles is about 50/50 of retained particles and reparticipated WC content in the matrix. The trend for WC powder retrieval in figure 7-13 is similar to the trend for the single beads as shown in figure 6-19. Only at PFR = 100 g/min is a difference as the agglomeration did

not happen in the single beads. The overlap trials tend to agglomeration as the existing bead on the side supports access powder staying on the weld bead top. Single bead exploration to find the saturation point is possible, which is simplifying future process developments.

The total WC powder retrieval sometimes demonstrates values above the WC deposition rate. Technically this cannot be possible. The following reasons can cause these measurements:

- a microsection is only a display of a very short moment;
- the EDX analysis gives only some points of the WC distribution;
- the mass increase can be too small with low feeding rates and small cladding areas;
- A very significant issue could be that WC in the solution does not only build WC again. In fact it builds up different phases of WC, W_xC and Fe_yW_xC, as well as phases with the alloying elements.

Further analysis is necessary to be sure how much WC is in solution. However, as other analysis methods, such as EBSD, are more time-consuming, this was done on representative samples only. The analysis is shown in section 7.3.3.

7.4.2 Appearance of cracking in the layer (cross sectional)

Although cracking of surface clad layers with high hardness is not unusual [72], [126], in the aggressive atmosphere of wear and friction on a railway brake disc, it could cause severe damage [127], [128]. There are different types of cracking. Two common types in cladding layers are shown in figure 7-14.
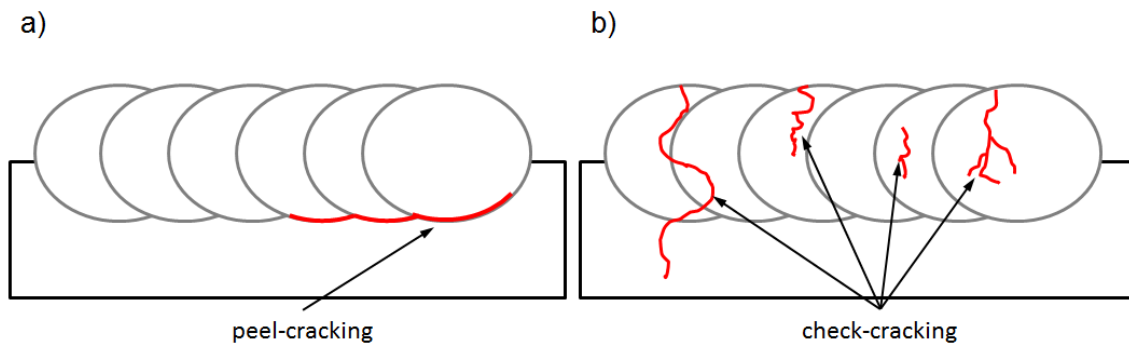
Figure 7-14: Sketch of two common found types of cracking in cladding layers; a) peel-cracking is along the boundary of the layer and the HAZ; b) check-cracking, cracks are vertically in the layer, sometimes into the HAZ

Peel-cracking (see figure 7-14 a)) is commonly known in pure ceramic layers bond on metal. It initiates the risk of chips of the clad peeling off the metal surface during abrasive wear to the layer. Less harmful check-cracking is commonly found to stretch macroscopic in a 90° angle to the cladding direction over the cladding layer. It is usually recognised by vertical cracks in the microsection (see figure 7-14 b)). Check-cracking was the only cracking found in the samples of this thesis.

The cracks initiated during cladding could grow into the bulk material during service due to fatigue. Substantial dynamometer testing would be necessary to characterise the behaviour of cracks from check-cracking. As mentioned in chapter 6, an important indicator is if the crack is already in the heat affected zone (HAZ, see figure 7-14 b)). In figure 7-15, the cracks noticed in the microsection are documented. All cracks seen in the microsections were counted and the three longest cracks were measured for their length. The longest crack is shown in figure 7-15.
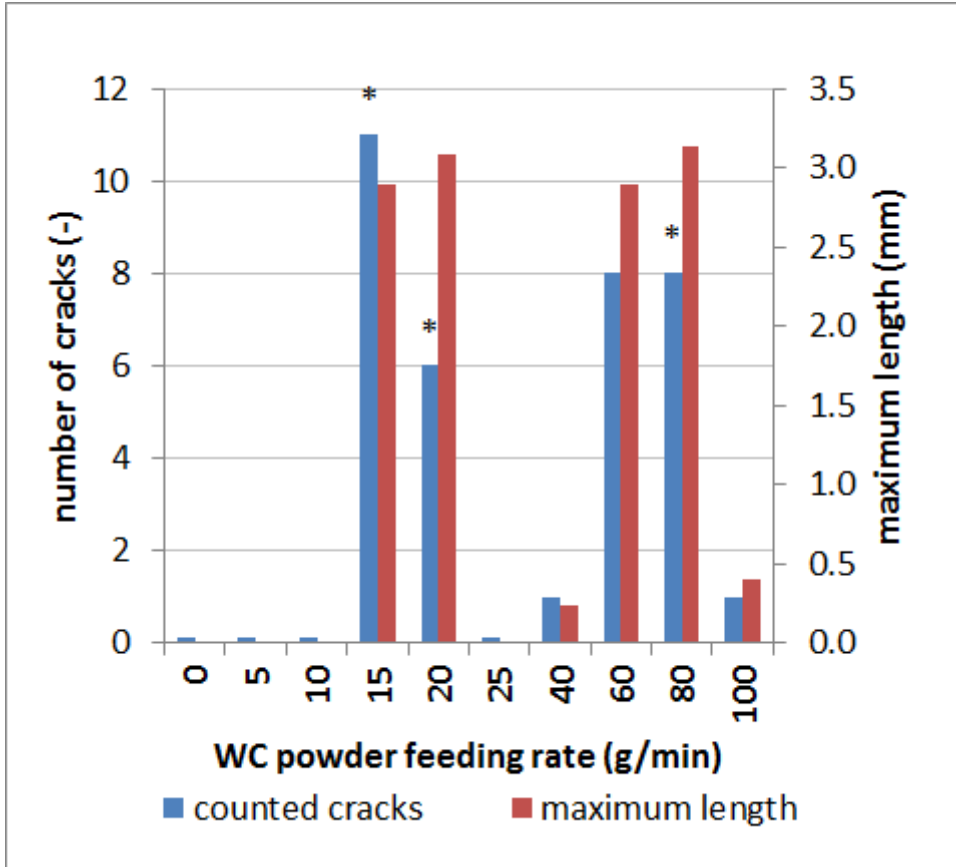
Figure 7-15: Appearance of cracking in the microsection; "*" Minimum of one crack penetrates the HAZ; Number of cracks at "0.1": No cracks found in sample.

The highest crack lengths measured in the microsections were for PFR = 15 g/min, 20 g/min, 60 g/min and 80 g/min. As seen in figure 7-15, most of them penetrated into the HAZ. Only one crack was seen in the samples clad with PFR = 40 g/min and 100 g/min. All other samples were crack free. This result agrees with the observation of the surface cracking in section 7.2 of chapter 7.

7.5 Hardness test of the WC MMC layer

For a better understanding of the effect of WC powder in steel cladding layers, hardness tests were conducted, as an improvement in hardness would potentially lead to higher wear resistance of the surface. Knowledge of the dissolved WC in the matrix of the MMC produces the important decision to split the hardness testing into the following three tests:

- Effect of the WC powder feeding rate increase of the matrix hardness,
- Hardness of the WC particles in the clad layer, and
- Hardness of the MMC matrix.

The hardness will always be compared to the unused original railway brake disc steel. Further details about the machine used are in Appendix I and the tolerance measurement is in section I.1.

7.5.1 Effect of WC powder increase on the matrix hardness

Two samples of each WC powder feeding rate were tested. On each sample two indentation tracks were executed – transverse and downwards – in the hardness test; the former was done in the middle of the cladding layer (lh_{max}) and the latter from the layer surface into the bulk material (see sketch figure 7-16).
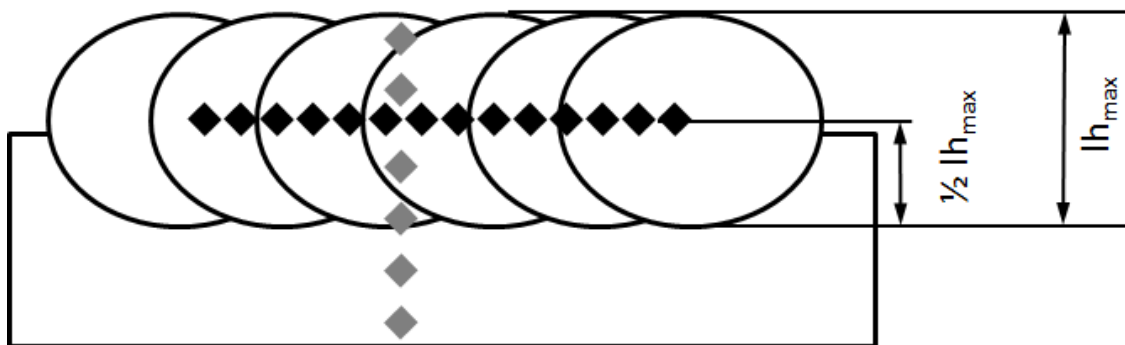
Figure 7-16: Sketch of the position of the hardness indentations on the samples, grey: downwards hardness testing, black: transverse hardness testing; centre line of the transverse indentations was half of the maximum layer height (lh_{max})

As the microsection of the layer only gives the option for a microhardness test, a hardness test according to Vickers with 0.2 kg normal load was chosen. The results are illustrated in figure 7-17. It can be seen that the Vickers hardness of the brake disc material is already in the range between 370HV0.2 and 401HV0.2. These values confirm the converted values of the supplier with 330 - 375 HBW 10/3000 from section 4.2.1 in chapter 4. This is very high for steel.
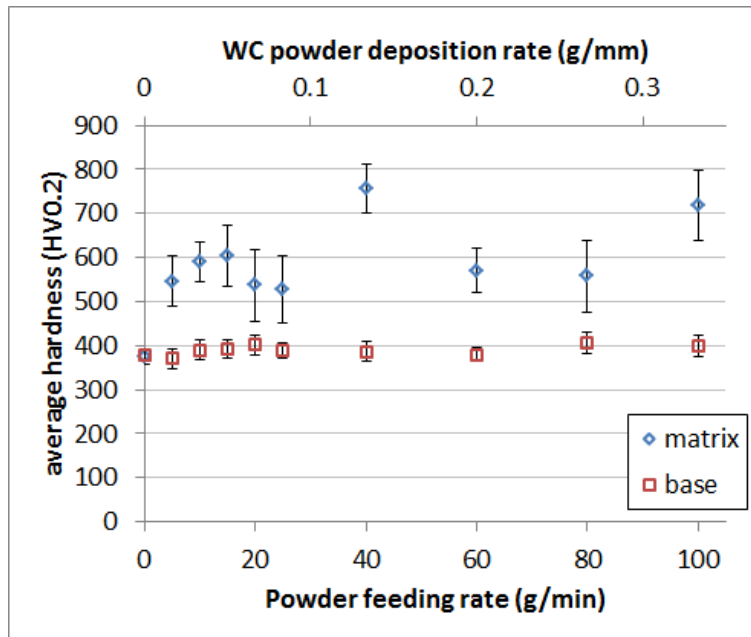
Figure 7-17: Average results of 25 hardness indents in the matrix material and the base material

Furthermore, the hardness value of 374HV0.2, without any powder feeding (PFR = 0 g/min), is almost the same as the base material. The matrix phase has values between 528HV0.2 and 604HV0.2 and comes into the area of hardened steel. The difference of 76HV0.2 is a very small range compared to the increase in WC powder feeding. It was seen that all hardness values stay the same once WC powder is in use. Two outliers, with 757HV0.2 and 719HV0.2, can be seen at PFR = 40 g/min and PFR = 100 g/min, respectively. These outliers could come from a high number (above ¾ of the total) of indentations close to or above particles or in WC enriched areas.

7.5.2 Hardness of the particles after cladding

Heat input on the WC particles could lead to a change in hardness of the WC particles found. Therefore, some selected WC particles have been tested according to Vickers in different microsections. Additionally, the nano-hardness of WC particles in a single bead trial with PFR = 5 g/min was established.
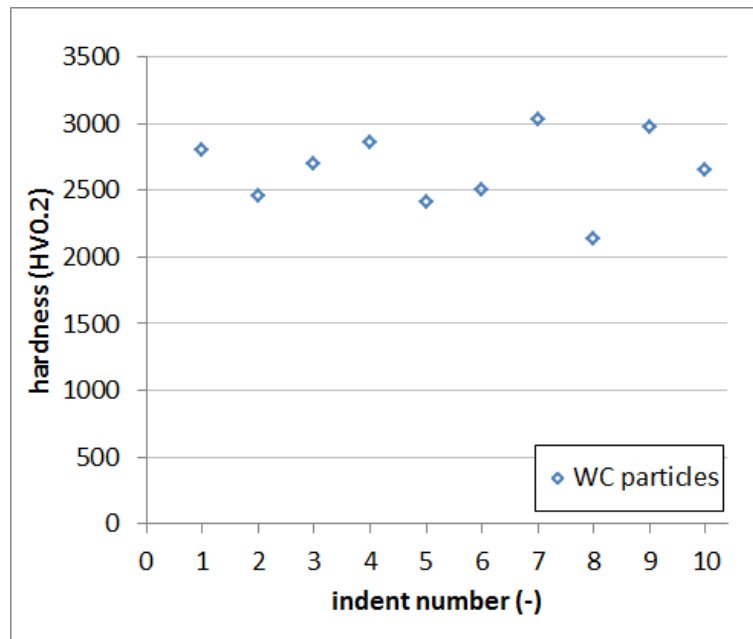
Figure 7-18: Hardness test according to Vickers of selected WC particles in the matrix material after cladding

The results in figure 7-18 did not confirm the hardness values stated by the supplier; with 2500HV0.3 – 3500HV0.3 (according to figure I-13 in the appendix), as values on selected WC particles were measured between 2137HV0.2 and 3036HV0.2. This could come from the dissociation and heat effect of the GTA cladding; however, it could also come from hollow particles. It is more likely that the lower hardness comes from the influence of the welding heat on the WC particles. This is probably due to the observed diffusion of Ni into the particles as seen in table 7-2 of section 7.3.2. A second hardness test with the nano-indenter confirms the high hardness of the WC particles.
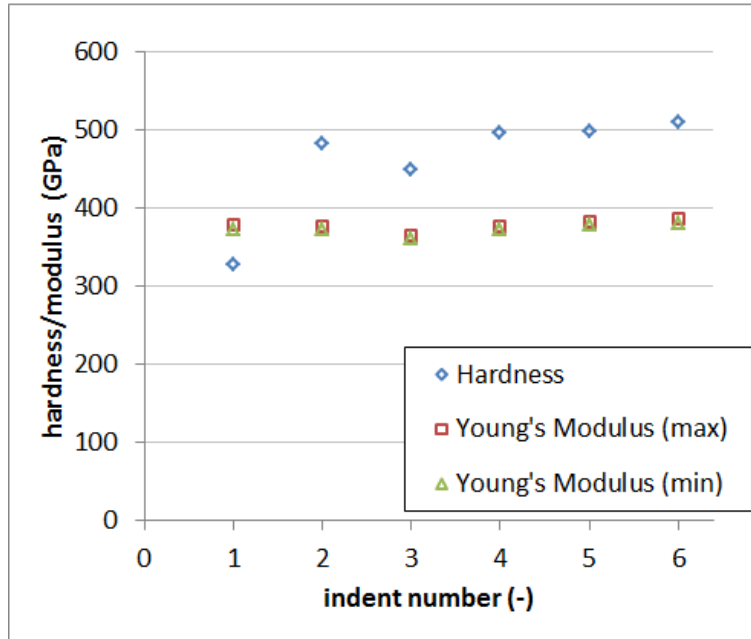
Figure 7-19: Nano-hardness test of selected WC particles in the matrix material after cladding including Young's Modulus

In figure 7-19, it can be seen that the hardness of four particles was between 448 GPa and 509 GPa. One particle can be seen as an outlier with 328 GPa. Notably, the Young´s modulus is within a range of 360 GPa to 385 GPa. These values are approximately half of the values found in the literature, as seen in table 4-6 (with 620 GPa – 720 GPa) [92], [93]. Therefore, an evident influence of the GTAW process on the mechanical properties of the WC particles can be seen. The Young's modulus could have changed because of the diffusion of Fe and Ni into the WC particles and Ti and Ta out of them (see table 7-2 and following).

7.5.3 Vertical hardness scanning (through-thickness direction) of the matrix

A representative sample of the WC cladding layer microsection is displayed to present the trend of the Vickers hardness within the layer, HAZ and bulk material. One microsection of the sample with PFR = 5 g/min in transverse cross section was chosen and the development of the hardness variation is shown in figure 7-20 a). The cladding layer (between 0 mm to 2 mm) increases

in hardness from 461HV0.2 to 743HV0.2 towards the layer surface. A steady hardness between 387HV0.2 and 408HV0.2 in the HAZ (between -2 mm and 0 mm) provides evidence of less microstructure changes in the HAZ. Thus the rest of the bulk material follows the HAZ with values between 321HV0.2 and 390HV0.2 (between -5.5 mm to -2 mm).
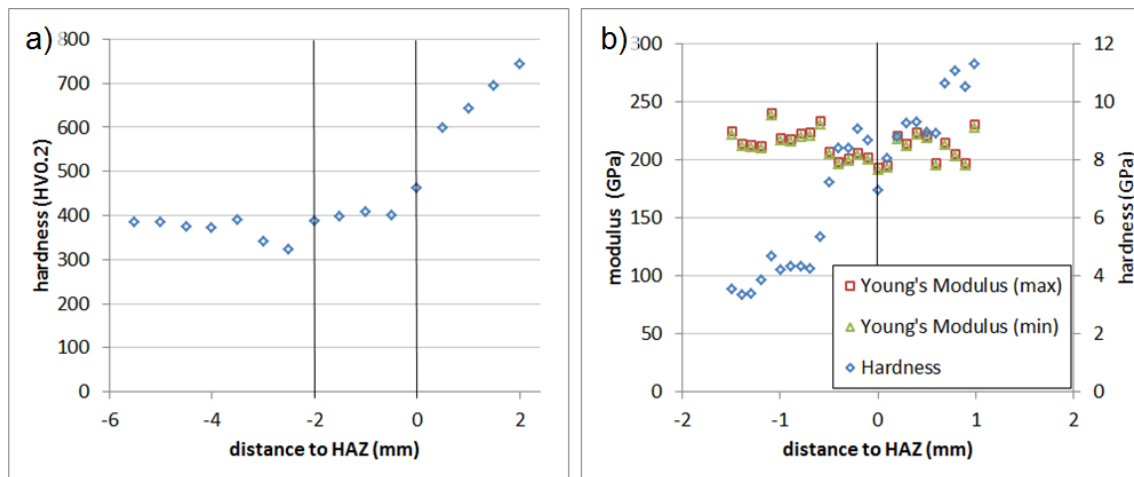
Figure 7-20: Hardness test of the matrix in a PFR = 5 g/min sample; a) cladding layer tested according to Vickers, 0 mm to 2 mm is the layer, -2 mm to 0 mm is the HAZ and -5.5 mm to -2 mm is the bulk material; b) nano-hardness test of a single bead sample, 0 mm to 0.99 mm is the clad; -2 mm to 0 mm is the HAZ

Compared to hardness effects in welds in general, the HAZ showed no significant difference to the brake disc material. A further hardness test with the nano-indenter on a single bead trial demonstrated a change within the HAZ. As shown in figure 7-20 b), the hardness increases in the HAZ from 3.32 GPa to 9.06 GPa (between -1.49 mm to -0.10 mm). The increase in nano-hardness is between -0.49 mm and 0 mm and, therefore, not in the resolution of the microhardness test according to Vickers. Unfortunately, the bulk material has not been tested with the nano-indenter. A further increase in nano-hardness is seen in the matrix material from 6.94 GPa to 11.29 GPa (between 0 mm to 0.99 mm). Just less than one millimetre of the layer thickness was tested by nano-indentation. However, the matrix material in the nano-hardness test follows the trend of the Vickers hardness test. Additionally, the Young´s modulus of the matrix material and the HAZ show values between 190 GPa and 240 GPa.

156

These are normal values for steel which has an approximate value of 210 GPa according to the literature [94].

7.6 Summary

For the post-processing usage, as an abrasive layer, is only the useful area of interest. The peak area gets cut off on one side and is a mixture of HAZ and clad on the other side. This reason lead to the decision to concentrate on the useful area in the summary.

Considerably flat cladding layers were achieved with 50 % overlap weld beads. The increase in WC powder feeding showed surface cracking in the low feeding rate of PFR = 15 g/min. This is due to high longitudinal stresses as the crack direction is perpendicular to the welding direction. The overlap layer surface increased in waviness with increasing WC powder feeding; WC reinforcement increases with a growing powder feeding rate until 80 g/min in the useful area. The particle inclusion drops with PFR = 100 g/min down to 3.5 % WC reinforcement. Low porosity was found in the WC cladding layers made. When the WC powder feeding rate grows, it increases the peak layer height. However, no benefit in the useful layer height is seen. It was revealed that the dissolved WC fraction in the matrix is approximately the same as the WC particle fraction in the cladding layer, which shows that the dissolved WC in the matrix has a significant effect on the WC powder pick-up. WC particles show an embedding with a gradual transition to the matrix. The dissolution of WC from the powder and reprecipitation in the matrix is mainly created by Fe_6W_6C. This phase is also found as the main structure of the tungsten phases in the matrix. Once there, it refines the grains and builds a network along the grain boundaries. The matrix becomes medium hard and its Vickers hardness is within 527HV0.2 and 757HV0.2 between the hardness of the steel base (average of 374HV0.2) and the WC particles (measured between 2137HV0.2 and 3036HV0.2). The matrix hardness does not change significantly with the WC powder feeding alternation. From further analysis, it is seen that the hardness of the cladding layer increases from the base material to the surface.

This was also shown in a microhardness test according to Vickers and in extracts from a nano-hardness test. The Young´s Modulus of the matrix is comparable with the modulus from mild steel. Some WC particles are softer than delivered, when measured in the cladding layer which might be a result of the heat input from the GTAW process. Nevertheless, the hardness is still respectable for wear resistance surfaces. A nano-hardness test has shown WC particle results between 448 GPa and 509 GPa hardness and a Young´s modulus in the range of 360 GPa to 385 GPa. These are enormously high values which give a suitable foundation for the wear test.

7.7 Conclusions

The objectives set for an investigation into a WC ceramic MMC layer in overlap in this chapter leads to the following conclusions:

- WC reinforcements were possible to enrich from 1.1 % to 17.5 % WC reinforcement in the useful layer area by only changing the WC powder feeding rate. The amount of WC powder picked up is significantly higher than the amount of WC reinforcement in particles due to the reprecipitation of WC in the matrix.

- The WC reinforced layer had a useful layer height of approximately 1.2 mm. It was found that the useful layer height remained almost constant with increasing WC powder feed rate. Instead WC powder increase resulted in higher waviness.

- WC of the particles gets into solution in the matrix and reprecipitates in Fe_6W_6C along the grain boundaries. The microstructure of the surface clad confirmed a metallurgical bond of the WC particles to the matrix with a boundary consisting of Fe_6W_6C. The matrix shows a grit of Fe_6W_6C and steel grains. The ratio of remaining austenite to ferrite increases substantially with enhanced WC powder feeding rate. This might give an additional strengthening effect to the matrix by forming martensite during deformation. Hardness values of the matrix reveal a growth from about 400HV0.2 (base material) to about 570HV0.2 with low WC powder

feeding. An increase in WC powder feeding rate had no influence on this upsurge. The matrix hardness intensifies from the boundary of the HAZ through the cladding layer to the surface. Despite the alloying of WC into the matrix, the Young´s Modulus stayed on the same level as for mild steel. The WC particles softened during the GTAW cladding process slightly.

8 Comparison of WC MMC surface clads in the friction behaviour of a Pin-on-Disc wear test

Railway brake discs are large and testing them on a full size dynamometer test rig takes a lot of time and resources. To optimise the GTA cladding process of WC ceramic MMC described in chapter 7, a small scale tribometer test is economical. For this a Pin-on-Disc (POD) test has been chosen. The fact that it tests only over a relatively short time (Pin-on-Disc test: 4 - 6 h; Dynamometer test: approximately 1008 h) and with constant sliding speed, makes the results of the friction coefficient (μ) quickly accessible. However, the wear loss is very hard to establish after such a short time. The following objectives are set for this chapter:

- Spiral clads with the functional graded structure of WC ceramic and steel are developed in POD sample size.
- The functional graded layer reaches similar friction coefficients (μ) than the brake disc steel.

The results of the μ for the WC MMC should stay in the same range as the existing brake discs, when paired with a common wear pad material. As a common wear pad material, the Ferodo 3216F Pad from Federal Mogul Friction Products Ltd. was chosen to be customised into a wear pin for the POD test machine. It is to remark that the geometry of the geometry of the disc and the POD specimen vary significantly from brake discs and pads, which could influence the outcome of this test.
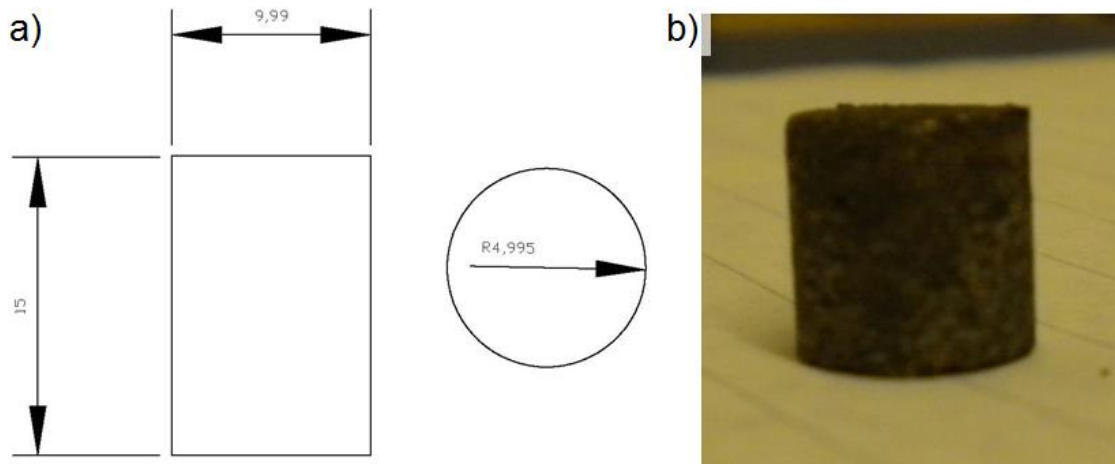
Figure 8-1: Wear pin of the Pin-on-Disc test; a) technical drawing of the pin (9.99 mm diameter, 15 mm long); b) Close up photo of one customised pin made of Ferodo 3216F pad material

The customised layout of the pin is seen in figure 8-1 a) with a pin ready for use in figure 8-1 b). Its mechanical properties are given in figure_apx I-18. The pin dimensions have been chosen with 9.99 mm diameter and a length of 15 mm, resulting in a wear area of 78.383 mm^2.

8.1 Disc geometry and disc welding and grinding process

Pin-on-Disc wear test discs have been produced with 15CDV6 brake disc material. The material properties of the 15CDV6 are very similar to those properties of the G-22 NiMoCr 5 6 (used in chapters 6 and 7), which can be seen in table 4-5 of chapter 4. These discs were made in the size of 120 mm diameter and 12 mm thickness. A technical drawing and a sample disc are shown in figure 8-2 a) and b), respectively.
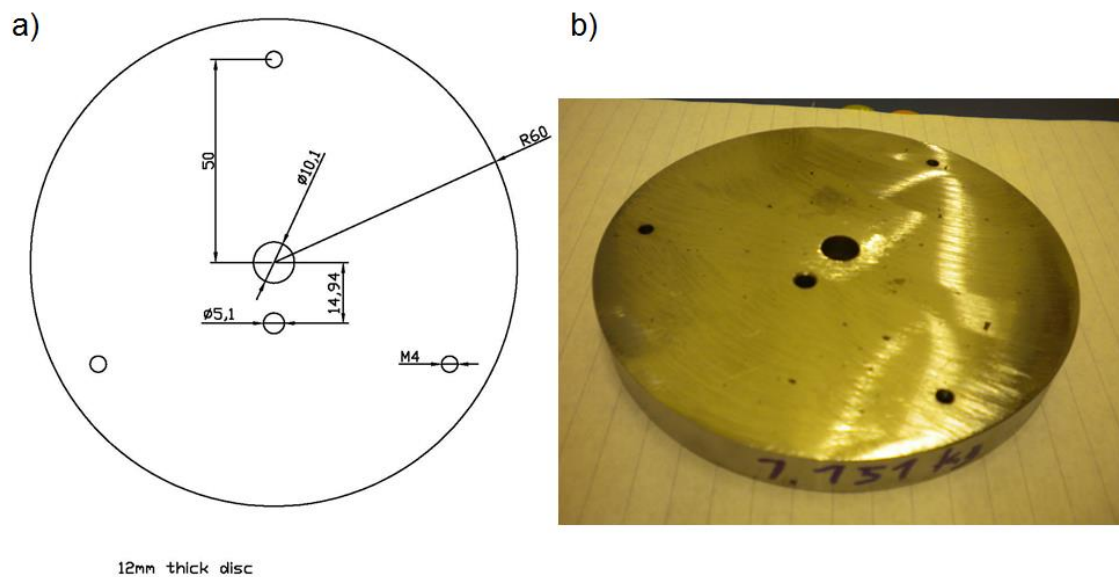
Figure 8-2: Disc for the Pin-on-Disc test; a) technical drawing of the disc (120 mm diameter; 12 mm thick; ⌀ 10.1 mm centering hole; ⌀ 5.1 mm drive hole; 3 x M4 grub screw levelling); b) specimen before welding

The WC cladding trials were performed using two different approaches:

- The first approach is a spiral welding with the WC reinforcement on a square plate with measurements of 140 mm x 140 mm x 12 mm. Its condition after welding can be seen in figure 8-3 a). The cladding followed a machining and grinding process to a finished disc.

- The second approach was an already machined disc which had four holders tack welded on the side. This disc was then clad with a spiral clad of the functional clad layer. The surface of the clad had to be diamond ground later on. The second approach is shown in figure 8-3 b) after cladding. The tack welded holders were removed before testing.
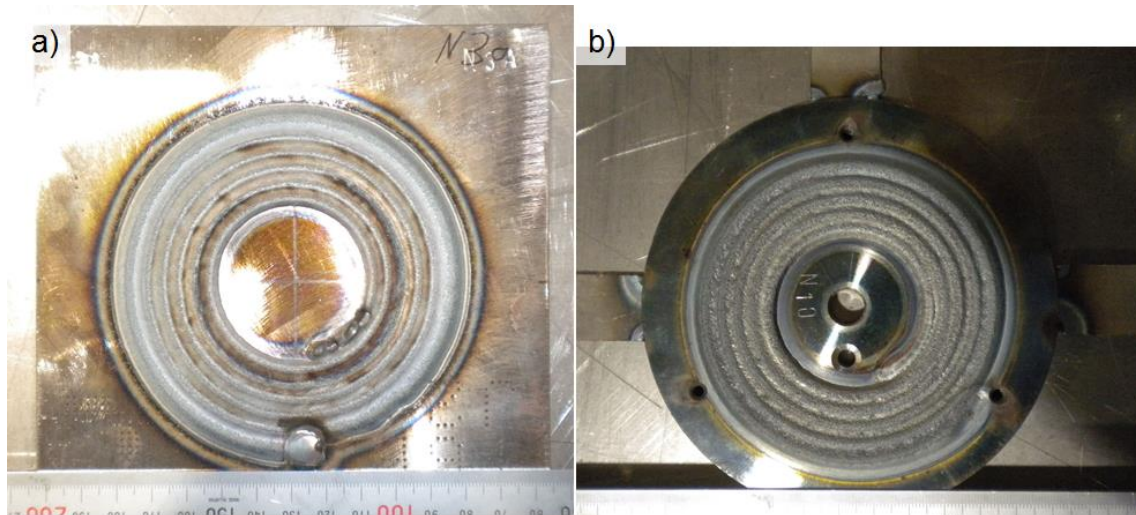
Figure 8-3: Two ways to produce the WC reinforced layer; a) Cladding before machining; b) Cladding on a machined sample

Both approaches were tested for distortion due to the high heat input in the relatively small discs. However, after preparing specimens in both ways there was no significant difference in flatness found. The detailed welding and WC cladding set up is shown in figure 8-4. It can be seen that the GTA welding torch was set-up in the middle point prior to welding. Powder feeder nozzle and wire feeder nozzle were mounted on supports as shown in figure 8-4. The ceramic tube has been used as the powder feeder nozzle. The clamping of the base material was on all four corners in the case of the plate, but on tack welded holders of the disc. A Cu backing of 10 mm thickness has been used to extract heat during cladding. An eventual overheating of the plate, resulting in a burn through, has been limited. This gives the base material closer heat sink behaviour towards the much greater brake disc. Additionally, the GTA cladding trials were welded from the inside to the outside to direct the heat into the periphery of the small steel plates.
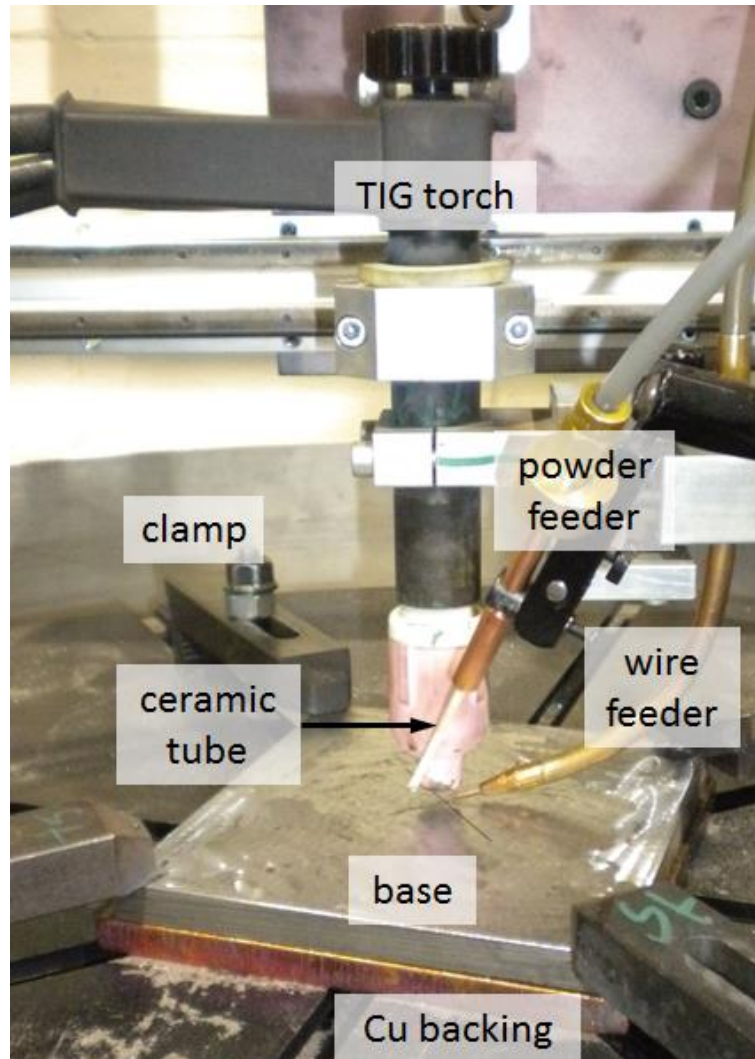
Figure 8-4: Spiral GTA cladding for POD test specimen; TIG torch for the welding arc; four clamps to maintain the sample position; powder feeder with ceramic feeding nozzle for the WC powder; wire feeder nozzle for the matrix material supply; base as an approximately 140 mm x 140 mm x 12 mm steel plate; Cu backing (10 mm thick) to obtain similar cooling to a brake disc

The welding process followed a continuous spiral trajectory. To keep a steady linear travel speed, the TrioMotion control was programmed for changing the rotational speed due to the GTAW torch position. The process parameters for the GTA cladding with WC ceramic particles are given in table 8-1. The angles of the feeder nozzle and the distances a, b, c, d are shown according to figure 6-1.

Table 8-1: Cladding parameters set for the Pin-on-Disc specimen

					wire feeder nozzle			
Current	travel speed	wire feed speed	a	b	c	d	α	β
A	m/min	m/min	mm	mm	mm	mm	°	°
216	0.35	2.46	3.5	0.2	1.4	13.8	180	20
		powder feeder			powder feeder nozzle			
		Ar pressure	Ar flow rate	Ar flow rate	c	d	α	β
		bar	NLPM	l/min	mm	mm	°	°
		3	5	5	3	9	112	50

It was necessary to adjust the powder feeding angles because of the sharp radius of curvature at the small radii of the POD discs. G4Si1 wire was used as a matrix material. The following WC powder feeding steps have been chosen for POD testing:

- 0 g/min WC feeding rate
- 5 g/min WC feeding rate
- 10 g/min WC feeding rate
- 15 g/min WC feeding rate
- 20 g/min WC feeding rate
- 25 g/min WC feeding rate

A thermocouple was set up in the centre of the samples welded in plate form for further investigations into the heat distribution behaviour during cladding.
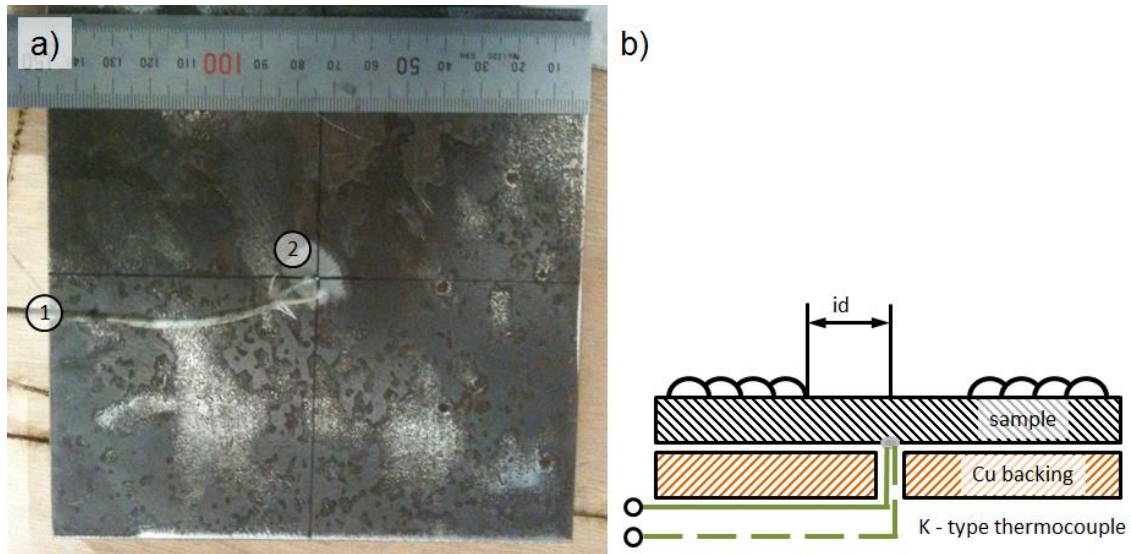
Figure 8-5: Temperature profile monitoring arrangement during cladding of the base material; a) back of the base plate, 1: thermocouple, 2: thermocouple welding point in the centre of the sample; b) schematic assemble of the sample to the set up seen in figure 8-4, id: distance between the centre of the sample and the first weld bead

Temperature profile monitoring was carried out with a thermocouple fixed on the back of the rectangular plate's clad with a spiral, as shown in figure 8-5 a). The sample assemble on the WC cladding set up is seen in figure 8-5 b). The cross sectional view shows the thermocouple attached to the sample plate by a tack weld. It has been put through a hole in the Cu backing, which is seen in figure 8-4. The distance of the centre of the plate to the inner clad (id) of the spiral was between id = 38.9 mm and id = 42.1 mm, depending on the measurement at the beginning of the spiral weld or after one circumference.
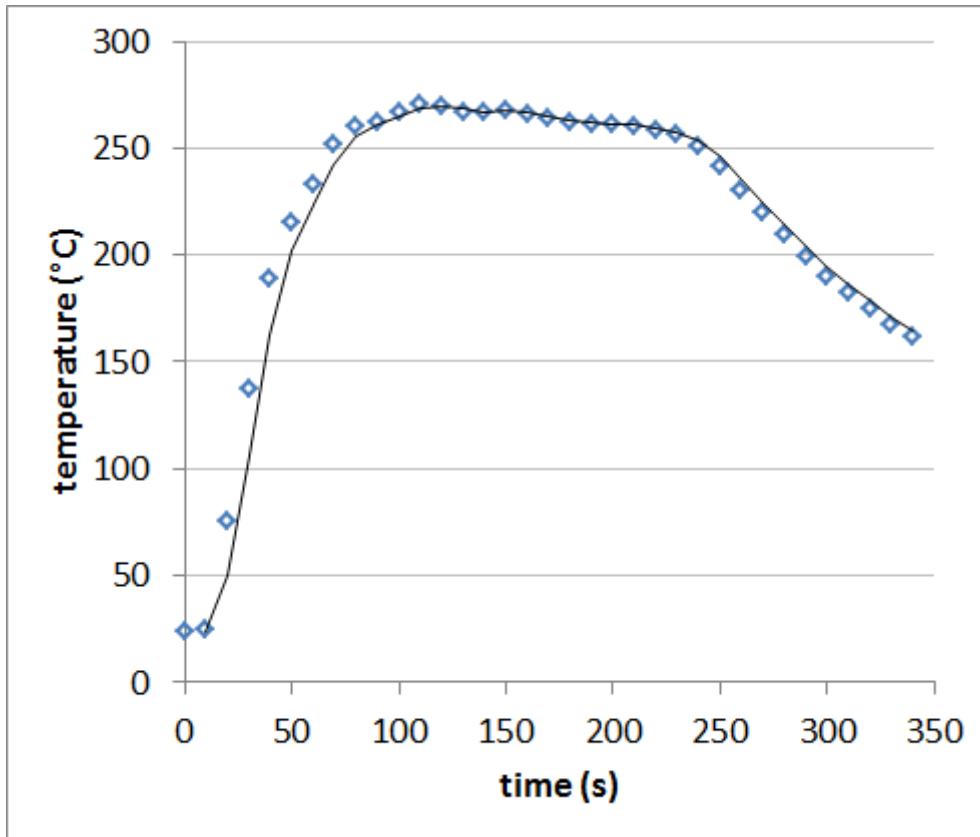
Figure 8-6: typical temperature-time plot of a POD cladding cycle

The position in the middle of the plate showed a good reading and a typical temperature curve from a welding process can be seen in figure 8-6. The peak temperatures recorded have been between 234 °C and 313 °C, e.g. figure 8-6 shows a maximum at 271 °C. These temperature curves give a scope for calibrating finite element (FE) modelling of the cladding process. In chapter 9 these temperatures will be compared with a full railway disc cladding bead to understand the heat sink difference. GTA cladding trials have also been performed for comparison of the microstructure. Welding procedures with the same process parameters are used to obtain a similar WC reinforcement to the POD specimen. An overview of the microsection of the spiral weld can be seen in figure 8-7.

Figure 8-7: Control microsections of specimen welds like those of the POD wear test specimen; a) PFR = 0 g/min; b) PFR = 5 g/min; c) PFR = 10 g/min; d) PFR = 15 g/min; e) PFR = 20 g/min, cracks have been found; f) PFR = 25 g/min, cracks have been found; i: inner side of the spiral, o: outer side of the spiral

Microsections of the different powder feeding rates show weld beads with low waviness. Figure 8-7 shows the microsections in unetched conditions. The inner side of the spiral is indicated with an ´i´ and the outer side with an ´o´. Cracks were seen in higher magnifications of the microsections made with the WC powder feed rates 20 g/min and 25 g/min. It can be seen that the amount of WC reinforcement increases in all welds from the inner to the outer side of the spiral. The increased WC feeding rate is reflected in the higher WC powder incorporation as well (Figure 8-7 from a) to f)). The microsection was divided

into five areas of the same length in order to measure the WC reinforcement. The results of these measurements are shown in figure 8-8.
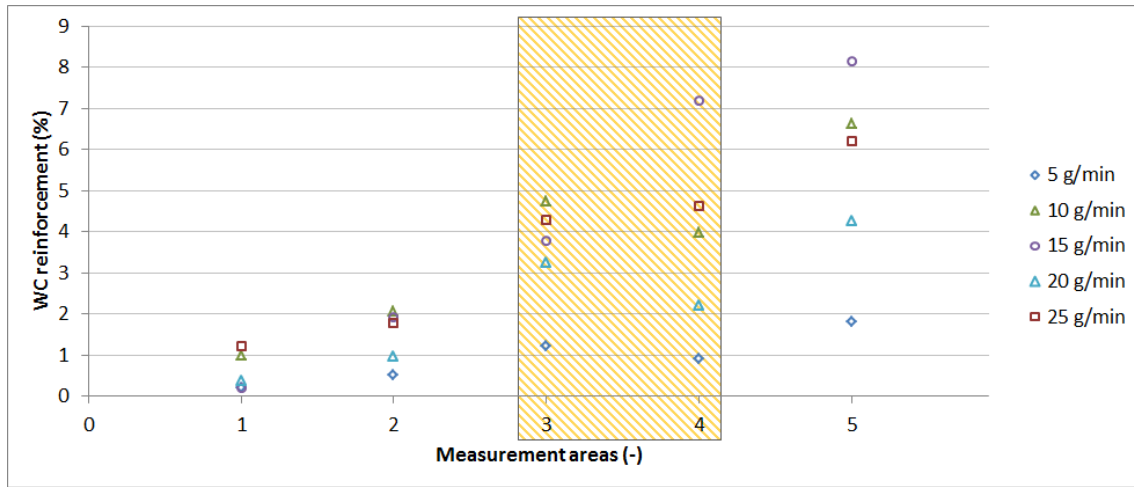
Figure 8-8: WC particle reinforcement measured on the microsection shown in figure 8-7 in five equal, long area sections of the microsection. 1: inner side of the spiral, 5: outer side of the spiral; yellow area: indicates the area where the pin is wearing

Figure 8-8 shows how the WC reinforcement rises with the WC powder feeding rate. The WC retrieval improves with increasing PFR up to PFR = 10 g/min. The GTA clads with feeding rates between PFR = 15 g/min and 25 g/min show a decrease in WC reinforcement in all areas except area 1. WC reinforcement is seen significantly different from the inner side to the outer side of the spiral. This effect comes from the heating effect of the weld beads in the spiral. The inner round of the spiral was made on a cold base material. The following rounds were laid down on a continuously heating up base material. The weld bead stayed open longer before it solidified and more powder can enter the weld pool.

The distance to the POD specimen middle was measured to identify the important area for the wear test. It emerged that areas 3 and 4 are in the region of the pin in the POD. These two areas were hatched in yellow in figure 8-8. These WC reinforcement values will be used in the Pin-on-Disc testing.

8.2 Friction and wear test set-up

The friction and wear resistance was tested on the Pin-on-Disc wear machine seen in figure 8-9. The machine gives a constantly normal force F_N with a pin on a disc, whereby the pin is made of brake pad material and the disc of the test specimen.
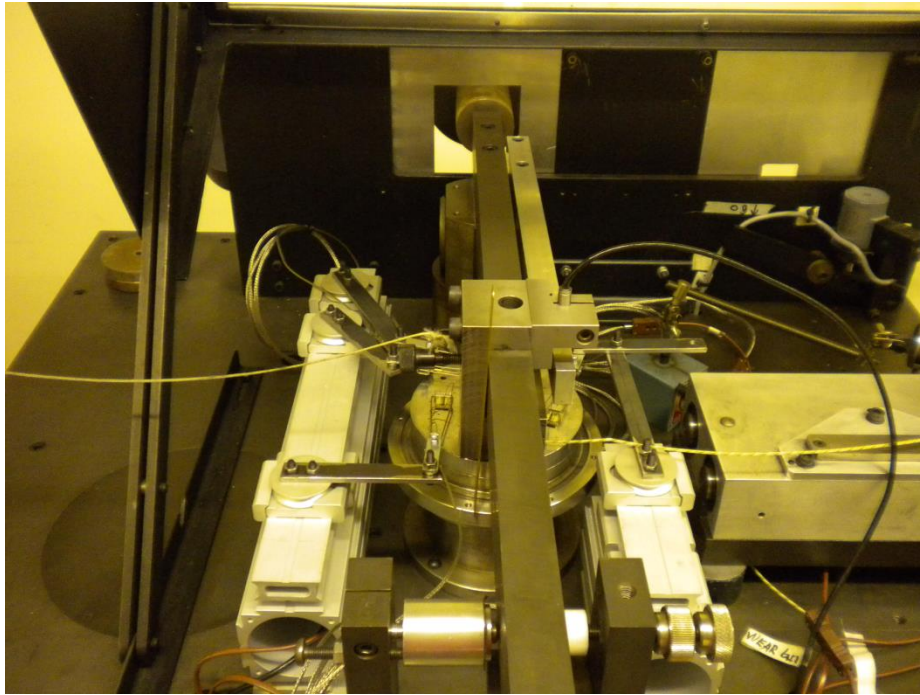
Figure 8-9: Pin-on-Disc wear test machine, top view

To measure friction, a constant rotation velocity (v_{rot}) on the disc is used. As a reaction to the velocity, a friction force (F_T) is caused in the lever holding the pin. The measured torque force F_T, disc temperature (T) and total wear distance gives the values to calculate the friction coefficient (μ), the power (P) needed to overcome frictional load, the heat flux (Φ_p) generated, rate of heating (R_h) and rate of cooling (R_c). The POD machine was commissioned and calibrated from Lockyer [55], [56]. A schematic drawing of the pivot arm in figure 8-10 a) shows the important points of influence in the wear test. The disc is in the middle under the pivot arm, with the pin holder on the right of the disc. A reference beam with a wear transducer can record extreme wear behaviours. Its function is explained in the work of Lockyer and Angelinas [55], [56], [121]. However, the wear transducer was not used for this thesis. A counterweight on

171

the very left of the pivot arm keeps the arm in balance on the pivot joint. It also gives the possibility of having no weight force from the pivot arm added to the normal load. The normal load is set up by a dead weight on a free hanging rope on the very right of the pivot arm.
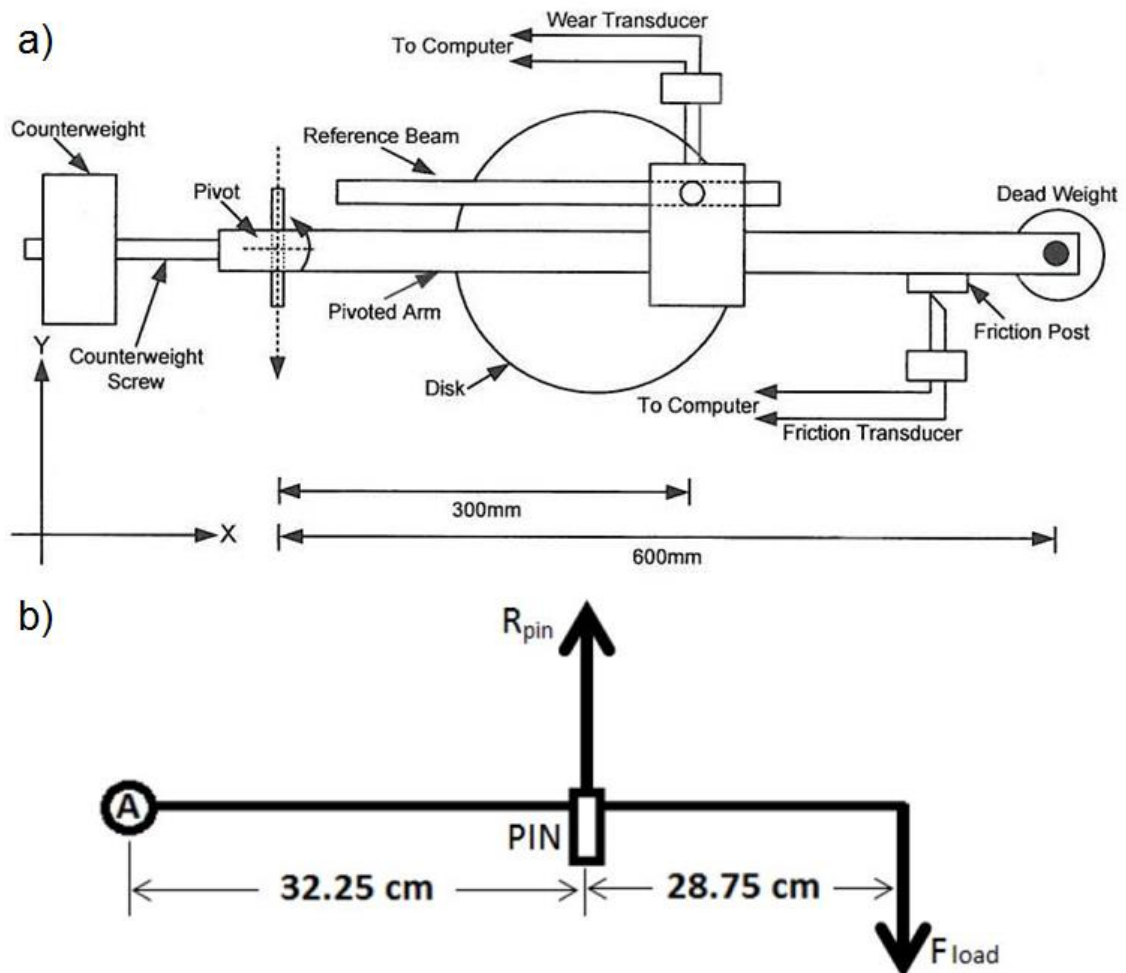
Figure 8-10: Drawing of the pivoted arm; a) Sketch with details by Lockyer [55], [56]; **b) Effect of the lever sketched by Angelinas** [121]

A friction transducer in the form of a load cell was fixed to the friction post. It was situated between the pin holder and the dead weight. The pivot arm presses against the friction transducer when the disc rotates. For calculation of the friction coefficient according to equation (3-5), the calculation of the leverage from the pin to the friction transducer is important. The effect of the lever to the measured force is sketched in figure 8-10 b) by Angelinas [121].

Additionally, rubbing thermocouples were applied to the disc. Four K-type thermocouples were employed to measure the temperature of the disc in the friction area. Calibration of the thermocouples took place in ice-water with a reference thermocouple. The water was kept at a constant temperature of 0 °C. Correction of the thermocouples thermo-voltage signal could have been done using the National Instruments software, if necessary. The load cell was calibrated over dead weights mounted on the pin holder with a rope. The nylon rope was transferred from the pin holder over a deflexion roller to the side to give this set up enough space, as shown in figure 8-11.
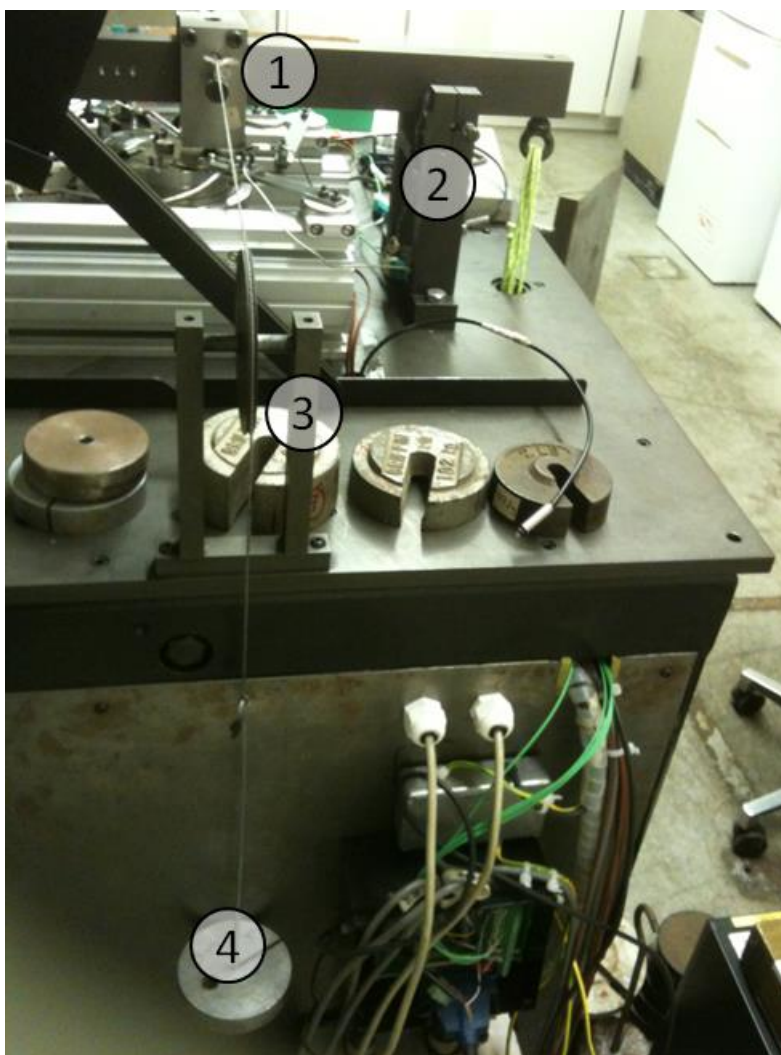
Figure 8-11: Load cell calibration, 1: Pivoted arm with pin holder, 2: Load cell in friction post, 3: Deflexion roller, 4: Dead weight (load mass)

The dead weight generates a signal in the friction cell which replicates an equal friction force (F_T). This signal is used to generate a calibration curve in the National Instruments software. Significant impact on the stability of the friction force is the disc flatness. The disc has to be perpendicular to the pin at all times of the rotation to obtain a smooth signal. Lockyer was investigating the impact of an inclined mounted disc [55], [56]. Part of his findings can be seen in figure 8-12.
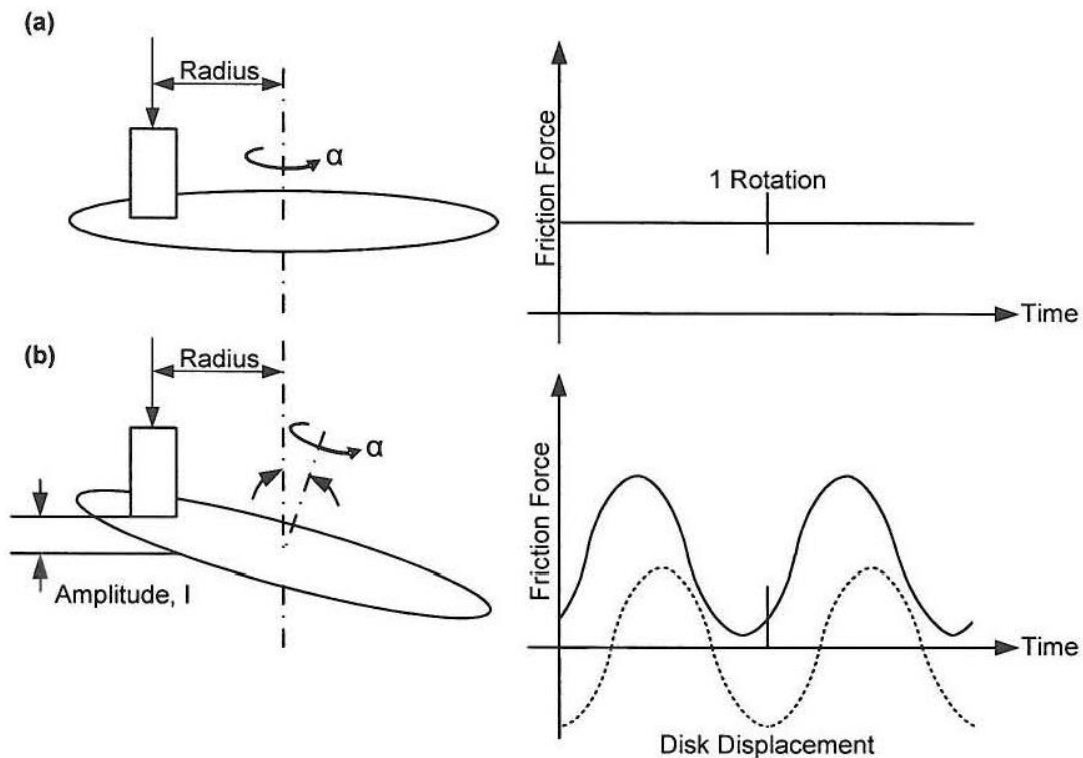
Figure 8-12: Effect of inclination of the disc on the friction results; a) perfect orthogonal rotation; b) inclined disc rotation [55], [56]

Figure 8-12 makes it clear that a slight incline of the disc causes a very noisy friction force reading. Thus the friction coefficient (μ) would result in a signal with too much variation. The disc specimen is aligned to the fixture of the rig and can be shifted into a perpendicular position by three grub screws (see figure 8-2). This ensures mechanically a smooth friction force signal. Dynamic friction effects generated from the mechanism of wear, as described in chapter 3.7, could lead to a small variation of the signal.

174

8.3 Pin-on-Disc test temperature and friction results

POD wear tests were done with every clad disc described in section 8.1. Each disc had to undergo a series of wear tests. Parameters for the different wear tests were disc rotation speed, dead weight for the normal load and sliding test length. The series of wear tests and parameters were as follows:

Test number	rotation speed	weight	test length
1.	1000 rpm	3 kg	approx. 15000 m
2.	1000 rpm	6 kg	approx. 15000 m
3.	2000 rpm	3 kg	approx. 15000 m
4.	2000 rpm	6 kg	approx. 15000 m

After each test the discs were left to cool down on the rig. The heating and cooling curves were recorded for thermo mechanical modelling.
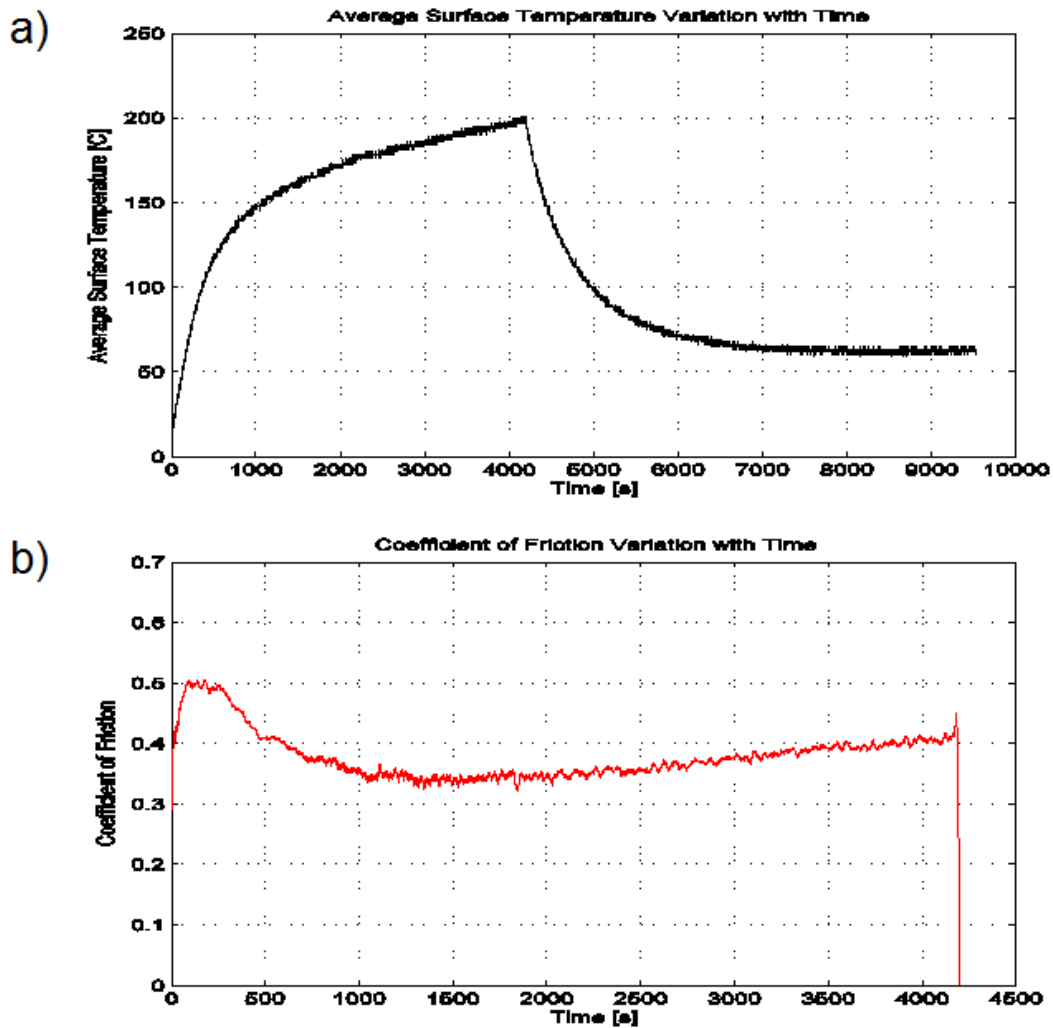
Figure 8-13: Raw data of Pin-on-Disc wear test for a test with a 15CDV6 disc (blank) with F_N = 112.5 N (6.062 kg on lever), normal pressure: 1.46 MPa, v_{rot}: 1000 rpm, total test distance: 15373 m; a) smoothened average temperature curve of the four K-Type thermocouples, cooling down with disc rotation; b) filtered signal of the coefficient of friction (μ)

Further analysis of the rate of heating (R_h) and the rate of cooling (R_c) is given in the work of Angelinas, who worked closely with the author on the POD wear tests [111]. An example of the recorded test data is displayed in figure 8-13. The test procedure and results for the POD test in figure 8-13 were the following:

- Deadweight: 6.062 kg
- Normal load on pin: 112.5 N

- Rotational speed setting: 1000 rpm
- Linear speed: 3.4 m/s (12.24 km/h)
- Nominal pressure: 1.46 MPa
- Average friction coefficient (μ): 0.38
- Average power: 156 kW
- Average heat flux: 71.89 kW/m^2
- Distance travelled: 15.373 km
- Wear area on disc: 0.002174 m^2
- Wear area on pin: 0.000077 m^2.

The temperature rose significantly in the first 500 s test time, as expected. In parallel, the μ is relatively high at approximately μ = 0.5. After 500 s the temperature increases steadily from about 120 °C to about 200 °C as shown in figure 8-13 a), over the rest of the test time. The μ drops after the run in, down to μ = 0.33 at about 1850 s and increases from there slowly to about μ = 0.41. This correlates up to 200°C to the graph previously shown as figure 3-11 from the literature found. The POD test was stopped after approximately 4200 s, which resulted in about 15 km travelling distance. The cooling down was recorded with the disc still rotating at 1000 rpm. A rapid cooling took place during the time between approximately 4200 s and 6000 s. However, it was difficult to cool the disc down to less than 60 °C with the rotation still in place. Cooling behaviours of different geometries of discs, e.g. with and without cooling vanes, are explained in Angelinas *et al.*'s work on the improvement of convective heat dissipation [119].

The five GTA clad discs with the WC reinforcement were tested. Blank steel discs of different grades and an aluminium disc were selected to compare the test results. The following discs were tested:

GTA clad discs

- 0 g/min WC feeding rate   0 % WC reinforcement
- 5 g/min WC feeding rate   0.92 % to 1.22 % WC reinforcement
- 10 g/min WC feeding rate   3.98 % to 4.74 % WC reinforcement

- 15 g/min WC feeding rate   3.77 % to 7.19 % WC reinforcement
- 20 g/min WC feeding rate   2.21 % to 3.24 % WC reinforcement
- 25 g/min WC feeding rate   4.28 % to 4.63 % WC reinforcement

<u>Blank discs</u>

- 15CDV6 brake disc steel
- G-22 NiMoCr 5 6 (called GS22) brake disc steel
- S355J2+N mild steel
- Aluminium alloy, 7xxx series (called Al)

An average of the measured friction coefficients for each test series was calculated and is displayed in figure 8-14. The aim of this test was to find out whether the friction coefficient of the GTA clads is the same or close to brake disc steel or not.   The pad material is confirmed as generating a friction coefficient between $\mu = 0.32$ and $\mu = 0.39$ according to the technical data sheet in figure_apx I-18 b) on all common steel brake discs. It is worth mentioning that the tests with Al had to be stopped after a very short time. Usually in the tests with the Al disc, the pin broke or was worn down after about 700 s to 800 s.

Pure Al is not used for wear and friction applications because of its smear wear. In brake disc applications Al MMCs infused with SiCp are common. The Al matrix ensures a better heat transfer compared to the most other metals due to its high thermal conductivity [129], [130]. Additionally, the pad material used in this POD test is for steel surfaces and steel matrices. Different pads would be necessary for Al and Al matrices [131].

The test results are shown in figure 8-14. For test number 1 the parameters of 1000 rpm (3.4 m/s), 2984 g normal load and approx. 15300 m sliding distance were chosen. As seen in figure 8-14 a) all samples of test number 1 with a steel matrix or pure steel have indicated a friction coefficient between $\mu = 0.40$ and $\mu = 0.47$. The exception is the GTA clad with 3.77 % - 7.19 % WC reinforcement, which has shown a value of $\mu = 0.37$. Aluminium has shown a very low friction coefficient of $\mu = 0.25$. Runs with the parameters of 1000 rpm

(3.4 m/s), 6062 g normal load and approx. 15300 m sliding distance of test number 2 are shown in figure 8-14 b). Tests for test number 2 achieved friction coefficients between µ = 0.31 and µ = 0.38.
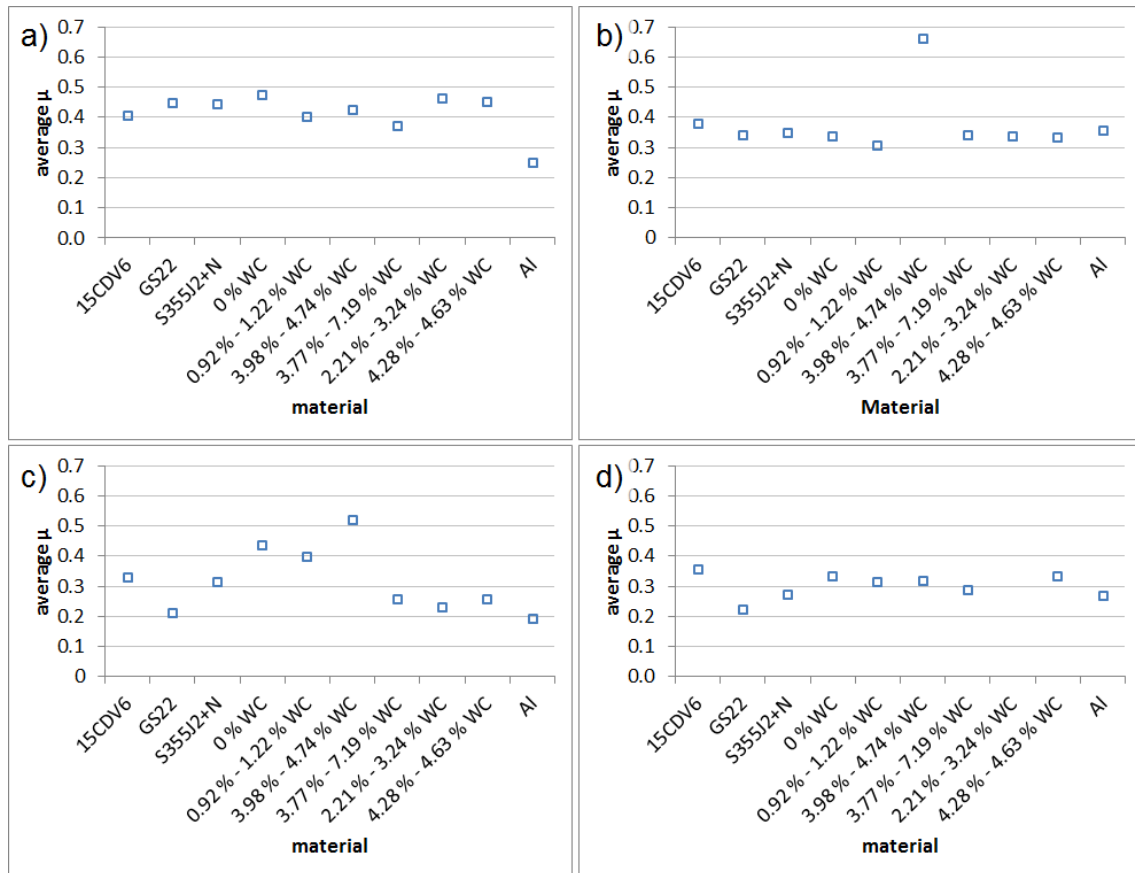
Figure 8-14: Measured average coefficient of friction (µ) for different POD tests and materials; a) 1000 rpm (3.4 m/s), 2984 g normal load, approx.: 15300 m travel distance; b) 1000 rpm (3.4 m/s), 6062 g normal load, approx.: 15300 m travel distance; c) 2000 rpm (6.8 m/s), 2984 g normal load, approx.: 15300 m travel distance; d) 2000 rpm (6.8 m/s), 6062 g normal load, approx.: 15300 m travel distance

The exception is the GTA clad with 3.98 % to 4.74 % WC reinforcement, which has a µ of 0.66. This result could have come from an inconsistent WC inclusion. POD tests with higher speeds, according to test number 3, were executed and the average µ results are disclosed in figure 8-14 c). The results indicate a dramatic difference between the blank steels. The 15CDV6 and the S355J2+N steel present a similar friction coefficient of µ = 0.33 and µ = 0.31.

The GS22 steel fell down to μ = 0.21 for the higher speed of 6.8 m/s and a low pin pressure of 0.72 MPa (2984 g normal load). GTA clad discs indicate a scattering of the μ. The results are varying between μ = 0.23 and μ = 0.52. This could come from a too low pin pressure for the speed of 6.8 m/s. Figure 8-14 c) provides a good foundation to look into the POD wear test for lower pressure and higher speeds again. A very consistent friction coefficient can be seen for tests with the parameter of test number 4. The test parameters of 2000 rpm (6.8 m/s), 6062 g normal load and approx. 15300 m travel distance were chosen for high speed and high load tests. Figure 8-14 d) reveals friction coefficients between μ = 0.27 and μ = 0.35 for all materials other than GS22. The GS22 material has once again a low friction coefficient with μ = 0.22. The POD wear test revealed maximum temperatures between 143 °C and 290 °C. These temperatures might be too low for the GS22 to give a sufficient friction response.

Over all, the GTA clad discs indicate similar friction behaviour to the blank steel discs in the POD wear test. As mentioned in chapter 3 section 3.8 the friction coefficient for brake discs is recommended to be between μ = 0.25 and μ = 0.45 [61]. This gives a strong argument to go ahead with a full size brake disc test.

The wear rate was not measured on the POD test rig as the wear of the discs was too low to be recognised. Much longer testing times (or distances) are needed to establish a wear rate over the mass change. Additionally, oxidation of the wear surface during wear conditions could increase the total mass initially.

8.4 Summary

A POD wear test is a quick solution to find the friction behaviour of the GTA clad surface with WC reinforcement. In contrast to a full size brake disc test this is a constant sliding of a pin applied to the disc surface. Testing times are as short as approx. 4 h and the disc size is much smaller. Welding parameters have been developed for spiral shape cladding. The distortion of the discs or plates

after welding was within a reasonable limit. A temperature recording during welding has revealed a maximum temperature of 313 °C on the centre back of the plate. This recording can be compared with the full size disc welding later on in order to look for similar heat sink behaviour. The functional graded layer was not uniform throughout the clad spirals. An increase in WC embedding from the inner to the outer side was exhibited in the microsections. WC reinforced GTA cladding trials demonstrate similar friction coefficients to blank steel discs with pins made of Ferodo 3216F pad material.

8.5 Conclusions

The following conclusions can be drawn from the preparation of POD specimen and POD wear testing:

- Welding parameters for a spiral clad with small radii must be optimised as the WC reinforcement is not uniform. Spiral clads were achieved with a WC reinforcement from 0.92 % to 7.19 % area fraction. A flat surface for POD testing was achieved by diamond grinding

- POD wear testing takes less time than dynamometer testing. The friction coefficient can be determined within 4 h instead of 1008 h. POD wear testing is a constant sliding test rather than a brake test. The type of loading on a POD test is significantly different than on a dynamometer test. Therefore the μ gives only an indication whether to scale up or not. POD wear tests with the machine at Cranfield University run at lower speeds and lower contact pressure than dynamometer tests. In spite of the constant sliding the generated temperature is still at low levels for braking. POD wear test results demonstrated a similar friction coefficient of the WC reinforced discs to the blank steel discs.

The WC clad can be tested on a dynamometer test rig to determine the wear loss on a prototype specimen.

9 Creation of design geometry prototype as a full-size railway brake disc

WC reinforcement as a wear resistant layer is well known [26], [48], [132]. New approaches for the WC reinforcement layers include: round, atomised WC particles (instead of broken WC) in a low Ni content steel matrix and the use of the GTAW process. Additionally, WC reinforcement surface layers were rarely tested for brake discs. The previous POD test offers the potential for using WC as reinforcement. One of the main reasons for a large scale GTAW test is to observe the issues associated with producing the prototype, i.e. GTAW process with wire and powder. This complex set up could show the different problems when a design geometry structure, like a railway brake disc, is clad. This is especially the case when the cladding trial is significantly larger than the single bead trials in chapter 6 and the overlap trials in chapter 7. This chapter highlights the different issues related to creating a prototype of functional surface layer on a railway brake disc structural component. Therefore, the following objectives are investigated:

- The possibility of a large WC reinforced layer on both wear surfaces of a railway brake disc with well distributed WC ceramic particles.
- Examination of distortion of the brake discs during GTA cladding and post-processing diamond grinding.

In the railway industry, axle mounted and wheel mounted brake discs are commonly used. This feasibility study concentrates on GTA cladding of axle mounted brake discs. Therefore, the discs will have two wear surfaces. Axle mounted brake discs are produced with and without ventilation. According to some previous investigations by Angelinas *et al.*, the thermo-mechanical behaviour of ventilated (with vanes) and unventilated discs are significantly different during braking operation [119], [121], [133]. The vanes could also have significant effects on the GTA cladding process by altering heat flow from the deposit zone.

The following railway brake discs were GTA clad:

- Two 640 mm outer diameter discs, ventilated, PFR = 15 g/min;
- Two 460 mm outer diameter discs, unventilated, PFR = 10 g/min.

The issues of lower WC powder feeding rates with GTA cladding are also tested with the unventilated disc.

9.1 GTA cladding of a ventilated full-size brake disc

The ventilated railway brake discs were delivered in the size of 640 mm outer diameter and 404 mm inner diameter, giving a wear section with width of 118 mm. GTA cladding of the full-size disc was done on the 5-axis rig with some adjustments to the TrioMotion controller programme. Figure 9-1 shows the set-up of the welding rig for cladding with ceramic powder for full-size railway brake discs.

Figure 9-1: GTA brake disc cladding with WC powder, overview of the welding rig; 1: TIG torch on z-axis; 2: Turntable with brake disc mounted on; 3: Pressure releasing container with valve; 4: Ar transport gas bottle; 5: Powder feeder; 6: 5-axis-rig controller; 7: KT4 wire feeder; 8: AMV display and recorder (arc current, arc voltage and wire feed speed)

The WeldTech TIG welding torch was situated on the z-axis (Figure 9-1 1) with the turntable and brake disc (Figure 9-1 2) underneath. The WC powder was fed by the powder feeder (Figure 9-1 5), using the Ar transport gas (Figure 9-1 4). The WC powder was fed through the pressure releasing container (Figure 9-1 3) and from there by gravity to the powder feeder nozzle next to the TIG torch (Figure 9-2 2). Wire was delivered by the wire feeder (Figure 9-1 7) to the wire feeder nozzle next to the TIG torch (Figure 9-2 3). The GTAW power source is not displayed (see section 4.1 of chapter 4 for details). The process parameters were arc current, arc voltage and wire feed speed. They were recorded and displayed with the AMV (Figure 9-1 8). Movement of both the torch and turntable were controlled by the programmable TrioMotion controller (Figure 9-1 6). Additionally, the height of the torch could be adjusted manually during the programmed cladding process. This allowed the arc length to be adjusted if the voltage changes.
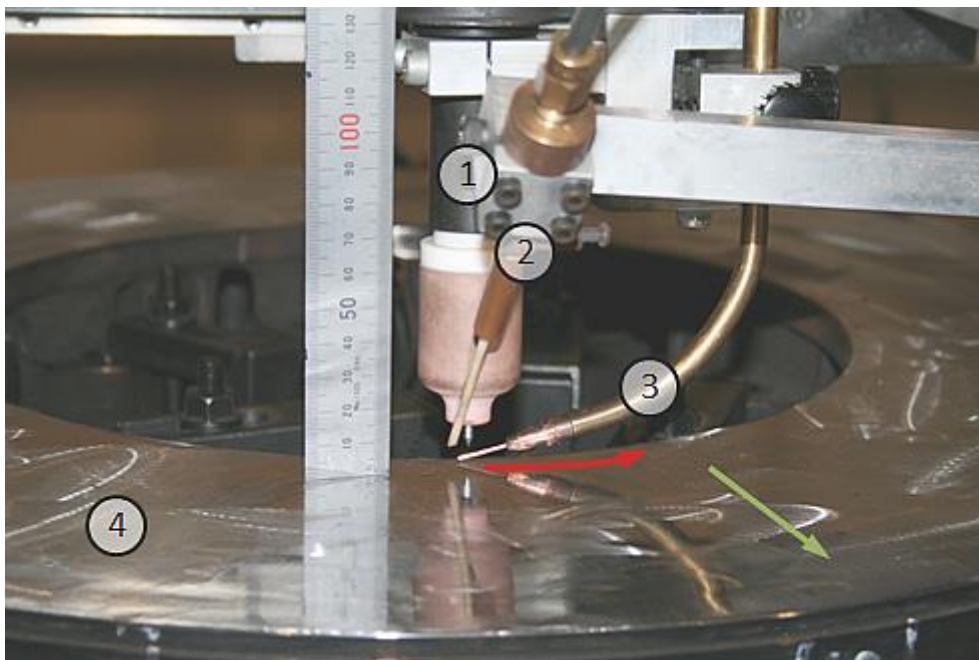
Figure 9-2: GTA brake disc cladding, starting position before welding (sample: 640 mm outer diameter disc); 1: TIG torch; 2: Powder feeder nozzle; 3: Wire feeder nozzle; 4: Fresh ground brake disc; red arrow: cladding direction (or direction of disc movement); green arrow: overlapping bead direction

A close-up image of the welding torch in the starting position is given in figure 9-2. For GTA cladding, the TIG welding torch (Figure 9-2 1) was arranged perpendicular to the brake disc (Figure 9-2 4). The angles of the wire feeder (Figure 9-2 3) and powder feeder (Figure 9-2 2) are given in table 9-1. Brake disc cladding was performed with the welding parameters shown in table 9-1.

Table 9-1: Brake disc welding parameter

					wire feeder nozzle			
Current	travel speed	wire feed speed	a	b	c	d	α	β
A	m/min	m/min	mm	mm	mm	mm	°	°
200	0.3	1.5	3.4	8	1.5	14.1	180	19

		powder feeder			powder feeder nozzle			
		Ar pressure	Ar flow rate	Ar flow rate	c	d	α	β
		bar	NLPM	l/min	mm	mm	°	°
		3	5	5	5.8	3.9	103	37

The angles of the feeder nozzles and the distances a, b, c, d are in accordance with figure 6-1 . The Ar transport gas for the WC powder was fully released at the pressure reducing container (Figure 9-1 3 and figure 4-6). G3Si1 mild steel welding wire was used for all brake disc cladding trials and its mechanical properties are shown in table 4-5. Four surfaces needs to be covered for two brake discs. Only one layer in overlap was planned for each trial. The off-set distance for the overlaps was varied between 3.8 mm and 4.3 mm and, therefore, became greater than that in section 7.2 of chapter 7. Figure 7-3 shows an off-set of 3.5 mm for PFR = 10 g/min and PFR = 15 g/min.

A thermocouple was attached to the side of the inner diameter of the brake disc in a 5 mm to 8 mm depth from the original wear surface (dh), as shown in figure 9-3.
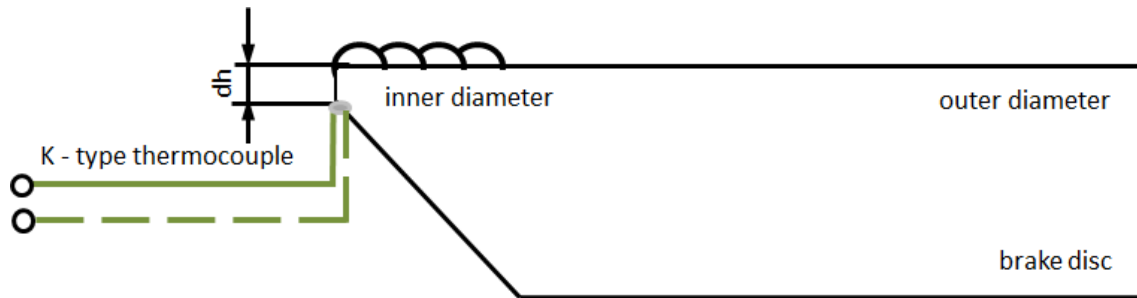
Figure 9-3: Schematic position of thermocouple on the inner diameter of the brake disc, dh: depth from the wear surface

The temperature profile was measured on the inner radius and was connected to the disc by a resistance spot weld. This was done for every welding trial as shown in figure 9-4.
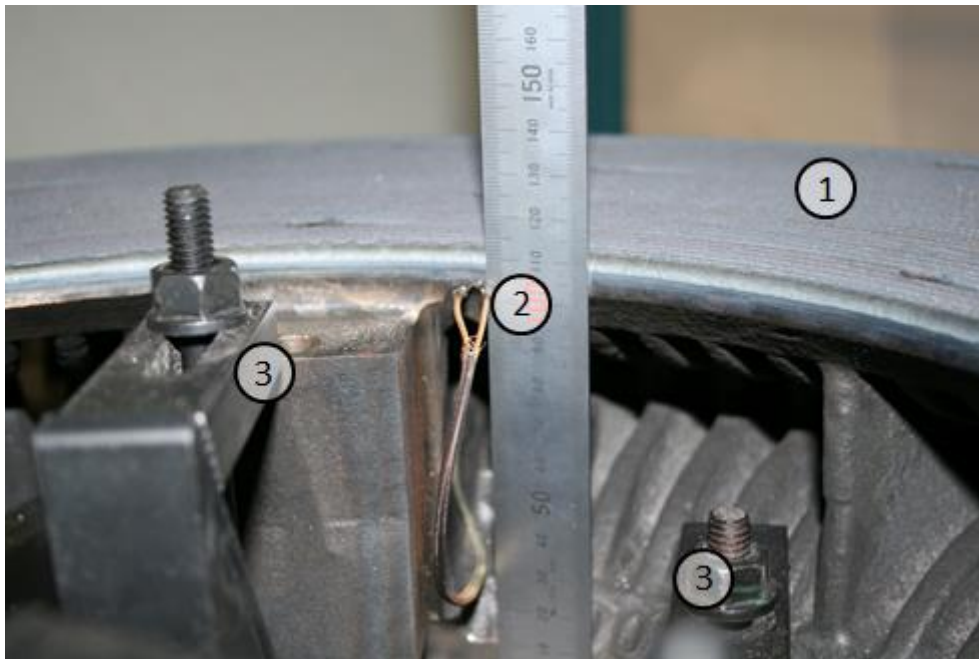
Figure 9-4: Typical temperature measurement of the brake disc during welding; Thermocouple contact; 1: brake disc wear surface; 2: thermocouple contact point (dh = 5 mm to 8 mm); 3: clamps

A data logger with display (Figure 9-5 3) was connected to the thermocouple (Figure 9-5 2).

Figure 9-5: Typical temperature measurement of the brake disc during welding; Temperature display; 1: brake disc; 2: thermocouple lead; 3: temperature display apparatus; 4: powder tray

Therefore the first GTA cladding trails were very close to the thermocouple. An example of the WC cladding temperature values recorded is shown in figure 9-6.
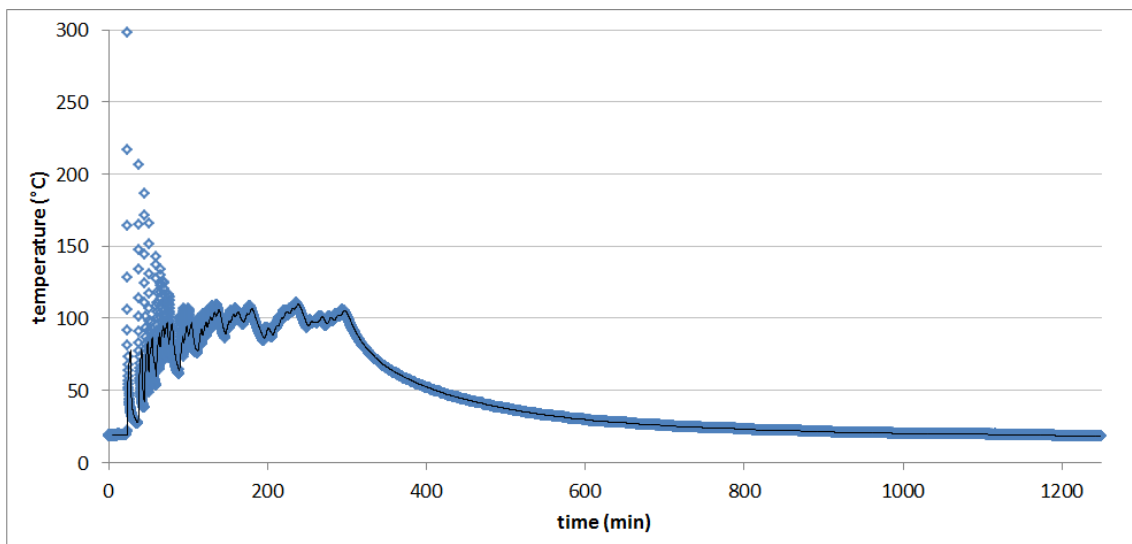
Figure 9-6: Typical time - temperature plot of a cladding trial on the ventilated railway brake disc measured as shown in figure 9-4

The heating curve of the GTA brake disc cladding in figure 9-6 indicates scattered peaks above 124 °C at the beginning of the welding trial. These peaks come from the short distance of the inner diameter cladding rounds to the thermocouple, which leaves the torch passing close by. After around 30 min welding, the occurrence of scatter disappears and a stable reading follows. The trend line of the moving average gives a better understanding of the transient thermal cycle of the brake disc. Those values can supplement the finite element modelling in future work. Figure 9-6 points out that the railway brake disc heats up in a cycle of heating and cooling from the average of 18 °C to the average of 97 °C within the first 94 minutes of GTA cladding. The cycle of heating and cooling continues for the rest of the welding time (for another 202 minutes) within the moving average temperatures of 92 °C and 109 °C. The average temperature during this 202 minutes time is 97 °C. The cycles of heating and cooling appear to be generated during the passing of the GTAW torch. It comes once every round closely to the thermocouple. The cooling curve after welding demonstrates a time of 698 minutes to cool down to the average of 20 °C again; however, the cooling from an average of 97 °C to an average of 50 °C took place in the first 109 minutes of cooling.

Figure 9-6, compared to the time - temperature curve of the POD specimen welding in figure 8-6, reveals a much lower maximum temperature. The POD specimen measured with thermocouples produced maximum temperatures between 234 °C and 313 °C, where, the four brake disc welding trials, on the two 640 mm outer diameter brake discs, exhibited average temperatures between 94 °C and 103 °C. The bigger mass of the brake disc, as well as the cooling vanes, was the reason of the lower base material temperature with much faster transient thermal cycles.
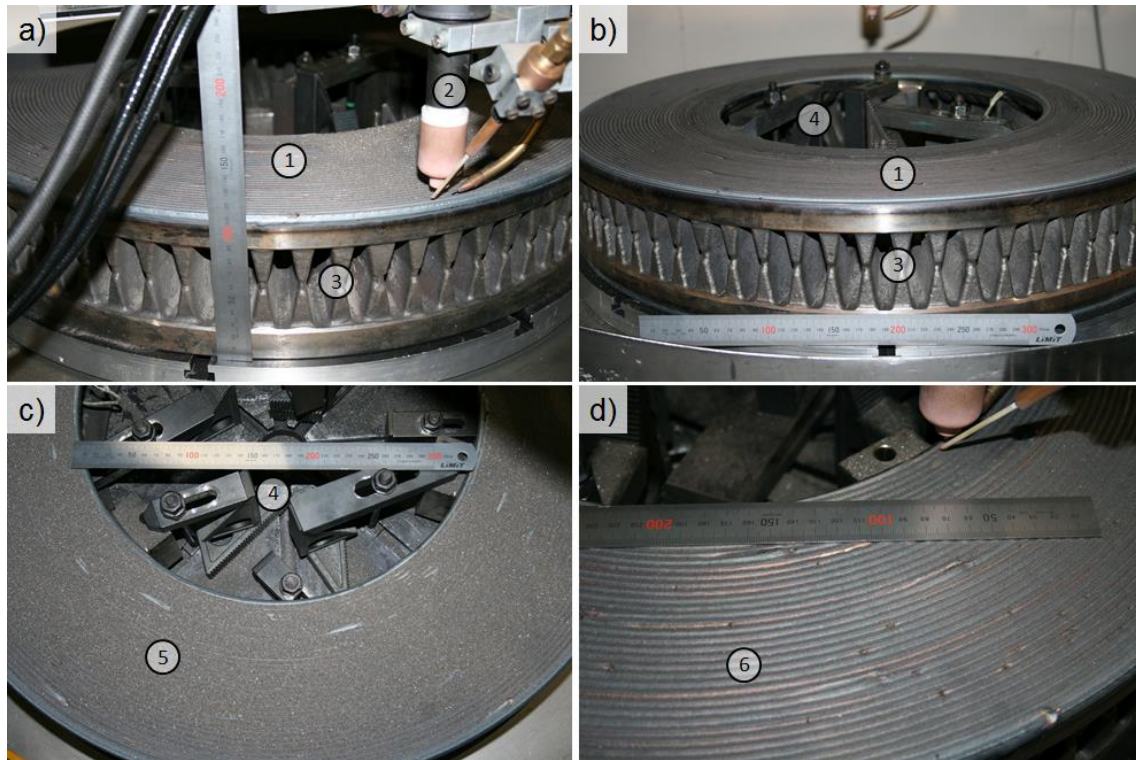
Figure 9-7: 640 mm railway brake disc; a) GTA clad disc with TIG torch still in position; b) overview disc after second cladding; c) top view after cladding (WC powder left on the disc; d) cleaned disc section; 1: wear surface; 2: TIG torch; 3: cooling vanes; 4: clamping system; 5: GTA clad surface; 6: brush cleaned welding trials

Another view of the GTA welding set up of the 640 mm outer diameter railway brake disc with WC powder feeding is presented in figure 9-7. The GTA cladding was performed from the inside to the outside with a WC powder feeding rate of PFR = 15 g/min. The cladding was completed in concentric circles. However, the turntable was turned additionally $^1/_8$ of a round after each run. This was necessary to obtain the starting point of the next round in a different position from the start/finish point of the previous round. Figure 9-7 a) illustrates the brake disc after a complete cladding trial with the TIG welding torch in the finish position. An overview of the full brake disc after cladding is given in figure 9-7 b). Left-over WC powder was not removed during the GTA cladding procedure (Figure 9-7 c) 5. This prevented impurities from brushing and kept the heat longer in the brake disc. A brushed and cleaned WC

reinforced layer can be seen in figure 9-7 d) 6.   Some key values of the GTA
cladding with functional graded layer are as mentioned below:

- the total arc on time for a layer was 5 h 17 min
- 32 rounds were welded

Microsections were prepared of one 640 mm outer diameter railway brake disc.
Therefore one brake disc has been cut and the other was left for dynamometer
testing.   A full length microsection of the 640 mm brake disc is shown in figure
9-8.

**Figure 9-8: Microsection of GTA cladding trial on 640 mm outer diameter railway
brake disc; yellow window: extract shown in figure 9-9; left: inner diameter, start
cladding; right: outer diameter, finish cladding**

The cladding layer is approx. lh_{min} = 1.7 mm high with a low waviness to allow a
grinding of only 0.3 mm off (lh_{max} = 2.0 mm) for a flat surface.   Figure 9-9 is an
extract of figure 9-8 and demonstrates a well distributed WC reinforcement in
the GTA cladding layer.   Porosity only appears in the WC powder particles and
is not caused by the welding process.
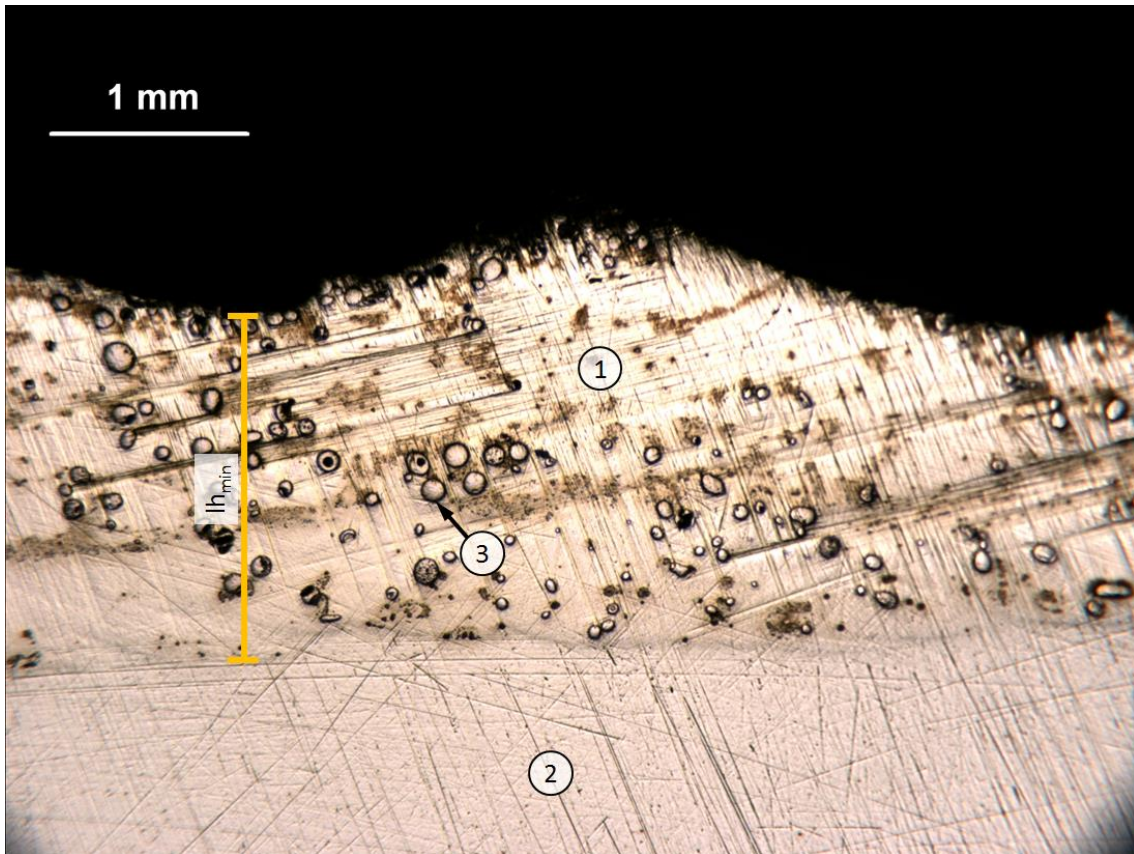
Figure 9-9: Extract of figure 9-8, microsection of the 640 mm brake disc cladding layer, one welding trial; lh_{min}: useful layer height; 1: functional graded layer; 2: HAZ; 3: WC particle

The WC reinforcement was measured according to the method used in section 7.3 of chapter 7. Three areas on the microsection have been chosen to quantify the WC reinforcement. Numbers have been given to the welds, starting from the inner disc diameter, to give a better orientation of the position of the measurements. Table 9-2 reveals the WC reinforcement in the area with peaks and the useful area for the layer serial numbers three to six, 14 to 16 and 29 to 31.

Table 9-2: WC reinforcement measured in different cutting areas of the microsection (PFR = 15 g/min)

Cutting area	-	inner side	middle	outer side
Layer serial No.	-	03 to 06	14 to 16	29 to 31
WC reinforcement with peaks	%	3.95	2.47	5.53
WC reinforcement useful area	%	3.44	5.32	3.95

The WC reinforcement with peaks indicates values between 2.47 % and 5.53 %. The average WC reinforcement is 3.98 %, which is under half of the value measured in chapter 7.4.1. In recapitulation, the WC reinforcement in the area with peak for flat plates shows 9.2 % for PFR = 15 g/min. A similar picture is seen when the results of the WC reinforcement in the useful area is compared. WC reinforcement for the useful area is between 3.44 % and 5.32 %, with an average of 4.24 %. The samples of the flat plate (chapter 7.4.1) show a WC reinforcement of 9.8 %. This difference could come from the susceptibility of the liquid steel or the weld pool length during cladding as the transient thermal profile is indicating. Both can be significantly influenced by the size of the samples and its heat sink. Further analyses are necessary as the WC could also be dissolved in the steel matrix.

A diamond grinding process of the second disc has been done by an external company. The GTA clad disc with 640 mm outer diameter is displayed in figure 9-10. The cladding layer surface is visibly flat and the grinding dust has been removed.
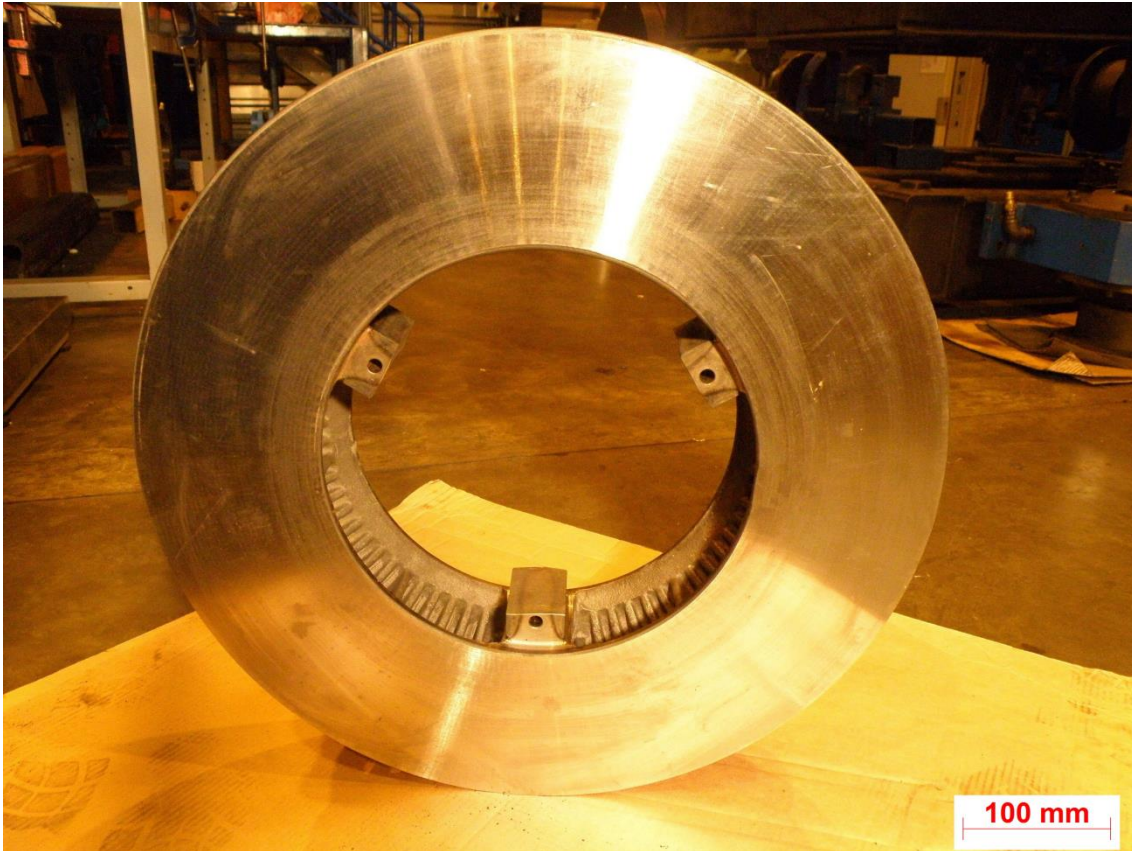
Figure 9-10: Clad brake disc with 640 mm outer diameter after diamond grinding

Chapters 6 and 7 have shown cracks in the WC reinforced cladding layer. Some cracks have also been found in the brake discs after GTA cladding. With this in mind, a non-destructive crack testing was organised. The surface of the 640 mm outer diameter disc has been tested in full with the dye penetrant inspection method. This method results in the full surface being covered with white dye and a contrasting red dye marks the surface cracks or voids.
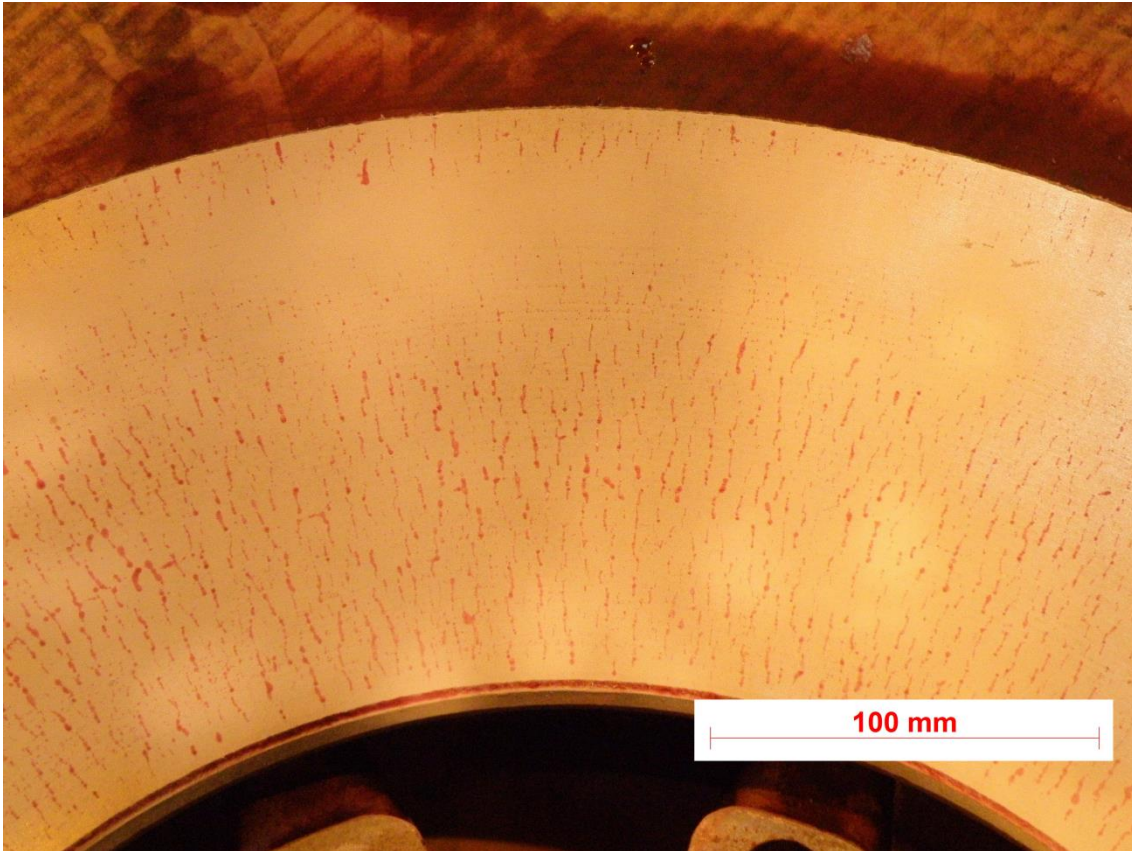
Figure 9-11: Surface crack testing on the ground 640 mm outer diameter disc (dye penetrant inspection)

Figure 9-11 shows a section of the dye penetrant inspection on the wear surface. It is clearly presented that a large number of microcracks are in the WC reinforced GTA cladding layer. The cracks are typically perpendicular to the welding direction. Although the surface layer is designed for brake disc application, the main focus of this work was to improve wear resistance. Crack resistance or crack fatigue needs to be followed up in future work. Another possibility for the future is to avoid cracks by a softer matrix material or a pre-heated brake disc. Post process heat-treatment would not prevent cracks as these were appearing already during the welding process. Another idea was hot isostatic pressing of the premixed WC and matrix powder. However, this will lead to a heat treatment of the full brake disc and, therefore, change the properties of the high strength steel as a bulk material.

A hardness test of the railway brake disc on the ground surface has been executed to obtain a comparison with the samples generated in chapter 7.4. A schematic drawing indicating the location of the hardness indentations is shown in figure 9-12.
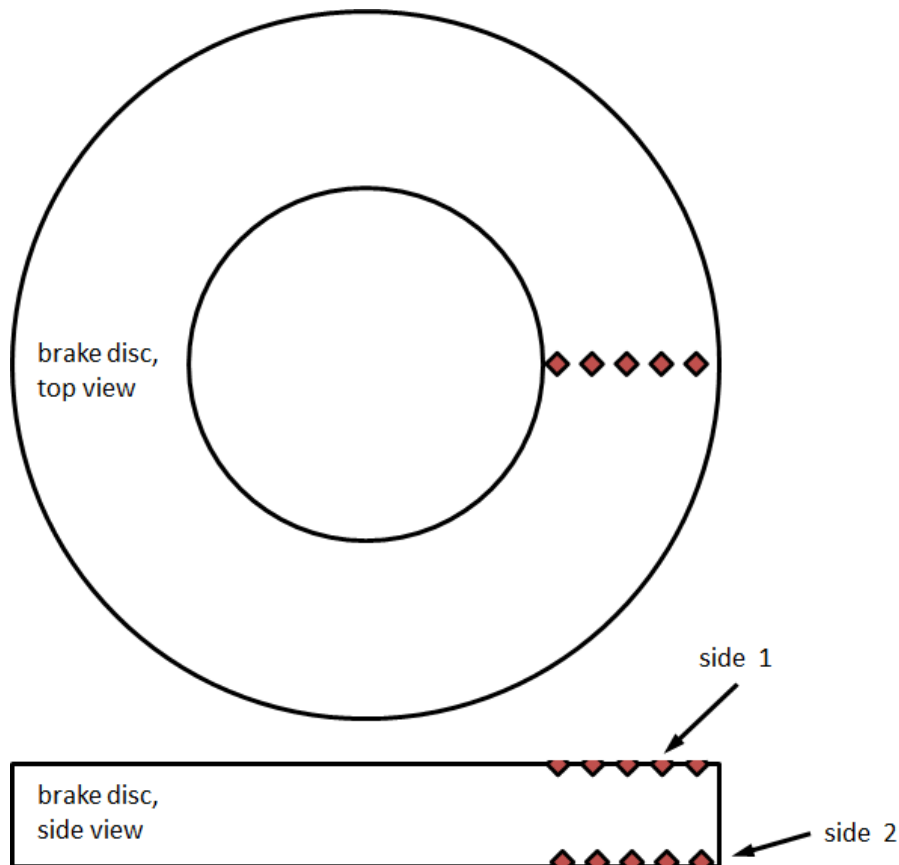
Figure 9-12: Schematic drawing of the location of the hardness indentations according to Vickers on the ventilated brake disc

The hardness values are shown in figure 9-13. The number of eight indentations was evenly distributed in a line over the wear surface of the 640 mm brake disc. This resulted in hardness indentations with a distance of 13.1 mm from the inner to the outer radius on both sides of the disc. As shown in figure 9-13, the inner diameter is 404 mm and the outer diameter is 640 mm.
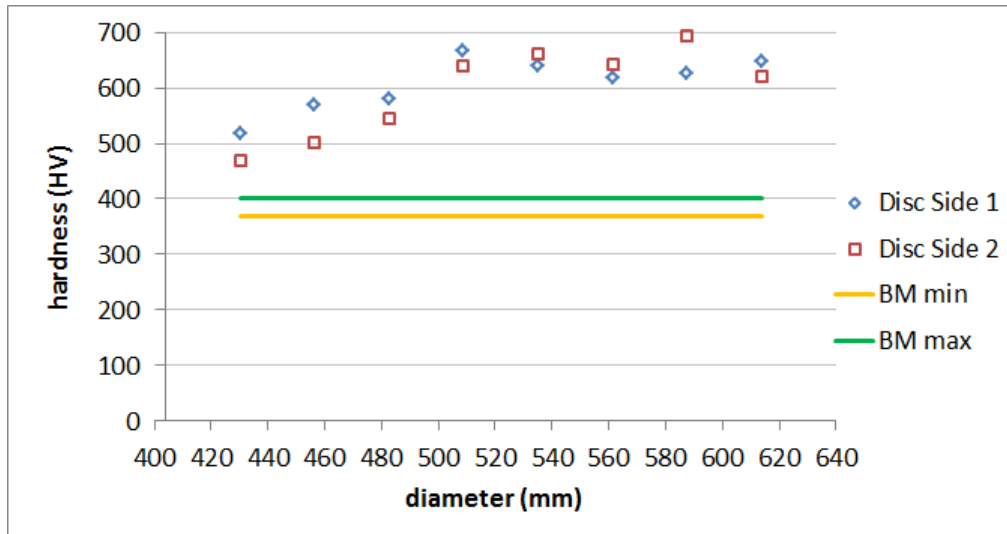
Figure 9-13: Macro hardness test according to Vickers on the surface of the ground cladding layer, ventilated 640 mm disc (results converted from Leeb rebound HL measurements); inner diameter starts at 404 mm; outer diameter ends at 640 mm; BM: base material hardness (as delivered)

The hardness test was done with a much greater load and the results are indicating similar values to those in section 7.5.1 of chapter 7 for the matrix material. The description of the Leeb rebound hardness tester is given in Appendix I. The GTA clad disc increases hardness from 468HV to 640HV in the first 104.9 mm of the inner diameter (disc side 2). These are the four measurements on both sides of the disc in the diameter from 404 mm to 508.9 mm, as presented in figure 9-13. Both sides of the brake disc cladding layer indicate that this hardness increase is almost linear towards the middle of the wear surface. This effect could come from the increase of the brake disc temperature during the first welding rounds. A higher pre-heating temperature could lead to a higher dissociation of WC particles and/or a wider weld pool size with more WC powder incorporation. The hardness stays between 618HV and 693HV for the outer diameters from 508.9 mm to 640 mm. The average hardness of the matrix for the WC PFR = 15 g/min in section 7.5.1 of chapter 7 was 604HV0.2. This is in the lower hardness range of the measured brake disc surface hardness. The indentations on the brake disc surface were large (macro hardness testing), therefore, they could be partially on the WC particles.

An extract of the dynamometer test results as produced by the sponsor Faiveley Transport Ltd. is given in Appendix K.

9.2 GTA cladding of an non-ventilated full-size brake disc

The two non-ventilated discs with an outer diameter of 460 mm were GTA clad in a similar way to the 640 mm disc. The GTA cladding parameters were the same and can be seen in table 9-1. As shown in figure 9-14, the TIG torch was set up at the inner side of the disc as a starting point as well. The WC powder feeding rate was reduced to 10 g/min to minimise cracking.
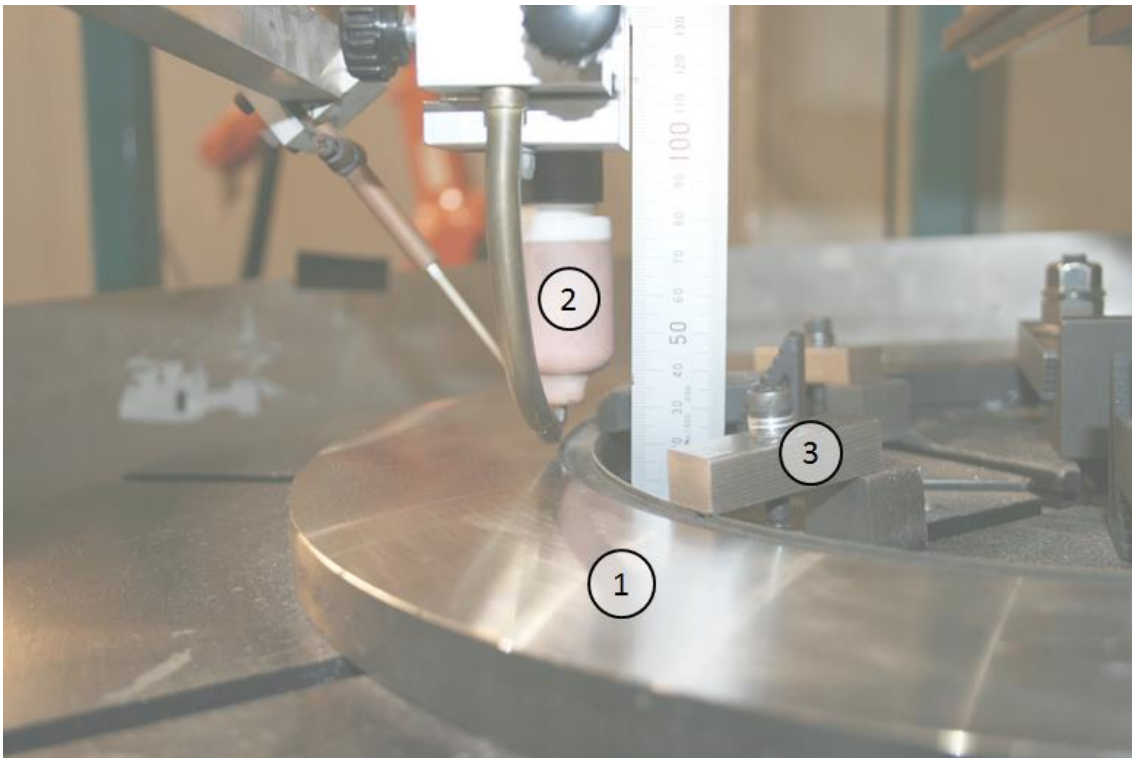
Figure 9-14: 460 mm railway brake disc (non-ventilated), disc with TIG torch in start position for GTA cladding; 1: wear surface; 2: TIG torch; 3: clamping system

Figure 9-15 illustrates the cladding of one WC reinforced surface layer. The overview in figure 9-15 a) demonstrates the fully clad disc with the clamping only from the inner side.
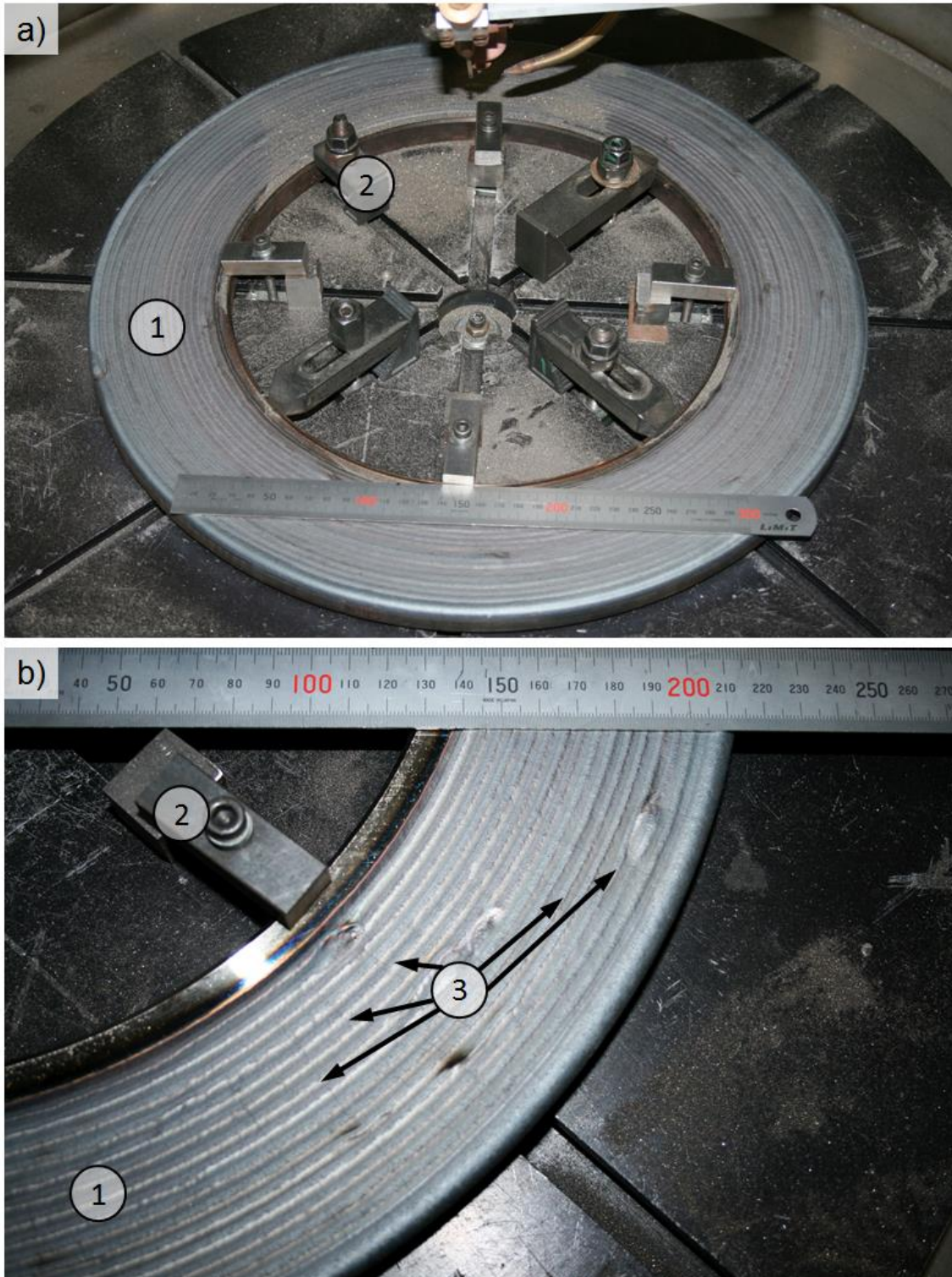
Figure 9-15: 460 mm railway brake disc (non-ventilated), a) overview disc after first cladding; b) quarter view after first cladding; 1: wear surface; 2: clamping system; 3: radial cracks

Figure 9-15 b) presents the WC reinforced cladding surface after brushing. It can be seen that cracks have gone through from the inner side to the outer side of the disc (see figure 9-15 b) 3). Further analysis of the cracks will be made after diamond grinding.
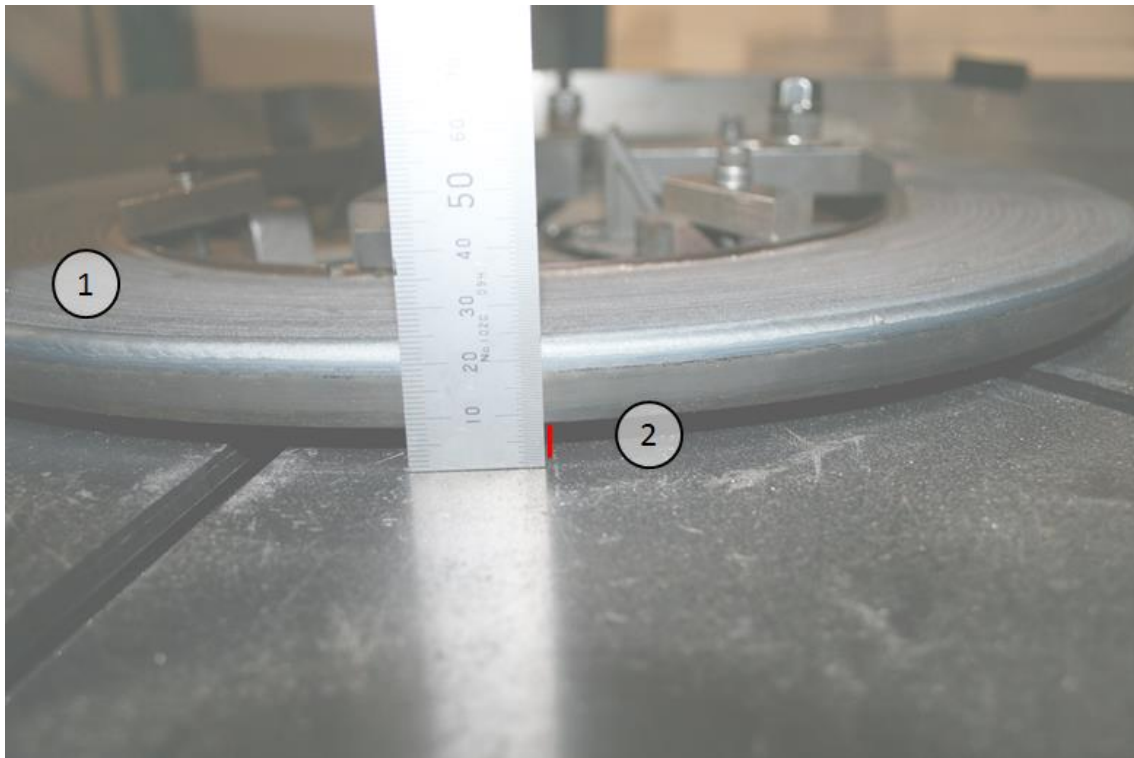
Figure 9-16: 460 mm railway brake disc (non-ventilated), side view after first cladding; 1: wear surface; 2: lifted disc due to distortion (red line indicates the distance between the disc and the turntable)

Distortion of about 8 mm on the outer edge has been measured against the turntable after the first WC reinforced cladding layer (Figure 9-16 2). Welding of the second layer on the opposite wear surface of the disc bent the disc back and removed the distortion. The bolts of the clamping system had to be tightened after every round of cladding the disc. The disc was good enough to be used in dynamometer testing. However, the high working process of bending and back-bending could have raised the residual stress in the disc significantly. The key welding values are:

- 1h 45 min arc on time
- 19 cladding rounds

Microsections were prepared of one 460 mm outer diameter railway brake disc. Therefore one brake disc has been cut and the other was sent for dynamometer testing. A flatter GTAW surface layer has been achieved on the 460 mm outer diameter brake disc than on the 640 mm disc. The full size microsection is revealed in figure 9-17. It can be seen that the waviness is very low.

Figure 9-17: microsection of GTA cladding trial on 460 mm outer diameter railway brake disc; yellow window: extract shown in figure 9-18; left: inner diameter, start cladding; right: outer diameter, finish cladding

The reduction in WC powder feed rate did not affect significantly the WC reinforcement. As seen in figure 9-18, the WC particles are also well distributed in the GTAW surface layer. Diamond grinding was required to eliminate the waviness of the disc and a 0.2 mm cladding layer was removed.
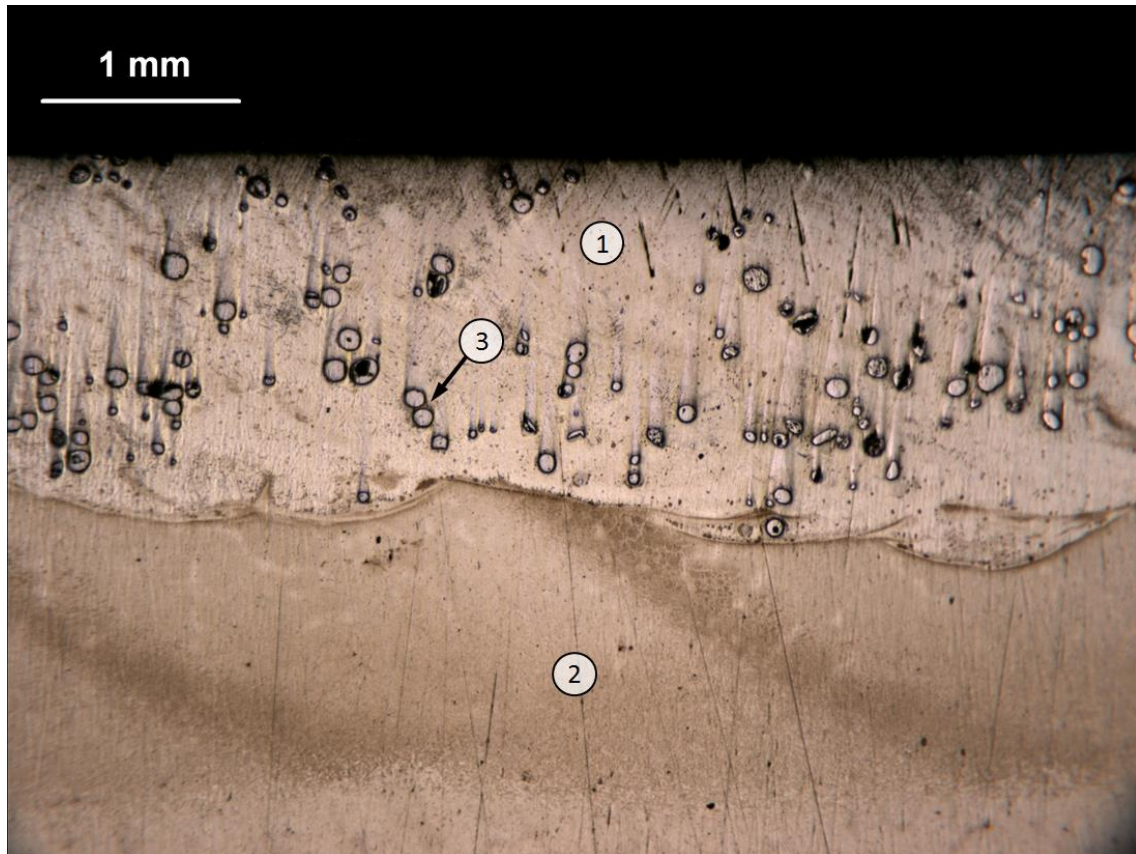
Figure 9-18: extract of figure 9-17, microsection of the 460 mm brake disc cladding layer, one welding trial; 1: functional graded layer; 2: HAZ; 3: WC particles

The WC reinforcement of the 460 mm diameter railway brake disc was measured at three different areas on the microsection. The measured values are shown in table 9-3.

Table 9-3: WC reinforcement measured in different cutting areas of the non-ventilated brake disc

Cutting area	-	inner side	middle	outer side
Layer serial No.	-	03 to 05	09 to 11	12 to 13
WC reinforcement with peaks	%	7.96	6.83	7.45
WC reinforcement useful area	%	8.68	7.20	8.06

WC reinforcement in the area measured with peaks indicates the lower readings then the WC reinforcement in the useful area. This is beneficial as only the useful area is used for braking. The values between 7.20 % and 8.68 % WC reinforcement in the useful area (Table 9-3) are up to 2.5 times higher than the WC reinforcement in the ventilated brake disc (see table 9-2). To remember: The WC powder feeding rate of the ventilated disc was as high as 15 g/min and from the non-ventilated disc was as low as 10 g/min. There is a high probability that the shape of the discs, as well as the cooling vanes, resulted in different cooling rates of the brake discs. Either the ratio of the WC reinforcement to dissolved WC changed and/or the WC powder pick-up got influenced by the cooling rate (weld pool size larger). Future work should concentrate on different layouts of brake discs to confirm this behaviour of WC reinforcement.

For the 460 mm outer diameter brake disc, a magnetic detection method for surface cracks was chosen. A section of the disc is shown in figure 9-19.
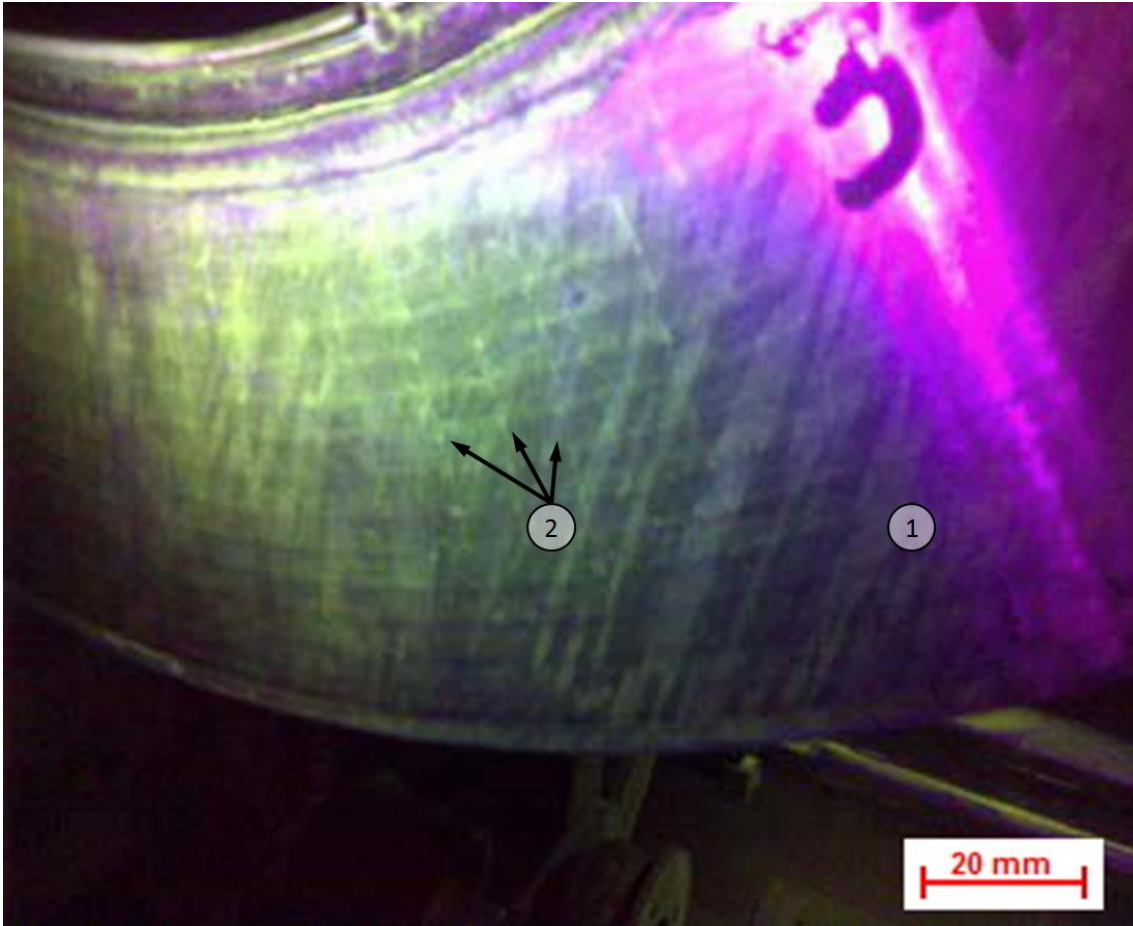
Figure 9-19: Surface crack testing on the ground 460 mm outer diameter brake disc (magnetic crack detection); 1: wear surface; 2: radial cracks

Magnetic crack detection works by using a fluorescent liquid infused with ferritic particles. If an electric current is applied to the brake disc, a magnetic field results within the disc. This magnetic field has its highest magnetic force where cracks appear. Therefore the fluorescent liquid concentrates along the cracks and can be seen in contrast to the general surface in very thin lines. A photo taken to visualise these lines, see figure 9-19 2, indicates some cracks perpendicular to the rotation axis (welding direction). The cracks are similar to the cracks discovered in the 640 mm outer diameter discs.

A hardness test of the railway brake disc on the ground surface has been executed to obtain a comparison with the samples generated in chapter 7.4.

The location of the hardness indentations are shown schematically in figure 9-20.
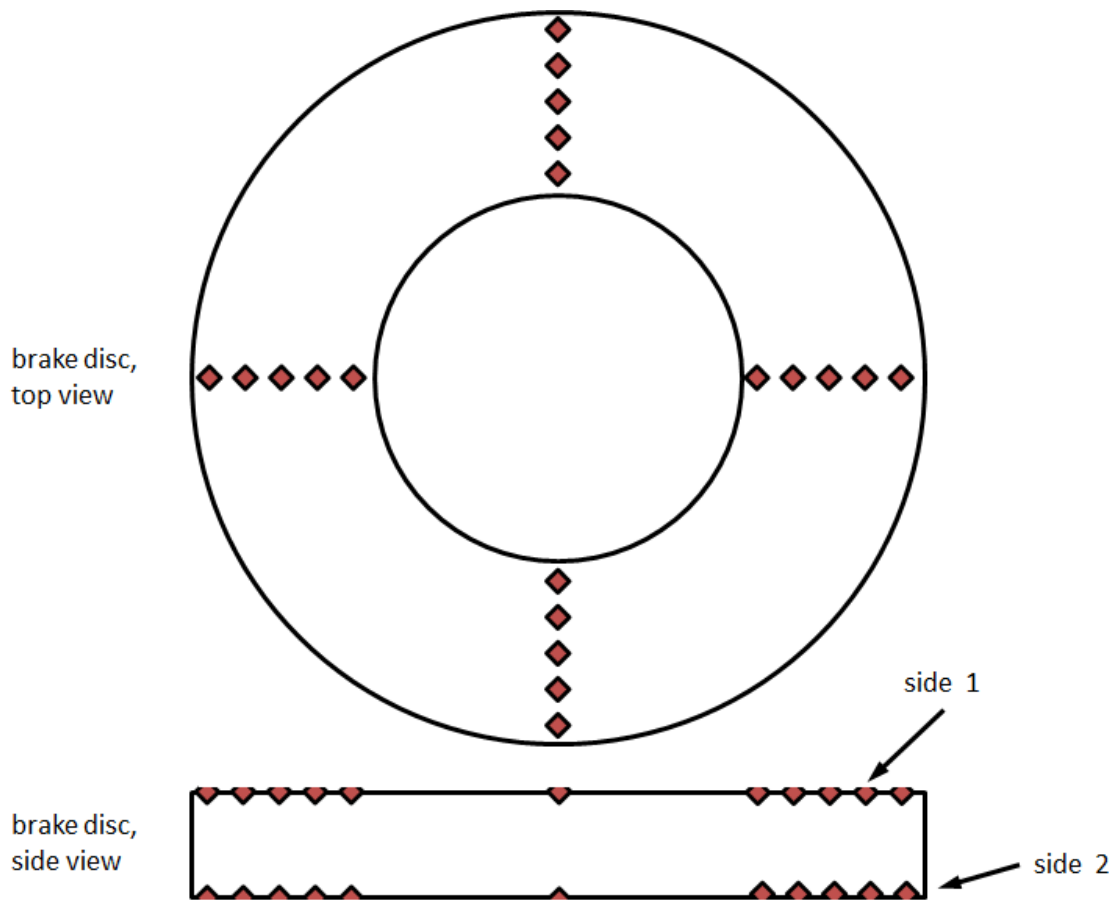
Figure 9-20: Schematic drawing of the location of the hardness indentations according to Vickers on the non-ventilated brake disc

The hardness values are shown in figure 9-21. The number of four indentations was evenly distributed in a line over the wear surface of the 460 mm outer diameter brake disc. This resulted in hardness indentations separated by a distance of 16.5 mm from the inner to the outer radius. Additionally, the brake disc was measured in four lines at 90° as shown in figure 9-20. The average hardness was taken from the four radial locations for the same side (see figure 9-20).
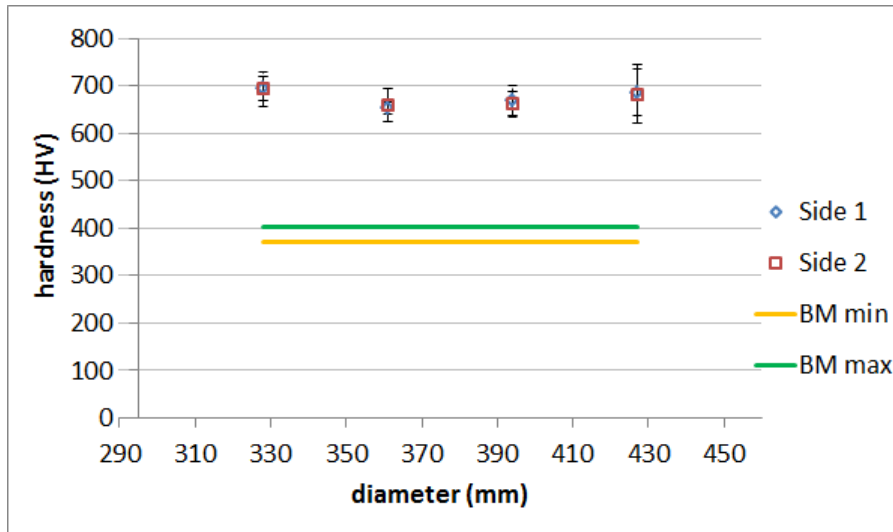
Figure 9-21: Macro hardness test according to Vickers on the surface of the ground cladding layer, 460 mm disc, average of four measurements; BM: base material hardness (as delivered)

As shown in figure 9-21 the inner diameter is 295 mm and the outer diameter 460 mm. The hardness test was done with a much greater load and the results are indicating similar values to those in section 7.5.1 of chapter 7 for the matrix material. The four values for each side are given in figure 9-21. The wear surface reveals an evenly distributed hardness between 652HV0.2 and 695HV0.2 in the full range from 295 mm diameter to 490 mm diameter. There are four measurements on both sides of the disc, as presented in figure 9-21. The railway non-ventilated brake disc clad results in an evenly distributed hardness. The average hardness for the WC PFR = 10 g/min in section 7.5.1 was 590HV0.2. This hardness is lower than the measured brake disc surface hardness. Although these tests are on the surface layer, the increased hardness on the brake disc could be an indication of residual stress coming from the high bending load.

The dynamometer test was produced by the sponsor Faiveley Transport Ltd. and an extract of the results is given in Appendix K.

9.3 Summary

Dynamometer brake tests were planned with ventilated (with vanes) and unventilated axle mounted discs. These are surface coated by the GTA cladding process with WC ceramic powder feeding and wire matrix feeding. The GTA cladding process was successfully carried out on two ventilated 640 mm outer diameter railway brake discs and two non-ventilated 460 mm outer diameter railway brake discs. Welding parameters have been chosen similarly to those for the overlap trials in section 7.1 of chapter 7.

The following results were found for the ventilated railway brake disc:

- The temperature profile of the 640 mm outer diameter disc indicates a temperature of the bulk material between 92 °C and 109 °C. This is significantly lower than that of the GTA cladding process of the POD samples in section 8.1 of chapter 8, which can lead to a different susceptibility of WC powder in these samples.
- One disc has been cut for microstructure analysis. A microsection of the disc shows that the WC reinforcement particles are well distributed in the surface layer.
- The measured WC reinforcement is between 3.44 % and 5.32 % area fraction (measurement on microsection).
- The brake disc reveals microcracks in non-destructive testing (NDT) on the wear surfaces.
- A hardness test on the cladding layer surface was done and the results are indicating similar values to those in section 7.5.1 of chapter 7 for the matrix material.
- The GTA clad disc (640 mm outer diameter) increases in hardness from 468HV to 640HV in the first 52.5 mm of the inner diameter. After that the hardness stays between 618HV and 693HV towards the outer diameter.

The following results were found for the non-ventilated 460 mm railway brake disc:

- Distortion recognised during the GTA cladding of the 460 mm outer diameter discs bent back with welding on the opposite side.

- One disc has been cut for microstructure analysis. Similar to the ventilated disc, a microsection of the disc shows that the WC reinforcement particles are well distributed in the surface layer.

- The WC reinforcement was measured with values between 7.20 % and 8.68 % area fraction (measurement on microsection).

- The brake discs in all diameters reveal radial microcracks in non-destructive testing (NDT) on the wear surfaces.

- A hardness test on the cladding layer surface was done and the results are indicating similar values to those in section 7.5.1 of chapter 7 for the matrix material.

- The wear surface of the 460 mm disc reveals an evenly distributed hardness between 652HV0.2 and 695HV0.2.

The cracks and the observed disc thickness variation (DTV), as seen in appendix K.3.2, could be reduced by adjustments to the GTA cladding parameters. An important future role could be the choice of the matrix material and pre-heating of the disc surface.

9.4 Conclusions

Following conclusions of the WC reinforced full-size railway brake disc cladding can be drawn:

- The GTA welding process of full-size discs was successful with the parameters chosen. The WC reinforcement is well distributed in contrast to the POD discs. Fine surface cracks have been observed on all discs after grinding.

- Distortion of the 460 mm outer diameter discs (non-ventilated) needs to be controlled. The ventilated discs (630 mm outer diameter) are not

showing recognisable distortion, which comes from the disc thickness and additionally cooling of the vanes.

10 Thesis summary

There are two distinct microstructures for wear resistant surfaces:

On one hand a ceramic phase in the form of particles in a metal matrix [38], [67], [72] and on the other hand a fully dissolved ceramic phase building new structures with the matrix [16], [26], [134]. Understanding the interaction of ceramic particles and steel matrix is crucial when using low Cr and Ni steel matrices.

Background of ceramic MMCs in braking applications

Surface cladding layers, built up with fully dissolved particles, resulting in a hardness between the hardness of the matrix material and the hardness of the ceramic used. Cladding layers with fully separated ceramic and matrix result in a high hardness for the ceramic and a low hardness for the matrix. These layers are known for their good wear resistance in braking. However, cladding layers with ceramic inclusions are only known for Aluminium matrices [135]–[137]. For railway brake discs, Al is hardly suitable because of the high braking energies generated. Matrices for layers on steel are usually alloys of high Ni content, Cr content or both (Inconel, Stellate)™. Ni and Cr in too high concentrations are not allowed in brake discs because of health and environmental issues regarding brake dust.

Decision for the GTAW process and SiC and WC ceramic

This work researches the ability to obtain a ceramic reinforced cladding layer with low Cr and Ni content (under 3 wt% each) for railway brake discs. The work focusses on the production and analysing of ceramic reinforced layers with mild steel and high strength steel matrices. A pre-study of the GMAW process for cladding indicated that surface layers less than 1.78 mm would not be possible. This would be too high for the vision of a functional graded material (FGM) with increasing ceramic content up to a thickness of 8 mm. The peak layer height of 8 mm would only allow five layers to be built up. A GTAW process with in situ matrix and ceramic powder mixing was chosen instead. SiC

and WC ceramic powders were chosen for the investigation of the metal matrix composite (MMC) surface layers.

Result of SiC for steel MMCs

A feasibility study with SiC ceramic powder in a GTAW process demonstrated fully dissolved SiC ceramic, which built new structures with the steel matrix. The hardness of the newly built structures is up to 1183HV0.5.

WC powder pick up in single bead cladding trials

In single bead cladding trials, WC powder was found to embed into the steel matrix. It was confirmed that MMC structures are able to be built up with WC and low mild alloy steel. An examination of Ar and He as a shielding gas was launched and the outcome indicates that increasing He leads to increased cracking. Further analysis provided evidence of dissolved WC in the steel matrix. This led to the investigation of the matrix to obtain the full powder pick-up during the GTA cladding process. The powder pick-up increases with the WC powder feeding rate up to PFR = 40 g/min. After PFR = 40 g/min the powder pick-up retains within a stable range. The powder pick-up contains two components: WC reinforcement and dissolved WC. The dissolved WC in the matrix increases in parallel with the WC reinforcement when WC powder feed rate rises. Mid-range hardness values of the matrix with a maximum of 775HV0.2 were obtained.

Effect of WC in a steel matrix in overlap cladding trials

GTA cladding of overlap trials with WC powder and steel wire was successfully conducted. The surface of the WC reinforced layers increases in waviness as WC powder feeding rate rises. This effect could come from improving WC feeding during constant welding power input. The heat input into the steel melt could become too little for a certain amount of cold WC powder feeding. In that case the melt pool solidifies too early for powder capture. Possibilities of investigating this effect could be to pre-heat the WC powder or vary the power of the welding process. If the cladding layer is measured in full (with the peaks of the welding process), the WC reinforcement increases linearly with the WC

powder feeding rate to 15.85 % WC reinforcement at PFR = 40 g/min. Higher WC feeding rates show no significant improvement. Nevertheless, when only the useful area (cladding layer without peaks) is considered, the WC reinforcements increase to 17.48 % WC reinforcement at PFR = 80 g/min.

High W concentrations in the matrix indicated an even distribution of W in the matrix. This confirms a constant dissociation process during GTA cladding. An example of EBSD analysis with one sample gave the elementary structures in the matrix out as Fe bcc, Fe fcc, Fe_6W_6C WC and W_2C. However, a grid of Fe_6W_6C is built throughout the matrix. Within the grid, the two steel phases are Fe bcc (ferrite) and Fe fcc (austenite). The austenite phase increases in proportion with the rise of WC powder feeding. This could lead to a formation of martensite when deformed, known as the TRIP or TWIP effect. Nonetheless, more investigations into this possibility are needed. Hardness testing of the matrix shows the hardness in the range of 527HV0.2 and 757HV0.2 for all WC powder feeding rates. In contrast, the hardness of the particles is much greater, with values between 2137HV0.2 and 3036HV0.2 and a Young´s Modulus between 360 GPa and 385 GPa. Both matrix and particles show a huge contrast to the brake disc steel with values between 370HV0.2 and 401HV0.2.

Furthermore, the WC matrix hardness can be compared to the SiC matrix hardness. A similar volume feeding rate must be found. SiC was only fed in PFR = 22 g/min mass feeding rate, calculated over the density (see table 4-6), it equals a WC mass feeding rate of about 112 g/min. The closed WC feeding rate used in the experiments was 100 g/min. If the hardness is compared in one graph the distribution is as followed in figure 10-1.
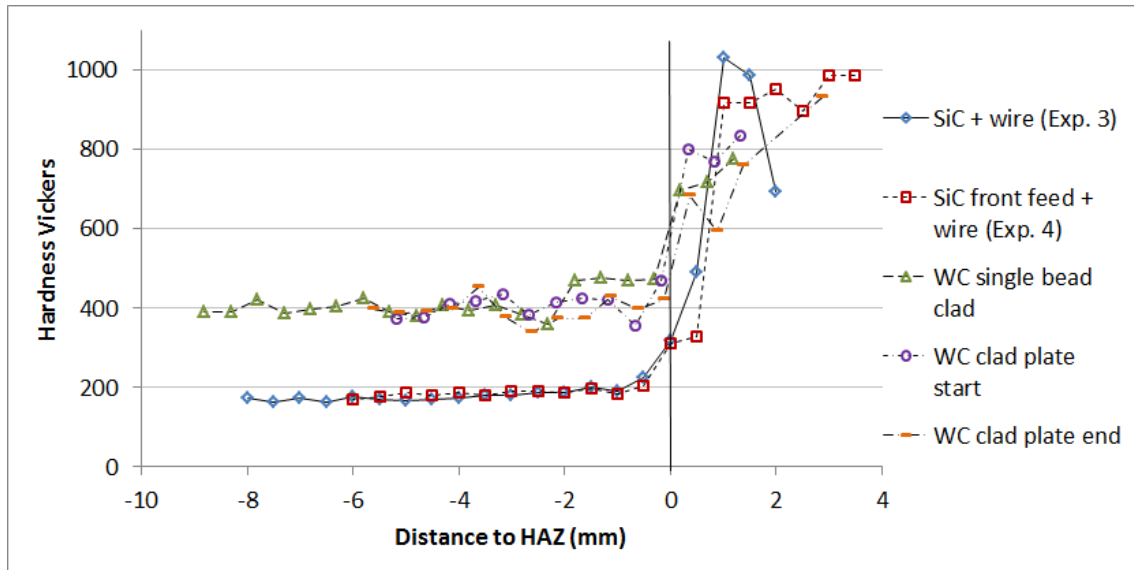
Figure 10-1: Hardness Vickers distribution of the SiC and WC cladding layer 0 mm to 3.5 mm is from HAZ to clad surface; 0 to − 8.8 mm is through HAZ into base material; SiC samples: tested with HV0.5, S275JR base plate, G4Si1 wire and PFR = 22 g/min; WC samples: tested with HV0.2, G-22 NiMoCr 5 6 base plate, G89 6 M Mn4Ni2CrMo wire and PFR = 100 g/min

Figure 10-1 shows the significant difference of the hardness of the two base materials with averages of about 171HV0.5 and 393HV0.2 for S275JR and G-22 NiMoCr 5 6, respectively. The difference between the HAZ and the base plate cannot be identified on the hardness distribution. There is a slightly increase of hardness in the HAZ when looking closer to the clad for all samples (between - 1 mm and 0 mm in figure 10-1). However, with the clad starting (0 mm distance in figure 10-1) the hardness of all samples expands significantly. The matrix of SiC proliferates at strongest with peak values of 1028HV0.5 and 984HV0.5 (for Exp. 3 and Exp. 4 from chapter 5, respectively). Despite the high strength wire and base material used for the WC clads the matrix of the WC cladding trails does not reach the peak values of the SiC matrix. The clad in single bead-on-plate (from section 6.3.2 of chapter 6) demonstrates a peak at 775HV0.2 (at 1.2 mm in figure 10-1) towards the clad surface. The peaks of the matrix of the WC clads in overlap on a plate (from section 7.5.1 of chapter 7) are higher than the single bead with 833HV0.2 and 929HV0.2 at the start of the plate as well as the end, respectively.

The WC matrix is softer than the SiC matrix because of WC reinforcement still existing in WC particle form. Lower WC feeding rates generate higher WC penetration of the weld pool. Nevertheless, figure 7-17 shows that WC in general delivers lower matrix values.

Effect of deposition arrangement

The progress of WC cladding layer size goes along the different, but still interpedendent, chapters with WC powder usage. Scaling up the clad starts from single bead-on-plate trials (see chapter 6) over overlap cladding of plates (see chapter 7) and small scale Pin-on-Disc discs (see chapter 8) to cladding layer on large 640 mm outer diameter railway brake discs (see chapter 9). A comparison in WC reinforcement and matrix hardness was made for PFR = 15 g/min.

Figure 10-2 shows the average WC reinforcement for each development stage.
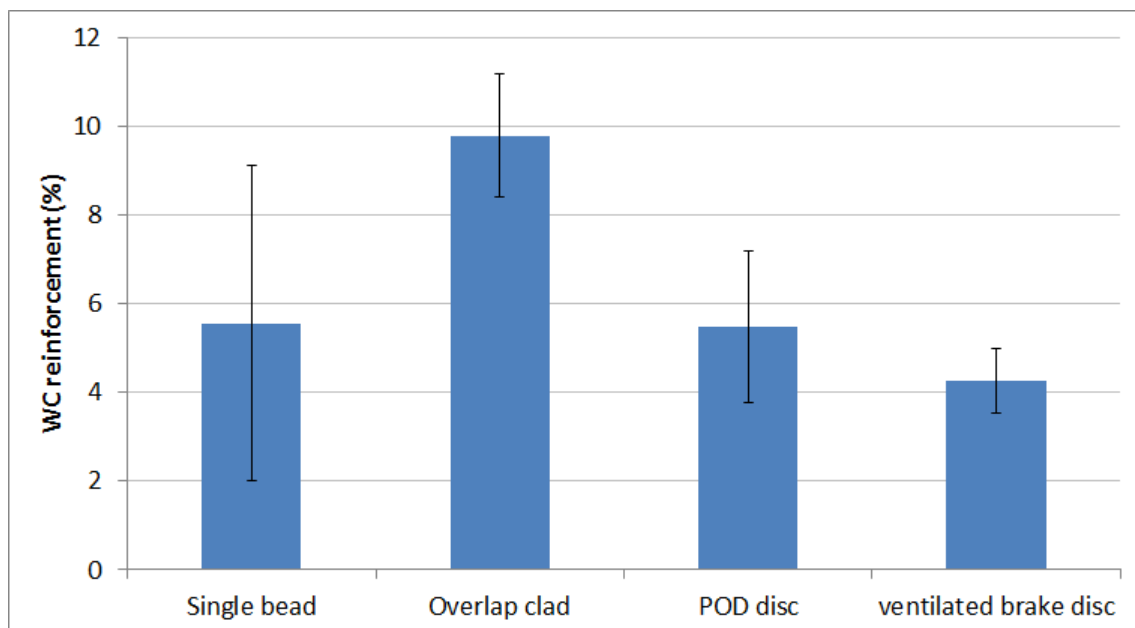
Figure 10-2: WC reinforcement comparison with PFR = 15 g/min, single bead from section 6.3.1 of chapter 6, overlap clad is useful area from section 7.4.1 of chapter 7, POD disc is average of area 3 and 4 of figure 8-8 from section 8.1 of chapter 8, ventilated brake disc is the average of the useful area of the 640 mm outer diameter brake disc in section 9.1 of chapter 9

Hereby, the material or process parameter changes were not taken into account. Only the area 3 and 4 of the measurements for the POD disc was taken into account (see figure 8-8 from section 8.1 of chapter 8), knowing the WC reinforcement has a gradient in the measurement areas. Single bead clads and POD spiral welds indicate a medium WC reinforcement with 5.55 % and 5.48 %, respectively. The overlapping clads on brake disc parts points out the highest average WC reinforcement with 9.78 %. The small sample area heated quickly up when covered with multi-beads. This and the supporting bead on the side helped to keep the WC particle retrieval high. In contrast to the overlapping clads is the large 640 mm outer diameter railway brake disc. The WC reinforcement was measured at three points and the average resulted in a low of 4.24 %. The temperature of the disc heated up to a constant which was too low to lengthen the weld pool enough. The PCE stayed low. But the constant temperature and making cladding tracks round by round (without break) hinders a gradient of WC reinforcement.

In summary, the different arrangements affect the thermal behaviour of the part, which then affects the PCE. The general behaviour of the WC incorporation (thus WC reinforcement) is there when you take into account the PCE. Therefore, single bead developments can be used to explore the WC reinforcement.

The matrix hardness of the cladding trails are illustrated in figure 10-3. A hardness testing was not carried out on the POD disc trail. Similar parameters in the comparison in figure 10-3 were the WC powder feeding rate with 15 g/min, the welding power (current and electrode to work piece distance (a)), travel speed with 0.3 m/min, the wire feed speed with 1.5 m/min and the base material G-22 NiMoCr 5 6.
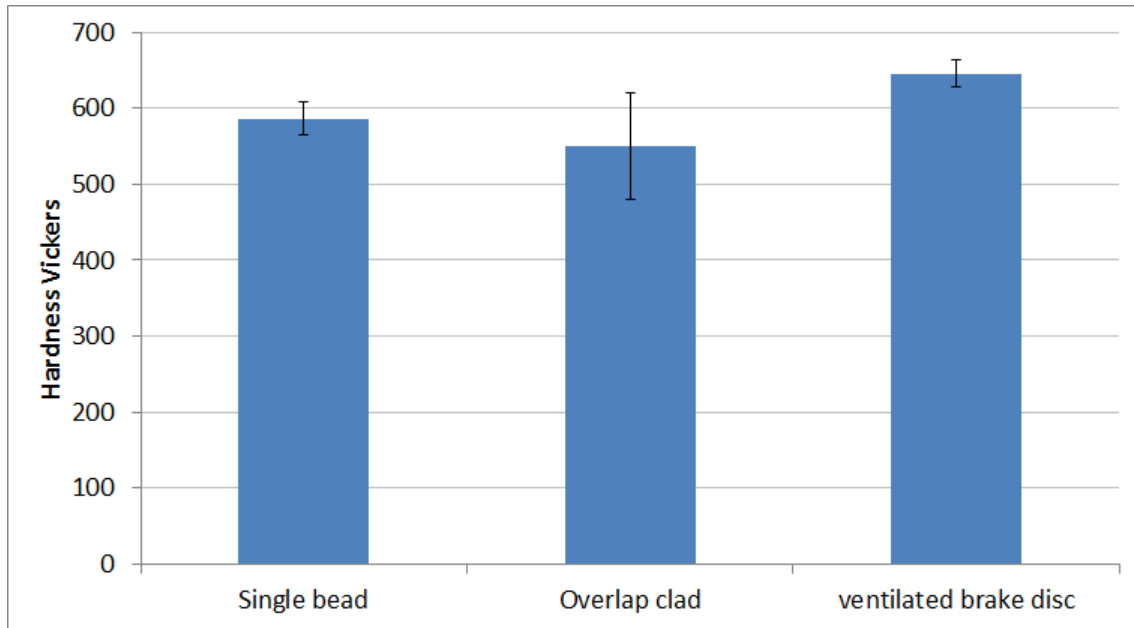
Figure 10-3: Hardness Vickers comparison of the average matrix hardness of a clad with PFR = 15 g/min, single bead from section 6.3.2 of chapter 6, overlap clad from section 7.5.1 of chapter 7, ventilated brake disc is the average of the values between 508.9 mm and 640 mm diameter of figure 9-13 in section 9.1 of chapter 9

As seen in figure 10-3, the matrix of the single bead clad turns out to have a middle range hardness average with 587HV0.2. Its tolerance is small and similar with the ventilated brake disc. The ventilated brake disc has representative results in the outer diameters between 508.9 mm and 640 mm. Despite of the G3Si1 mild steel used for the disc, the measured average hardness is the highest with 646HV. However, this could come from the use of a macro hardness test instead of a micro hardness test and some WC particles could be peripheral as well. The overlap clad has the lowest average hardness with 549HV0.2, but the measurement is from the highest sample rate. The tolerance increased with the number of samples measured. A higher WC reinforcement and WC matrix content was measured for the overlap clads than for the single beads. Contradicting, the average matrix hardness falls marginal by 37HV0.2. This could come from the ratio of austenite to ferrite in the microstructure. Austenite is softer; however, here it stands under stress and

forms martentiste through plastic deformation. This theory needs to be followed up in future work.

Wear performance of WC cladding layer

A tribology test performed on a Pin-on-Disc wear and friction machine confirmed friction coefficients between μ = 0.21 and μ = 0.52. These were achieved from different WC reinforcements, sliding speeds and pin pressures.

Cladding of real railway brake discs in two different sizes was successfully accomplished. The friction coefficient of the POD test was confirmed by the dynamometer testing with values between μ = 0.33 and μ = 0.46 (see Appendix K). Further testing with different WC reinforcements is recommended.

11 Conclusions and future work

This chapter is to summarise the conclusions drawn from each chapter and to give suggestions for future research.

11.1 Conclusions

During the study of the surface layer reinforcement structure and tribology testing, the following effects were seen:

- Using SiC or WC as the reinforcement ceramic in steel matrices leads to some dissolutions of the ceramic into the matrix. This leads to a hardening of the matrix material.

- Under these conditions SiC proved ineffective for this application as the particles completely dissolved in the matrix with no original SiC particles remaining in the bulk of the matrix.

- For WC the material captured was split roughly 50/50 between dissolved and reprecipitated material and WC particles.

- The powder capture efficiency (PCE) was very dependent on the weld pool size when using a constant powder feed position. If the thermal conditions make the weld pool shorter, the PCE went down.

- The total amount of WC incorporated in the weld increased with powder feed rate until a certain value was reached. This is due to the effect of cooling the weld pool by adding the powder leading to a reduction in the PCE. This could be compensated for by increasing the heat input rate by increasing the current or reducing the travel speed.

- For large area cladding layers, the amount of incorporated WC would increase with time as the component heated up. This can be compensated by reducing the current or increasing the travel speed.

- The measured friction coefficient of the clad layers is in the range that is suitable for railway brake disc applications using standard brake pad compositions.

- Cracking was observed in most samples with WC. This could be a problem for industrial applications.

The summary of impact was derived from the objectives shown in chapter 2.1 and are presented as follows:

- WC was identified as the best ceramic reinforcement out of the two investigated.
- The optimum welding process of these studied was GTAW.
- Process parameters that affect the characteristics of the reinforcement are:
    - Current
    - Voltage
    - Electrode profile
    - Geometric arrangement of powder and wire feeder
- The microstructural characteristics of the layers were determined.
- The friction coefficient of the layer was measured. It was not possible to characterise the wear behaviour.
- Cladding of a full size railway brake disc was demonstrated.

<u>Contribution to science and knowledge</u>

- Studied a new process combined wire and powder feeding with a GTAW heat source.
- Studied the interaction of SiC/WC MMC´s with low Ni/Cr matrix materials.
- Showed the importance of the thermal conditions on the PCE and how that may change both for different arrangements and during cladding over an extended period.
- Observed the dissociation of the ceramics into the matrix and provided analysis and interpretation of this effect.

11.2 Future work

Deeper analysis of the mechanical properties and wear properties of the hard surface generated with SiC on steel

To add to the knowledge of hard-surfacing with SiC on steel, the newly structured surface layer made by the GTA cladding process should be extended to full overlap trials. This would allow an evaluation of the mechanical properties within the newly built structure and its usage for wear resistance surfaces. A wear and friction test of the newly built structure could give the final verification.

Change from GTA cladding to Plasma-transferred arc (PTA) cladding with SiC ceramic as well as WC ceramic on steel

First autogenous PTA cladding trials have been performed with SiC on steel. As seen in figure 11-1, there are some SiC particles bonded on the steel plate.

Figure 11-1: autogenous PTA cladding trial with SiC feeding on steel; 1: steel base plate; 2: weld area; 3: HAZ; 4: bonded SiC particles; 5: steel and SiC mixed

Further investigation, with the addition of a matrix material, could lead to SiC particles bonded in steel. This would be a fundamental change in MMC cladding on steel. SiC is much cheaper and lighter than most ceramic particles used for MMC cladding. The cost reduction could be enormous.

Cladding with PTA has the potential to obtain low dilution and high deposition rates. An investigation into PTA cladding with WC particles and low Ni and Cr steel wire could have the potential to increase the productivity and quality of the WC MMC ceramic layer. Lower dilution during the cladding process could reduce cracking.

Variation of heat input during the GTA process to establish the dissociation behaviour of WC in steel.

The amount of WC reinforcement and dissolved WC has been shown to be similar in the cladding layer. The heat input of the GTA welding process could be influenced to change the cooling curve. This could lead to either a higher WC particle sinkage, or a higher WC reinforcement and lower dissolved WC. The following GTA process parameters are to be investigated:

- vary the power of the welding process
- pre-heat the base plate (e.g. 50°C, 100°C, 150°C)
- pre-heat the WC powder in the hopper
- pre-heat the wire material using an induction heater
- vary the impingement point of WC powder into the melt pool
- use hot-wire TIG

A study in hot-wire TIG was done for higher deposition rates and higher layer thicknesses [138]. This work could be adjusted for WC powder reinforcement of steel matrices.

Investigation of the austenite phases in the steel matrix of WC reinforced surface layers

WC reinforced surface layers made with medium or high WC powder feeding rates show a large proportion of austenite phases in the matrix. This could lead to a formation of martensite when deformed, known as the TRIP or TWIP effect. This might give an additional strengthening effect to the matrix by forming

martensite during deformation. A thorough investigation with tensile tests of the different surface layers could explain this phenomenon.

Different matrix materials for ceramic MMC cladding have the potential of cast iron cladding.

Railway brake discs are not always made of low carbon steel. Some of them are made of cast iron. Improved wear resistance surfaces on cast iron discs could keep the costs low and give the brake disc an improved lifetime. However, cast iron tends to crack during welding. A feasibility study was accomplished to understand the usage of different matrix materials such as Cu [139].
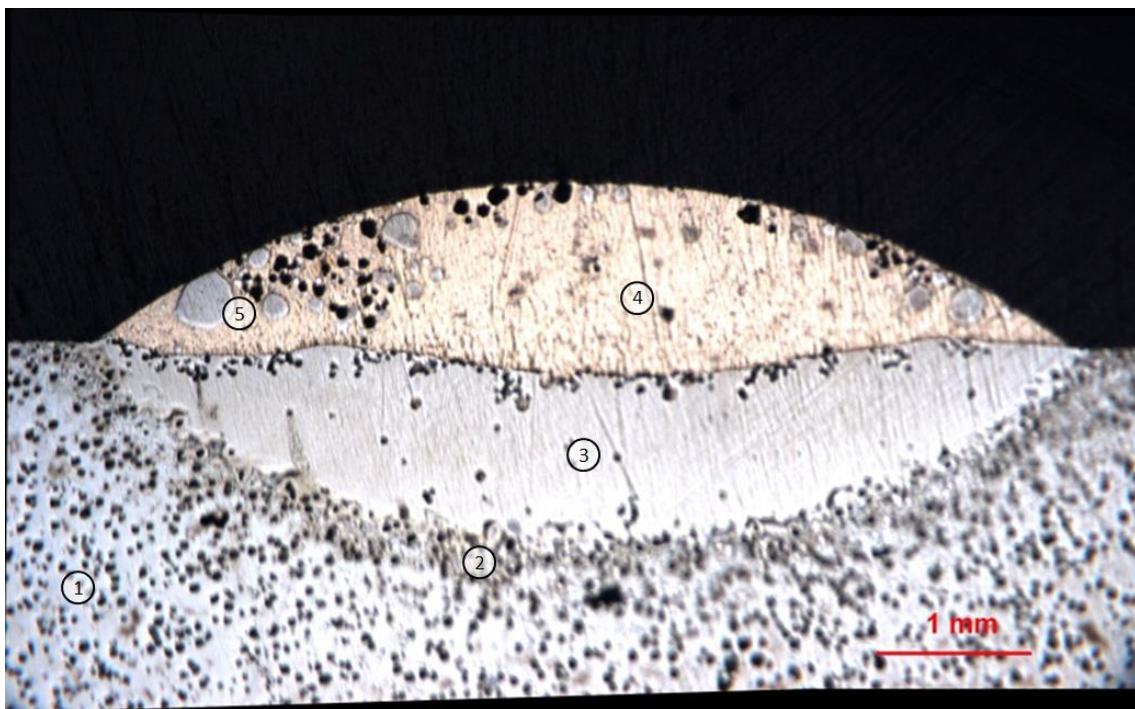
Figure 11-2: GTA cladding trials with WC ceramic and Cu matrix on cast iron [139]**; 1: Spheroidal cast iron base material; 2: HAZ; 3: Melted cast iron; 4: Mixture of cast iron and Cu matrix; 5: Particles of WC and graphite**

Although Cu would be one possibility as a matrix material on cast iron, other materials such as mild steel, aluminium or bronze need to be investigated. Modelling of the thermal properties during braking could give an indicator of the

right choice of material. The weldability of each matrix material to the base also needs to be examined. In the end, only wear and friction tests can determine the best fitting surface layer for braking.

Advanced production of surface cladding layers on round shapes with improved welding control

The POD test specimen surface layers were manufactured in a spiral weld. Nevertheless, the WC reinforcement was not well distributed. On the other hand, the brake disc surface layer was manufactured in overlapping cycles to obtain a well distributed WC reinforcement. A sophisticated welding automation with spiral shape welding could improve the layer's continuity and quality. Necessarily, it would be an arc-voltage-control system and a more ridged holder for the wire and powder feeder.

Dynamometer test regime with different ceramic surface cladding layers

In order to investigate the high wear loss observed in Appendix K, a full test series with selected WC reinforcements of brake discs is necessary. The surface cladding layer should be at least three layers high and a minimum of 10 different WC reinforcement area fractions need to be explored in the dynamometer test. Only conventional pads are recommended to be used on the layer to minimise hot spots and disc thickness variation (DTV). Two different brake pads, one organic and one synthetic, should be considered for each variation of WC reinforcement area fraction.

Furthermore, these dynamometer tests would also verify the crack resistance or crack fatigue for the ceramic MMC reinforced surface layer.

REFERENCES

[1] F. Wang and S. Williams, "Proposal for Investigation of Manufacturing Methods for High Performance Low Cost Brake Discs," Cranfield, 2009.

[2] P. Goodwin, "Laser cladding process of a train brake disc." LCT Laser Cladding Technology Ltd, Worksop, p. spoken communication, 2012.

[3] J. F. Ready, *Industrial Applications of Lasers (Second Edition)*, 2nd ed. Elsevier Inc, 1997, p. 599.

[4] F. Lancaster, *The Metallurgy of Welding, Brazing and Soldering*, 3rd ed. London, Bristol: George Allen and Unwin Ltd, 1974, p. 303.

[5] "Welding and allied processes — Welding positions (BS EN ISO 6947:2011)," London, Milton Keynes, 2011.

[6] W. Lucas, *Tig and plasma welding: process techniques, recommended practices, and applications*. Cambridge, UK: Angleterre: Abington, 1990, p. 111.

[7] S. Zheng, K. Min, and P. Dayou, "Twin Wire Gas Tungsten Arc Cladding," Singapore, 1999.

[8] J. Dave, "Evaluation of key welding parameters on weld dilution level of GTAW overlay welds," Cranfield University, 2009.

[9] E. O. Correa, "Weldability of Iron Based Powder Metal Alloys Using Pulsed GTAW Process," in *Arc Welding*, W. Sudnik, Ed. Rijeka, Croatia: InTech, 2011, pp. 109–126.

[10] W. Xinhong, C. Lin, Z. Min, and Z. Zengda, "Fabrication of multiple carbide particles reinforced Fe-based surface hardfacing layer produced by gas tungsten arc welding process," *Surf. Coatings Technol.*, vol. 203, no. 8, pp. 976–980, 2009.

[11] Y. C. Lin and S. W. Wang, "Wear behavior of ceramic powder cladding on an S50C steel surface," *Tribol. Int.*, vol. 36, pp. 1–9, 2003.

[12] Y. C. Lin and K. Y. Chang, "Elucidating the microstructure and wear behavior of tungsten carbide multi-pass cladding on AISI 1050 steel," *J. Mater. Process. Technol.*, vol. 210, pp. 219–225, 2010.

[13] S. Lu, H. Fujii, and K. Nogi, "Marangoni convection and weld shape variations in Ar–O2 and Ar–CO2 shielded GTA welding," *Mater. Sci. Eng.*, vol. 380, no. 1–2, pp. 290–297, Aug. 2004.

[14] J. F. Lancaster, *Metallurgy of welding*. Abington, Cambridge, 1999.

[15] B. Maamache, Y. Yahmi, and M. Bouaabdellah, "The effect of successive repairs on the weldment quality of API 5L X 70 steel pipes," in *Euromat 2011*, 2011, p. 1.

[16] B. C. S. Hunt, "Plasma transferred arc (PTA) surfacing of small and medium scale components - a review," *WELDING INSTITUTE MEMBERS REPORT*, vol. 364, no. March, Cambridge, UK, pp. 1 – 48, Mar-1988.

[17] J. F. Ready, "Chapter 15 Applications for Surface Treatment," in *Industrial Applications of Lasers*, San Diego, CA, USA: Academic Press Inc, 1997, pp. 373–383.

[18] B. K. Henon, "Technical paper: Hot wire narrow groove welding and cladding with nickel-based alloys," 2010.

[19] R. Anandkumar, A. Almeida, and R. Vilar, "Wear behavior of Al-12Si/TiB2 coatings produced by laser cladding," *Surf. Coatings Technol.*, vol. 205, pp. 3824–3832, 2011.

[20] G. Abbas and D. R. F. West, "Laser surface cladding of stellite and stellite-SiC composite deposits for enhanced hardness and wear," *Wear*, vol. 143, no. 2, pp. 353–363, 1991.

[21] Q. Zhang, J. He, W. Liu, and M. Zhong, "Microstructures and properties of Ceramic particles- Reinforced metal matrix composite layers produced by laser cladding," in *Lasers in Material Processing and Manufacturing II*, 2005, vol. 5629, pp. 1–8.

[22] S. Ala-kleme, P. Kivikytö-Reponen, J. Liimatainen, J. Hellman, and S.-P. Hannula, "Abrasive wear properties of metal matrix composites produced by hot isostatic pressing," *Proc. Est. Acad. Sci. Eng.*, vol. 12, no. 4, pp. 445–454, 2006.

[23] M. Belmonte, M. I. Nieto, M. I. Osendi, and P. Miranzo, "Influence of the SiC grain size on the wear behaviour of Al2O3/SiC composites," *J. Eur. Ceram. Soc.*, vol. 26, no. 7, pp. 1273–1279, Jan. 2006.

[24] E. Gemelli, A. Gallerie, F. C. T. Kopp, and N. H. A. Camargo, "Improved surface properties of D2 steel by laser surface alloying," *J. Mater. Sci.*, vol. 40, no. 21, pp. 5649–5653, 2005.

[25] M. H. KORKUT, O. YILMAZ, and S. BUYTOZ, "Effect of aging on the microstructure and toughness of the interface zone of a gas tungsten arc (GTA) synthesized Fe-Cr-Si-Mo-C coated low carbon steel," *Surf. Coat. Technol.*, vol. 157, no. 1, pp. 5–13, 2002.

[26]   M. J. Tobar, C. Álvarez, J. M. Amado, G. Rodríguez, and A. Yáñez, "Morphology and characterization of laser clad composite NiCrBSi-WC coatings on stainless steel," *Surf. Coatings Technol.*, vol. 200, no. 22–23 SPEC. ISS., pp. 6313–6317, 2006.

[27]   L. J. Prakash, "Weiterentwicklung von Wolframcarbid Hartmetallen unter Verwendung von Eisen- Basis-Bindelegierungen," TH Universität Karlsruhe, 1980.

[28]   W. Weißbach and U. Bleyer, *Werkstoffkunde und Werkstoffprüfung*, 12th ed., vol. 12. Wiesbaden: Vieweg Friedr. + Sohn Ver, 1998, p. 373.

[29]   "BS ISO 8486-1:1996 Bonded abrasives — Determination and designation of grain size distribution — Part 1: Macrogrits F4 to F220," London, 1996.

[30]   "BS ISO 6344-2:1998 Coated abrasives — Grain size analysis — Part 2: Determination of grain size distribution of macrogrits P12 to P220," London, 1998.

[31]   T. Mousavi, F. Karimzadeh, and M. H. Abbasi, "The Effect Of Al2O3 Content On The Formation Mechanism And Properties Of Niti-Al2O3 Nanocomposite Synthesized By Mechanical Alloying," in *Euromat 2011*, 2011, p. 1.

[32]   V. Shcheretskyi, O. Shcheretskyi, and A. Zatulovskyi, "Production of the Al-based composite materials with complex re-enforcement of micro - and nano-scale components by microgranules method," in *Euromat 2011*, 2011, p. 1.

[33]   L. H. Dai, Z. Ling, and Y. L. Bai, "Size-dependent inelastic behavior of particle-reinforced metal–matrix composites," *Compos. Sci. Technol.*, vol. 61, no. 8, pp. 1057–1063, Jun. 2001.

[34]   C.-W. Nan and D. R. Clarke, "The influence of particle size and particle fracture on the elastic/plastic deformation of metal matrix composites," *Acta Mater.*, vol. 44, no. 9, pp. 3801–3811, Sep. 1996.

[35]   J. M. Amado, M. J. Tobar, J. C. Alvarez, J. Lamas, and A. Yáñez, "Laser cladding of tungsten carbides (Spherotene) hardfacing alloys for the mining and mineral industry," *Appl. Surf. Sci.*, vol. 255, no. 10, pp. 5553–5556, Mar. 2009.

[36]   S. Zhang, F. Jiang, and W. Ding, "Microstructure and mechanical performance of pulsed current gas tungsten arc surface engineered composite coatings on Mg alloy reinforced by SiCp," *Mater. Sci. Eng. A*, vol. 490, no. 1–2, pp. 208–220, Aug. 2008.

[37] N. Chawla and Y. Shen, "Mechanical Behavior of Particle Reinforced Metal Matrix Composites," *Adv. Eng. Mater.*, vol. 6, no. 3, pp. 357–370, 2001.

[38] R. Prieto, J. M. Molina, J. Narciso, and E. Louis, "Thermal conductivity of graphite flakes–SiC particles/metal composites," *Compos. Part A Appl. Sci. Manuf.*, vol. 42, no. 12, pp. 1970–1977, Dec. 2011.

[39] D. Meresse, M. Watremez, L. Dubar, M. Siroux, and S. Harmand, "MODELLING REINFORCEMENT DEBONDING IN BRAKING CONDITIONS FOR SIMPLIFIED PHENOLIC MATRIX MATERIAL," in *Eurobrake 2012*, 2012, pp. 1–9.

[40] H. Tan, C. Liu, Y. Huang, and P. H. Geubelle, "The cohesive law for the particle/matrix interfaces in high explosives," *J. Mech. Phys. Solids*, vol. 53, no. 8, pp. 1892–1917, Aug. 2005.

[41] M. del R. M. Colmenares, "Investigation of WC-FeMn (Si) sintered hardmetal." Ruhr-Universität Bochum, Bochum, pp. 1–115, 2011.

[42] R. Kaplan and V. M. Bermudez, "Surface structure and metallization of SiC," in *Properties of Silicon Carbide*, G. L. Harris, Ed. Inspec, 1993, pp. 99–120.

[43] J. Y. Liu, J. Liu, X. Y. Gao, and M. L. Shi, "Study on Formation Mechanism of WC in Carburized Layer of Fe-1.57W Binary Alloy," *Adv. Mater. Res.*, vol. 154–155, pp. 11–18, Oct. 2011.

[44] E. Riedel, *Allgemeine und Anorganische Chemie.*, vol. 7. Berlin: Gruyter, 1999, p. 398.

[45] A. Dlouhy, G. Eggeler, and N. Merk, "A micromechanical model for creep in short fibre reinforced aluminium alloys," *Acta Metall. mater.*, vol. 43, no. 2, pp. 535–550, 1995.

[46] D. Kurumlu, "Mechanische und mikrostrukturelle Untersuchungen an einer kurzfaserverstärkten Aluminiumlegierung," Ruhr-Universität Bochum, 2010.

[47] J. M. Molina, J. Narciso, L. Weber, A. Mortensen, and E. Louis, "Thermal conductivity of Al–SiC composites with monomodal and bimodal particle size distribution," *Mater. Sci. Eng. A*, vol. 480, no. 1–2, pp. 483–488, May 2008.

[48] K. Seol, a. D. Krawitz, J. W. Richardson, and C. M. Weisbrook, "Effects of WC size and amount on the thermal residual stress in WC–Ni composites," *Mater. Sci. Eng. A*, vol. 398, no. 1–2, pp. 15–21, May 2005.

[49]   S. Hernik, "Double direction FGM modelling of brake disk against TEI," in *6th European Conference on Braking JEF 2010, Lille, France*, 2010, pp. 1–7.

[50]   L. Agudo, D. Eyidi, C. H. Schmaranzer, E. Arenholz, N. Jank, J. Bruckner, and A. R. Pyzalla, "Intermetallic Fe x Al y -phases in a steel/Al-alloy fusion weld," *J. Mater. Sci.*, vol. 42, no. 12, pp. 4205–4214, Mar. 2007.

[51]   H. Lee and Y. H. Jang, "Effect of the volume of a functionally graded material layer on frictionally excited thermoelastic instability," *Tribol. Int.*, vol. 49, pp. 103–109, May 2012.

[52]   Y. H. Jang and S. Ahn, "Frictionally-excited thermoelastic instability in functionally graded material," *Wear*, vol. 262, no. 9–10, pp. 1102–1112, Apr. 2007.

[53]   S. W. Lee and Y. H. Jang, "Effect of functionally graded material on frictionally excited thermoelastic instability," *Wear*, vol. 266, no. 1–2, pp. 139–146, Jan. 2009.

[54]   I. M. Hutchings, *Tribology Friction and Wear of Engineering Materials*. London, Bristol: Edward Arnold Hodder Headline Group, 1992, p. 273.

[55]   A. P. Lockyer, "The machine characteristics of a pin-on-disc machine," Cranfield University. School of Industrial and Manufacturing Science, Cranfield, 2003.

[56]   A. P. Lockyer, "Investigation of the influence of the design of a pin-on-disk tribometer on friction data," Cranfield University. School of Industrial & Manufacturing Science, Cranfield, 2007.

[57]   B. Bhushan, *Introduction to Tribology*. New York, Columbus: John Wiley & Sons, 2002, p. 732.

[58]   M. B. Peterson, J. J. Florek, and R. E. Lee, "Sliding characteristics of metals at high temperatures," *Am. Soc. Lubr. Eng. Trans.*, vol. 3, pp. 101 – 109, 1960.

[59]   D. Kopeliovich, "Mechanisms of wear," *SubsTech Substances & Technology*, 2014. [Online]. Available: http://www.substech.com/dokuwiki/doku.php?id=mechanisms_of_wear. [Accessed: 17-Dec-2014].

[60]   X. H. Wang, S. W. Zhang, D. G. Wang, and N. Wu, "Research on Worn Mechanism of Disc-Brake Pair Materials for Drilling Rig," in *CIST2008 & ITS-IFToMM2008*, 2008, pp. 338–343.

[61] A. Cristol, Y. Desplanques, W. Osterle, and G. Degallaix, "Coupling between thermal localisation and friction mechanisms: heat accumulation effect," in *6th European Conference on Braking JEF 2010*, 2010, p. 9.

[62] X. Dong, S. . Jahanmir, and L. K. Ives, "Wear transition diagram for silicon carbide," *Tribol. Int.*, vol. 28, no. 8, pp. 559 – 572, 1995.

[63] R. Anandkumar, A. Almeida, R. Colaço, R. Vilar, V. Ocelik, and J. T. M. De Hosson, "Microstructure and wear studies of laser clad Al-Si/SiC(p) composite coatings," *Surf. Coatings Technol.*, vol. 201, no. 24, pp. 9497–9505, 2007.

[64] a. T. Alpas and J. Zhang, "Effect of SiC particulate reinforcement on the dry sliding wear of aluminium-silicon alloys (A356)," *Wear*, vol. 155, no. 1, pp. 83–104, May 1992.

[65] R. Anandkumar, R. Colaço, V. Ocelik, J. T. M. De Hosson, and R. Vilar, "Microstructure and abrasive wear studies of laser clad Al-Si/SiC composite coatings," in *5th Hungarian Conference on Materials Science, Testing and Informatics*, 2007, vol. 537–538, pp. 89–95.

[66] B. J. Zheng, X. M. Chen, and J. S. Lian, "Microstructure and wear property of laser cladding Al+SiC powders on AZ91D magnesium alloy," *Opt. Lasers Eng.*, vol. 48, no. 5, pp. 526–532, May 2010.

[67] R. N. Rao and S. Das, "Wear coefficient and reliability of sliding wear test procedure for high strength aluminium alloy and composite," *Mater. Des.*, vol. 31, no. 7, pp. 3227–3233, Aug. 2010.

[68] K. M. Shorowordi, A. S. M. A. Haseeb, and J. P. Celis, "Velocity effects on the wear, friction and tribochemistry of aluminum MMC sliding against phenolic brake pad," *Wear*, vol. 256, no. 11–12, pp. 1176–1181, 2004.

[69] R. J. K. Wood, "Tribology of thermal sprayed WC–Co coatings," *Int. J. Refract. Met. Hard Mater.*, vol. 28, no. 1, pp. 82–94, Jan. 2010.

[70] M. Watremez, J. P. Bricout, B. Marguet, and J. Oudin, "Friction, Temperature, and Wear Analysis for Ceramic Coted Brake Disks," *J. Tribol.*, vol. 118, no. 3, pp. 457 – 465, 1996.

[71] A. I. . Som, "Science: New plasma torches for PTA-surfacing," *Pat. Weld. J.*, no. 7, pp. 44–48, Mar. 1999.

[72] A. Liu, M. Guo, and H. Hu, "Improved Wear Resistance of Low Carbon Steel with Plasma Melt Injection of WC Particles," *J. Mater. Eng. Perform.*, vol. 19, no. 6, pp. 848–851, Oct. 2009.

[73] A. P. Patel, "The Study of the Deposition of Hardfacing Alloys using the GTAW Process," Cranfield University, 1985.

[74] S. Buytoz and M. Ulutan, "In situ synthesis of SiC reinforced MMC surface on AISI 304 stainless steel by TIG surface alloying," *Surf. Coatings Technol.*, vol. 200, no. 12–13, pp. 3698–3704, Mar. 2006.

[75] Q. Wang and X. Li, "Effects of Nb, V, and W on Microstructure and Abrasion Resistance of Fe-Cr-C Hardfacing Alloys," *Weld. J.*, vol. 89, no. 7, p. 133–s–139–s, 2010.

[76] A. M. Jacobsen, "Migatronic Automation INSTRUCTION MANUAL DIGITAL PLASMA COMMANDER 240 - 320 & 400 DC 240 - 320 & 400 AC/DC," MIGATRONIC AUTOMATION A/S Knosgaardvej 112, Aabybro, 2007.

[77] S. C. Jensen, "INSTRUCTIONS MANUAL KT-4 Cold Wire Feed Unit," Aabybro, 2004.

[78] "Sulzer Metco TWIN-10-C Powder Feeder Product Manual," Wohlen, 2003.

[79] V. Lüthy, "Sulzer Metco TWIN-10-C Powder Feeder circuit diagram," Wohlen, 2000.

[80] "Sulzer Metco TWIN-10-C Powder Feeder APS Powder Insert," Wohlen, 2002.

[81] "BS EN 10027-1:2005 Designation system for steels. Part 1: Steel names," British Standard, Milton Keynes, London, 2005.

[82] "EN 10025-2:2004 Hot rolled products of structural steels— Part 2: Technical delivery conditions for non-alloy structural steels," London, Milton Keynes, 2004.

[83] "BS EN 440:1995 Welding consumables— Wire electrodes and deposits for gas shielded metal arc welding of non alloy and fine grain steels — Classification," British Standard, Milton Keynes, London, 1995.

[84] "NF F 11-416 Disques de frein avec couronne en acier," Paris, 1994.

[85] "BS EN ISO 16834:2012 Welding consumables — Wire electrodes , wires , rods and deposits for gas shielded arc welding of high strength steels — Classification (ISO 16834:2012)," London, Milton Keynes, 2012.

[86] "IIW Doc. IX-535-67 Technical Report Carbon Equivalent and Weldability," Cambridge, UK, 1967.

[87] J.-H. Song and H.-J. Kim, "Sliding wear performance of cobalt-based alloys in molten-Al-added zinc bath," *Wear*, vol. 210, no. 1–2, pp. 291–298, 1997.

[88] S. Guicciardi, C. Melandri, F. Lucchini, and G. de Portu, "On data dispersion in pin-on-disk wear tests," *Wear*, vol. 252, no. 11–12, pp. 1001–1006, 2002.

[89] K. Miyoshi and D. H. Buckley, "Surface chemistry and friction behavior of the silicon carbide (0001) surface at temperatures to 1500 C," Nasa, Washington, D.C., 1981.

[90] N. Langhof, R. Voigt, H. Mucha, and W. Krenkel, "The Effect of Residual Silicon in CMC Brake Pads on Friction and Wear," in *6th European Conference on Braking JEF 2010*, 2010, pp. 1–8.

[91] H. O. Pierson, "Characteristics and Properties of Silicon Carbide and Boron Carbide," in *Handbook of Refractory Carbides and Nitrides Properties, Characteristics, Processing and Applications*, 1996, pp. 137 – 155.

[92] H. O. Pierson and N. J. Park Ridge, *Handbook of Refractory Carbides and Nitrides Properties, Characteristics, Processing and Applications*. Norwich, N.Y.: Noyes Publications, 1996, p. 340.

[93] C. T. Lynch, *Handbook of Materials Science Volume II: Metals, Composites, and Refractory Materials*. Cleveland, Ohio: CRC Press, Inc., 1975, p. 440.

[94] M. Heinzler, R. Kilgus, and F. Näher, *Tabellenbuch Metall (mit Formelsammlung). Tabellen, Formeln, Übersichten, Normen*, vol. 41. Haan-Gruiten: Europa Lehrmittel Verlag, 2002, p. 336.

[95] M. Rühle, A. G. Evans, M. F. Ashby, and J. P. Hirth, *Metal-Ceramic Interfaces: Proceedings of workshop "Bonding, Structure and Mechanical Properties of Metal-Ceramic Interfaces."* Santa Barbara: Pergamon Press, 1990.

[96] G. L. Harris, R. Kaplan, V. M. Bermudez, and A. O. Konstantinov, *Properties of Silicon Carbide*. London, Stevenage: Institution of Electrical Engineers, 1995.

[97] Y. MIZOKAWA, S. NAKANISHI, and S. MIYASE, "AES Study of the Reaction between a Thin Fe-Film and b-SiC (100) Surface," *Jpn. J. Appl. Phys.*, vol. 28, no. 12, pp. 2570–2575, 1989.

[98] J. C. Schuster, "Silicon Carbide and Transition Metals: A Critical Evaluation of Existing Phase Diagram Data Supplemented by New

Experimental Results," *Int. J. Refract. Met. Hard Mater.*, vol. 12, pp. 173–177, 1994.

[99]   R. Telle, H. Salmang, and H. Scholze, "10.5.2 Siliciumcarbid," in *Keramik*, 7th ed., 2007.

[100]   J. Wang, J. Xing, L. Cao, W. Su, and Y. Gao, "Dry sliding wear behavior of Fe3Al alloys prepared by mechanical alloying and plasma activated sintering," *Wear*, vol. 268, no. 3–4, pp. 473–480, Feb. 2010.

[101]   L. Mortelette, Y. Desplanques, M. Chamignon, O. Martin, M. Henrion, J. F. Brunel, and P. Dufrénoy, "Friction material for reduction of windturbine brake squeal noise.," in *6th European Conference on Braking JEF 2010*, 2010, pp. 1–7.

[102]   S. Herbst, S. Williams, and S. Ganguly, "A Feasibility Study on Manufacturing of Functionally Graded Structures Using SiC Ceramic Powder in a Steel-Based Matrix by Gas Tungsten Arc Welding (GTAW)," *steel Res. int.*, vol. 83, no. 6, pp. 546–553, 2012.

[103]   S. Herbst, S. Williams, and S. Ganguly, "A feasibility study on manufacturing of functionally graded structures using SiC ceramic powder in a steel based matrix by Gas Tungsten Arc Welding (GTAW)," in *Euromat 2011*, 2011, no. Figure 1, p. 1.

[104]   M. Wegst, *Stahlschlüssel-Taschenbuch: Wissenswertes über Stähle*. Marbach am Neckar: Stahlschlüssel; Auflage: 19. Auflage, 2001, p. 203.

[105]   W. Domke, *Werkstoffkunde und Werkstoffprüfung*, vol. 10., verb. Berlin: Cornelsen Lehrbuch, 2001, p. 424.

[106]   A. O. Konstantinov, "Sublimation growth of SiC," in *Properties of Silicon Carbide*, no. January, London, Stevenage: Institution of Electrical Engineers Michael Faraday House, Six Hills Way, Stevenage, Herts. SG1 2AY, United Kingdom, 1995, pp. 170–203.

[107]   R. Kaplan and V. M. Bermudez, *Surface structure, metallization and oxidation of SiC*. London, Stevenage: Institution of Electrical Engineers Michael Faraday House, Six Hills Way, Stevenage, Herts. SG1 2AY, United Kingdom, 1993, pp. 99–120.

[108]   ESK-SIC GmbH, "Material Safety Data Sheet According to 91/155 EEC and ISO-Standard 11014 Silicon Carbide (SiC)," Frechen-Grefrath, 2007.

[109]   Saint-Gobain, "SIKA ABR III Black Silicon Carbide grains for abrasive applications," Saint-Gobain, Lillesand, 2007.

[110] "Procedures: Copper Welding," Plainview NY, 2010.

[111] "Electrode Tip Geometry Selection," *Pro-Fusion*, 2013. [Online]. Available: http://www.pro-fusiononline.com/tungsten/geometry.htm. [Accessed: 23-Sep-2013].

[112] B. Torres, M. a. Garrido, a. Rico, P. Rodrigo, M. Campo, and J. Rams, "Wear behaviour of thermal spray Al/SiCp coatings," *Wear*, vol. 268, no. 5–6, pp. 828–836, Feb. 2010.

[113] F. Lusquiños, J. Pou, F. Quintero, and M. Pérez-Amor, "Laser cladding of SiC/Si composite coating on Si–SiC ceramic substrates," *Surf. Coatings Technol.*, vol. 202, no. 9, pp. 1588–1593, Feb. 2008.

[114] K. M. Shorowordi, T. Laoui, A. S. M. A. Haseeb, J. P. Celis, and L. Froyen, "Microstructure and interface characteristics of B4C, SiC and Al2O3 reinforced Al matrix composites: A comparative study," *J. Mater. Process. Technol.*, vol. 142, no. 3, pp. 738–743, 2003.

[115] T.-Y. Kuo and Y.-D. Lin, "Effects of Different Shielding Gases and Power Waveforms on Penetration Characteristics and Porosity Formation in Laser Welding of Inconel 690 Alloy," *Mater. Trans.*, vol. 48, no. 2, pp. 219–226, 2007.

[116] "Standard Hardness Conversion Tables for Metals Relationship Among Brinell Hardness, Vickers Hardness, Rockwell Hardness, Superficial Hardness, Knoop Hardness, and Scleroscope Hardness," West Conshohocken, United States, 2002.

[117] M. S. Alam, "STRUCTURAL INTEGRITY AND FATIGUE CRACK PROPAGATION LIFE ASSESSMENT OF WELDED AND WELD-REPAIRED STRUCTURES," Louisiana State University and Agricultural and Mechanical College, 2005.

[118] M. T. Rush, P. A. Colegrove, Z. Zhang, and D. Broad, "Liquation and post-weld heat treatment cracking in Rene 80 laser repair welds," *J. Mater. Process. Tech.*, vol. 212, no. 1, pp. 188–197, 2012.

[119] S. Angelinas, P. Gibbens, P. Roberts, M. Taylor, K. Stevens, and M. Tirovic, "Improvement of Convective Heat Dissipation from Commercial Vehicle Disc Brakes by Implementing Geometric Design Alternatives," in *Eurobrake 2012*, 2012, no. m, pp. 1–10.

[120] R. Tione, F. DeMaria, A. Grasso, A. Melhan, and B. Kurek, "REAL TIME DISK TEMPERATURE SIMULATION FOR RAILWAIS APPLICATIONS . LYFE CYCLE COST AND SAFETY BENEFITS," in *Eurobrake 2012*, 2012, pp. 1–10.

[121] S. ANGELINAS, "DESIGN STRATEGIES FOR THE THERMO-MECHANICAL OPTIMISATION OF HEAVY-DUTY BRAKE DISCS," CRANFIELD UNIVERSITY, 2013.

[122] G. Krauss, *Steels: Processing, Structure, and Performance*. Materials Park, OH 44073-0002: ASM International, 1933, p. 613.

[123] A. V Ilyasov, A. A. Ryzhkin, and V. V Ilyasov, "ELECTRONIC STRUCTURE AND CHEMICAL BOND IN CARBIDES CRYSTALLIZING IN THE Fe – W – C SYSTEM," *J. Struct. Chem.*, vol. 49, no. 5, pp. 827–834, 2008.

[124] W. B. Pearson, *A Handbook of Lattice Spacings and Structures of Metals and Alloys*. London: Pergamon Press, 1958, p. 1044.

[125] "ULSAB Ultra Light Steel Auto Body Phase 2: Findings," Middletown, OH, USA; Brussels, Belgium, 1998.

[126] C. Zhenda, L. I. M. L. Chewh, and Q. Mingh, "Materials Processing Technology Laser cladding of WC - Ni composite," *Mater. Sci.*, 1996.

[127] P. Raninger, S. Marsoner, W. Ecker, R. Ebner, and T. Antretter, "Characterization of damage at the friction surface of wheel mounted brake disks for railway applications," in *Eurobrake 2012*, 2012, no. 7, p. 12.

[128] A. J. Day, M. Tirovic, and T. P. Newcomb, "Thermal effects and pressure distributions in brakes," *Proc. Inst. Mech. Eng. Part D J. Automob. Eng.*, vol. 205, no. 3, pp. 199–206, 1991.

[129] M. Walczak, D. Pieniak, and M. Zwierzchowski, "The tribological characteristics of SiC particle reinforced aluminium composites," *Arch. Civ. Mech. Eng.*, pp. 4–11, Jun. 2014.

[130] E. European Aluminium Association, "Applications – Chassis & Suspension – Brake system 5 Brake system," 2011.

[131] "New Brake Pad Technology for Aluminum Discs," *Honeywell International Inc*, 2014. [Online]. Available: http://www.honeywell-frictionmaterials.com/original-equipment/innovations/brake-pad-technology-for-aluminum-discs.html. [Accessed: 12-Jul-2014].

[132] C. Hanyaloglu, B. Aksakal, and J. D. Bolton, "Production and indentation analysis of WC/Fe–Mn as an alternative to cobalt-bonded hardmetals," *Mater. Charact.*, vol. 47, no. 3–4, pp. 315–322, Sep. 2001.

[133] M. Tirovic and G. P. Voller, "Commercial vehicle brake cooling - Ventilated disc or ventilated wheel carrier?," in *International Conference -*

Braking 2004: Vehicle Braking and Chassis Control, 2004, vol. Leeds, pp. 241–250.

[134] J. K. N. Murthy, D. S. Rao, and B. Venkataraman, "Effect of grinding on the erosion behaviour of a WC – Co – Cr coating deposited by HVOF and detonation gun spray processes," *Wear*, vol. 249, pp. 592–600, 2001.

[135] M. A. Maleque, S. Dyuti, and M. M. Rahman, "Material Selection Method in Design of Automotive Brake Disc," in *Proceedings of the World Congress on Engineering 2010*, 2010, vol. III, pp. 1–5.

[136] G. Bozic, A. Alnaqi, P. Brooks, and D. Barton, "THERMAL CHARACTERISATION OF LIGHTWEIGHT BRAKE ROTORS FOR PASSENGER CAR APPLICATION USING A SMALL SCALE BRAKE DYNAMOMETER AND ONE DIMENSIONAL MODEL," in *Eurobrake 2012*, 2012, pp. 1–10.

[137] D. Gultekin, M. Uysal, S. Aslan, M. Alaf, M. O. Guler, and H. Akbulut, "The effects of applied load on the coefficient of friction in Cu-MMC brake pad / Al-SiCp MMC brake disc system," *Wear*, vol. 270, no. 1–2, pp. 73–82, 2010.

[138] R. CHEN, "EFFECTS OF CLADDING HEAT INPUT ON TMCP STEEL PIPES," CRANFIELD UNIVERSITY, 2012.

[139] O. Asipa, "DEVELOPMENT OF A FUNCTIONALLY GRADED FRICTION SURFACE FOR WEAR RESISTANT ENGINEERING APPLICATIONS," CRANFIELD UNIVERSITY, 2012.

[140] E. Henry and S. Williams, "COMPONENT PRODUCTION THROUGH THE Metal Additive Layer Manufacture," Cranfield University, Welding Engineering Research Centre, College Road, Bedfordshire, MK43 0AL, UK, 2010.

[141] P. M. S. ALMEIDA, "PROCESS CONTROL AND DEVELOPMENT IN WIRE AND ARC ADDITIVE MANUFACTURING," CRANFIELD UNIVERSITY, 2012.

[142] S. Angelinas, M. Tirovic, and P. Roberts, "Development Strategy for Thermo-Mechanical and Weight Improvements in Commercial Vehicle Brake Discs," in *Eurobrake 2013*, 2013, pp. 1–10.

APPENDICES

The appendices below are essential material to the thesis. With the help of this material all work can be followed up and explained.

Appendix A List of Figures in the Appendix

Appendix B List of Tables

Appendix C List of Equations

Appendix D Pre-study of Gas Metal Arc Welding for cladding

This appendix is an examination to understand the physical limits of the GMA welding process for cladding. It should only be seen as a short summary of a Gas Metal Arc Welding process for cladding.

D.1 GMAW process parameters

The idea for the brake disc cladding was a FGM made of a ceramic reinforcement in a steel matrix, whereby more matrix material in the first layer should bring a strong metallurgical bonding on the base material. This is already demonstrated in figure 4-1. An assumption of a minimum single layer height of 1.0 mm has been made to give the necessary material composition gradient. A study with a Gas Metal Arc Welding (GMAW) process and active gas has been executed to understand the challenges of this minimum layer height under the following conditions:

- Power source: Lincoln Electrics Power Wave 455 / STT
- Shielding gas: Ar/CO_2 (2.5%) BOC Specshield CO_2/Ar mixture, see appendix L.4, figure_apx I-14
- Gas flow (L/min): 15
- Base material: S275JR, see appendix L.1, figure I-1.
- Deposited material: EN 440.94 G3Si1 (AWS:A5.18ER70S-6), see appendix L.2.1, figure_apx I-5.
- Electrode diameter (mm): 1.0
- Torch angle: 90° (perpendicular to surface)
- TRIM value: 1.00

For the base material, a surface ground base with the following measurements was used:

$$V = c \times e \times h \qquad\qquad \textbf{(D-1)}$$

Whereby:　　V　　　　　　　　　– volume

　　　　　　　c, e　　　　　　　– side of the plate

　　　　　　　h　　　　　　　　– depth

- V (mm³) = 140 mm x 140 mm x 12 mm = 235200 mm³

D.2 Experimental results

The variables were the travel speed (TS) and the wire feed speed to travel speed ratio (WFS/TS).

$$\frac{WFS}{TS} ratio = \frac{WFS}{TS} \qquad \textbf{(D-2)}$$

Whereby:　　TS　　　　　　　– Travel speed

　　　　　　　WFS　　　　　　　– Wire feed speed

　　　　　　　WFS/TS ratio　　– wire feed speed to travel speed ratio

The lowest bead layer height achieved with the GMAW welding system is 2.55 mm. A transverse cross section of the single weld bead was prepared and is shown in figure_apx d-1. The travel speed was maintained at 0.7 m/min and the WFS/TS ratio was 21.4.
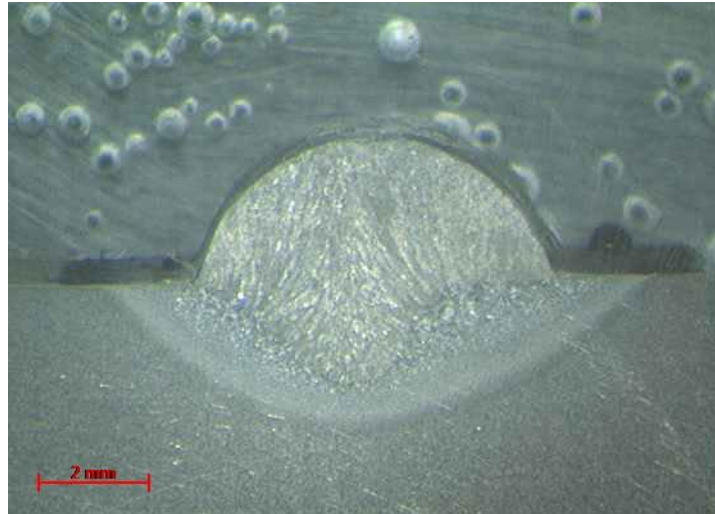
Figure_apx D-1: Single bead-on-plate GMAW weld

Important metallurgical parameters for cladding are the aspect ratio (AR) and the dilution (DL), which are explained in depth in chapter 6. The aspect ratio of AR = 0.132 and the dilution of DL = 0.375 are promising although the values are relatively low. A cladding trial of five overlaps was tested. Figure_apx D-2 illustrates the overlap clads achieved with the GMAW welding process. The first weld has a straight half-round shape, whereby the following welds are leaned against the first and stay in an incline.
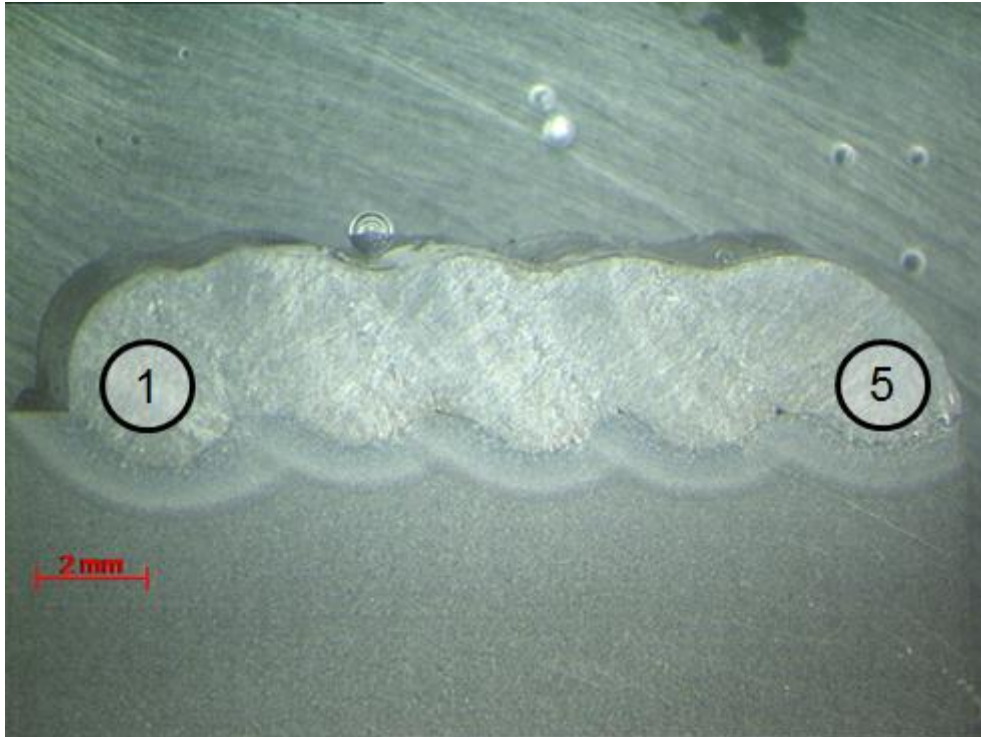
Figure_apx D-2: GMAW overlap welds with an offset of 3 mm; weld 1 (first) and weld 5 (last) are marked

The surface of the cladding trial shows a small waviness which causes a low effort in post-processing, e.g. flat grinding, for a smooth surface. A high deposition rate of 370 g/min was achieved from a wire only deposition.

D.3 Discussion

Despite the achievements, a deeper literature research confirmed a layer height of 1.0 mm is difficult to accomplish [140]. Almeida clarifies in his thesis that the minimum layer height reached with the Lincoln Electrics Power Wave 455 / STT was 1.78 mm [141]. His WFS/TS ratio was WFS/TS = 10 with a wire feed speed of WFS = 8 m/min. The WFS/TS ratio of WFS/TS = 21.4 has therefore been chosen for a high deposition rate. Even with a power source proposed for cladding, the Fronius CMT, a layer height of minimum 1.96 mm was accomplished [141]. Thus it was not possible to achieve the assumption made. GTAW is known as a welding process with wire feed speed independent from the welding power. Therefore it should be possible to reach lower layer heights.

D.4 Conclusion

Functional graded structures need low cladding layer heights, therefore the GMAW and GTAW processes were tested. Minimum layer heights of 1.78 mm can be achieved with the GMAW process. Nevertheless, with the GTAW process layer heights lower than that are achievable, as the current and voltage are controlled independently from the wire feed speed.

Appendix E Calibration of the motion axis

The distances on the 5-axis rig shown in figure 4-2 b) are driven and controlled by a Trio Motion controller. Torque is given on the axis by stepper motors for movements. Stepper motors have a set of steps for one rotation which give an accurate drive of the axle to a certain point. For this movement, the number of steps for a specific distance must be measured and entered into the motion coordinator. On the 5-axis rig the Motion Coordinator MC216 from Trio Motion is mounted. The software of the system is "Motion Perfect", also from Trio Motion. The following program code has been introduced in the "start-up" program to maintain the correct distance:

Linear axis

```
BASE(2)                 → Axle number
SERVO=OFF               → Axis is in run open loop
UNITS = 3210 ' steps/mm → 3210 steps (or units) are 1 mm
SPEED=5                 → demand speed in units per second
ACC(500)                → acceleration in units per second square
DEC(500)                → deceleration in units per second square
```

Rotating axis

```
BASE(3)                 → Axle number
SERVO=OFF               → Axis is run in open loop
UNITS=11870 'rpm        → 11870 steps (or units) are 1 round
SPEED=5                 → demand speed in units per second
ACC(50)                 → acceleration in units per second square
DEC(50)                 → deceleration in units per second square
```

Travel speeds are obtained over the motion controller. This adjustment makes it possible to operate the axis at a constant speed for a set distance.

Appendix F Calculation of the error bar

For statistical analysis, the standard derivation was used to calculate the error of the measurements. The standard deviation of a set of numbers $\{x_1, x_2, ..., x_n\}$ is:

$$D_n = \sqrt{\frac{1}{n-1} \sum_{i=1}^{n} (x_i - m(X))^2} \qquad (D_n >= 0)$$

<div align="right">(F-3)</div>

Whereby:

D_n - is the standard deviation,

n – number of data elements

x_i - is the data element, and

m(X) - is the chosen measure of central tendency of the data set – here the arithmetic mean.

The standard derivation approves a respectable error bar for the experiments made.

Appendix G Cross section sample preparation and light microscope tolerances

All cross section samples were prepared according to the standardised method described here. The preparation and analysis is sectioned into the following:

- Cross section sample preparation
- Light microscope and its tolerances
- Single weld bead sample analysis
- Multi-bead overlap clad analysis

G.1 Cross section sample preparation

Sectioning for microsections needs to be done with care. Overheating of the cutting face can cause microstructure changes and, therefore, misleading results. This was prevented by the use of the correct cutting speed, load and coolant. A rubber bonded abrasive SiC cutting-wheel (MetPrep Type T) was recommended for samples with carbide inclusions. This cutting wheel was used for all samples. After sectioning the samples out of the areas described in the chapters 5, 6, 7 and 9 above, the samples were usually mounted into resin. The epoxy resin is there to fix the samples tilted on the cross section and to give every sample a standard shape. Large samples (above 40 mm longest length) were prepared in un-mounted condition. Grinding of the samples was obtained to reduce the surface roughness. For this task, the following rotating grinding and polishing machine was used:

- Make: Buehler
- Model: Metaserv Cross Section Polisher
- with Motopol

The Metaserv machine can rotate the grinding disc and the sample holder in the same direction or opposite. Cooling water can be supplied when the lubrication is too low. The following table shows the grinding stages:

Table_apx G-1: Grinding stages of cross section preparation

Stage	Grinding paper	Rotating direction	Water cooling	grinding disc speed	sample holder force	typical duration
-	mesh	-	-	rpm	N	min
1	P120	opposite	On	150 – 180	89 - 178	3
2	P120	opposite	On	150 – 180	89 - 178	3
3	P120	opposite	On	150 – 180	89 - 178	3
4	P220	opposite	On	150 – 180	89 - 178	3
5	P1000	opposite	On	150 – 180	89 - 178	3

Cleaning of the sample and sample holder with water was necessary after every stage. This prevented contamination of the next stage with grinding particles and carbides. Additional examination under the microscope can ensure that particles are removed and sawing or grinding grooves from the former stage are removed. Stage one, two and three are the same. However, it was found that strict water cleaning at this stage helped significantly to reduce further scratches. The grinding paper was changed as soon as it was worn out or after each stage.

The next step was polishing the surface down to a surface roughness with scratches of a maximum width of 3 µm. This is necessary to get a clear picture of the microstructure. Polishing was utilised on the same machine after thorough cleaning. The following parameters were used:

- Polishing disc cloth: Struers MD-Dur
- Polishing suspension: MetPrep diamond compound in disposable syringes, size 3 µm, green
- Rotating direction: same direction
- Lubrication / cooling: MetPrep diamond lubricant, alcohol base, blue
- Grinding disc speed: 110 rpm – 140 rpm

- Sample holder force: 89 N – 133 N
- Typical duration: 1 min – 2 min

After polishing, the following activities were: cleaning with water and cotton wool, drying with isopropanol and a hot air stream. Sometimes the polishing had to be repeated for up to five times. The samples were ready if unetched samples were required. Otherwise a 1 min etching with 2 % nitric acid (HNO_3) in alcohol was utilised.

G.2 Light microscope and its tolerances

Microscopic images were captured with the following light microscope:

- Nikon Optiphot-66 optical microscope
- Qimaging Go-3-CLR-10 high-resolution digital colour CMOS camera
- AcQuis image acquisition software for microscopy (version 4.01.10) from Syncroscopy.

The tolerances were measured and the results depend on the objective lens of the revolver. The following results are achieved:

Table_apx G-2: Light microscope tolerances for each objective lens

lens	tolerance
-	μm
2.5 x	± 3
5 x	± 2
10 x	± 1
20 x	± 0.5
40 x	± 0.5

G.3 Single weld bead sample analysis

Cross-sectional cuts through single weld bead were photographed at 2.5 times magnification under the light microscope described in section G.2. A single weld bead usually has a larger profile than the area visible in the microscope. Therefore, several photos had to be taken in a planar area without refocussing to stich them together to one image. The stitching was performed with the Microsoft Image Composite Editor software (Version 1.4.4.0). An example of the stitching can be seen in Figure_apx G-1.
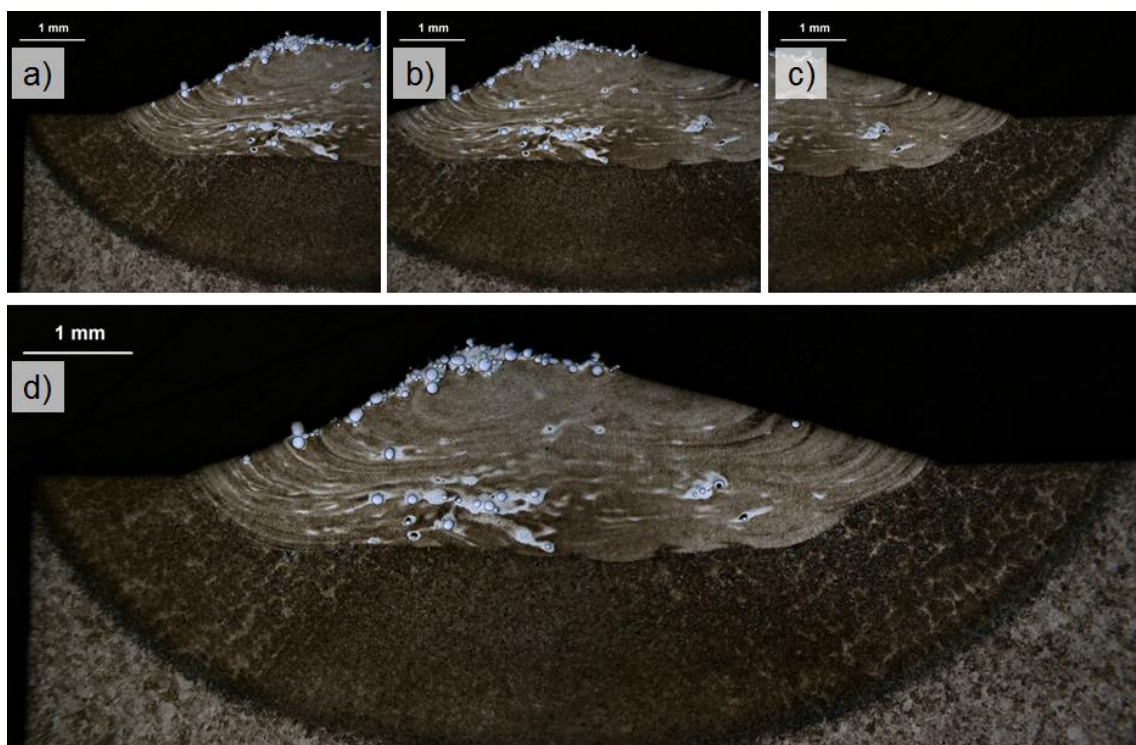
Figure_apx G-1: Single bead stitching of three microscope images; a) left side of the weld bead; b) middle of the weld bead; c) right side of the weld bead; d) result of stitching with Microsoft Image Composite Editor software

The dimensions, as described in chapter 6 section 6.2.2, are measured on the stitched images with the software AxioVision (Version: AxioVs 40 V 4.8.2.0) from Carl Zeiss MicroImaging GmbH.

G.4 Multi-bead overlap clad analysis

A clad area with overlapping weld beads was measured for its dimensions by imaging software. Microsections were taken and prepared as described in section G.1. Photos of the full sample were taken with the microscope detailed in section G.2 at 2.5 times magnification. The photos were stitched together with the method described in section G.3. The measurements of the dimensions were made similar to the analysis of single weld bead. An example of the measurement is shown in Figure_apx G-2.
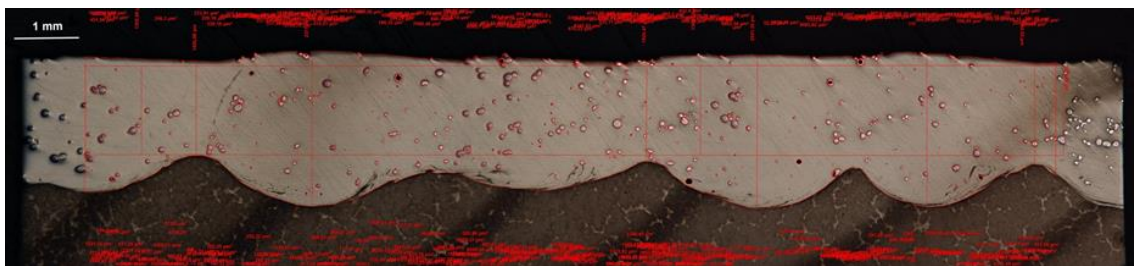
Figure_apx G-2: Multi-bead overlap clad with dimension measurements

The software AxioVision (Version: AxioVs 40 V 4.8.2.0) from Carl Zeiss MicroImaging GmbH was used to get the dimensions of lengths and areas. These were given in a spreadsheet by the program and were used in the calculations as described in each relevant chapter of the thesis.

Appendix H Scanning Electron Microscope and its detection sensors

A Scanning Electron Microscope (SEM) was used to take some images and analyse the chemical elements and elementary cells of selected areas of specimen. The following detection sensors were used:

- Secondary electron detector   for imaging
- Energy-dispersive X-ray detector   for EDS chemical element analysis
- Electron backscatter diffraction detector   for crystallographic analysis of elementary cells.

The specimens were prepared as described in section G.1 of chapter Appendix G.

The SEM used was the following:

- Environmental Scanning Electron Microscope FEI XL30 from Philips
- EDS hardware is Oxford Instruments, Swift-ED, model 6650 with the software Aztec
- EBSD hardware is Oxford Instruments, NordlysNano EBSD detector with the software AZtecHKL EBSD.

SEM images were made in High Vac mode (high vacuum) and with a working distance of 10 mm. The resolution of images made by the secondary electron detector is dependent on the voltage (usually 20kV), the spot size, and scan speed used. The highest resolution which can be achieved is 20nm in High Vac mode and 100nm in ESEM mode. The same parameters influence the tolerance of EDS analysis. Additionally, the analysis dead time has an important influence and was set at 100 s for all analysis. However, chemical elements with a presence of <0.1 wt% are difficult to resolve against the background noise and can be seen as the limit of the detector.

The EBSD detector had to be calibrated for the elementary cells to be analysed. This is explained in section H.1 below.

H.1 EBSD detector calibration

Electron backscatter diffraction (EBSD) scan is done at selected points. Some assumptions had to be made prior to the EBSD detector calibration to limit the factors of the calibration. The focus of the EBSD scan is on the microstructure of the matrix of the WC cladding layer in overlap. It was proven that WC particles partially dissolve in the Fe matrix during GTAW cladding. The EBSD scan should give the structure in which W and C builds up in the matrix during solidification and cooling down.

Before any EBSD scan could happen, the Densities of Electronic States at the Fermi Level of each phase to be investigated had to be found. This background data had been originated for the phases Fe bcc (body-centred cubic iron, Ferrite), Fe fcc (face-centered cubic iron, Austenite), Fe_3W_3C, Fe_6W_6C, WC and W_2C [41], [123]. The crystal structure and the lattice spacing distance can be obtained from the literature. Figure_apx H-1 shows the crystal structure of Fe bcc, Fe fcc, WC, W_2C, Fe_3W_3C and Fe_6W_6C.
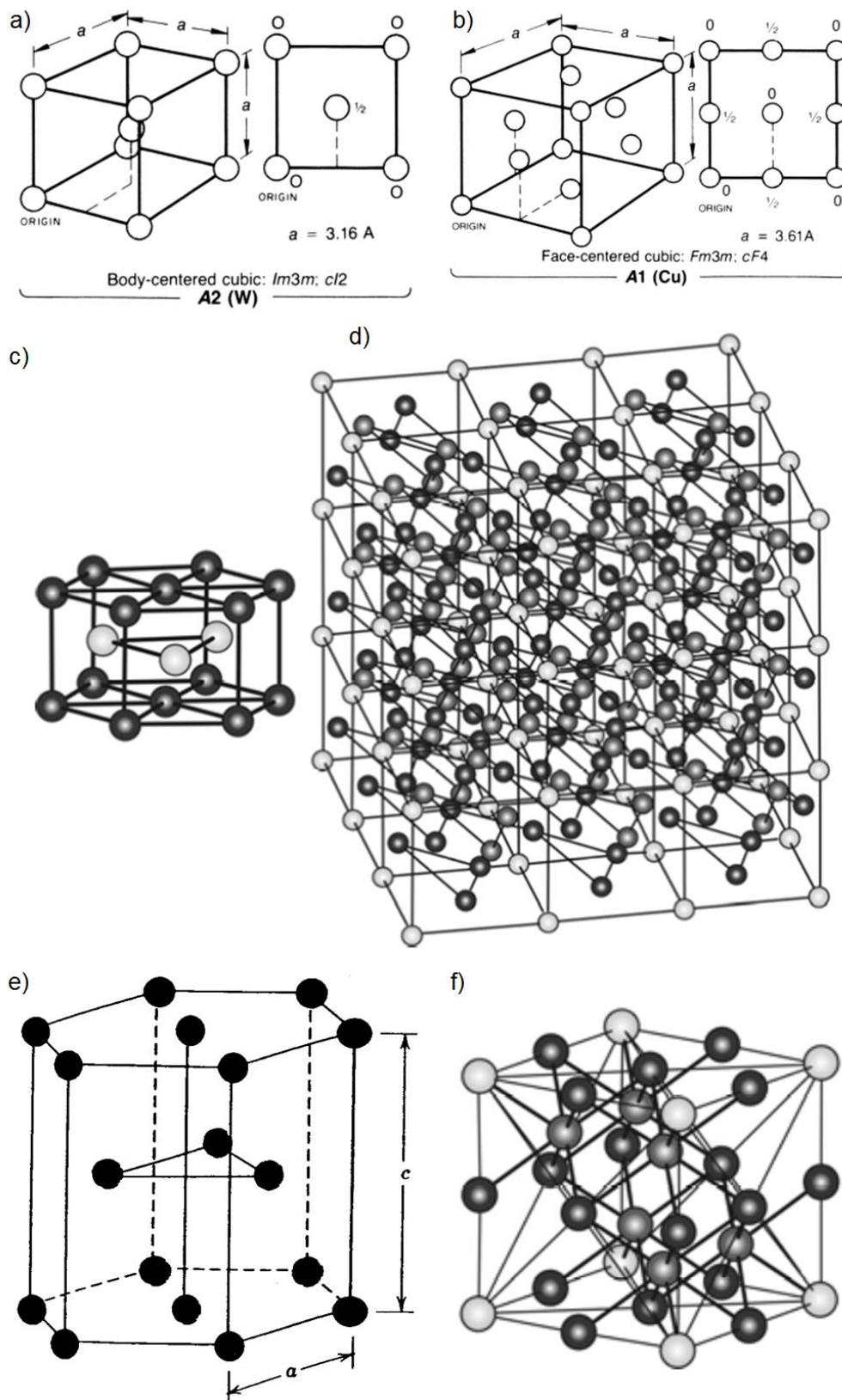
Figure_apx H-1: Crystal structures of possible Fe-W-C combinations; a) Fe bcc [122]; **b) Fe fcc** [122]; **c) WC** [123]; **d) Fe3W3C** [123]; **e) W2C** [124]; **f) Fe6W6C** [123]

The crystal structure and lattice spacing distance are used afterwards to obtain a calibration diffraction pattern. The calibration images can be seen in Figure_apx H-2.
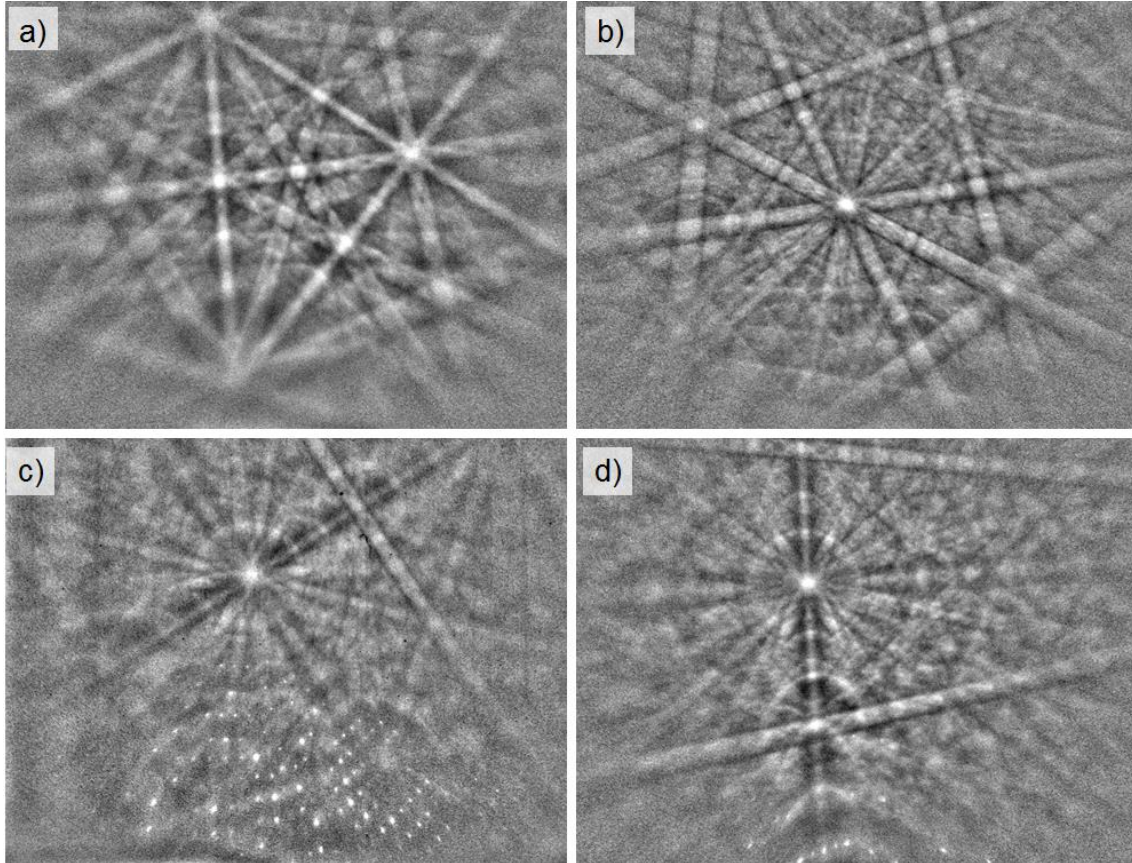
Figure_apx H-2: EBSD calibration diffraction pattern on different phases; a) Fe bcc; b) Fe$_6$W$_6$C; c) WC; d) W$_2$C

The calibration diffraction pattern enabled the EBSD detector to identify the phases which were measured by quantity and location. A coloured picture gives an overview of the majority of elementary cells in each location.

Appendix I Hardness testing equipment

The hardness tests in this thesis were performed according to Vickers and Leeb. The following testing equipment was used:

- Hardness Vickers tester: ZHV1 micro-hardness tester from Zwick Roell with the hardware and software C.A.M.S. with traverse options (Version: C.A.M.S._Win V.3.2) from Newage Testing Instruments, Inc..
- Leeb rebound tester: MH310, portable hardness tester from Mitech Co. Ltd..

The micro-hardness tester according to Vickers was tested for its tolerance. The results are shown in section I.1 below. Whereby, the Leeb rebound tester had a hardness measurement range between 170HLD and 960HLD and an accuracy of ±4HLD, which equals ±5HRC or ±1HB according to the specification.

I.1 Hardness Vickers machine tolerance

The micro-hardness tester ZHV1 from Zwick Roell for tests according to Vickers was examined on its tolerance. For this was a standardised test plate used which had a certified hardness of 356.1HV1. The plate was tested with a load of 0.2 kg to keep the tolerance test consistent with the measurements in this thesis. The 24 indentations made are shown in Figure_apx I-1.
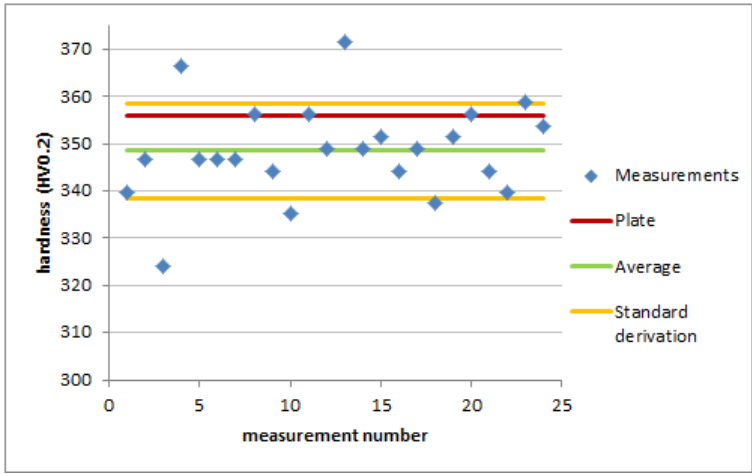
Figure_apx I-1: Hardness Vickers tolerance test against a certified plate with 356.1HV1.

As shown in Figure_apx I-1, the average of the measurements (green line) is 348.5HV0.2. The standard derivation of the measurements is 10HV0.2. It shows the spreading of the hardness measurements. Therefore, the standard derivation is shown as a positive and negative value from the average in Figure_apx I-1 in yellow. The plate value is shown as a red line in Figure_apx I-1 and is 7.6HV above the average value measured.

Appendix J Overview overlap clad surface increased WC feed rate

The cladding trails in overlap from chapter 7 section 7.2 are given in enlarged figures in this section. This can make the surface description in table 7-1 clearer to the reader and may point out important parts not seen on the small images.
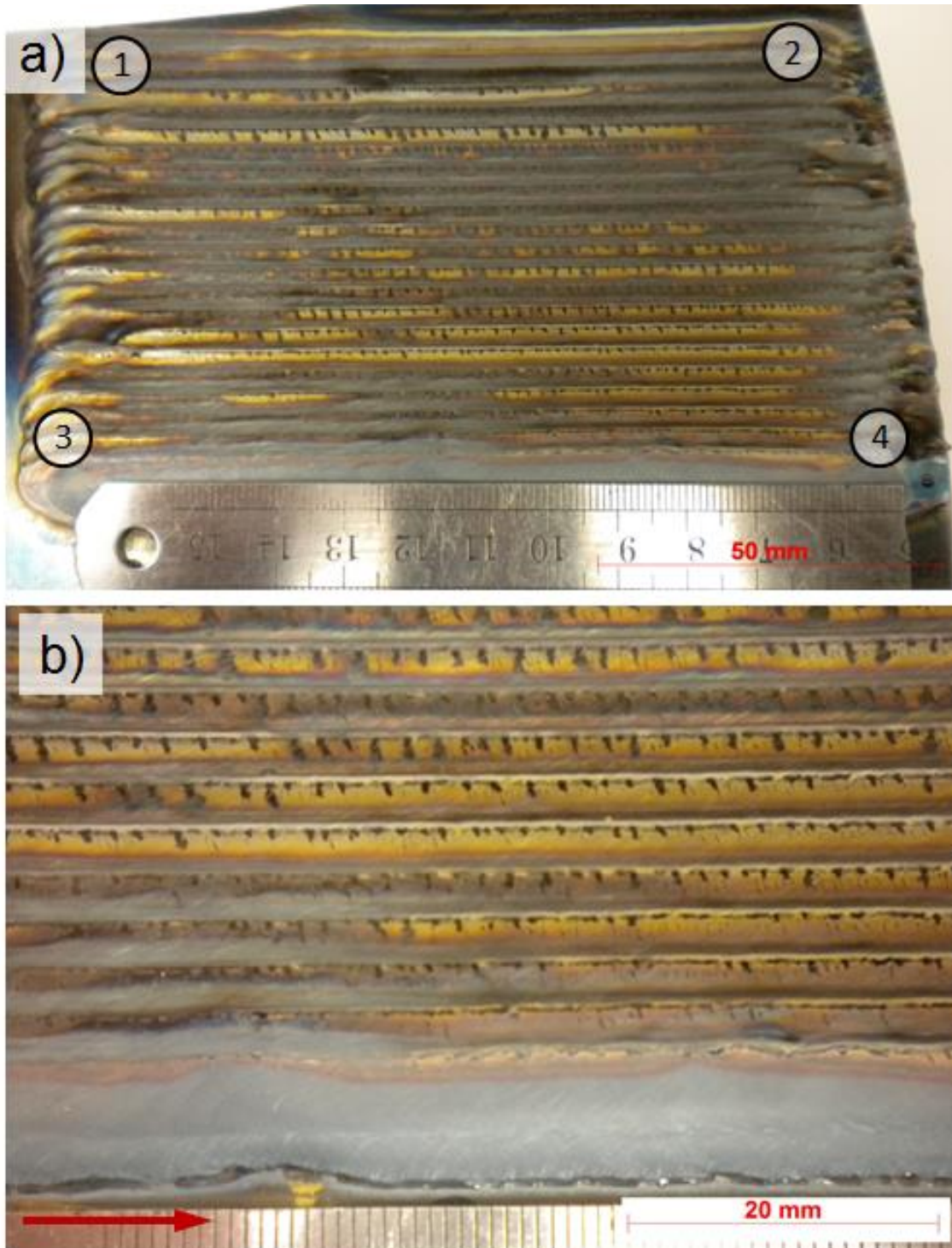
Figure_apx J-1: Cladding trial in overlap; a) PFR = 0 g/min; b) magnified image of a); 1: Beginning of first weld; 2: finish of first weld; 3: beginning of last weld; 4: finish of last weld; red arrow: welding direction
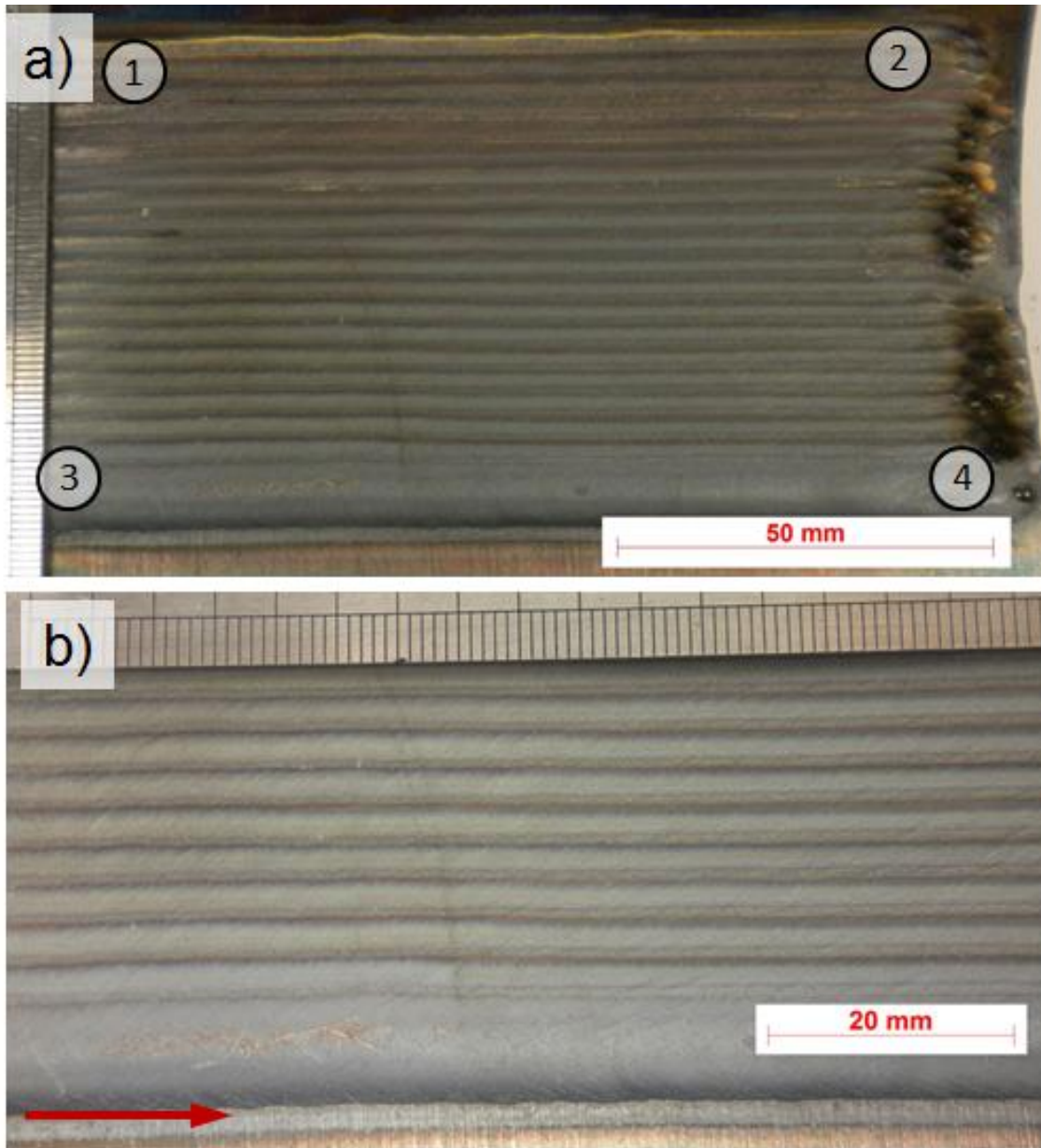
Figure_apx J-2: Cladding trial in overlap; a) PFR = 5 g/min; b) magnified image of a); 1: Beginning of first weld; 2: finish of first weld; 3: beginning of last weld; 4: finish of last weld; red arrow: welding direction
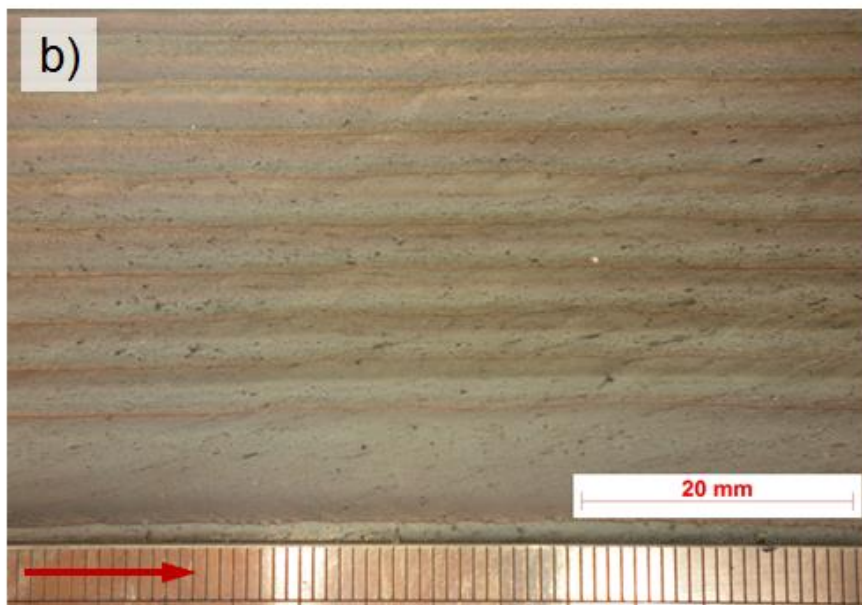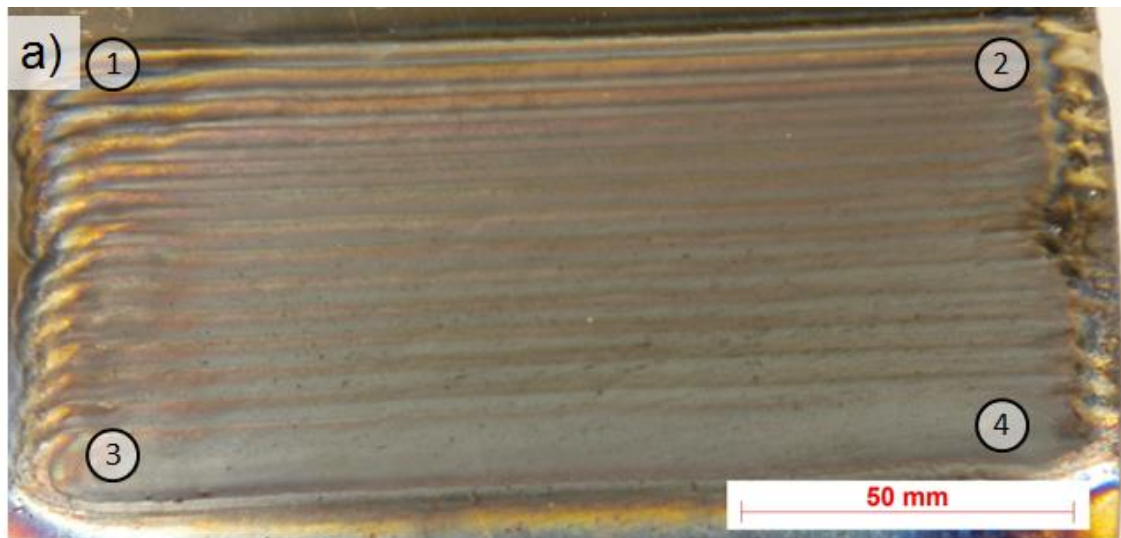
Figure_apx J-3: Cladding trial in overlap; a) PFR = 10 g/min; b) magnified image of a); 1: Beginning of first weld; 2: finish of first weld; 3: beginning of last weld; 4: finish of last weld; red arrow: welding direction
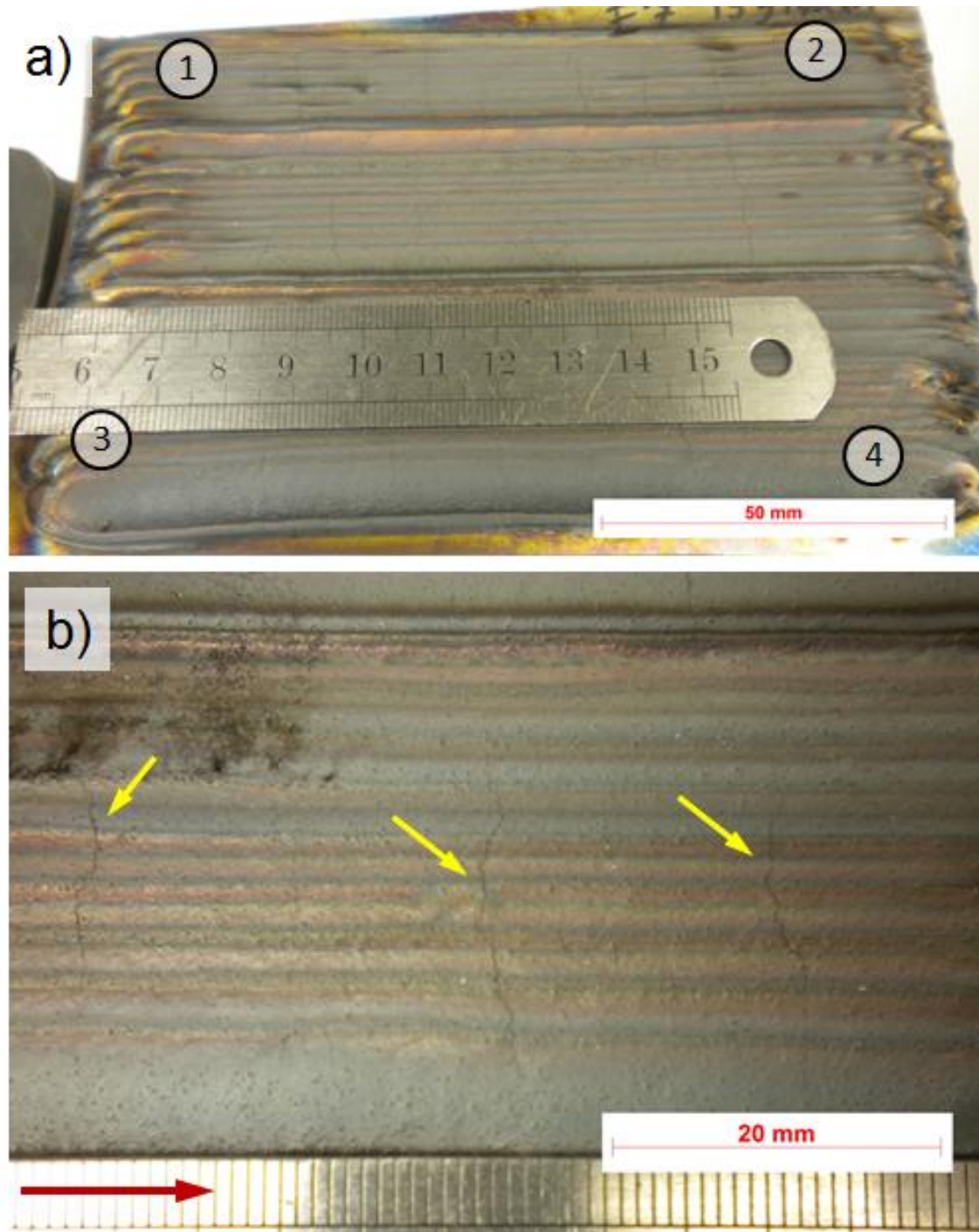
Figure_apx J-4: Cladding trial in overlap; a) PFR = 15 g/min; b) magnified image of a); 1: Beginning of first weld; 2: finish of first weld; 3: beginning of last weld; 4: finish of last weld; red arrow: welding direction; yellow arrows: check cracks
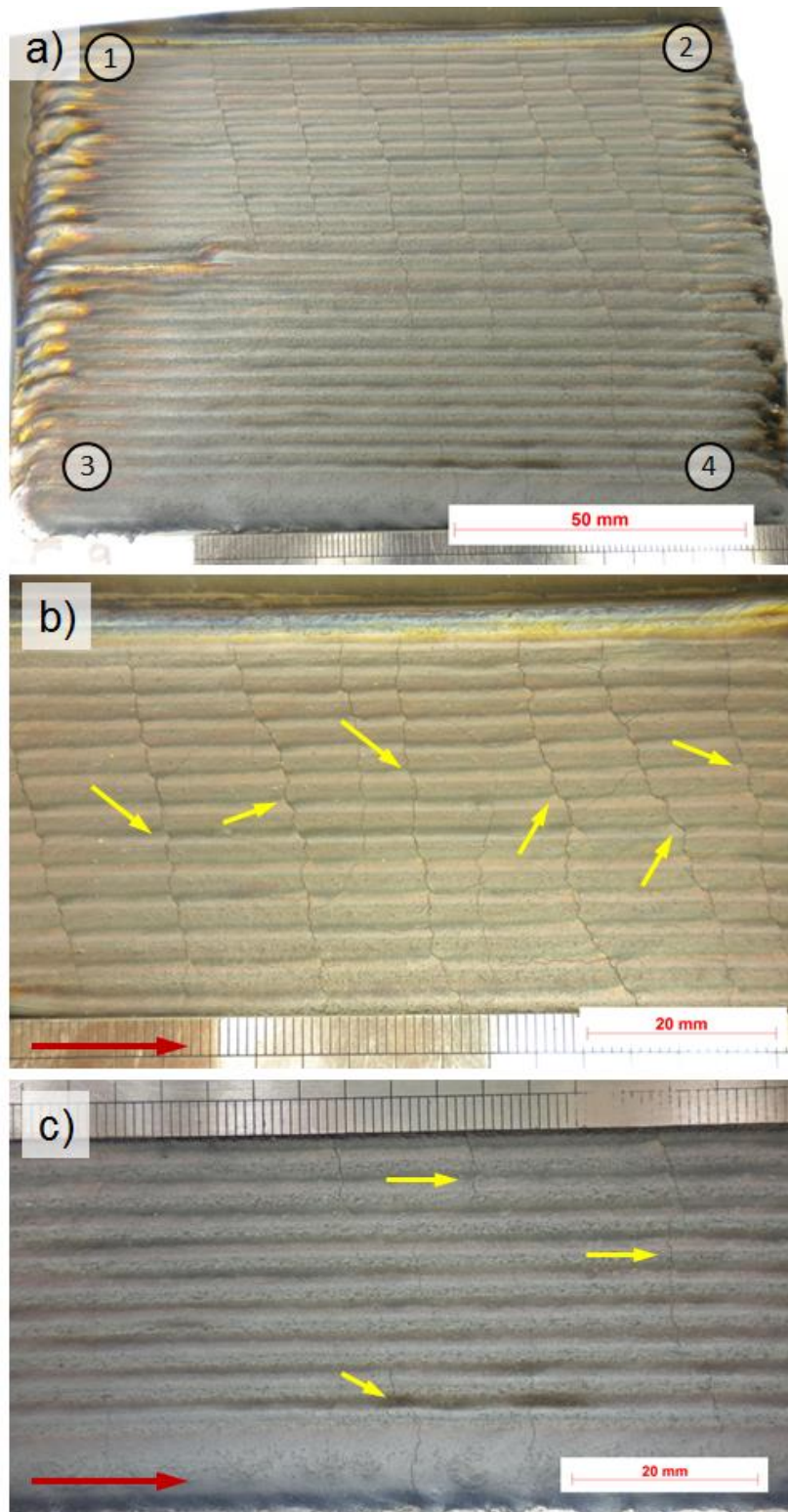
Figure_apx J-5: Cladding trial in overlap; a) PFR = 20 g/min; b) magnified image of a) beginning; c) magnified image of a) finish; 1: Beginning of first weld; 2: finish of first weld; 3: beginning of last weld; 4: finish of last weld; red arrow: welding direction; yellow arrows: check cracks
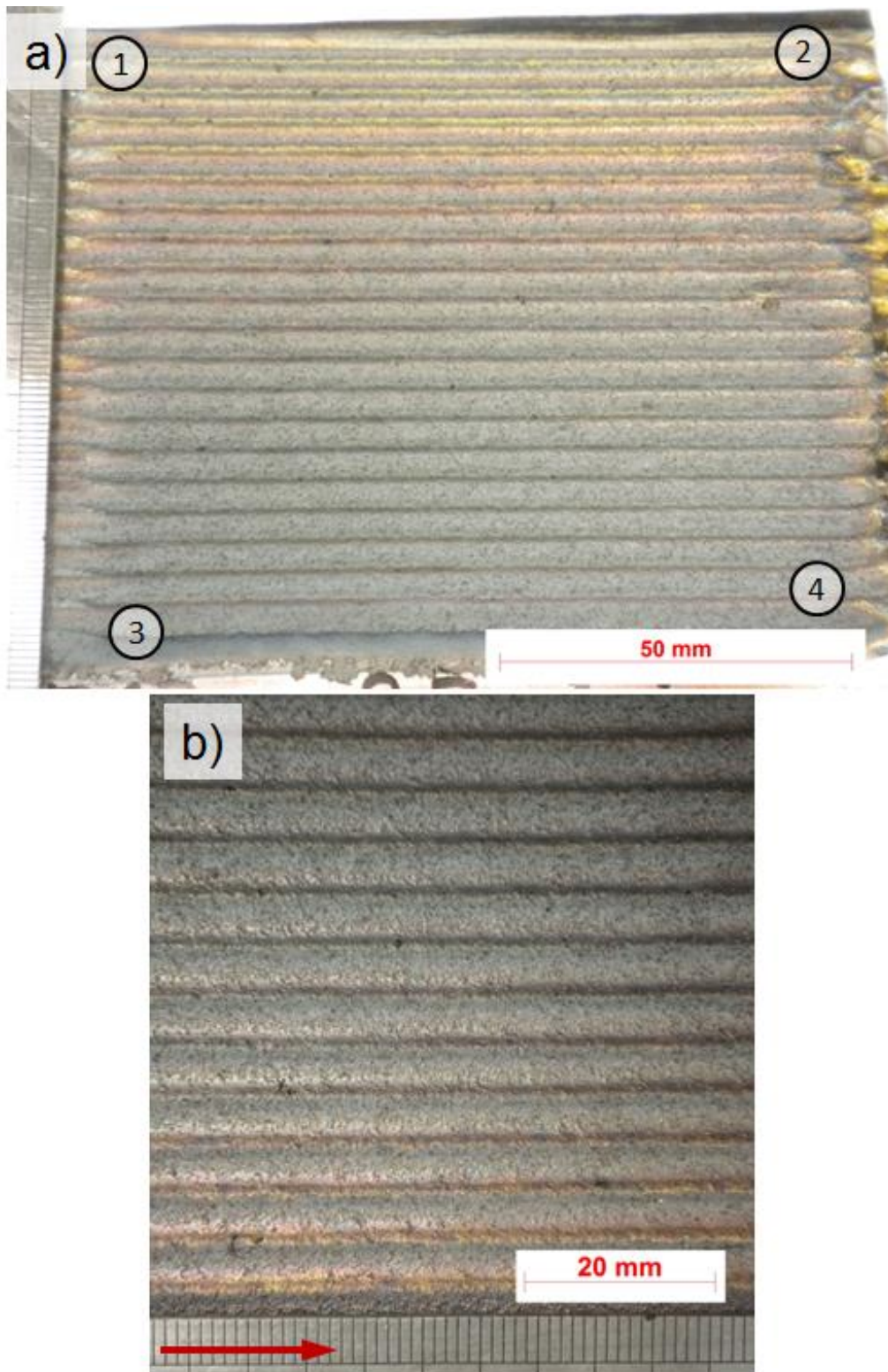
Figure_apx J-6: Cladding trial in overlap; a) PFR = 25 g/min; b) magnified image of a); 1: Beginning of first weld; 2: finish of first weld; 3: beginning of last weld; 4: finish of last weld; red arrow: welding direction
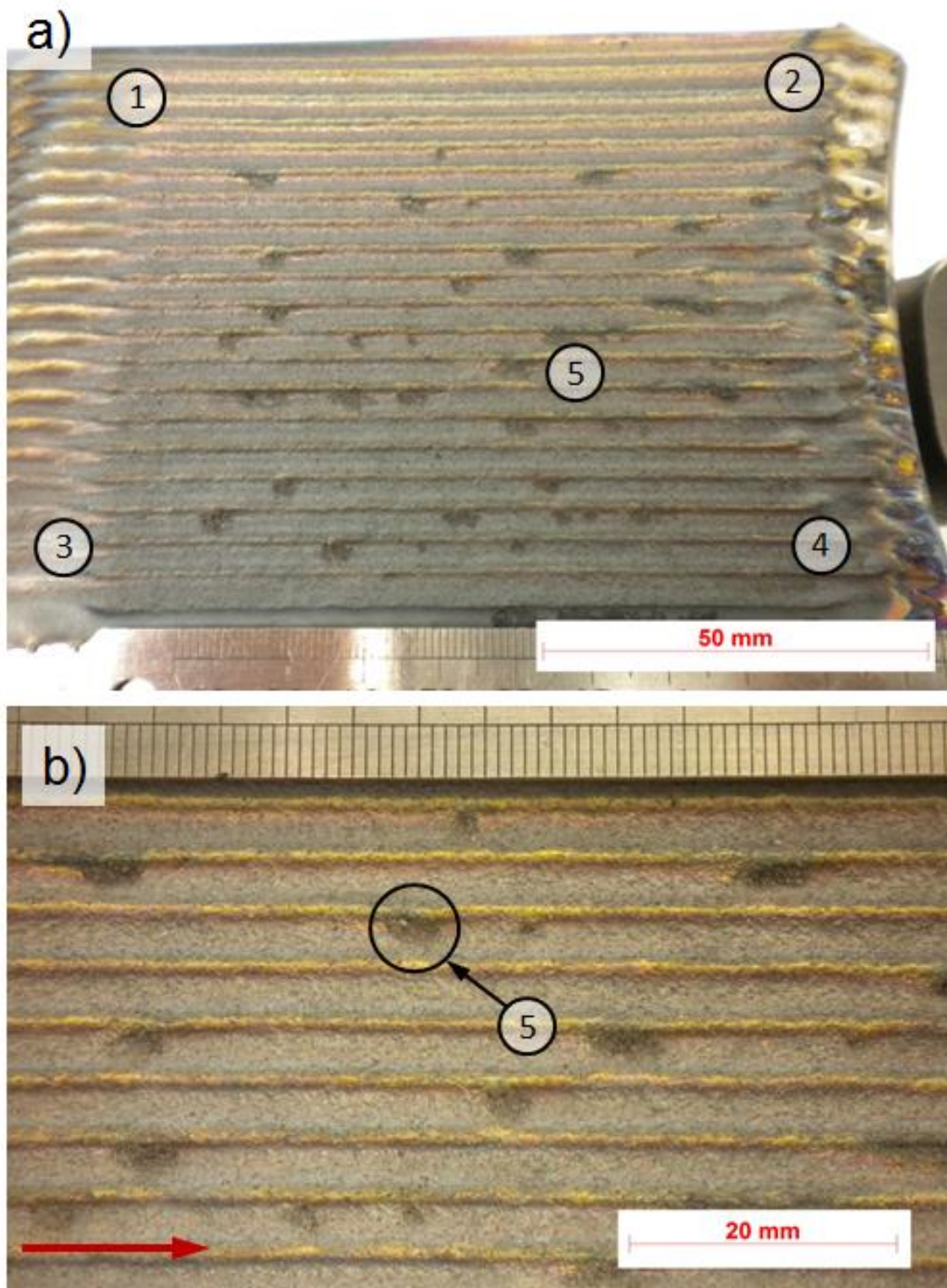
Figure_apx J-7: Cladding trial in overlap; a) PFR = 40 g/min; b) magnified image of a); 1: Beginning of first weld; 2: finish of first weld; 3: beginning of last weld; 4: finish of last weld; 5: unconfined WC powder; red arrow: welding direction
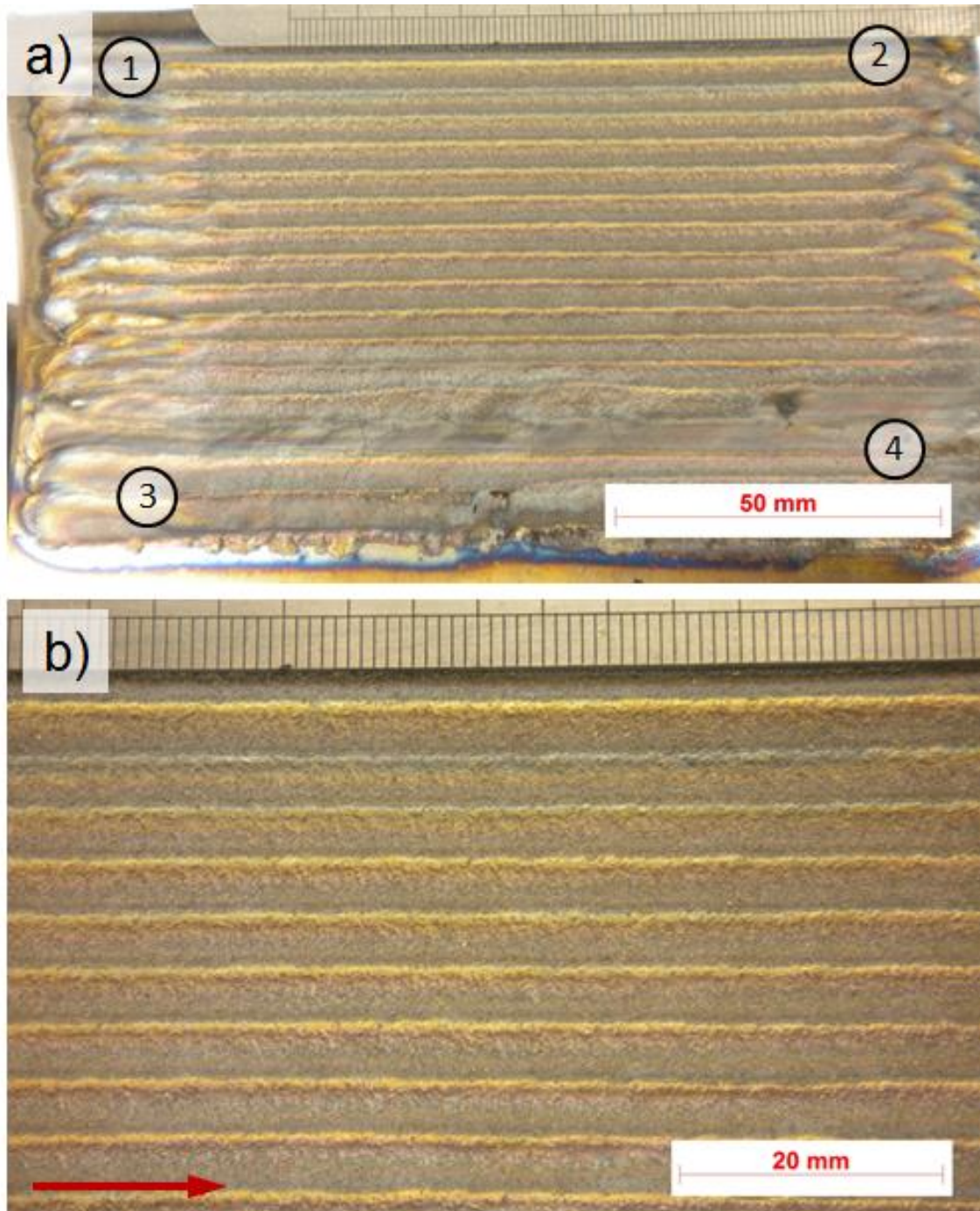
Figure_apx J-8: Cladding trial in overlap; a) PFR = 60 g/min; b) magnified image of a); 1: Beginning of first weld; 2: finish of first weld; 3: beginning of last weld; 4: finish of last weld; red arrow: welding direction
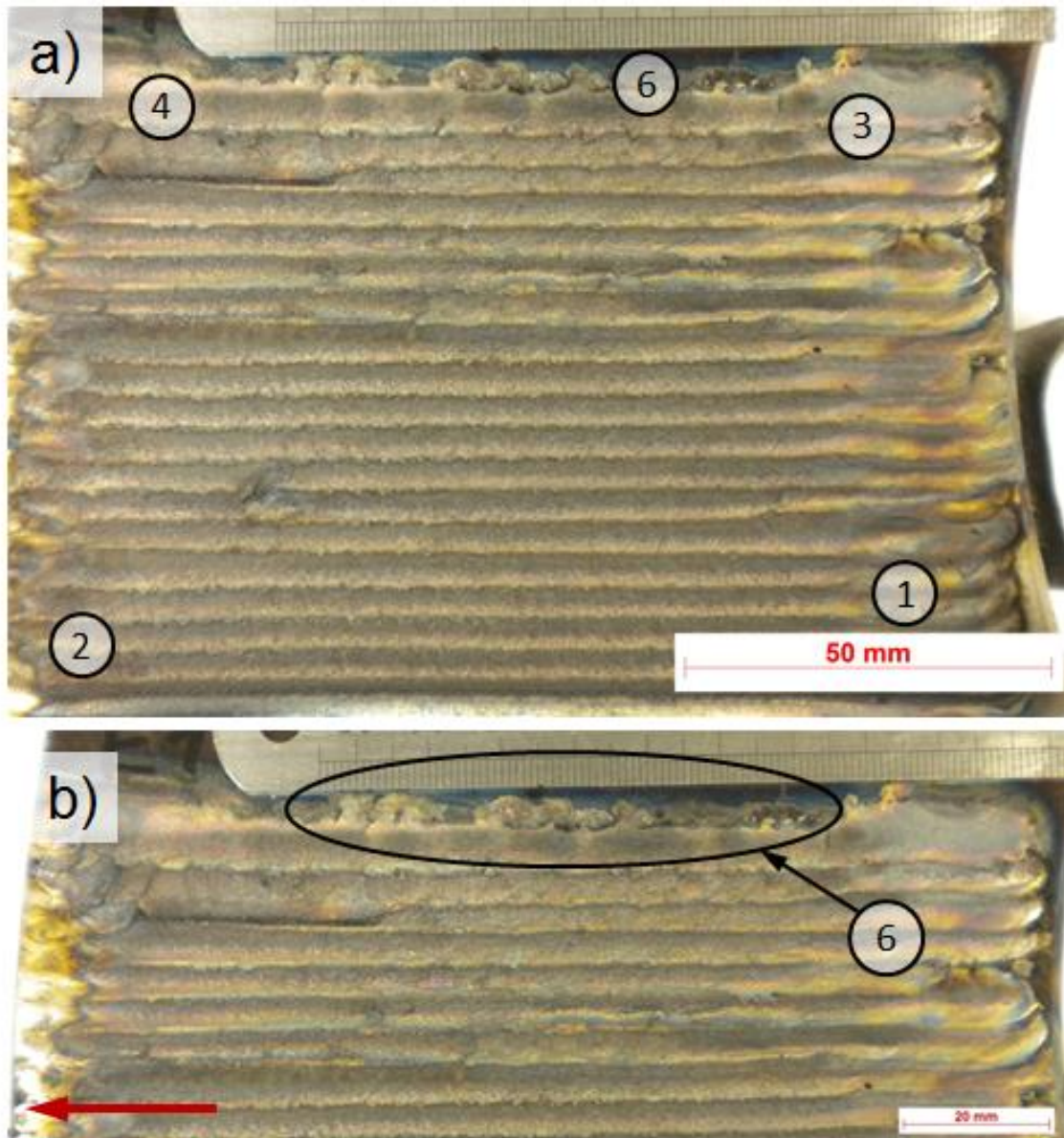
Figure_apx J-9: Cladding trial in overlap; a) PFR = 80 g/min; b) magnified image of a); 1: Beginning of first weld; 2: finish of first weld; 3: beginning of last weld; 4: finish of last weld; 6: bond and sputtered WC powder; red arrow: welding direction
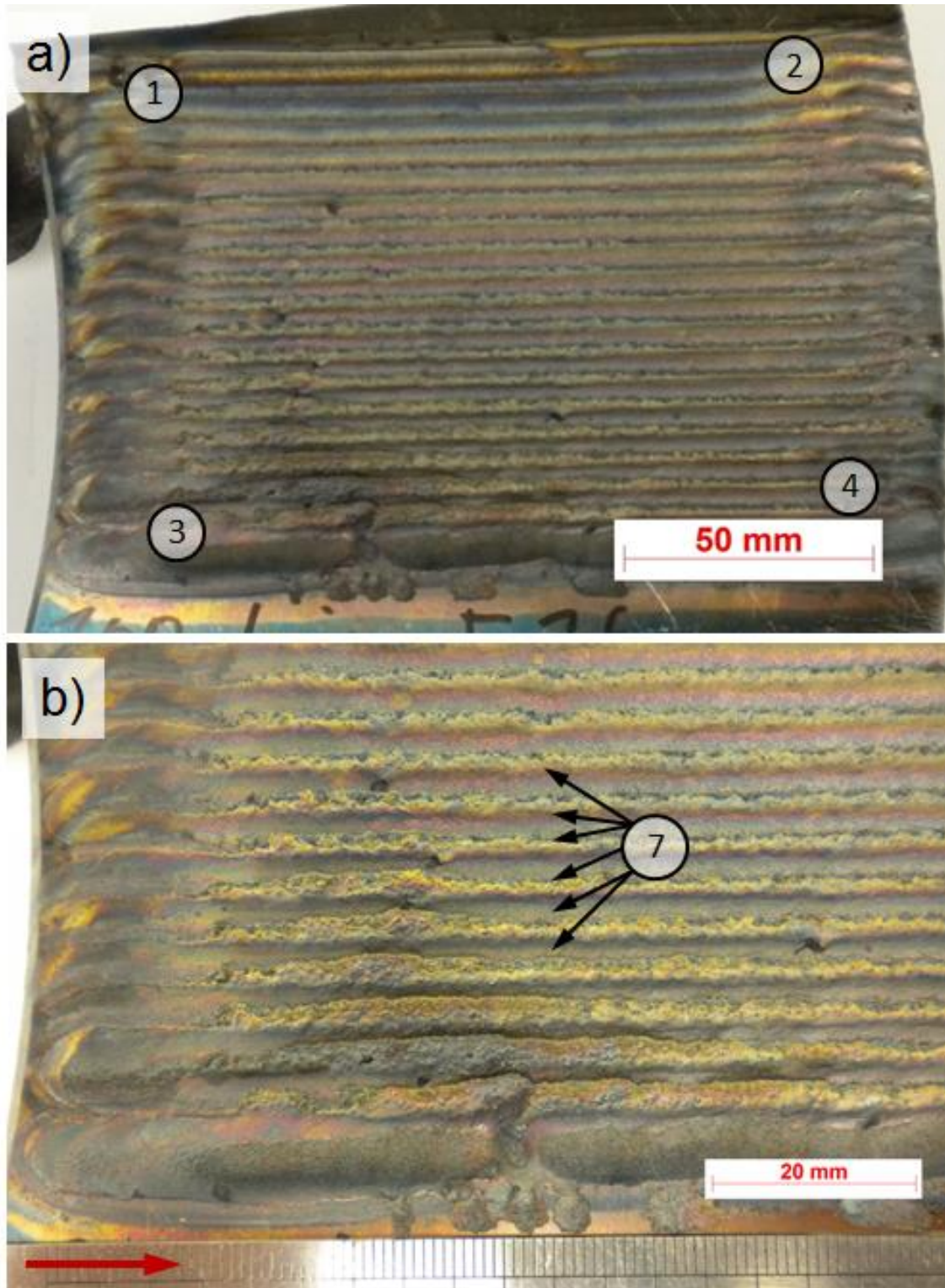
Figure_apx J-10: Cladding trial in overlap; a) PFR = 100 g/min; b) magnified image of a); 1: Beginning of first weld; 2: finish of first weld; 3: beginning of last weld; 4: finish of last weld; 7: very wavy surface; red arrow: welding direction

Appendix K Full-size railway brake disc dynamometer prototype testing

WC reinforcement as a wear resistant layer is well known [26], [48], [132]. Nevertheless, new approaches for the WC reinforcement layers include: round, atomised WC particles (instead of broken WC) in low Ni content matrix and the use of the GTAW process. Additionally, WC reinforcement surface layers have never been tested for brake discs. The previous POD test offers the potential for using WC as reinforcement. One of the main reasons for a large scale GTAW test is to observe the issues associated in producing the prototype, i.e. GTAW process with wire and powder. This complex set up could lead to different problems when a design geometry structure, such as a railway brake disc, is clad. This is especially the case if the area of the disc is significantly larger than the single bead trials in chapter 6 and the overlap trials in chapter 7. These tests are set as an initial trial to determine the feasibility of the WC reinforced surface layer on brake discs.

K.1 Selection of prototype full-size brake disc

In the railway industry, axle mounted and wheel mounted brake discs are commonly used. However, in the dynamometer test, only axle mounted brake discs are tested. Therefore the discs have two wear surfaces. Axle mounted brake discs are produced with and without ventilation. According to some previous investigations by Angelinas, the thermo-mechanical behaviour of ventilated (with vanes) and unventilated discs are significantly different [119], [121], [133]. Dynamometer brake tests were planned with both kinds of discs. The GTAW process and its achievement are refined in chapter 9. The GTAW process will also be compared with a Laser based cladding process which is fully powder based. Hereby, the matrix material and the reinforcement material (WC) are powder. This prototype development was done at LCT Laser Cladding Technology Ltd.. The railway brake disc clad with the laser cladding

process has an evenly distributed hardness between 592HV and 700HV. The following train brake discs were clad for dynamometer testing:

- A 640 mm outer diameter disc, ventilated; GTAW process with PFR = 15 g/min;
- A 640 mm outer diameter disc, ventilated; Laser cladding process, powder based, approx. 10 vol % WC powder reinforcement in steel powder matrix;
- A 460 mm outer diameter discs, unventilated; GTAW process with PFR = 10 g/min.

K.2 Full size dynamometer test rig

A dynamometer test rig is a machine which simulates the train on a journey. A railway carriage axle is driven over an engine, gear box and fly wheel. The brake disc is fixed on the axle. A normal braking operation is simulated with a calliper and brake pads apply force to the brake disc. Adjustable parameters are usually starting speed, deceleration (or brake force) and air cooling flow. The small disc dynamometer test rig has only an axle without wheels and is shown in figure_apx k-1.
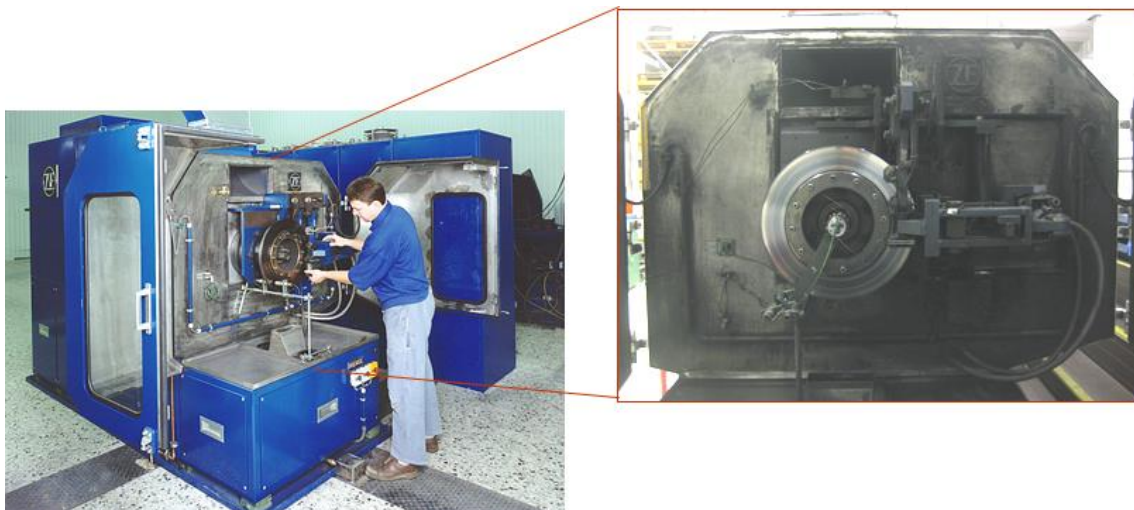
Figure_apx K-1: Brake disc dynamometer test rig for 460 mm brake discs

In figure_apx k-1, a 460 mm brake disc is mounted on the test rig. Rubbing thermocouples can also be applied to measure the surface temperature. The brake disc dynamometer for 460 mm outer diameter brake discs has the following key parameters:

- Input power: 132 kW
- Brake force setting: 0 N to 100.000 N
- Maximum rotation speed: 2700 rpm
- Maximum linear speed: 54 m/s (194.4 km/h)

The brake disc dynamometer test rig for the 640 mm outer diameter brake discs is principally the same. However, it has a slight adjustment in the way that it holds a full train axle with wheels. This axle can load up to three axle mounted brake discs. The test is performed in steps. Every brake disc is tested separately from each other to exclude interference of the braking results.

K.3 Dynamometer test results

A typical dynamometer test programme was chosen in order to obtain comparable results.

K.3.1 Dynamometer testing of ventilated brake discs

The 640 mm outer diameter test sequence for ventilated discs has been given and the results are described as follows. Speeds for the braking operation start have been set for high speed trains. Two different pad materials have been selected. Firstly, a pad called Pagid P40 was decided as it comes from a research series. This pad runs only at the first testing cycle. The second pad is a commonly used railway brake pad called BM47NT. It runs over cycles 2 to 5. All pads need bedding cycles before the testing cycles. Three brake discs have been tested in one test. A comparison 15CDV6 brake disc and the laser clad disc as well as the GTA clad disc were set up on one axle. The full dynamometer test sequence is given in table_apx k-3.

Table_apx K-3: Dynamometer test sequence for the 640 mm outer diameter brake discs

Test	Disc + Pad 1	Disc + Pad 2	Disc + Pad 3
4 Cycles bedding	15CDV6	Laser clad	GTA clad
	BM47NT	Pagid P40	Pagid P40
1 Cycle brake testing	15CDV6	Laser clad	GTA clad
	BM47NT	Pagid P40	Pagid P40
	New Pads on all discs		
2 Cycles bedding	15CDV6	Laser clad	GTA clad
	BM47NT	BM47NT	BM47NT
4 Cycles brake testing	15CDV6	Laser clad	GTA clad
	BM47NT	Pagid P40	Pagid P40

The bedding cycles were driven with moderate speed and low brake force. The brake test cycles were driven with 30 brakes for different speeds. The four speeds for each cycle were:

- 120 km/h
- 160 km/h
- 200 km/h
- 250 km/h.

Deceleration values between 0.5 m/s^2 and 1.0 m/s^2 have been chosen according to a real travel route. The average friction coefficient for the bedding cycles are presented in figure_apx k-2.
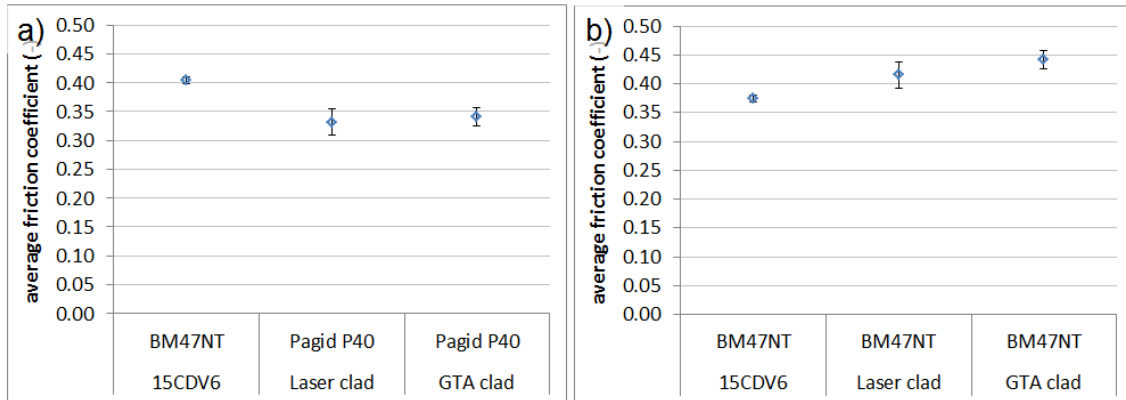
Figure_apx K-2: Friction coefficient (μ) measured during bedding; a) First bedding with four cycles; b) Second bedding with two cycles

In general, a typical friction coefficient of approx. μ = 0.30 to μ = 0.40 is defined by brake manufacturers as a good frictional performance [121]. The bedding revealed lower friction coefficients for the WC reinforced discs with the Pagid P40 pad than the comparison disc, as exhibited in figure_apx k-2 a). However, the Pagid P40 pad was not used on the 15CDV6 because it has been designed for ceramic brake discs. All brake discs performed well according to the manufacturer's recommendation and revealed values between μ = 0.33 and μ = 0.40 in the first bedding. The second bedding was done after the first cycle. It became necessary because of the use of new pairs of brake pads on each disc. The new brake pads were the commonly used BM47NT railway brake pads. The second bedding, shown in figure_apx k-2 b), indicates a slightly higher friction coefficient for the WC reinforced discs. The 15CDV6 comparison disc was performed with a friction coefficient of μ = 0.37 within the given manufacturer's range. Measurements of the friction coefficient were seen out of range with values of μ = 0.42 and 0.44 for the laser clad and GTA clad discs, respectively. This could come from the use of the research pad Pagid P40 in the first bedding and test cycle.

A detailed view of the average friction coefficient of cycle 1 is given in figure_apx k-3. Cycle 1 was the brake tests with the Pagid P40 pad on the ceramic reinforced brake discs.
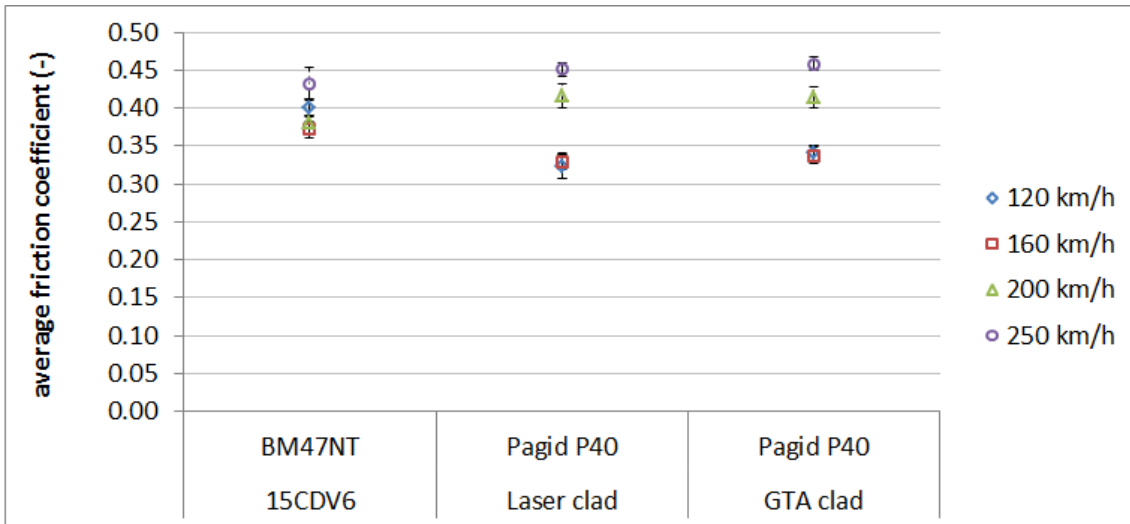
Figure_apx K-3: First brake cycle; reference disc with sintered pad, clad discs with ceramic pad

Within cycle 1, there were brake tests with starting speeds of 120 km/h, 160 km/h, 200 km/h and 250 km/h. These speeds were braked down in different deceleration stages. An average friction coefficient for all stages of deceleration is shown in figure_apx k-3. It becomes clear that the lower starting speeds of 120 km/h and 160 km/h result in lower average friction coefficients, whereas, the higher starting speeds of 200 km/h and 250 km/h result in high friction coefficients. Almost all of them are outside the manufacturer's recommended range. The brake disc testing for the low speeds (120 km/h and 160 km/h) for the 15CDV6 comparison brake disc with the BM47NT pad, exhibited friction coefficients of μ = 0.37 and μ = 0.40. This is within the manufacturer's general guidelines. However, the same friction pair reveals friction coefficients of μ = 0.38 and μ = 0.43 with 200 km/h and 250 km/h, respectively. The higher speed of 250 km/h generates a friction coefficient which is just outside the manufacturer's recommendation. The difference of the friction coefficient becomes greater for low and high speeds when looking at the WC reinforced discs. The low speeds of 120 km/h and 160 km/h indicate a friction coefficient within the guidelines. The laser clad disc shows a friction coefficient of μ = 0.32 and μ = 0.33, respectively and the GTA clad disc shows μ = 0.34 for both low speeds. On the other hand, the results of the high speeds of 200 km/h and 250 km/h gave friction coefficients just above the guidelines for good friction

performance, whereas, the laser clad and GTA clad performed with the same friction coefficient of μ = 0.41 for the 200 km/h examinations. In the tests with a starting speed of 250 km/h, the friction coefficient was slightly different for the laser clad and GTA clad disc with μ = 0.45 and 0.46, respectively.

Furthermore, braking tests continued with new BM47NT pads on all three discs after bedding. The average friction coefficient of the second dynamometer test cycle is shown in figure_apx k-4.
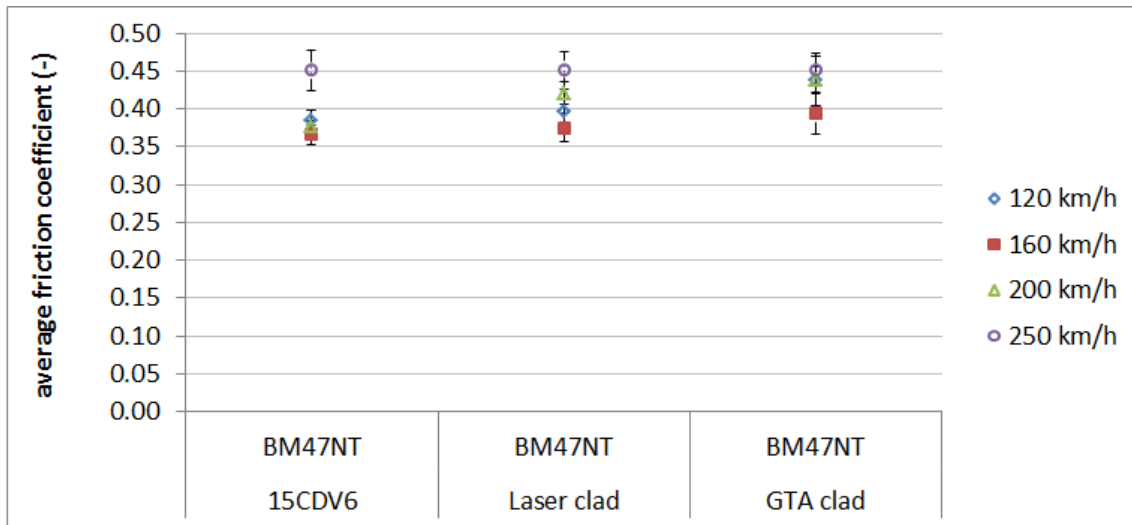
Figure_apx K-4: Second brake cycle; all discs with sintered pad

In contrast to the first cycle, the friction coefficient increases for lower speeds of all three discs. The 15CDV6 comparison brake disc indicates a similar friction coefficient for the speeds 120 km/h, 160 km/h and 200 km/h in the range of μ = 0.37 and μ = 0.38. Only the tests with 250 km/h present a high average friction coefficient of μ = 0.45 for the 15CVD6 disc. The WC reinforcement with the laser cladding method shows a friction coefficient of μ = 0.40, μ = 0.38, μ = 0.42 and μ = 0.45 for the speeds 120 km/h, 160 km/h, 200 km/h and 250 km/h, respectively. Therefore the lower speeds are just inside the guideline of approx. μ = 0.30 to μ = 0.40 and the higher speeds of 200 km/h and 250 km/h generate values just above the guideline of the friction coefficient. A different pattern is shown from the GTA clad brake disc. The brake test generates friction

coefficient results between μ = 0.44 and μ = 0.45 for the starting speeds of 120 km/h, 200 km/h and 250 km/h. The only friction coefficient under μ = 0.40 was recorded from the brake starting speed of 160 km/h with μ = 0.39.

Angelinas shows in his parallel works that cooling of the discs is very important [121], [142]. The design of the disc, together with the shape and order of the disc vanes, needs to be checked for good or bad conclusions of wear rate from a ceramic layer.

The aim of the project was to build up a ceramic metal matrix composite as a surface layer for improved wear resistance. To determine the wear resistance, the wear loss in volume of worn material has been measured. An improvement can be seen if the braking energy absorbed by the disc increases with the wear loss volume. Figure_apx K-5 illustrates absorbed energy per volume loss for the three discs. The first cycle with the Pagid P40 pad was separated from the following cycles, and tested with the BM47NT pad.
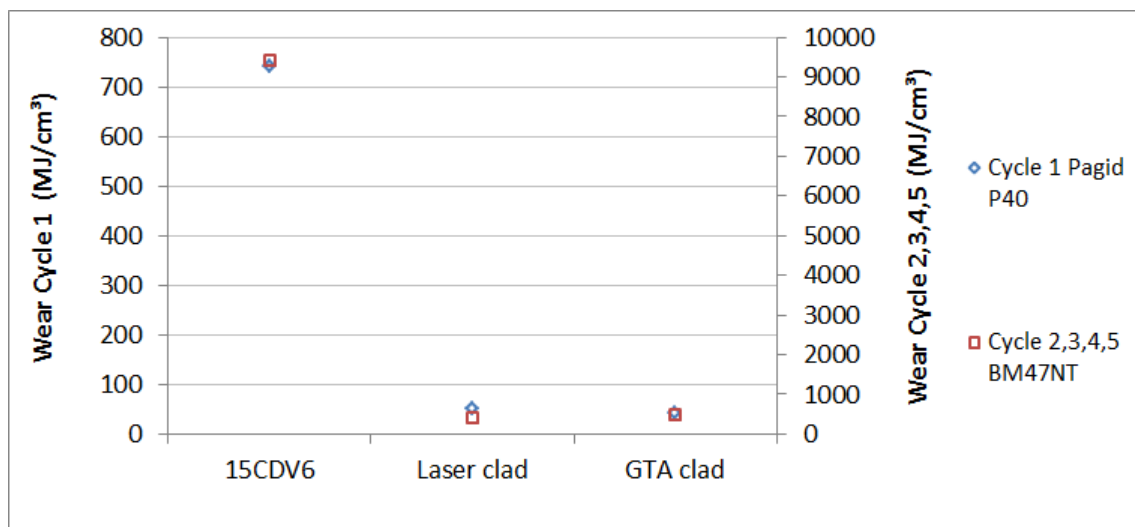
Figure_apx K-5: Wear loss for the separate discs in energy consumption per volume loss

The basic trend for the first cycle and the other cycles is the same. The energy absorbed per volume loss is the highest with the 15CDV6 brake disc while the WC reinforced discs show about 10 times worse results. The laser clad disc runs a little bit better than the GTA clad disc with the Pagid P40 pad. The

absorbed energy was 50 MJ/cm^3, which is 8 MJ/cm^3 higher. However, the GTA clad disc absorbed more energy than the laser clad disc with the BM47NT pad. The GTA clad disc absorbed 503 MJ/cm^3 over four cycles compared to 421 MJ/cm^3 for the laser clad disc for the same number of braking cycles. The difference from the 15CDV6 comparison disc is still very high. The 15CDV6 disc exhibited an energy absorption of 742 MJ/cm^3 for the first braking cycle and 9408 MJ/cm^3 for the following four cycles.

K.3.2 Dynamometer testing of non-ventilated brake discs

The 460 mm outer diameter disc test sequence was not provided by the sponsor. However, the wear pattern is still seen on the unventilated railway brake disc. The GTA cladding was done with PFR = 10 g/min. Figure_apx K-6 shows a section of the disc after the dynamometer brake disc testing from both sides. It can clearly be seen that the brake disc becomes wavy on the wear surface when in use. This effect is known as disc thickness variation (DTV). The peaks and valleys are more intense towards the outer diameter.
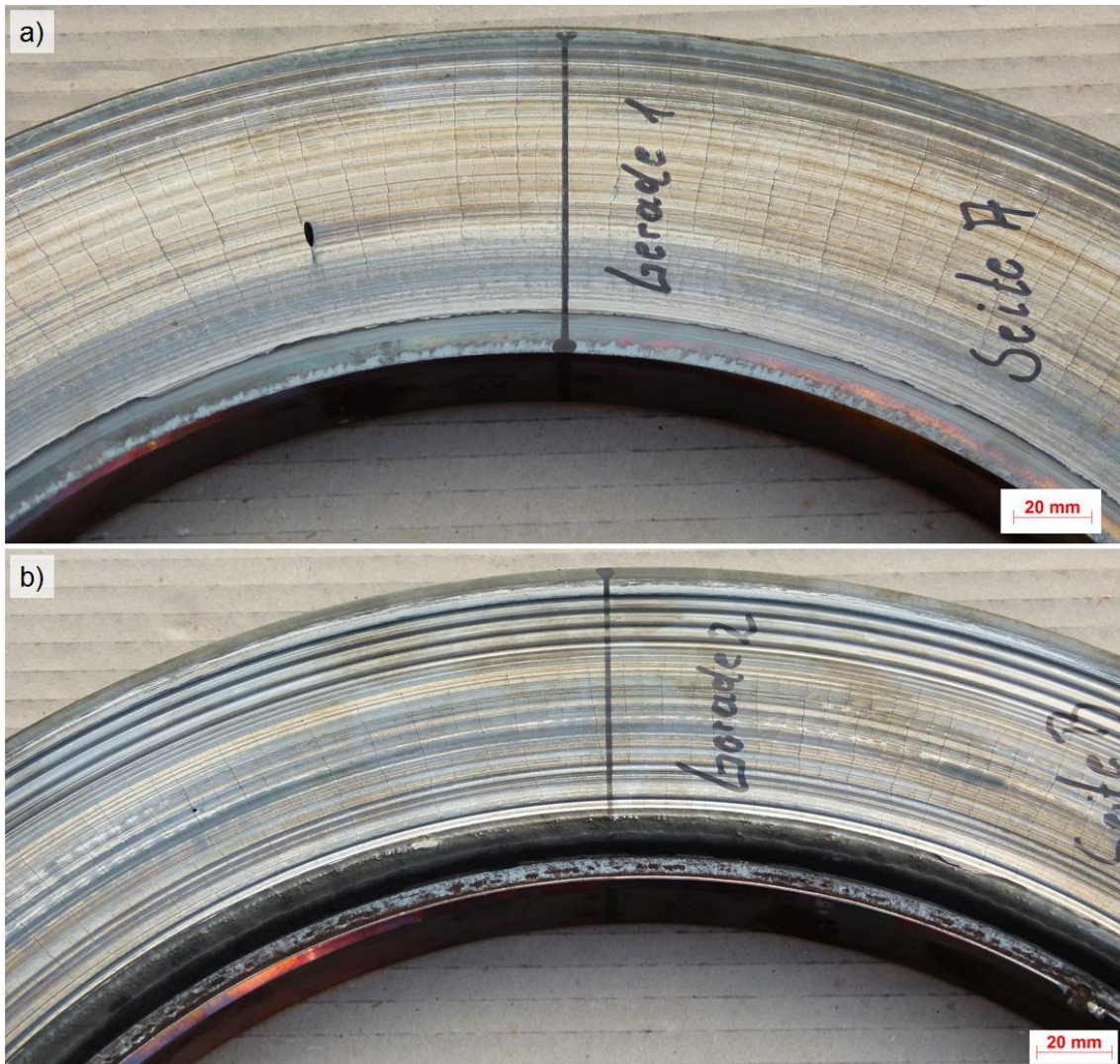
Figure_apx K-6: Surface of the 460 mm outer diameter brake disc after dynamometer testing; a) Side 1; b) Side 2

On side 1 (Figure_apx K-6 a)) radial surface cracks are macroscopic visible. The mircocracks found in section 9.2 of chapter 9 (Figure 9-19) have probably been opened up during the braking cycles. The opposite side (Figure_apx K-6 b)) does not show visible cracks. However, the DTV is more intense here.

DTV can cause judder which can lead to excessive problems in the brake system. This could come from a non-optimised surface cladding.

The cladding of the disc is feasible as the surface layer does not peel off. Nevertheless, more dynamometer examination with different WC reinforcement volume fractions and matrix combinations (high strength wire, mild steel wire)

needs to be done to understand the process window for optimised braking parameters.

K.4 Summary

Dynamometer brake tests have been executed with ventilated (with vanes) and unventilated axle mounted discs. These are surface coated by the GTA cladding process with WC ceramic powder feeding and wire matrix feeding. The GTAW process is also compared with a laser based cladding process which is fully powder based. Braking operations with low starting speeds (120 km/h and 160 km/h) and Pagid P40 pads show friction coefficients within the manufacturer's guidelines. The results for the WC reinforced discs were between μ = 0.32 and μ = 0.34 regardless of the cladding process. On the other hand, the results of the high speeds of 200 km/h and 250 km/h with friction coefficients between μ = 0.41 and μ = 0.46 were just above the guidelines for good friction performance. However, the laser clad and GTA clad performed slightly differently from the laser clad and GTA clad disc with μ = 0.45 and 0.46, respectively.

When changing to the BM47NT pad, the WC reinforcement with the laser cladding method shows a friction coefficient of μ = 0.40, μ = 0.38, μ = 0.42 and μ = 0.45 for the speeds 120 km/h, 160 km/h, 200 km/h and 250 km/h, respectively. Therefore the lower speeds are just inside the guideline of approx. μ = 0.30 to μ = 0.40 and the higher speeds of 200 km/h and 250 km/h generate values just above the guideline of the friction coefficient. The GTA clad brake disc generates friction coefficient results between μ = 0.44 and μ = 0.45 for the starting speeds of 120 km/h, 200 km/h and 250 km/h. The starting speed of 160 km/h for brake testing disclosed a friction coefficient of μ = 0.39, which was the only friction coefficient below μ = 0.40.

Wear results exposed a bad result for the clad discs. The energy absorbed per volume loss is as high as the 15CDV6 brake disc and the WC reinforced discs show about 10 times worse results. This is regardless of the cladding process

method or pad material. However, the discs have been tested with the research pad material Pagid P40 first. This pad is designed for 100 % ceramic brake discs. Only 2.47 % to 5.53 % WC ceramic reinforcement is actually present in the case of the cladding layer. Braking with these pads could therefore lead to locally overheated areas (hot-spots). The WC reinforcement has probably reacted with the pad and/or matrix material and could not perform as expected. Dynamometer brake tests with softer pad material on clad layers would give an indication. However, only a microsection through the worn disc would provide evidence. The cracks and the observed disc thickness variation (DTV) can be reduced by adjustments to the GTA cladding parameters. An important role could be the choice of the matrix material and pre-heating of the disc surface prior to welding.

A far too aggressive pad used in the first cycle might have damaged the surface cladding layer. Further dynamometer testing with different WC reinforcements is recommended in order to find the reason of decreasing wear resistance when the brake discs are clad.

K.5 Conclusions

Dynamometer brake testing of the WC reinforced discs leads to the following résumé:

- The braking with the Pagid P40 pads and low speeds performed well, but high speeds resulted in high friction coefficients;
- Braking with the BM47NT pad and the GTA clad disc resulted in too high friction coefficients for nearly all speeds;
- Wear on the WC reinforced discs was severe and could not compete with the comparison disc;
- The laser clad disc indicated less wear than the GTA clad disc with the Pagid P 40 pads. However, the GTA clad disc indicated less wear with the BM47NT pad;

- DTV was observed on the non-ventilated 460 mm outer diameter brake disc;

- A full dynamometer test series with different cladding parameters needs to be set up.

<u>Wear performance of WC cladding layer</u>

Cladding of real railway brake discs in two different sizes was successfully accomplished (see chapter 9). The friction coefficient of the POD test was confirmed by the dynamometer testing with values between $\mu = 0.33$ and $\mu = 0.46$. Further testing with different WC reinforcements is recommended.

Appendix L Material certificates of the consumables

In this appendix, the material certificates of the consumables are displayed for which the following sub-headings are given:

- Substrate materials, also called base or bulk material,
- Matrix materials, also called wire material,
- Reinforcement ceramics, also called composite materials,
- Shielding and powder transport gases,
- Pin-on-Disc wear test consumables.

These certificates are displayed for reference.

L.1 Substrate materials

The substrate materials were always steel. However, standard mild steel as well as high strength steel have been used.

L.1.1 Mild steels

The material certificate of the S275JR mild steel is revealed in figure I-1.

Figure L-1: Material certificate of the S275JR mild steel; the yellow underlined batch is used in the experiments of this thesis.

The yellow underlined batch of figure I-1 is the material used in this thesis. As shown in the certificate, yield strength of 300 MPa is measured.

The material certificate of the S355J2+N mild steel is revealed in Figure L-2.

Figure L-2: Material certificate of the S355J2+N mild steel; the yellow underlined batch is used in the experiments of this thesis.

The yellow underlined batch of figure l-2 is the material used in this thesis. As shown in the certificate, yield strength of 415 MPa is measured.

L.1.2 High strength steels

The material certificate of the 15CDV6 high strength steel is revealed in figure_apx l-3.

SAB WABCO

Material specification
Material Spezifikation

Material sheet No.:
Werkstoffblatt Nr.:
MS-0067-S

Comparable to / Vergleichbar	14 CrMoV 6 9	Base / Grundlage :	TD 5654	Product marking: / Produkt kennzeichnen mit:
Material no.: / Werkstoff-Nr.	1.7735		15 CDV 6	**0067**

Prefered application :
Bevorzugte Verwendung :

Chemical composition in % (Cast analysis):
Chemische Zusammensetzung in % (Schmelzanalyse)

Elements to be certified are marked with x
Die zu bescheinigenden Elemente sind angekreuzt

C x	Si x	Mn x	P x	S x	Cr x	Mo x	Ni	V x	Cu	Ti	Al	N	
0,15 - 0,18	max. 0,20	0,80 - 1,10	max. 0,015	max. 0,015	1,25 - 1,50	0,80 - 1,10	-	0,20 - 0,30	-	-	-	-	-

Heat treatment : Quenched and tempered

Wärmebehandlung : Vergütet

Mechanical properties : The hardness values are reference data. The tensile test is decisive
Mechanische Eigenschaften : Bei den Härteangaben handelt es sich um Richtwerte. Maßgebend ist der Zugversuch.

	Yield stress / 0,2%-Proof stress Streckgrenze / 0,2% Dehngrenze $R_{el}/R_{p0,2}$ [N/mm²]	Tensile strength Zugfestigkeit R_m [N/mm²]	Elongation Bruchdehnung A [%]	Reduction of area Einschnürung Z [%]	Notched bar impact test Energy value Kerbschlagarbeit Av ISO-U [J] At / bei	Av (ISO-V) [J] At / bei °C	Hardness HB 10/3000 Härte HB
l	min. 900	1030 - 1200	min. 10		min. 23 1.)		331 - 388
		-					-
		-					-
		-					-
		-					-

Separately or attached cast on test coupon Getrennt oder angegossene Probe		Excess material (at forgings) Übermaterial (bei Schmiedewerkstoffen)	**X**	Product specimen acc. to sketch (prototypes) Bauteilprobe gem. Skizze (bei Prototypen)	**X**

Remarks : 1.) Minimum average of 3 pieces, individual minimum 16 J.

Bemerkungen : 1.) Mittelwert aus 3 Proben, kein Einzelwert unter 16J

Prepared Erstellt	Approved Genehmigt	Status of revision Revisionsstand	
Eisleben (VTA)	Dr. Merkel (VTA)	01	02.02.05

Figure_Apx L-3: Material certificate of the 15CDV6 high strength steel

The material certificate of the GS22 high strength steel, also called G-22 NiMoCr 5 6, is revealed in figure_apx I-4.

Faiveley TRANSPORT

Material specification
Material Spezifikation

Material sheet No.: Werkstoffblatt Nr.: **MS-0005-S**

| Comparable to : Material no. : Vergleichbar mit : Werkstoff-Nr. : 1.6760 | Base : Grundlage SEW 520 09/1996 **G-22 NiMoCr 5 6** | FT name FT Bezeichnung **0005** |

Prefered application : General
Bevorzugte Verwendung : Allgemein

Chemical composition in % (Cast analysis):
Chemische Zusammensetzung in % (Schmelzanalyse):

Elements to be certified are marked with x
Die zu bescheinigenden Elemente sind angekreuzt

C x	Si x	Mn x	P x	S x 1.)	Cr x 1.)	Mo x	Ni	V	Cu	Ti	Al x	N x	
0,18 - 0,24	max. - 0,60	0,80 - 1,20	max. - 0,015	max. - 0,015	0,60 - 1,10	0,50 - 0,80	0,80 - 1,30	-	-	-	max. - 0,050	max. - 0,010	-

Heat treatment : Liquid heat treated

Wärmebehandlung : Flüssigkeitsvergütet

Mechanical properties : The hardness values are reference data. The tensile test is decisive
Mechanische Eigenschaften : Bei den Härteangaben handelt es sich um Richtwerte. Maßgebend ist der Zugversuch.

Strength class Festigkeits stufe	Ruling section thickness Maßgebende Wanddicke	Yield stress / 0,2%-Proof stress Streckgrenze / 0,2% Dehngrenze $R_{eH}/R_{p0,2}$ [N/mm²]	Tensile strength Zugfestigkeit R_m [N/mm²]	Elongation Bruchdehnung A [%]	Reduction of area Einschnürung Z	Notched bar impact test Energy value Kerbschlagarbeit Av ISO-V [J] At / bei RT	Av (ISO-V) [J] At / bei °C	Hardness HBW10/30 00 Härte HB
I		min. 825	930 - 1080	min. 10		min. 40 1.)		290 - 340 3.)
II		min. 900 1.)	1050 - 1200	min.10		min. 27 1.)		330 - 375 3.)
			-					-
			-					-
			-					-
			-					-

| X | Separately or attached cast on test coupon Getrennt oder angegossene Probe 2.) | | Excess material (at forgings) Übermaterial (bei Schmiedewerkstoffen) | X | Product specimen acc. to sketch (prototypes) Bauteilprobe gem. Skizze (bei Prototypen) |

Remarks : 1.) In deviation of SEW 520

2.) Dimensions of test coupons in correlation wall thickness.

3.) Converted in acc. To EN ISO 18265 table B.2

Bemerkungen : 1.) Abweichend von SEW 520

2.) Die Abmessungen der Proben sind auf die maßgebliche Wanddicke der Gussstücke abzustimmen

3.) Umgerechnet nach EN ISO 18265 Tabelle B.2

Prepared Erstellt	Approved Genehmigt	Status of revision Revisionsstand	
Eisleben (VTA)	Dr. Merkel (VTA)	R0000036 B	01.02.07

Figure_Apx L-4: Material certificate of the G-22 NIMOCR 5 6 high strength steel

L.2 Matrix materials

The matrix materials were always steel. Standard welding wire in 1 mm diameter was ordered. However, standard mild steel as well as higher strength steel has been used.

L.2.1 Mild steels

The material certificate of the G3Si1 mild steel is revealed in figure_apx l-5.

Test Report

Product Class	SupraMIG ISO 14341-A : G424M21 G3Si1 G383C1 G3Si1 AWS A5.18-93 ER70S-6	Item No. Lot/batch Size(s) mm	16S0815PR 3524 0.8 X 15 Kg Plastic Random
		Product Line	MIG Wire
Customer	CRANFIELD UNIVERSITY WHARLEY END CRANFIELD MK43 0AL UNITED KINGDOM	Customer ref. Our reference: Quantity	F O C SU361090 1.0 CO

Chemical analysis (%)   According to EN10204:2004   2.2

C	Si	Mn	P	S	Cr	Ni	Mo	Cu	V	Al	Ti+Zr
0.070	0.820	1.450	0.01	0.010	0.025	0.030	0.010	0.021	0.005	0.005	0.003

Mechanical tests, all weld metal   According to EN10204:2004   2.2
Tensile testing   Impact testing

Rel N/mm2	Rm N/mm2	A5 %		Temp. c	Impact min. Average J
466	577	30		-40	92

Additional information   According to EN10204:2004
Other tests

Remarks

The product identified above has been manufactured, tested and supplied in compliance with a certified ISO 9001 Quality Assurance Programme.
It should be noted that the mechanical properties of all weld metal specimens could vary from those obtained in production joints because of differences in welding procedures.

Company Lincoln Electric (U.K.) Ltd Registered office: Mansfield Road Aston Sheffield S26 2BS UNITED KINGDOM	Printed by P. RICHARDSON Telephone: 0114 2872401	Function Fax: 0114 2673628	Date 16/07/2010	Cert. No. 11174683

Figure_Apx L-5: Material certificate of the G3Si1 steel welding wire

The material certificate of the G4Si1 mild steel is revealed in figure_apx I-6.

Test Report

Product Class	SupraMIG ULTRA ISO 14341-A : G4Si1 AWS A5.18-93 ER70S-6	Item No. Lot/batch Size(s) mm Product Line	1631015PR 3218 1.0 X 15 Kg Plastic Random MIG Wire
Customer	CRANFIELD UNIVERSITY BUILDING 46 WELDING ENGINERRING CRANFIELD MK43 0AL UNITED KINGDOM	Customer ref. Our reference: Quantity	NIELSEN FLEMMING SU358382 2.0 CO

Chemical analysis (%) — According to EN10204:2004   2.2

C	Si	Mn	P	S	Cr	Ni	Mo	Cu	Ti	Zr
0.060	0.940	1.640	0.0130	0.0160	0.020	0.020	0.0050	0.020	0.0040	0.0020

Mechanical tests, all weld metal — According to EN10204:2004   2.2
Tensile testing   Impact testing

Rel N/mm2	Rm N/mm2	A5 %		Temp. c	Impact min. Average J
500	566	26		-40	86

Additional information — According to EN10204:2004
Other tests

Remarks

The product identified above has been manufactured, tested and supplied in compliance with a certified ISO 9001 Quality Assurance Programme.
It should be noted that the mechanical properties of all weld metal specimens could vary from those obtained in production joints because of differences in welding procedures.

Company	LINCOLN ELECTRIC (U.K.) LIMITED	Printed by	Function	Date	Cert. No.
Lincoln Electric (U.K.) Ltd.	QUALITY ASSURANCE	P. RICHARDSON		01/06/2010	11172312
Registered office: Mansfield Road Aston Sheffield S26 2BS UNITED KINGDOM		Telephone: 0114 2872401	Fax: 0114 2873628		
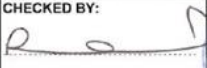
certificateV7.2

Figure_Apx L-6: Material certificate of the G4Si1 steel welding wire

L.2.2 Higher strength steel wire

The material certificate of the 15CDV6 high strength steel welding wire is revealed in figure_apx l-7.

CERTIFICATE OF CONFORMANCE, RELEASE & DELIVERY NOTE

	Despatched From	Head Office
vbc group	VBC Group Ltd Castle Business Park Pavilion Way Loughborough, LE11 5GW Tel +44 (0)1509 218008 Fax +44 (0)1509 211552 Website: www.vbcgroup.com	VBC Group Ltd Castle Business Park Pavilion Way Loughborough, LE11 5GW Tel +44 (0)1509 218008 Fax +44 (0)1509 211552 Website: www.vbcgroup.com

Invoice To
CRANFIELD UNIVERSITY
CRANFIELD UNIVERSITY
CRANFIELD
BEDFORDSHIRE
Bedfordshire
MK43 0AL
England

Deliver To
CRANFIELD UNIVERSITY
BUILDING 46 (J SAVILL)
46 WELDING RESEARCH CENTRE
CRANFIELD UNIVERSITY
CRANFIELD
BEDFORDSHIRE
MK43 0AL
England

Release No: RN E 39127
Date: 03/06/2010
PO: 719969
Order Qty: 15 Kgs
Release Qty: 15 Kgs
Tot Shipped: 15 Kgs
Outstanding: 0 Kgs
Transport: UPS

PRODUCT DETAILS

Product Name	Specification	Extra	Product Type	Cust. Part No	Labelling Info.
VBC ALLOY 9415 15CDV6	1.0 mm Dia		Spool Wire		
Primary Rel Spec	**Associate Rel Spec**	**Add. Spec 1**	**Add. Spec 2**	**Add. Spec 3**	**Add. Spec 4**
STANDARD YOURS					

CHEMICAL ANALYSIS

Analysis Type	Code	Mesh Analysis	Chemical Analysis					
Batch	B75144Y		Fe	* 94.4661	W	1.7734	Cr	1.40	Mn	0.93
Lot	LW7664		Mo	0.90	V	0.24	Si	0.15	C	0.130
			P	< 0.009	S	< 0.0015				

Account Manager: Nathan Hargrave
Contact: MR STEPHAN HERBST
Packaging Information
Health & Safety
Tariff Code: 7229909000
Expiry Date
Special Instructions: FAO FLEMMING NEILSEN AS PER E-MAIL 09/07/2010
Notes
Revison No
Change Made

CHECKED BY:	SIGNED ON RECEIPT BY:	CERTIFICATE OF COMPLIANCE
PLEASE NOTIFY US IMMEDIATELY IF ERROR IS FOUND IN SHIPMENT		CERTIFIED THAT THE SUPPLIES/SERVICES DETAILED HEREON HAVE BEEN INSPECTED AND TESTED UNDER A QUALITY ASSURANCE SCHEME CONFORMING TO BS EN ISO 9001:2008, IN ACCORDANCE WITH THE CONDITIONS AND REQUIREMENTS OF THE CONTRACT OR PURCHASE ORDER. AND UNLESS OTHERWISE NOTED CONFORM IN ALL RESPECTS TO THE SPECIFICATION(S) DRAWING(S) RELEVANT THERE TO. MILL SOURCE HAS TESTED FOR CONFORMITY IN ACCORDANCE WITH CUSTOMER STATED REQUIREMENTS, MSRR AND NADCAP. RELEASED TO RR9XXX SABRe.

Form Number: VF02/11 (01 Sep 2009)
Please Note Copy: Customer Copy 2

www.vbcgroup.com

Registered Address: Unit 12, Castle Business Park, Pavilion Way, Loughborough, Leicestershire. LE11 5GW. Registered Number: 2572306. VAT Number: 974887935.

Figure_Apx L-7: Material certificate of the 15CDV6 steel welding wire

The material certificate of the GMn4Ni2CrMo higher-strength, fine-grained constructional steel wire is revealed in figure_apx I-8.

Classification:
EN 12 534 — 89 6M GMn4Ni2CrMo
ASME/AWS SFA 5.28 — ER 120 S-G
EN ISO 16834-A — G89 6 M Mn4Ni2CrMo
EN ISO 16834-B — G 83A 6 M N4M4T

elektrode jesenice d.o.o.

MIG 90

Description and application:

Mn, Ni, Cr and Mo alloyed metal inert gas welding wire is suitable for welding of higher-strength, heat treated, fine - grained constructional steels with a minimum yield strength of 890 N/mm^2

Base materials:

High-strength fine grained steels	S890Q, XABO 890, MICRAL 890

Chemical composition of welding wire (wt. %) :

C	Si	Mn	Cr	Ni	Mo
0,10	0,8	1,8	0,35	2,0	0,5

Mechanical properties of all weld metal (wt. %) :

Yield strength	Rp_{eL} / $Rp_{0.2}$:	> 890	N/mm2
Tensile strength	Rm:	940-1180	N/mm2
Elongation	A5:	> 15	%
Impact energy	Av :	> 47	J (-60°C)

Suitable shielding gases: Ar + 15 - 25% CO_2, (M21 according to EN 439)

Wire sizes available: 1,0 ; 1,2 ; 1,6 (ϕ mm)

Form of delivery: Wire electrodes are spooled in accordance with AWS A5. 18 and EN 759 - basket spools precision layer wound. Wire can be packed in drums – 250kg or 350kg

Approvals:

Figure_Apx L-8: Material certificate of the GMn4Ni2CrMo steel welding wire

L.3 Reinforcement ceramics

Reinforcement in the metal matrix composites were reviewed by the ceramics silicon carbide (SiC) and tungsten carbide (WC). SiC was commissioned from two different sources. The material certificate of the silicon carbide ceramic from ESK-SiC is revealed in figure_apx I-9 and figure_apx I-10.

ESK

ESK-SIC GmbH

**Product Information
Silicon Carbide**

Application	Product (data sheets available on request)	
SiC for vitrified bonded abrasive products and chip removal operations with loose abrasive grains according to - FEPA 42-GB-1984 R 1993 - ISO 8486	SiC green/green I	macro-/microgrits F 8 - F 220
	SiC green	microgrits F 230 - F 1200
	SiC dark	macrogrits F 8 - F 220
	SiC dark	microgrits F 230 - F 1200
	SiC dark	KAN-E macrogrits F 8 - F 220
SiC for resin, gum and magnesite bonded abrasive products and chip removal operations with loose abrasive grains according to - FEPA 42-GB-1984 R 1993 - ISO 8486	SiC dark	KAN-E macrogrits F 8 - F 220
	SiC green	macro-/microgrits F 8 - F 1200
	SiC dark	macro-/microgrits F 8 - F 1200
SiC for coated abrasive products according to - FEPA 43-GB-1984 R 1993 - ISO 6344	SiC dark	macro-/microgrits P 12 - P 2500
	SiC black	macro-/microgrits P 12 - P 1200
Brake linings	SiC dark	microgrits F 230 – F 1200
	Silcar	standard fractions
SiC for wire sawing	SiC green/dark	microgrits
SiC for sawing of granite, marble etc.	Performit	standard fractions
SiC for recrystallized kiln furniture and advanced ceramics	SiC green I	standard fractions
	SiC green/dark	macro-/microgrits
	SiC green/dark	fine fractions and powders
	SiC dark	FF-standard fractions
SiC for kiln furniture and advanced ceramics	SiC dark	FF-standard fractions
SiC for bricks, monolithics, crucibles etc.	SiC dark	standard fractions
SiC for refractory applications	REFSiC 94/97	standard fractions
SiC for the paint industry	SiC dark	standard fractions
	Kristallit®	0,5 - 3 mm
	Silcar	standard fractions
	SiC dark	microgrits F 230 - F 1200
SiC for wear resistant and anti static flooring	Kristallit®	0,5 - 3 mm
	SiC dark	standard fractions
	SiC dark	macrogrits F 8 - F 220
	SiC dark	KAN-E macrogrits F 8 - F 220
SiC for ceramic filters	SiC dark	standard fractions
SiC for Diesel particle filters	SiC dark	standard fractions
	SiC green/dark	macro-/microgrits
	SiC green/dark	fine fractions and powders
SiC for metal matrix composites (MMC)	SiC green/dark	microgrits
	SiC green/dark	micro fractions
SiC for the production of wear resistant surface layers	SiC Ultrafein	standard grits

E-SIC Applications.doc-01/08   ISO 9001 : 2000 certified

ESK-SIC GmbH
Günter-Wiebke-Str. 1
D-50226 Frechen-Grefrath
Telefon +49 (0) 22 34-512-0
Telefax +49 (0) 22 34-512-100

Figure_Apx L-9: ESK-GmbH, Product Information Silicon Carbide; the yellow underlined material with the macrogrit F90 has been used

Werkstoffdatenblatt
Siliciumcarbid
(α-SiC)

Chemische Formel		SiC
Relative Molmasse	g/mol	40,097
Chemische Zusammensetzung - Si - C	% %	70,05 29,95
Dichte	g/cm³	3,21
Härte - Mohs - Knoop HK 0,1		9,5 - 9,75 2500-2900
Schmelzpunkt (Zersetzung)	℃	> 2300
Wärmekapazität - 20 ℃ - 1000 ℃	J/g · K J/g · K	0,67 1,27
Wärmeleitfähigkeit - 20 ℃ - 1400 ℃	kJ/m · h · K kJ/m · h · K	150 54
Linearer thermischer Ausdehnungskoeffizient zwischen (20 - 1400) ℃	K^{-1}	$4,7 \cdot 10^{-6}$
Standardbildungsenthalpie Δ H° $_{298K}$	kJ/mol	$- 71,6 \pm 6,3$
Entropie S°$_{298K}$	J/mol · K	$16,50 \pm 0,13$
Spezifischer elektrischer Widerstand	Ω · cm	$0,1 - 1 \cdot 10^{12}$
Modifikationen α-SiC; verschiedene hexagonale und rhomboedrische Polytypen		6 H, 15 R, 4 H u.a.
Farbe		grün, dunkel, schwarz

Brechungsindex n$_D$
 	
              n$_E$ (Na 589 nm
                        bei 20 ℃)
		2,647 - 2,649
		2,688 - 2,693

Chemische Eigenschaften		Beständig gegen Säuren und Laugen, beständig beim Erhitzen an Luft bis ca. 1500 ℃. Zersetzung durch schmelzende Alkalien wie $Na_2O_2 + Na_2CO_3$ oder $KNO_3 + Na_2CO_3$ löslich in Eisenschmelzen.

Figure_Apx L-10: ESK-GmbH, material data sheet Silicon Carbide

The material certificate of the silicon carbide ceramic from Saint Gobian is revealed in figure_apx I-11 and figure_apx I-12.

Product information

SIKA

Silicon Carbide

SIKA® ABR I

Green Silicon Carbide grains for abrasive applications

Chemically treated, high purity green silicon carbide in macro and micro grains, produced to comply with FEPA standard and particularly suitable for high quality vitrified bonded grinding wheels, honing stones, lapping and polishing applications.

Packaging

25 kg paper bags or 1.000 kg big bags.
30 kg steel drums for F1500 and F2000.

Typical Chemistry

	SiC	Free-C	Free-SiO_2	Free-Si	Fe_2O_3	MI
Macro	99,40 %	0,25 %	0,20 %	0,15 %	--	0,002 %
Micro	99,50 %	0,20 %	0,15 %	0,10 %	0,05 %	--

Grit Sizes and Shapes

Macro grits				Micro grits		
Grit No.	Mean-Ø mm	LPD g/cm³		Grit No.	Ø d_{50} µm	LPD g/cm³
F 8	2,460	1,32 – 1,42	sharp grain	F 230 S	53,0 ± 3,0	1,20 – 1,30
F 10	2,085	1,34 – 1,44		F 240 S	44,5 ± 2,0	1,17 – 1,27
F 12	1,765	1,35 – 1,45		F 280 S	36,5 ± 1,5	1,14 – 1,24
F 14	1,470	1,37 – 1,47		F 320 S	29,2 ± 1,5	1,09 – 1,25
F 16	1,230	1,39 – 1,49		F 360 S	22,8 ± 1,5	1,05 – 1,21
F 20	1,040	1,40 – 1,50		F 400 S	17,3 ± 1,0	0,96 – 1,12
F 22	0,885	1,41 – 1,51		F 500 S	12,8 ± 1,0	0,87 – 1,03
F 24	0,745	1,43 – 1,53		F 600 S	9,3 ± 1,0	0,80 – 0,96
F 30	0,625	1,45 – 1,55		F 800 S	6,5 ± 1,0	0,70 – 0,86
F 36	0,525	1,46 – 1,56		F 1000 S	4,5 ± 0,8	na
F 40	0,438	1,49 – 1,59		F 1200 S	3,0 ± 0,5	na
F 46	0,370	1,49 – 1,59		F 1500 S	2,0 ± 0,4	na
F 54	0,310	1,49 – 1,59		F 2000 S	1,2 ± 0,3	na
F 60	0,260	1,49 – 1,59				
F 70	0,218	1,47 – 1,57	blocky grain	F 360 B	22,8 ± 1,5	1,12 – 1,28
F 80	0,185	1,46 – 1,56		F 400 B	17,3 ± 1,0	1,15 – 1,35
F 90	0,154	1,43 – 1,53		F 500 B	12,8 ± 1,0	1,10 – 1,30
F 100	0,129	1,48 – 1,58		F 600 B	9,3 ± 1,0	1,04 – 1,24
F 120	0,109	1,42 – 1,52		F 800 B	6,5 ± 1,0	0,75 – 0,95
F 150	0,082	1,37 – 1,47				
F 180	0,069	1,34 – 1,47				
F 220	0,058	1,29 – 1,39				

Analytical Procedures:

Particle Size Distribution is measured according to FEPA Standard 42-1:2006 for Macro-, and 42-2:2006 for Micro-grains

LPD = Loose Pack Density is measured according to FEPA Standard 44-1:2006 for Macro-, and 44-2:2006 for Micro-grains
Magnetic Iron (MI) measured according ANSI B74.19-2002
Chemistry according ANSI B74.15 1992 (R2002)

www.sic.saint-gobain.com

SAINT-GOBAIN
GRAINS & POWDERS

Figure_Apx L-11: Saint-Gobain, product information Sika ABR I Silicon Carbide

Certificate of Analysis

Printed Date: 04.01.2011 15:08:46

Customer:	**206322 - Cranfield University**
Address:	MK43 0AL - Cranfield, Bedford - GB
Sales order number:	1015071
Your sales order ref.:	721049
Item:	410000570225 - SIKA ABR I F90 PaperBag25
Batch number:	101105502
Quantity of batch:	25,00
Customer item code:	

All meassurement are accordance to FEPA, ANSI or JIS,
or other methods in agreement with customer.

Char. description	Unit	Value	Lower Limit	Upper Limit
Sieve 60 (250µm)	%	0	-	0
Sieve 80 (180µm)	%	8	-	20
Sieve 100 (150µm)	%	47	40	-
Sieve 100 + 120 (150 + 125µm)	%	86	65	-
Sieve -140 (-106µm)	%	1	-	3
Magnetic Iron	%	0,0005	-	0,0020
LPD	g/cm³	1,45	1,43	1,53

Signature:

Figure_Apx L-12: Saint-Gobain, Certificate of Analysis Sika ABR I F90

The material certificate of the tungsten carbide ceramic from LCT Laser Cladding Technology is revealed in figure I-13.

a)

TECHNOGENIA

TECHNOGENIA S.A.S. - ZA DES MARAIS – BP 151
74410 SAINT-JORIOZ – France
Tel : +33.4.50.68.56.60 - Fax : +33.4.50.68.62.77
E-mail : technogenia@technogenia.fr

MATERIAL CERTIFICATE
CERTIFICAT MATIERE
CONFIDENTIAL

We, Technogenia, hereby certify that the products detailed below have been made strictly in accordance with company's secret formulation manufacturing processes and standard procedures. They have successfully passed all quality controls and tests.

Nous, Technogenia, certifions que le produit désigné dans cette page a été fabriqué selon les procédures et formulations en vigueur. Il a été contrôlé et testé avec succès.

Product / Produit	
Trademark / Marque	SPHEROTENE 40 - 160 µm
Description	Spherical fused Tungsten Carbide / Carbure de Tungstène fondu Sphérique
Batch number / N° lot	33323
Packaging / colisage	5 kg

Chemical Specifications / Composition Chimique	
Element	% Weight / Poids
Carbon (C)	3,95 max
Iron (Fe)	0,23 max
Titanium (Ti)	0,05 max
Tantalum (Ta)	0,05 mx
Tungsten (W)	Bal

Physical Properties / Propriétés physiques		
Particle Size Distribution / Répartition Granulométrique	< 40 microns -160 + 40 microns +160 + 210 microns	10% max Balance 5 % max
Micro Hardness / Microdureté	2500-3500 Hv0,3	
Specific gravity / Masse spécifique	16,4 g/cm3	

Imprimé d'ordinateur valable sans signature / Computer print out, valid without sign.
TECHNOGENIA QUALITY DEPARTMENT. ISSUED ON THE 26 January 2011

b)

TECHNOGENIA

MATERIAL SAFETY DATA SHEET

TECHNOGENIA S.A.S. - ZA DES MARAIS - BP 151
74410 SAINT-JORIOZ – France
Tel : +33.4.50.68.56.60 - Fax : +33.4.50.68.62.77
E-mail : technogenia@technogenia.fr

TRADE NAME: Spherotène®

Revision date 2006-09-27

1. Identification

Technical designation :	Fused tungsten carbide (spherical particles)
Type of product or uses :	Hardfacing powder for anti-wear protection
Manufacturer :	TECHNOGENIA S.A. ZA Des Marais ; 74410 Saint-Jorioz - France Tel +33.4.50.68.56.60. - Fax .33.4.50.68.62.77. E-Mail : technogenia@technogenia.fr

2. Information on ingredients

Substance	Weight percent	CAS number (Chemical Abstracts Service).	TLV (Threshold limit value recommended by American Conference of Governmental Industrial Hygienists) (mg/m3).	Symbol	Risk phrases
Fused tungsten carbide	100		5 (insoluble tungsten compounds).		

3. Hazards identification

Fused tungsten carbide (96 weight percent tungsten and 4 weight percent carbon) is free of cobalt, nickel and lead.

Inhalation :	Pure fused tungsten carbide has no known hazards other than an inert dust since it is not combined with nickel or cobalt. The dust is irritating for breathing. Inhalation of heavy dust-concentration in the long term may cause lung-disease.
Ingestion :	Unlikely. No identified risk.
Skin contact :	May cause sensitization.
Eye contact :	Unlikely. No identified risk.

4. First aid measures

Inhalation :	Fresh air. If suspect symptoms appear seek medical advice.
Ingestion :	Unlikely. If suspect symptoms appear seek medical advice.
Skin contact :	Wash with mild soap and water. If suspect symptoms appear seek medical advice.
Eye contact :	Rinse with plenty of lukewarm water. If suspect symptoms appear seek medical advice.

5. Fire-fighting measures

Extinguishing media	Dry reactants.

6. Accidental release measures

Spillage of small fragments should be cleared with vacuum equipment. Avoid spillage in water.

7. Handling and storage

AVOID DUST GENERATION.
Store at dry conditions -18°C +38°C.
NORMAL INDUSTRIAL HYGIENE.

8. Exposure controls/Personal protection

Preventive measures :	Use sufficient dust extraction during welding. Wash hands before meals, pauses and at the end of working day.
Personal protection :	In case of insufficient ventilation, suitable respiratory equipment with fine particle filter (P2) must be worn. For welding, wear suitable gloves and goggles.

CONFIDENTIAL

MSDS

issuing date 05 Aug. 10
Presentation and rules of drafting complying with 2001/58/CE.

Page 1 / 2

303

c)

TECHNOGENIA

MATERIAL SAFETY DATA SHEET

TECHNOGENIA S.A.S. - ZA DES MARAIS - BP 151
74410 SAINT-JORIOZ – France
Tel : +33.4.50.68.56.60 – Fax : +33.4.50.68.62.77
E-mail : technogenia@technogenia.fr

TRADE NAME: Spherotène®

Revision date 2006-09-27

9. Physical and chemical properties

General description (form, smell, ; ...) :	Grey, odourless, fine-grained metal powder.
Density :	16.4 g/cm3.
Melting point :	2750°C.
Solubility in organic solvents :	Insoluble.
Solubility in water :	Insoluble.

10. Stability and reactivity

| Chemical stability : | Stable at normal handling and storage conditions. |
| Materials to avoid : | Strong oxidizers and strong acids. |

11. Toxicological information

| On product : | No data available. |
| On ingredients : | Tungsten DL 50 =5000 mg/kg intra peritoneal rat. |

12. Ecological information

| On product : | No data available. |
| On ingredients : | No data available. |

13.Disposal considerations

Dispose in safe manner in accordance with local regulations. Avoid spillage in water.

14. Transport information

| UN-Nr : | None allocated. | IMDG-Code : | None allocated. |
| ICAO / IATA : | None allocated. | Packing : | None allocated. |

15. Regulatory information

Symbol(s) :	
R-phrase(s)	None Classified
S-phrase(s)	None Classified

16. Other information

Existing substances of the product are included in European Inventory of Existing Commercial Chemical Substances (EINECS).
Contents and format of this safety data sheet are in accordance with the EEC commission directive 2001/58/CE.
Disclaimer of liability : information in this safety data sheet was obtained from sources we believe are reliable. However, this information is provided without any warranty, expressed or implied, regarding its correctness. The conditions or methods of handling, storage, use or disposal are beyond our control and maybe beyond our knowledge. For this and other reasons, we do not assume responsibility and expressly disclaim liability for loss, damage or other expense arising out of or in any way connected with the handling, storage, use or disposal of this product.
This safety data sheet was prepared and is to be used only for this product. If this product is used as a component in other products, this safety data sheet may not be applicable.

CONFIDENTIAL

MSDS

issuing date 05 Aug. 10
Presentation and rules of drafting complying with 2001/58/CE.

Page 2 / 2

Figure L-13: Technogenia Spherotene tungsten carbide (WC) from LCT Laser Cladding Technology; a) Materials Certificate, b) and c) Materials safety data sheet

L.4 Shielding and powder transport gases

In welding many different shielding gases are used. However, none of them was tested for the application of metal matrix composite cladding. The following gases were used as shielding gases in this thesis:

- Ar/CO2 (2.5%) BOC Specshield CO2/Ar mixture,
- Pureshield Argon,
- Argon Helium mixture, and
- Pureshield Helium.

Despite the fact that argon, nitrogen or under a special calibration helium can be used as powder transport gas, only pureshield Argon was used for ceramic powder feeding.

The material safety data sheet of the shielding gas Ar/CO2 (2.5%) BOC Specshield CO2/Ar mixture is revealed in figure_apx I-14.

a)

BOC GASES

Specshield 20% CO₂, Ar and Specshield 2.5% CO₂, Ar

PRODUCT: SPECSHIELD CO₂, Ar MSDS NR: 300-15-0002 BOC VERSION: I DATE: 03/07/1997 PAGE: 1/1
FORMERLY: PURESHIELD P3 AND ARGON/CARBON DIOXIDE MIXTURES

1 IDENTIFICATION OF THE SUBSTANCE/ PREPARATION AND OF THE COMPANY

Product name	Specshield CO₂, Ar
Company identification	see footer
Emergency phone Nos	see footer

2 COMPOSITION/INFORMATION ON INGREDIENTS

Substance/ Preparation	Preparation
Components/ Impurities	Contains the following components:
Specshield 20% CO₂, Ar	20% CO₂ balance Ar
Specshield 2.5% CO₂, Ar	2.5% CO₂ balance Ar

3 HAZARDS IDENTIFICATION

Hazards identification	In high concentrations may cause asphyxiation. Compressed gas.

4 FIRST AID MEASURES

Inhalation	In high concentrations may cause asphyxiation and death. Symptoms may include loss of mobility/ consciousness. Victim may not be aware of asphyxiation. Low concentrations of CO₂ cause increased respiration and headache. Remove victim to uncontaminated area wearing self contained breathing apparatus. Keep victim warm and rested. Call a doctor. Apply artificial respiration if breathing stopped.
Ingestion	Ingestion is not considered a potential route of exposure.

5 FIRE FIGHTING MEASURES

Specific hazards	Exposure to fire may cause containers to rupture/explode. Inform Fire Brigade. Non flammable
Hazardous combustion products	None
Suitable extinguishing media	All known extinguishants can be used.
Specific methods	If possible, stop flow of product. Move container away or cool with water from a protected position.
Special protective equipment for fire fighters	In confined space use self-contained breathing apparatus.

6 ACCIDENTAL RELEASE MEASURES

Personal precautions	Evacuate area. Wear self-contained breathing apparatus when entering area unless atmosphere is proved to be safe. Post warning notices. Ensure adequate air ventilation.
Environmental precautions	Try to stop release. Prevent from entering sewers, basements and workpits, or any place where its accumulation can be dangerous.
Clean up methods	Ventilate area.

7 HANDLING AND STORAGE

Handling and storage	Suck back of water into the container must be prevented. Do not allow backfeed into the container. Use only properly specified equipment which is suitable for this product, its supply pressure and temperature. Contact BOC Gases if in doubt. Refer to BOC Gases container handling instructions. Keep container below 50°C in a well ventilated place.

8 EXPOSURE CONTROLS/PERSONAL PROTECTION

Exposure limits	Specshield 20% CO₂, Ar contains carbon dioxide, which has an Occupational Exposure Standard (OES) as described in the Health and Safety Executive Guidance Note EH40. It has a short term exposure limit (STEL) of 15000 vpm (1.5%), and a long term exposure limit (LTEL) of 5000vpm (0.5%). In a confined space, displacement of air may cause the exposure limits to be exceeded before the oxygen level drops below 18%.
Personal protection	Ensure adequate ventilation.

9 PHYSICAL AND CHEMICAL PROPERTIES

Relative density, gas	Heavier than air
Solubility mg/l water	Not known
Appearance/Colour	Colourless gas
Odour	None
Other data	Gas/vapour heavier than air. May accumulate in confined spaces, particularly at or below ground level. Will displace oxygen where ventilation is at a high point only.

10 STABILITY AND REACTIVITY

Stability and reactivity	Stable under normal conditions.

Please photocopy if further copies required

306

b)

SAFETY
DATA
SHEET

II TOXICOLOGICAL INFORMATION

General   Low concentrations cause rapid
                       circulatory insufficiency. Symptoms
                       are headache, nausea and
                       vomiting, which may lead to
                       unconsciousness.

12 ECOLOGICAL INFORMATION

General   No known ecological damage
                       caused by this product.

13 DISPOSAL CONSIDERATIONS

General   Do not discharge into any place
                       where its accumulation could be
                       dangerous. Contact BOC Gases
                       if guidance is required.

14 TRANSPORT INFORMATION

UN Nr   1956

Class/Div   2.2

Labelling ADR   Label 2: non flammable non toxic
                       gas

Other transport   Avoid transport on vehicles
information   where the load space is not
                       separated from the driver's
                       compartment. Ensure vehicle
                       driver is aware of the potential
                       hazards of the load and knows
                       what to do in the event of an
                       accident or an emergency.
                       Before transporting product
                       containers ensure that they are
                       firmly secured and:
                       - cylinder valve is closed and not
                         leaking.
                       - valve outlet cap nut or plug
                         (where provided) is correctly
                         fitted.
                       - valve protection device (where
                         provided) is correctly fitted.
                       - adequate ventilation.
                       - compliance with applicable
                         regulations.

15 REGULATORY INFORMATION

Labelling of cylinders   Road transport symbols are used
- Symbols   and selected according to the
                          most stringent product
                          classification - EC or ADR.
                          Label 2: non flammable
                          non toxic gas.

- Risk phrases   RAs Asphyxiant in high
                          concentrations.

- Safety phrases   S9 Keep container in well
                          ventilated place.
                          S23 Do not breathe the gas.

16 OTHER INFORMATION

Ensure all national/local regulations are observed.

The hazard of asphyxiation is often overlooked and must be
stressed during operator training.

Before using this product in any new process or experiment,
a thorough material compatibility and safety study should be
carried out.

Although this shielding gas alone does not exhibit
toxic/harmful effects, the fumes generated from a welding
process can be hazardous to health.

Always leak check cylinders when first collected, delivered
or used using an approved leak detection fluid.

Details given in this document are believed to be correct at
the time of going to press. Whilst proper care has been
taken in the preparation of this document, no liability for
injury or damage resulting from its use can be accepted.

For further safety information please refer to "Safe Under
Pressure" and "Safe handling, storage and transport of
industrial gas cylinders", both of which are available from
your local BOC Gases outlet.

BOC GASES   A member of The BOC Group
                 The Stripe Symbol and the word BOC are BOC Group Trademarks.

For product and safety enquiries please phone

BOC GASES Directline
0800 111 333

BOC Gases, Customer Service Centre
Priestley Road, Worsley
Manchester M28 2UT
Fax: 0800 111 555

In the Republic of Ireland:
Dublin (01) 409 1800

BOC Gases Ireland
P.O. Box 201, Bluebell
Dublin 12, Republic of Ireland
Fax: 01 409 1081

SFT/007278/BRUK/0997/2M(25)

Please photocopy if further copies required

Figure_Apx L-14: Safety data sheet BOC Gases Specshield 20 % CO₂, Ar and Specshield 2.5 % CO₂, Ar; a) Page1, the chemical composition of the Ar/CO2 (2.5%) BOC Specshield mixture is underlined in yellow; b) Page 2

307

The material safety data sheet of the shielding gas argon (Ar) BOC Pureshield Argon is revealed in figure_apx I-15.

a)

SAFETY DATA SHEET

▰▰▰ BOC GASES

Pureshield Argon

PRODUCT : PURESHIELD ARGON MSDS NR : 300-00-0001 BOC VERSION : 1 DATE : 21/06/1994 PAGE : 1/1

1 IDENTIFICATION OF THE SUBSTANCE/ PREPARATION AND OF THE COMPANY

Product name	Pureshield Argon
Chemical formula	Ar
Company identification	see footer
Emergency phone Nos	see footer

2 COMPOSITION/INFORMATION ON INGREDIENTS

Substance/ Preparation	Substance
Components/ Impurities	Contains no other components or impurities which will influence the classification of the product.
CAS Nr	07440-37-1
EEC Nr (from EINECS)	2311470
Specification	99.998% minimum

3 HAZARDS IDENTIFICATION

Hazards identification Compressed gas.
In high concentrations may cause asphyxiation.

4 FIRST AID MEASURES

Inhalation In high concentrations may cause asphyxiation and death. Symptoms may include loss of mobility/consciousness. Victim may not be aware of asphyxiation.
Remove victim to uncontaminated area wearing self contained breathing apparatus. Keep victim warm and rested. Call a doctor. Apply artificial respiration if breathing stopped.

5 FIRE FIGHTING MEASURES

Specific hazards	Exposure to fire may cause containers to rupture/explode. Inform Fire Brigade Non flammable
Hazardous combustion products	None
Suitable extinguishing media	All known extinguishants can be used.
Specific methods	If possible, stop flow of product. Move container away or cool with water from a protected position.
Special protective equipment for fire fighters	In confined space use self-contained breathing apparatus.

6 ACCIDENTAL RELEASE MEASURES

Personal precautions	Evacuate area. Wear self-contained breathing apparatus when entering area unless atmosphere is proved to be safe. Ensure adequate air ventilation. Post warning notices.
Environmental precautions	Try to stop release. Prevent from entering sewers, basements and workpits, or any place where its accumulation can be dangerous.
Clean up methods	Ventilate area.

7 HANDLING AND STORAGE

Handling and storage Suck back of water into the container must be prevented. Do not allow backfeed into the container. Use only properly specified equipment which is suitable for this product, its supply pressure and temperature. Contact BOC Gases if in doubt. Refer to BOC Gases container handling instructions. Keep container below 50°C in a well ventilated place.

8 EXPOSURE CONTROLS/PERSONAL PROTECTION

Personal protection Ensure adequate ventilation.

9 PHYSICAL AND CHEMICAL PROPERTIES

Molecular weight	40
Melting point	-189°C
Boiling point	-186°C
Critical temperature	-122°C
Relative density, gas	1.38 (air=1)
Relative density, liquid	Not applicable
Vapour pressure 20°C	Not applicable
Solubility mg/l water	61 mg/l
Appearance/Colour	Colourless gas
Odour	No odour warning properties
Other data	Gas/vapour heavier than air. May accumulate in confined spaces, particularly at or below ground level. Will displace oxygen where ventilation is at a high point only.

10 STABILITY AND REACTIVITY

Stability and reactivity Stable under normal conditions.

11 TOXICOLOGICAL INFORMATION

General No known toxicological effects from this product.

12 ECOLOGICAL INFORMATION

General No known ecological damage caused by this product.

b)

13 DISPOSAL CONSIDERATIONS

General — Do not discharge into any place where its accumulation could be dangerous. To atmosphere in a well ventilated place. Contact BOC Gases if guidance is required.

14 TRANSPORT INFORMATION

UN Nr	1006
Class/Div	2.2
ADR/RID Item Nr	2,1a
ADR/RID Hazard Nr	20
Groupcard Nr	20g01
Labelling ADR	Label 2: non flammable non toxic gas

Other transport information — Avoid transport on vehicles where the load space is not separated from the driver's compartment. Ensure vehicle driver is aware of the potential hazards of the load and knows what to do in the event of an accident or an emergency.

Before transporting product containers ensure that they are firmly secured and:
- cylinder valve is closed and not leaking.
- valve outlet cap nut or plug (where provided) is correctly fitted.
- valve protection device (where provided) is correctly fitted.
- adequate ventilation.
- compliance with applicable regulations.

15 REGULATORY INFORMATION

Number in Annex I of Dir 67/548 — Not included in Annex I.

EC Classification — Proposed by the industry. Not classified as dangerous substance.

Labelling of cylinders - Symbols — Road transport symbols are used and selected according to the most stringent product classification - EC or ADR. Label 2: non flammable non toxic gas

- Risk phrases — RAs Asphyxiant in high concentrations.

- Safety phrases — S9 Keep container in well ventilated place.
S23 Do not breathe the gas.

16 OTHER INFORMATION

Ensure all national/local regulations are observed.

The hazard of asphyxiation is often overlooked and must be stressed during operator training.

Before using this product in any new process or experiment, a thorough material compatibility and safety study should be carried out. Although this shielding gas alone does not exhibit toxic/harmful effects, the fumes generated from a welding process can be hazadous to health.

Always leak check cylinders when first collected, delivered or used, using an approved leak detection fluid.

Details given in this document are believed to be correct at the time of going to press.

Whilst proper care has been taken in the preparation of this document, no liability for injury or damage resulting from its use can be accepted.

For further safety information please refer to "Safe Under Pressure" and "Safe handling, storage and transport of industrial gas cylinders", both of which are available from your local BOC Gases outlet.

NOTES

1. Not all cylinder and MCP sizes are available from all locations.
2. The cylinder and MCP's have the same outlet connection designed primarily to receive the gas pressure regulator.
3. The nominal contents in ml are as measured at 15°C and 1013 mb pressure. Actual contents of gas may vary about the nominal figures indicated.
4. The length includes an allowance of 70 mm for the cylinder valve.
5. This is the weight of the cylinder without gas but including the cylinder valve. Some cylinders manufactured to older standards may weigh more than this. Add the nominal weight of gas to obtain the weight of a full cylinder.
6. The manifolded cylinder pallets comprise 15 cylinders all connected to a single outlet.
7. The outlet pressure of 300 bar cylinders is internally limited to approximately 60 bar.

CYLINDER CHARACTERISTICS

Cylinder Size (see Note 1)	Outlet Connection (see Note 2)	Nominal Contents (see Note 3) (ml)	Maximum Filled Pressure at 15°C (bar) (see note 7)	Nominal Weight of Gas (see Note 3) (kg)	Approx. Dimensions (see Note 4) (mm)	Approx. Cylinder Weight (see Note 5) (kg)
V Shieldpak 6	5/8" BSP Female	2.07	200	3.5	140 x 940	17
X Shieldpak 6		2.36	230	4.0	140 x 940	17
S Shieldpak 12	Right Hand	3.81	200	6.5	203 x 870	30
T Shieldpak 12	Cone	4.14	200	7.0	203 x 910	30
Y Shieldpak 12	Recessed	4.72	230	8.0	203 x 910	30
N		9.66	200	16.5	230 x 1460	65
W		11.01	230	18.6	230 x 1460	65
A		13.98	300	23.5	230 x 1460	65

Manifolded Cylinder Pallets (MCP's) (see Notes 1 & 6)	Outlet Connection (see Note 2)	Number of Cylinders	Nominal Contents (see Note 3) (m³)	Maximum Filled Pressure at 15°C (bar)	Nominal Weight of Gas (see Note 3) (kg)	Approx. Dimensions Including Cylinders (mm)	Maximum Gross Weight Incl Cyls & Gas (kg)
WN	5/8" BSP Female Right Hand Cone Recessed	15 x N	144.9	200	247.5	1290 x 1810 x 840	1500
WW		15 x W	165.1	230	279	1290 x 1810 x 840	1500

BOC GASES

A member of The BOC Group
The Stripe Symbol and the word BOC are BOC Group Trademarks.

For product and safety enquiries please phone

In the United Kingdom:
0800 111 333

In the Republic of Ireland:
Dublin (01) 450 1444

BOC Gases
Priestley Road, Worsley
Manchester M28 2UT
Fax: 0800 111 555

BOC Gases
P.O. Box 201
Bluebell, Dublin 12
Fax: 01 450 7054

SFT/00727S/BRUK/1097/5M(25)

Figure_Apx L-15: Safety data sheet BOC Gases Pureshield Argon; a) Page1; b) Page 2

The material safety data sheet of the shielding gas Argon Helium mixture (Ar/He 50/50) BOC Alushield Universal is revealed in figure_apx I-15.

a)

BOC GASES

Alushield
Light • Universal • Heavy

PRODUCT: ALUSHIELD HEAVY • LIGHT • UNIVERSAL MSDS NR: 300-10-0001 BOC VERSION: 2 DATE: 03/07/1997 PAGE: 1/1
FORMERLY: HELISHIELD H2/H3/H5 AND OTHER HELIUM/ARGON MIXTURES

1 IDENTIFICATION OF THE SUBSTANCE/ PREPARATION AND OF THE COMPANY

Product name	Alushield Heavy/Light/Universal
Company identification	see footer
Emergency phone Nos	see footer

2 COMPOSITION/INFORMATION ON INGREDIENTS

Substance/ Preparation	Preparation
Components/ Impurities	Alushield Heavy 75% He balance Ar
	Alushield Light 30% He balance Ar
	Alushield Universal 50% He balance Ar

3 HAZARDS IDENTIFICATION

Hazards identification — In high concentrations may cause asphyxiation. Compressed gas

4 FIRST AID MEASURES

Inhalation — In high concentrations may cause asphyxiation and death. Symptoms may include loss of mobility/ consciousness. Victim may not be aware of asphyxiation. Remove victim to uncontaminated area wearing self contained breathing apparatus. Keep victim warm and rested. Call a doctor. Apply artificial respiration if breathing stopped.

Ingestion — Ingestion is not considered a potential route of exposure.

5 FIRE FIGHTING MEASURES

Specific hazards — Exposure to fire may cause containers to rupture/explode. Inform Fire Brigade. Non-flammable.

Hazardous combustion products — None

Suitable extinguishing media — All known extinguishants can be used.

Specific methods — If possible, stop flow of product. Move container away or cool with water from a protected position.

Special protective equipment for fire fighters — In confined space use self-contained breathing apparatus

6 ACCIDENTAL RELEASE MEASURES

Personal precautions — Evacuate area. Wear self-contained breathing apparatus when entering area unless atmosphere is proved to be safe. Ensure adequate air ventilation. Post Warning Notices

Environmental Precautions — Try to stop release.

Clean up methods — Ventilate area.

7 HANDLING AND STORAGE

Handling and storage — Suck back of water into the container must be prevented. Do not allow backfeed into the container. Use only properly specified equipment which is suitable for this product, its supply pressure and temperature. Contact BOC Gases if in doubt. Refer to BOC Gases container handling instructions. Keep container below 50°C in a well ventilated place.

8 EXPOSURE CONTROLS/PERSONAL PROTECTION

Personal protection — Ensure adequate ventilation.

9 PHYSICAL AND CHEMICAL PROPERTIES

Relative density, gas	Lighter or similar to air
Solubility mg/l water	Not known.
Appearance/Colour	Colourless gas
Odour	None

10 STABILITY AND REACTIVITY

Stability and reactivity — Stable under normal conditions.

11 TOXICOLOGICAL INFORMATION

General — No known toxicological effects from this product.

12 ECOLOGICAL INFORMATION

General — No ecological damage caused by this product.

13 DISPOSAL CONSIDERATIONS

General — Do not discharge into any place where its accumulation could be dangerous. Contact BOC Gases if guidance is required.

Please photocopy if further copies required

b)

SAFETY DATA SHEET

14 TRANSPORT INFORMATION

UN Nr	1956
Class/Div	2.2
Labelling ADR	Label 2: non flammable non toxic gas
Other transport information	Avoid transport on vehicles where the load space is not separated from the driver's compartment. Ensure vehicle driver is aware of the potential hazards of the load and knows what to do in the event of an accident or an emergency.

Before transporting product containers ensure that they are firmly secured and:
- cylinder valve is closed and not leaking
- valve outlet cap nut or plug (where provided) is correctly fitted
- valve protection device (where provided) is correctly fitted
- adequate ventilation.
- compliance with applicable regulations.

15 REGULATORY INFORMATION

Labelling of cylinders

- Symbols	Road transport symbols are used and selected according to the most stringent product classification - EC or ADR .
- Risk phrases	RAs Asphyxiant in high concentrations.
- Safety phrases	S9 Keep container in well ventilated place. S23 Do not breathe the gas.

16 OTHER INFORMATION

Ensure all national/local regulations are observed.

The hazard of asphyxiation is often overlooked and must be stressed during operator training.

Before using this product in any new process or experiment, a thorough material compatibility and safety study should be carried out. Although this shielding gas alone does not exhibit toxic or harmful effects, the fumes generated from a welding process can be hazardous to health.

Always leak check cylinders when first collected, delivered or used, using an approved leak detection fluid.

Details given in this document are believed to be correct at the time of going to press.

Whilst proper care has been taken in the preparation of this document, no liability for injury or damage resulting from its use can be accepted.

For further safety information please refer to "Safe Under Pressure" and "Safe handling, storage and transport of industrial gas cylinders", both of which are available from your local BOC Gases outlet.

BOC GASES

A member of The BOC Group
The Stripe Symbol and the word BOC are BOC Group Trademarks.

For product and safety enquiries please phone

BOC GASES Directline
0800 111 333

In the Republic of Ireland:
Dublin (01) 409 1800

BOC Gases, Customer Service Centre
Priestley Road, Worsley
Manchester M28 2UT
Fax: 0800 111 555

BOC Gases Ireland
P.O. Box 201, Bluebell
Dublin 12, Republic of Ireland
Fax: 01 409 1081

SFT/007286/BRUK/0498/5M(25)

Please photocopy if further copies required

Figure_apx L-16: Safety data sheet BOC Gases Alushield Light Universal Heavy; a) Page1, the chemical composition of the Ar/He 50/50 mixture BOC Alushield Universal is underlined in yellow; b) Page 2

The material safety data sheet of the shielding gas helium (He) BOC Helium, compressed is revealed in figure_apx I-17.

a)

BOC
A Member of The Linde Group

Safety data sheet
Helium, compressed.

| Creation date : | 27.01.2005 | Version : 1.4 | GB / E | SDS No. : 8312 |
| Revision date : | 01.04.2011 | | | page 1 / 4 |

SECTION 1: Identification of the substance/mixture and of the company/undertaking

1.1. Product Identifier
Product name
Helium, compressed.
Trade name
Balloon Gas

EC No (from EINECS): 231-168-5
CAS No: 7440-59-7
Index-Nr. -
Chemical formula He
REACH Registration number:
Listed in Annex IV/V of Regulation (EC) No 1907/2006 (REACH), exempted from registration.

1.2. Relevant identified uses of the substance or mixture and uses advised against
Relevant identified uses
Industrial and professional. Perform risk assessment prior to use.
Uses advised against
Do not breathe the gas., Inhaling helium may cause asphyxiation followed by death.

1.3. Details of the supplier of the safety data sheet
Company Identification
BOC, Priestley Road, Worsley, Manchester M28 2UT
E-Mail Address ReachSDS@boc.com

1.4. Emergency telephone number
Emergency phone numbers (24h): 0800 111 333

SECTION 2: Hazards identification

2.1. Classification of the substance or mixture

Classification acc. to Regulation (EC) No 1272/2008/EC (CLP/GHS)
Press. Gas (Compressed gas) - Contains gas under pressure; may explode if heated.

Classification acc. to Directive 67/548/EEC & 1999/45/EC
Not classified as hazardous to health.
Asphyxiant in high concentrations.
Risk advice to man and the environment
In high concentrations may cause asphyxiation.
Compressed gas.

2.2. Label elements
- Labelling Pictograms

- Signal word
Warning

- Hazard Statements
| H280 | Contains gas under pressure; may explode if heated. |
| EIGA-As | Asphyxiant in high concentrations. |

- Precautionary Statements

Precautionary Statement Prevention

None.

Precautionary Statement Response
None.

Precautionary Statement Storage
P403   Store in a well-ventilated place.

Precautionary Statement Disposal
None.

2.3. Other hazards
None.

SECTION 3: Composition/information on ingredients

Substance / Mixture: Substance.

3.1. Substances
Helium, compressed.
CAS No: 7440-59-7
Index-Nr.: -
EC No (from EINECS): 231-168-5
REACH Registration number:
Listed in Annex IV/V of Regulation (EC) No 1907/2006 (REACH), exempted from registration.
Contains no other components or impurities which will influence the classification of the product.

3.2. Mixtures
Not applicable.

SECTION 4: First aid measures

4.1. Description of first aid measures
First Aid General Information:
Remove victim to uncontaminated area wearing self contained breathing apparatus. Keep victim warm and rested. Call a doctor. Apply artificial respiration if breathing stopped.
First Aid Inhalation:
Remove victim to uncontaminated area wearing self contained breathing apparatus. Keep victim warm and rested. Call a doctor. Apply artificial respiration if breathing stopped.
First Aid Skin / Eye:
Adverse effects not expected from this product.
First Aid Ingestion:
Ingestion is not considered a potential route of exposure.

4.2. Most important symptoms and effects, both acute and delayed
In high concentrations may cause asphyxiation. Symptoms may include loss of mobility/consciousness. Victim may not be aware of asphyxiation.

4.3. Indication of any immediate medical attention and special treatment needed
None.

SECTION 5: Fire fighting measures

5.1. Extinguishing media
Suitable extinguishing media
All known extinguishants can be used.

5.2. Special hazards arising from the substance or mixture
Specific hazards

8312 / EDV / 29.03.2011

b)

BOC
A Member of The Linde Group

Safety data sheet
Helium, compressed.

Creation date :	27.01.2005	Version : 1.4	GB / E SDS No. : 8312
Revision date :	01.04.2011		page 2 / 4

Exposure to fire may cause containers to rupture/explode.
Hazardous combustion products
None.

5.3. Advice for fire-fighters
Specific methods
If possible, stop flow of product. Move container away or cool with water from a protected position.
Special protective equipment for fire-fighters
In confined space use self-contained breathing apparatus.

SECTION 6: Accidental release measures

6.1. Personal precautions, protective equipment and emergency procedures
Evacuate area. Wear self-contained breathing apparatus when entering area unless atmosphere is proved to be safe. Ensure adequate air ventilation.

6.2. Environmental precautions
Try to stop release.

6.3. Methods and material for containment and cleaning up
Ventilate area.

6.4. Reference to other sections
See also sections 8 and 13.

SECTION 7: Handling and storage

7.1. Precautions for safe handling
Suck back of water into the container must be prevented. Use only properly specified equipment which is suitable for this product, its supply pressure and temperature. Contact your gas supplier if in doubt. Refer to supplier's handling instructions. Do not allow backfeed into the container. Only experienced and properly instructed persons should handle gases under pressure. Protect cylinders from physical damage; do not drag, roll, slide or drop. Never use direct flame or electrical heating devices to raise the pressure of a container. Do not remove or deface labels provided by the supplier for the identification of the cylinder contents. When moving cylinders, even for short distances, use a cart (trolley, hand truck, etc.) designed to transport cylinders. Leave valve protection caps in place until the container has been secured against either a wall or bench or placed in a container stand and is ready for use. Ensure the complete gas system has been (or is regularly) checked for leaks before use. If user experiences any difficulty operating cylinder valve discontinue use and contact supplier. Close container valve after each use and when empty, even if still connected to equipment. Never attempt to repair or modify container valves or safety relief devices. Damaged valves should be reported immediately to the supplier. Replace valve outlet caps or plugs and container caps where supplied as soon as container is disconnected from equipment. Keep container valve outlets clean and free from contaminates particularly oil and water. Never attempt to transfer gases from one cylinder/container to another. Do not smoke while handling product. The substance must be handled in accordance with good industrial hygiene and safety procedures.

7.2. Conditions for safe storage, including any incompatibilities
Keep container below 50°C in a well ventilated place. Observe all regulations and local requirements regarding storage of containers. Containers should not be stored in conditions likely to encourage corrosion. Containers should be stored in the vertical position and properly secured to prevent falling over. Stored containers should be periodically checked for general conditions and leakage. Container valve guards or caps should be in place. Store containers in location

free from fire risk and away from sources of heat and ignition. Keep away from ignition sources (including static discharges). Keep away from combustible materials.

7.3. Specific end use(s)
None.

SECTION 8: Exposure controls/personal protection

8.1. Control parameters
No occupational exposure limit.

8.2. Exposure controls
Appropriate engineering controls
Product to be handled in a closed system. Oxygen detectors should be used when asphyxiating gases may be released. The substance must be handled in accordance with good industrial hygiene and safety procedures. Consider work permit system e.g. for maintenance activities. Systems under pressure should be regularly checked for leakages. Provide adequate general or local ventilation.
Personal protective equipment
Eye and face protection
Wear eye protection to EN 166 when using gases.
Skin protection
Other protection
Wear leather safety gloves and safety shoes when handling cylinders.
Respiratory protection
Not required
Thermal hazards
Not required
Environmental Exposure Controls
Specific risk management measures are not required beyond good industrial hygiene and safety procedures. Refer to local regulations for restriction of emissions to the atmosphere. See section 13 for specific methods for waste gas treatment.

SECTION 9: Physical and chemical properties

9.1. Information on basic physical and chemical properties
General information
Appearance/Colour: Colourless gas.
Odour: None.
Melting point: -272,2 °C
Boiling point: -269 °C
Flash point: Not applicable for gases and gas mixtures.
Flammability range: Non flammable.
Vapour Pressure 20 °C: Not applicable.
Relative density, gas: 0,14
Solubility in water: 1,5 mg/l
Autoignition temperature: Not applicable.
Explosive properties:
Explosive acc. EU legislation: Not explosive.
Explosive acc. transp. reg.: Not explosive.
Oxidising properties: Not applicable.
Molecular weight: 4 g/mol
Critical temperature: -268 °C
Relative density, liquid: 0,12

9.2. Other information
None.

SECTION 10: Stability and reactivity

c)

Safety data sheet
Helium, compressed.

10.1. Reactivity
Unreactive under normal conditions.

10.2. Chemical stability
Stable under normal conditions.

10.3. Possibility of hazardous reactions
None.

10.4. Conditions to avoid
None.

10.5. Incompatible materials
No reaction with any common materials in dry or wet conditions.

10.6. Hazardous decomposition products
Under normal conditions of storage and use, hazardous decomposition products should not be produced.

SECTION 11: Toxicological information

11.1. Information on toxicological effects
General
No known toxicological effects from this product.

SECTION 12: Ecological information

12.1. Toxicity
No ecological damage caused by this product.

12.2. Persistence and degradability
Not applicable.

12.3. Bioaccumulative potential
Not applicable.

12.4. Mobility in soil
The substance is a gas, not applicable.

12.5. Results of PBT and vPvB assessment
Not classified as PBT or vPvB.

12.6. Other adverse effects
No ecological damage caused by this product.

SECTION 13: Disposal considerations

13.1. Waste treatment methods
Do not discharge into any place where its accumulation could be dangerous. Vent to atmosphere in a well ventilated place. Contact supplier if guidance is required.
EWC Nr. 16 05 05

SECTION 14: Transport information

ADR/RID

14.1. UN number
1046

14.2. UN proper shipping name
Helium, compressed

14.3. Transport hazard class(es)
Class: 2

Classification Code: 1A
Labels: 2.2
Hazard number: 20
Emergency Action Code: 2T

14.4. Packing group (Packing Instruction)
P200

14.5. Environmental hazards
None.

14.6. Special precautions for user
None.

IMDG

14.1. UN number
1046

14.2. UN proper shipping name
Helium, compressed

14.3. Transport hazard class(es)
Class: 2.2
Labels: 2.2
EmS: FC, SV

14.4. Packing group (Packing Instruction)
P200

14.5. Environmental hazards
None.

14.6. Special precautions for user
None.

14.7. Transport in bulk according to Annex II of MARPOL73/78 and the IBC Code
Not applicable.

IATA

14.1. UN number
1046

14.2. UN proper shipping name
Helium, compressed

14.3. Transport hazard class(es)
Class: 2.2
Labels: 2.2

14.4. Packing group (Packing Instruction)
P200

14.5. Environmental hazards
None.

14.6. Special precautions for user
None.

Other transport information
Avoid transport on vehicles where the load space is not separated from the driver's compartment. Ensure vehicle driver is aware of the potential hazards of the load and knows what to do in the event of an accident or an emergency. Before transporting product containers ensure that they are firmly secured. Ensure that the cylinder valve is closed and not leaking. Ensure that the valve outlet cap nut or plug (where provided) is correctly fitted. Ensure that the

d)

BOC
A Member of The Linde Group

Safety data sheet
Helium, compressed.

valve protection device (where provided) is correctly fitted. Ensure adequate ventilation. Ensure compliance with applicable regulations.

SECTION 15: Regulatory information

15.1. Safety, health and environmental regulations/legislation specific for the substance or mixture
Seveso Directive 96/82/EC: Not covered.

15.2. Chemical safety assessment
A CSA does not need to be carried out for this product.

SECTION 16: Other information

Ensure all national/local regulations are observed. The hazard of asphyxiation is often overlooked and must be stressed during operator training. Before using this product in any new process or experiment, a thorough material compatibility and safety study should be carried out.
Advice
Whilst proper care has been taken in the preparation of this document, no liability for injury or damage resulting from its use can be accepted. Details given in this document are believed to be correct at the time of going to press.
Further information
Note:
When using this document care should be taken, as the decimal sign and its position complies with rules for the structure and drafting of international standards, and is a comma on the line.
As an example 2,000 is two (to three decimal places) and not two thousand, whilst 1.000 is one thousand and not one (to three decimal places).

End of document

8312 / EDV / 29.03.2011

Figure_apx L-17: Safety data sheet BOC Gases Helium, compressed; a) Page1; b) Page 2; c) Page 3; d) Page 4

L.5 Pin-on-Disc wear test consumables

The wear pin of the POD is made of the pad material displayed in figure_apx l-18.

a)

FERODO™

THE FIRST NAME IN BRAKES

TECHNICAL DATA SHEET

FERODO 3216F

Description

Ferodo 3216F is a non asbestos-conformable pad suitable for mainline and LRV applications

Applications

Ferodo 3216F is used on various Mainline and Tram / Metro applications throughout Europe.

Characteristics

Ferodo 3216F offers:

> Suitable for a wide range of speeds.
> Suitable for a wide range of loads.
> 0.35 µ pad with good wet performance.
> High temperature pad.
> Noise free.
> Suitable for axle and wheel mounted discs.
> Excellent pad wear.
> Suitable for use with cast iron and steel discs.

FERODO 3216F PAD

FEDERAL MOGUL

Figure_apx L-18: Technical data sheet of the Ferodo 3216F pad, from which the POD test pins are made; a) Page 1; b) Page 2

- blank -